Functional Optical Surfaces by Colloidal Self-assembly: Colloid-to-film Coupled Cavities and Colloidal Lattices

Habilitationsschrift

vorgelegt

dem Bereich Mathematik und Naturwissenschaften

der Technischen Universität Dresden

von

Dr. rer. nat. Tobias A.F. König

geboren am 28. September 1978 in Karlsruhe

Eingereicht am: 13. Mai 2020

Tag der Probevorlesung bzw. des Abschlusses des Verfahrens durch den Fakultätsrat: 4. Dezember 2020

Die Habilitationsschrift wurde in der Zeit von September 2015 bis

Mai 2020 im Fachgebiet Physikalische Chemie angefertigt.

1   Abstract

Future developments in nanophotonics require facile, inexpensive and parallelizable fabrication methods and need a fundamental understanding of the spectroscopic properties of such nanostructures. These challenges can be met through colloidal self-assembly where pre-synthesized colloids are arranged over large areas at reasonable cost. As so-called colloidal building blocks, plasmonic nanoparticles and quantum dots are used because of their localized light confinement and localized light emission, respectively. These nanoscopic colloids acquires new hybrid spectroscopic properties through their structural arrangement. To explore the energy transfer between these nanoscopic building blocks, concepts from physical optics are used and implemented with the colloidal self-assembly approach from physical chemistry. Through an established synthesis, the nanocrystals are now available in large quantities, any they receive the tailored spectroscopic properties through directed self-assembly. Moreover, the tailored properties of the colloids and the use of stimuli-responsive polymers allow a functionality that goes beyond current developments. The basics developed in this habilitation thesis can lead to novel functional devices in the field of smart sensors, dynamic light modulators, and large-area quantum devices.

Zusammenfassung in deutscher Sprache

Zukünftige Entwicklungen in der Nanophotonik erfordern einfache, kostengünstige und parallelisierbare Herstellungsmethoden und benötigen ein grundlegendes Verständnis der spektroskopischen Eigenschaften solcher Nanostrukturen. Diese Herausforderungen können durch kolloidale Selbstorganisation erfüllt werden, bei der kostengünstige und zuvor synthetisierte Kolloide großflächig angeordnet werden. Als sogenannte kolloide Bausteine werden wegen ihrer lokalisierten Lichtfokussierung unterhalb der Beugungsbegrenzung plasmonische Nanopartikel sowie wegen ihrer lokalisierten Lichtemission Quantenpunkte verwendet. Diese nanoskopischen Kolloide werden in dieser Habilitationsschrift verwendet und durch Selbstanordnung in ihre gewünschte Nanostruktur gebracht, die neue hybride Eigenschaften aufweist. Um den Energietransfer zwischen diesen nanoskopischen Bausteinen zu untersuchen, werden Konzepte aus der physikalischen Optik verwendet und mit dem kolloidalen Selbstorganisationskonzept aus der physikalischen Chemie großflächig umgesetzt. Durch eine etablierte Synthese sind die Nanokristalle nun in großen Mengen verfügbar, wobei sie durch gerichtete Selbstorganisation die gewünschten spektroskopischen Eigenschaften erhalten. Darüber hinaus ermöglicht die Verwendung von stimulierbaren Polymeren eine Funktionalität, die über die bisherigen Entwicklungen hinausgeht. Die in dieser Habilitationsschrift entwickelten Grundlagen können bei der Entwicklung neuartiger Funktionsgeräte im Bereich für intelligente Sensorik, dynamischer Lichtmodulatoren und großflächiger Quantengeräte genutzt werden.

Table of content

2   State of the art

2.1   Metallic and semiconductive nanocrystals as colloidal building blocks

On a macroscopic scale, gold is yellow (Figure 1). A fascinating color change occurs when the size of gold particles reaches the nanoscopic scale: the gold becomes ruby-red. The reason for this is that incident light can now couple to the free electrons of the metal, which results in a localized osziallation. This effect is also known as localized surface plasmon resonance, and the nanoscale gold is deemed a plasmonic nanoparticle.[1] As nanoparticles, they exhibit scattering and absorption, which can be influenced by the coinage metal material, environment, size and geometry. The scientific evaluation of this effect begins with the chemical synthesis of colloidal gold by Michael Faraday.[2] Colloidal gold can be achieved by reducing chloroauric acid and adding sodium citrate as a stabilizing agent. Taking into account the general safety rules, this synthesis in a heated aqueous solution can be carried out on a desk.[3] With this method particles between 10 and 20 nm can be synthesized.[4] Larger particles can also be synthesized, whereby the size distribution increases and other non-spherical geometries occur more frequently. To meet today's requirements for a uniform particle size and shape, the seed-mediated growth method has been established. This approach separates the processes of nucleation and growth. The nuclides (or seeds) are created first by a fast reduction with a strong reducing agent. This step is followed by a controlled overgrowth to achieve the anticipated colloid.[5] A variety of particle sizes and particle shapes at various materials can be synthesized today, which are summarized in the review article by Xia.[6]
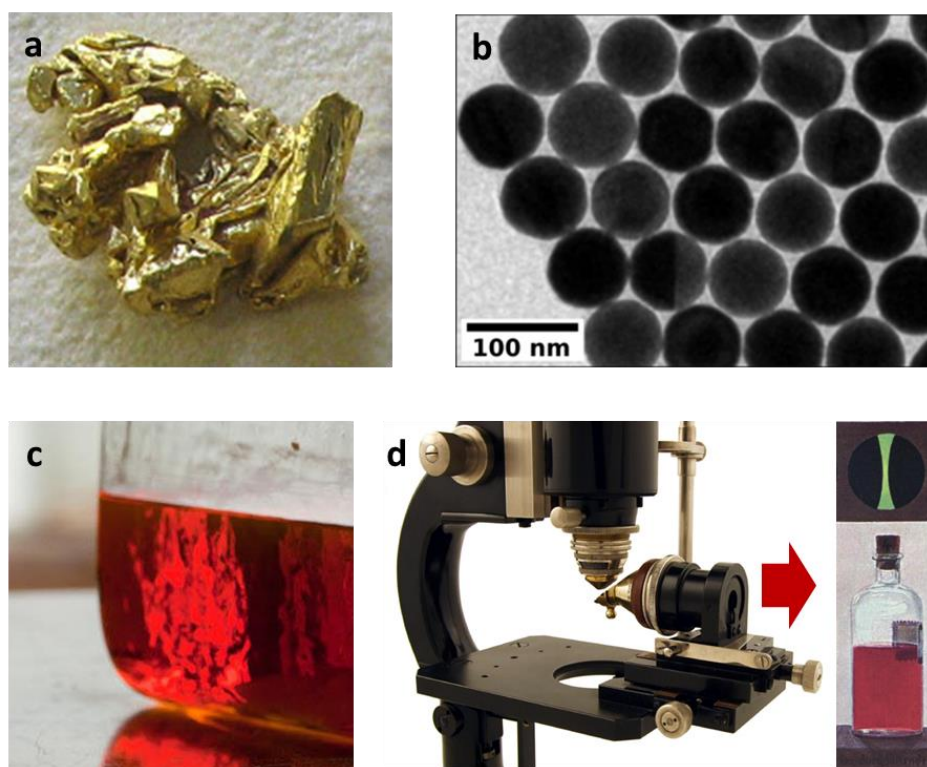
Figure 1: (a) Native gold nuggets. (b) Chemically synthesized gold nanoparticles.[7] (c) Suspension of colloidal gold synthesized by Michael Faraday in 1856.[2] The photo was taken 2015 in the basement laboratory of Royal Institution by Paul Wilkinson. (d) Immersion ultramicroscope according to Richard A. Zsigmondy from Winkel-Zeiss from 1930. The sample is observed perpendicular to the light exposure. The insert shows a painted picture by looking through the microscope (top image: green scattered light only) and the used colloidal gold solution in a flask (bottom image).[8]

This development in liquid synthesis methods is closely linked to the developments in theoretical and analytical methods. Richard A. Zsigmondy developed the immersion ultramicroscope known today as the dark field microscope.[8] With this method it was determined that the synthesized liquid must consist of nanoscaled colloidal particles, which cannot be observed in a regular microscope. Gustav Mie developed the theory of scattering and absorption by spherical particles, which is known today as the Mie theory.[9] With this knowledge, we can now describe the color scheme in Figure 1d. Golden nanoparticles with a size between 5 and 40 nm effectively absorb and scatter the light in the green color range. Their complementary color results in the color ruby-red, which can be observed with the naked eye. Other advanced microscopy methods have also made an important contribution to colloid research, such as scanning probe microscopy and electron microscopy.[10] This intermeshing between theory, synthesis and analysis has led to a multitude of applications of colloids. The plasmonic nanoparticle effect is most often applied as a sensor, since the slightest changes in the environment (up to one molecule) can be detected as a spectral change due to the localized field enhancement.[11] These advances in sensor technology are closely linked to bio or medical applications, such as tumor detection.[12] Recently, the plasmonic response has been used for plasmonic coloring.[13] This small selection should illustrate the potential of the plasmonic nanoparticles which will be used in this thesis in the context of nanophotonics. This means that the colloidal approach is combined with the basics and applications of optical processes such as energy transfer, storage and processing below the limit of diffraction.
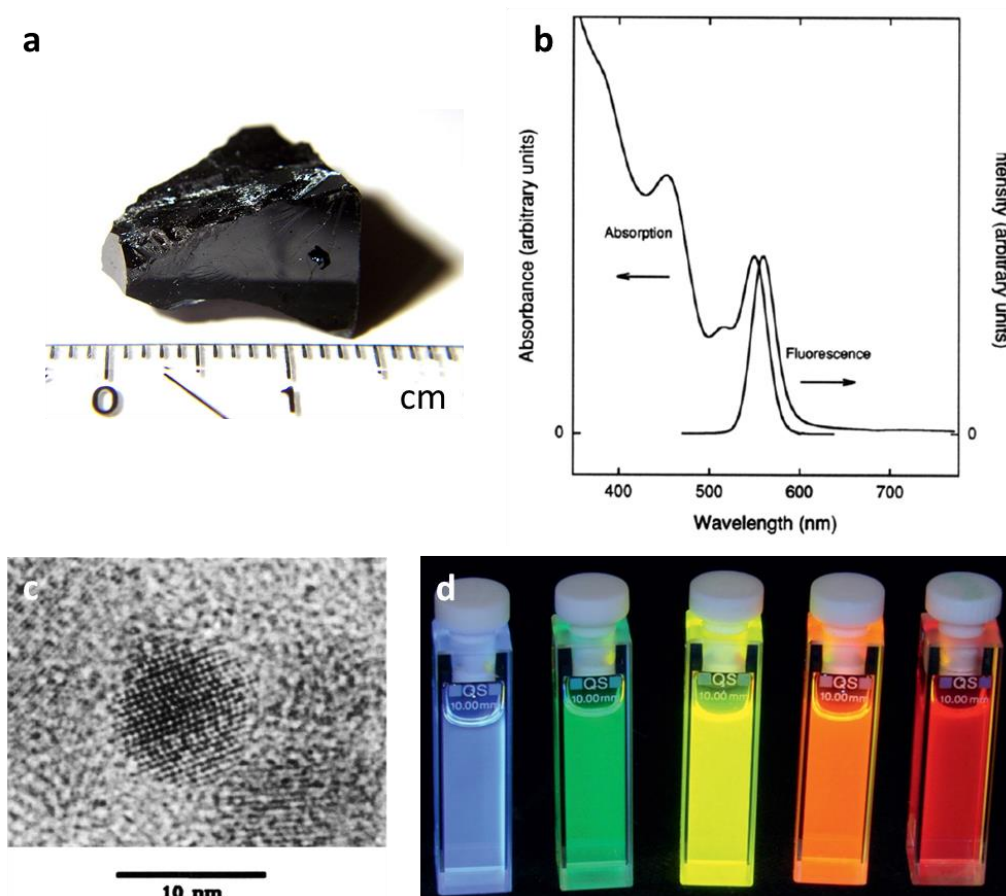

Figure 2: (a) Cadmium telluride in high purity. (b) Absorption and photoluminiscence spectra of a 0.35 nm and (c) electron bright field image of 0.8 nm sized cadmiumselenid nanocrystal.[14] (d) Representative photoluminiescence image of various nanocrystals who cover the full visible spectral range.[15]

An important aspect of nanoscopic colloids is their large surface area compared to their small volume. This ratio determines the chemical and physical properties of the nanoparticle and leads to the variety of applications of plasmonic nanoparticles. Instead of using a noble metal material, colloids can also be synthesized with a semiconducting material, such as cadmium telluride (Figure 2). Such nanocrystals can be synthesized by a so called hot-injection method, which was first established by Moungi Bawendi.[14] Reducing their dimensions to the De Broglie wavelength of the electron (<7.6 nm in vacuum) leads to characteristic changes in the electric and optical properties. This discovery and description of discrete absorption (quantum confinement) can be traced back to Louis E. Brus[16] and Alexander Efros.[17] This relatively young field of research in comparison to plasmonics has already significantly influenced the development of nanophotonics applications. The precisely adjustable photoluminescence make these quantum dots suitable for photonics applications such as photovoltaics,[18] display technology[19] and photocatalysts.[20] Recent improvement in the synthesis made it possible for the crystals not only to be present as a quantum point but also in the form of quantum rods, quantum platelets and other geometries. [21]

The metallic and semiconductive crystals generally differ in size by a factor of one hundred, and in order to create an assembly, the ligands and solvents must be similar. It is mainly electrostatic interactions, therefore, that are used to assemble those colloids. Exploring the potential of the arrangement is part of the following section, which concepts can be transferred to semiconductive nanocrystals.

2.2 Concept of large-scale colloidal self-assembly

Self-assembly is defined by building blocks that are ordered either by direct or indirect interaction to form macroscopic structures.[22] This self-assembly is associated with a thermodynamic equilibrium, *i.e.* that an organized structure is characterized by a minimum in free energy.[23] This interaction can take place through external/interparticle forces or indirectly through a template. It is noteworthy that self-assembly methods show a clear advantage in comparison to size-limited, time-limited and cost-intensive electron (ion) beam or pick-and-place methods, such as optical tweezers and scanning probe microscopy (all top-down methods). On the other hand, self-assembly mechanisms are programmable, scalable and robust; this makes the method very important for applications in nanophotonics.
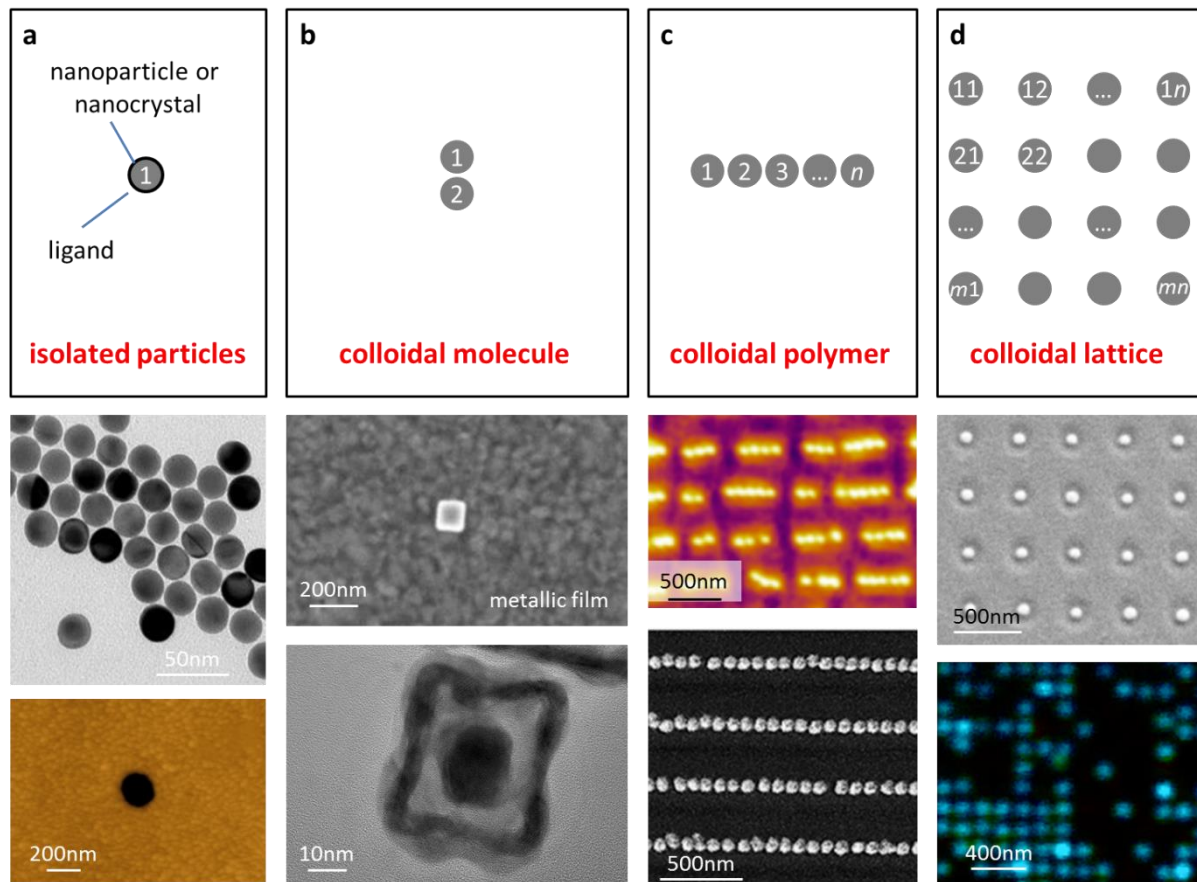

Figure 3: Self-assembly concept by incremental increase in the number of nanoscaled colloids. (a) Isolated particles stabilized with a ligand can be synthesized on a large scale using wet chemistry. Transmission electron microscopy (TEM) image of gold nanospheres[24] and atomic force microscopy (AFM) image of a nanohole.[25] Note, the same spectroscopic response can be obtained by the inverse structure. (b) Near-field coupling by a colloidal molecule. Scanning electron microscope (SEM) image of silver nanocube in a colloid-to-film coupled cavity[26] and TEM image of core-shell cavity.[27] (c) Collective coupling by a plasmonic polymer. AFM image of short plasmonic oligomers[28] and SEM image plasmonic polymers.[29] (d) From near-field coupling to far-field by colloidal lattice. SEM image of a plasmonic square lattice[30] and fluorescence lifetime image of photoluminescence colloids.

This habilitation thesis focuses on the spontaneous organization of pre-existing colloids, which are organized on the basis of particle interactions or pre-existing templates. Figure 3 shows the concept and selected results to create complex nanostructures in a stepwise fashion. This concept includes the arrangement of particles of the same type only. To achieve these structures, it is essential to

control the chemical and physical properties of the particles and surfaces together with their interactions. For individual particles or for an arrangement, the particles must be stable in the solution. This is ensured by the ligand, which is typically organic. The ligand can also determine the distance between the particles (spacer material) and is important for the interaction with the surface. The Figure 3a shows particles that are stabilized with the surfactant hexadecyltrimethylammonium chloride (CtaC), which results in a shell thickness of about 2 nm.[24] Note, the capping agent can also be modified or replaced in a further step by functionalization or ligand exchange. The selection of the appropriate ligand for the appropriate purpose can be found in the progress report of Fery *et al.*[31] An inverse structure, which shows the same spectroscopic property, can be produced by depositing an assembly of polystyrene particles followed by the deposition of a gold film and finally a particle lift-off step.[25]

Colloidal molecules can be arranged either in solution with the appropriate linker[32] or DNA origami.[33] Other self-assembly routes have been shown with Van der Waals,[34] electrostatic,[35] or magnetic interactions.[36] However, these methods show some disadvantages such as limited robustness, scalability or throughput. A scalable approach requiring reasonable effort is to create a colloidal molecule through a colloid-to-film coupled system[37] or a by plasmonic core-shell particle.[27] For device integration, the challenge of positioning large numbers of colloids with nanometer precision still remains.

This bottleneck can be solved by using template-assisted self-assembly. The role of the template is to guide self-assembly towards the anticipated structure. This function can be fulfilled by specific chemical bonds,[38] electric fields,[39] barriers[40] or by topographical traps.[41] For this purpose, the templates must be matched to the nanoparticles in terms of their size, shape and surface chemistry. Suitable templates for self-assembly can be fabricated by sub-micron-sized chemical contrast,[42] nano/micro-contact printing,[43] micro-phase separation (e.g. block-copolymers),[44] mechanical instabilities[45] or lithography.[40, 46] Isa *et al.* have studied a capillary self-assembly method on a topographical template.[47] The authors pointed out that the driving force is the moving meniscus at the predefined template, which forces the spherical polystyrene particles (diameter 1 µm) into a predefined trap. Vaia *et al.* have shown that this template-assisted self-assembly method also works for anisotropic plasmonic particles (dimensions <100 nm) using electrostatic and hydrophobic selectivity.[43a] With this template-based approach, plasmonic particles with any geometry or material can be arranged in the target structure such as a colloidal polymer[29, 48] or lattice.[49] Moreover, this colloidal concept can be linked to stimuli-responsive polymers to add a further level of sophistication: the spectral tunability. The Figure 3c shows a transition from long-chain structures (plasmonic polymers) to short-chain structures (plasmonic oligomers) by applying an external mechanical force.[28] Thus, all the necessary tools (i.e., stable colloids in high particle concentration, templates that specify the target structure and stimuli-responsive polymers) are now available to obtain customized functional nanostructures. This habilitation thesis will show that these colloidal self-assembly concepts can be applied to both plasmonic particles and semiconductive nanocrystals, as shown as a teaser in Figure 3d. Moreover, simulation methods allow prediction of the spectroscopic property based on the colloidal self-assembly concept. How these simulation, fabrication and analyzing methods are linked is part of the following section.

2.3 Functional optical nanomaterials by colloidal self-assembly

In order to describe the plasmonic effect of colloid arrangements, it is essential to start with the individual resonances. Theoretical calculations with Mie theory show the spectroscopic resonance at various sizes (Figure 4a). The Mie theory was chosen because these results can be reproduced with little computational effort and can serve as calibrations for other simulation methods such as the finite-difference time-domain (FDTD) method. All Mie theory and FDTD calculations in this habilitation thesis can be reproduced by using a MATLAB code published by Mätzler[50] or using the commercially available 3D electromagnetic simulator.[51] The theoretical introduction is supplemented by colloidal fabrication methods to produce these nanostructures. In analogy to metallic particle growth in solution, individual seed particles can also be grown at an interface to study their spectroscopic properties individually. In order to avoid coupling, a sufficiently thick separating coating such as poly(N-isopropylacrylamide) (PNIPAM) is necessary. Plasmonic coupling is avoided if the interparticle distance (IPD) exceeds 2.5 times the particle diameter of a gold colloid (or 5 times the diameter for silver colloid).[52] In a wet-chemical post-treatment step, this PNIPAM polymer allows a gold overgrowth at the particle surface to obtain various particle sizes over centimeter scale areas.[42a] This concept can be used to screen individual particles with respect to their environments, and the sensitivity can be shown by the plasmonic resonance shift in different environments such as water, polymer or glass (Figure 4c). The simulations show that an increase in the refractive index causes a red shift and an increase of extinction efficiency of the resonance. This behavior is related to the easier polarizability and the lower damping of the plasmonic resonance at longer wavelengths.[53] Thus, this approach provides a two-dimensional functional surface with a single particle resolution limit.[54]
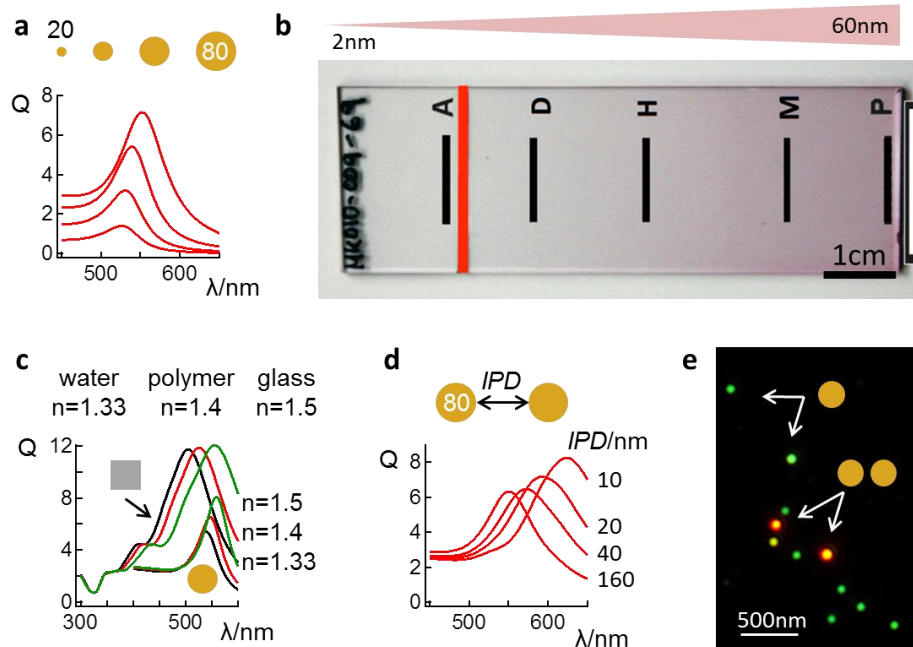
Figure 4: Electromagnetic simulation and large-scale self-assembly of plasmonic nanoparticles. (a) Theoretical calculations of golden particles with different sizes. Extinction efficiency Q defined as $Q = \sigma/A$, where σ is the extinction cross section, A is the area of the particle and λ wavelength. (b) Gradient in particle size on large-area by wet-chemical post-treatment.[42a] (c) Extinction efficiency of spherical and cubic particles in water, polymer and glass environment. (d) Simulation at different interparticle distance (IPC). (e) Dark-field image with randomly arranged individual nanoparticles.

A closer particle spacing can be obtained using ligands with lower molecular weight.[55] When colloidal particles aggregate from a monomer to dimer assembly, their optical properties change significantly. Because of the dipolar coupling between the particles, the plasmon mode shifts to a lower energy. The calculations in Figure 4d show electric field excitation along the line linking the two particles (longitudinal mode). To be complete, excitation perpendicular to the particle-linking axis results in a transverse mode, which occurs at the same energy as a single particle resonance. Upon assembly, a significant color shift can be observed from green to red through a scattering microscope (Figure 4e). These dimers can be effectively arranged by electrostatic interaction in an appropriate template.[56] This thesis will focus on the arrangement of particles of the same size only. Note that there are a number of other colloidal assemblies possible, e.g. arrangements of various sizes, shapes and geometries, which are described in detail in the review article from Liz-Marzán et al.[22]
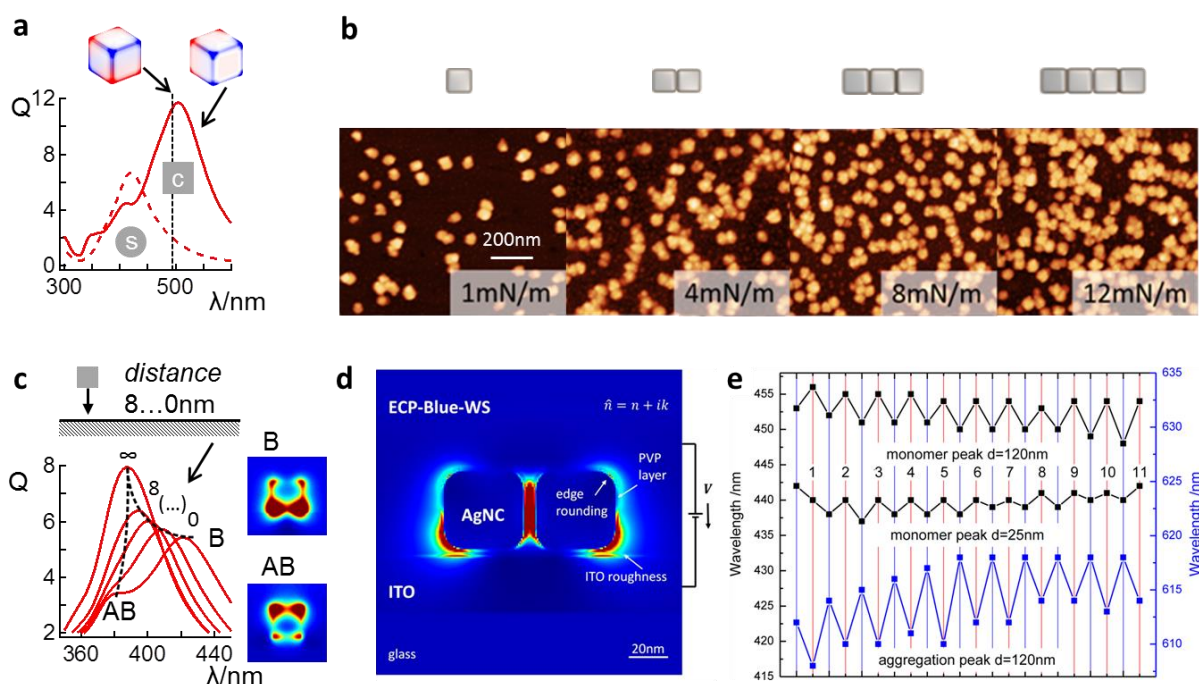

Figure 5: (a) Extinction efficiency of spherical in comparison to cubic nanoparticles (both silver material). The surface charge plots show the quadrupolar (left) and dipolar mode (right). The red color specifies the positive charge and the blue color specifies the negative charge. (b) Isolated silver nanocubes and their assembly into dimers, trimers and tetramers through adjustment of the surface tension during the assembly process.[57] (c) Plasmonic hybridization causes between a nanocube and a substrate, which results in a bonding (B) and anti-bonding (AB) mode (see insets of electric field intensity). (d) Schematic of a dimer assembly (electric field intensity) in an electrical cell to (e) tune two plasmonic resonances reversibly.[58]

Because of their large contact area, colloids with flat surfaces are particularly suitable for exploiting the spectroscopic potential of near-field coupling. The simulations in Figure 5a show that the plasmon mode redshifts, the efficiency increases and further higher plasmon modes arise if a cubic particle is used instead of a spherical particle. Such cubes that are stabilized with a poly(vinylpyrrolidone) (PVP) ligand can be arranged at a water-air interface using the Langmuir–Blodgett method. By adjusting the surface tension, the cubes can be arranged at an arbitrary interface with various arrangements using this scalable method (Figure 5b).[57] Moreover, the simulations show that cubes are not only more efficient in cross-section, cubes also can excite a

quadrupolar mode in addition to the dipolar mode. Strictly speaking, the quadrupolar mode occurs with every plasmonic particle. However at cubic colloids these two modes overlap energetically, which can results an emergent plasmon effect. This emergent effect is also known as plasmon hybridization or as substrate induced Fano resonance.[59] This means the arrangement results in bonding and anti-bonding modes that are composed of a linear combination of the dipolar and quadrupolar mode of an isolated nanocube. The intensity distribution as shown in Figure 5c of the corresponding modes has a far-reaching influence on the application. The energetically lower mode (B) is suitable for colloid-to-film coupled cavities and the energetically higher mode (AB) is suitable for the sensor applications.[60] The plasmonic resonances can be influenced energetically by using an electrochromic polymer. In this case the electrochromic polymer acts as an index change.[58] In addition, the plasmonic modes can also be combined with other materials such as liquid crystals to control the optical properties.[61] The advantage of emergent plasmon modes (Fano resonance) is also evident in the development of chemical and biological sensors, which Homola *et al.* summarized in their review.[62]
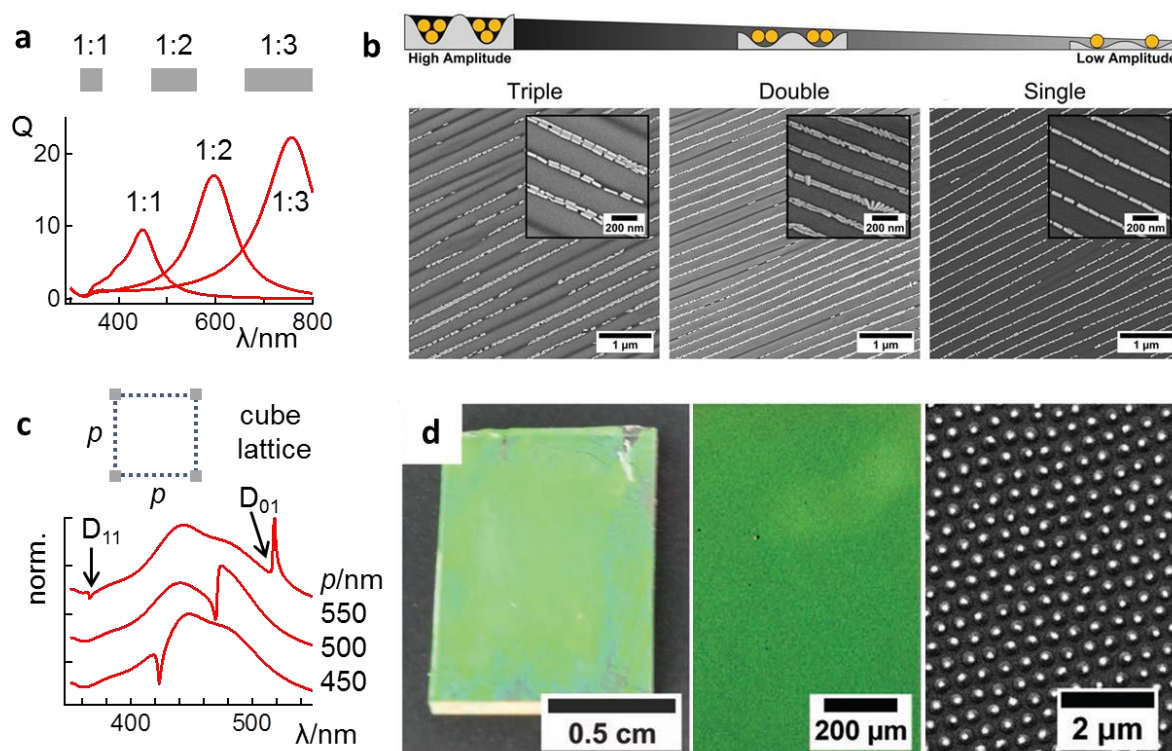

Figure 5: (a) Simulation of anisotropic silver colloids with different aspect ratios. (b) Template-assisted self-assembly of triple, double and single gold nanorods by using different template amplitudes.[48] (c) Simulation of the Fano resonance based on different lattice periods (*p*). D_{01} denotes the first and D_{11} the second diffraction order. (d) Large-scale arrangement of plasmonic core-shell particles using self-assembly at a glass-air interface.[42b]

Another approach toward an emergent effect is the coherent coupling of a plasmon mode with diffraction. From a colloidal point of view, a lattice arrangement can be produced particularly well with anisotropic particles, since the long axis can also be used for the assembly. Simulations in Figure 5a show that the mode redshifts significantly when the aspect ratio increases. Such silver rods can be synthesized by an overgrowth process[63] and can be assembled by a template-assisted approach.[48] In order to obtain an emergent effect, there must be an energetic overlap between plasmon mode and

diffractive mode. The simulations in Figure 5c show this approach where the relative broad resonance of silver cubes coherently couples with the first (D_{01}) or second (D_{11}) order of the grating. It has recently been shown that this emergent mode meets the plasmon hybridization conditions.[64] By using core-shell particles and a self-assembly method at a liquid-air interface, hexagonally densely packed particles can be arranged over a large area (Figure 5d).[42b] Through the use of a hydrogel shell (PNIPAM), the tunability by means of temperature could also be shown in this work. It should be noted that the same emergent resonances can be generated by an inverted structure, which can be a nanohole array. This structure and the work of Ebbesen *et al.*, who described it as extraordinary optical transmission, led to the rediscovery of plasmonics in the year 2001.[65] From a colloidal point of view, such nanohole arrays can be created by self-assembly at a liquid-air interface followed by an etching and metallic evaporation step.[66] In addition, other assemblies in two-dimensional arrays are possible through colloidal lithography, which are summarized in the review article by Zhang *et al.*[67] For further reading, Thomas *et al.* summarize the potential of such functional materials with respect to chemical (pH, solvent) and physical stimuli (pressure, temperature, etc.) in their review article.[68]

This colloidal concept is to be further studied in this habilitation thesis as follows: Each metallic nanoparticle can be replaced with a semiconductive nanoparticle.

2.4 Scope

This habilitation thesis focuses on the fabrication and the spectroscopic properties of nanostructures that are composed of self-assembled colloids. This approach can meet the demands of large-area, flexible, and ultrathin devices at reasonable cost. In order to make this development possible, the spectroscopic properties of individual and arranged colloids are predicted by modelling methods, synthesized by a wet chemistry approach and fabricated over a large area by directed self-assembly.

This interdisciplinary research field will be explored step by step: First, the near field enhancement by dipolar coupling within a single colloid cavity (chapter 3) will be studied systematically. This chapter builds on the concept of plasmonic hybridization and combines it with a synthetic approach to create axisymmetric colloids.[27] The fixed distance between the nanorod core and the surrounding box allows field strength that can exceed the intensity of the exciting field by multiple orders of magnitude. These high field strengths are particularly interesting for sensor applications and Raman spectroscopy. These properties will be further explored in the following with a focus on electric and magnetic fields[69] as well as their spectroscopic properties[70] (chapter 4). The colloid-to-film coupled cavities act as a simple and cost-effective nanoantenna to explore these properties statistically. This approach makes the nanostructures accessible for conventional and large-area measurement methods such as UV-vis-IR spectroscopy. The colloidal approach allows the study of various materials (gold and silver), shapes (spherical, cubic, penta-twinned), distances (layer-by-layer technique) and excitations (plane wave or point dipole) with reasonable efforts. This access can be used to generate simple nanocavities with an ultra-small mode volume, which have properties that are otherwise only possible with complex vacuum systems and at low temperatures.

The near field coupling will be further explored by adding additional particles to the assembly (chapter 5).[71] The formation of infinitely long particle chains is only possible with the directed self-assembly method. Current methods lead to limitations in particle numbers and in particle size. In this chapter the intermeshing of simulation, arrangement and spectroscopy methods led to the discovery of a degenerate plasmon mode that only occurs when the number of particles is greater than ten. These findings can be used for energy transport below the diffraction limit and for plasmonic enhanced photocatalysis.

Finally, the particle arrangements can be coupled to the far field. In chapter 6, the coherent coupling between the localized plasmon mode and the Bragg diffraction mode is discussed.[72] This emergent mode can also be explained by the plasmonic hybridized model. This emergent mode can be recognized by its asymmetric and sharp line-shape. The narrower resonance increases the mode quality and thus also improves the sensitivity by an order of magnitude.[30] In combination with a mechanically deformable polymer, it also allows the study of non-degenerate Fano modes. In other words, the plasmon mode can be specifically changed over a wide visible range by the large-scale self-assembly method. These colloidal concepts can also be transferred to semiconductor nanocrystals, which leads to lattice structures that were previously only possible in the micrometer range. This opens up mode interactions that are discussed in the form of Moiré interference. This resonance is especially interesting for the future development of nanophotonic devices due to their potential to increase the coupling strength, slowing down the group velocity and reduction of the metallic losses.

2.5 References

1. Eustis, S.; El-Sayed, M. A., Why gold nanoparticles are more precious than pretty gold: Noble metal surface plasmon resonance and its enhancement of the radiative and nonradiative properties of nanocrystals of different shapes. *Chemical Society reviews* **2006,** *35* (3), 209-217.

2. Faraday, M., X. The Bakerian Lecture. —Experimental relations of gold (and other metals) to light. *Philosophical Transactions of the Royal Society of London* **1857,** *147*, 145-181.

3. Kühne, T.; Aftenieva, O.; Schmalzriedt, S.; Niethamm, M.; König, T. A. F. Wissenschaftsvermittlung von Plasmonenresonanzen. https://nzone.info/.

4. Turkevich, J.; Stevenson, P. C.; Hillier, J., A study of the nucleation and growth processes in the synthesis of colloidal gold. *Discussions of the Faraday Society* **1951,** *11* (0), 55-75.

5. González-Rubio, G.; de Oliveira, T. M.; Altantzis, T.; La Porta, A.; Guerrero-Martínez, A.; Bals, S.; Scarabelli, L.; Liz-Marzán, L. M., Disentangling the effect of seed size and crystal habit on gold nanoparticle seeded growth. *Chemical Communications* **2017,** *53* (82), 11360-11363.

6. Rycenga, M.; Cobley, C. M.; Zeng, J.; Li, W.; Moran, C. H.; Zhang, Q.; Qin, D.; Xia, Y., Controlling the synthesis and assembly of silver nanostructures for plasmonic applications. *Chemical reviews* **2011,** *111* (6), 3669-712.

7. Mayer, M.; Steiner, A. M.; Röder, F.; Formanek, P.; König, T. A. F.; Fery, A., Aqueous Gold Overgrowth of Silver Nanoparticles: Merging the Plasmonic Properties of Silver with the Functionality of Gold. *Angewandte Chemie International Edition* **2017,** *56* (50), 15866-15870.

8. Sönnichsen, C.; Fritzsche, W., *100 years of nanoscience with the ultramicroscope*. 2007; p 116.

9. Mie, G., Beiträge zur Optik trüber Medien, speziell kolloidaler Metallösungen. *Annalen der Physik* **1908,** *330* (3), 377-445.

10. Binnig, G.; Quate, C. F.; Gerber, C., Atomic Force Microscope. *Physical Review Letters* **1986,** *56* (9), 930-933.

11. Mayer, K. M.; Hafner, J. H., Localized Surface Plasmon Resonance Sensors. *Chemical reviews* **2011,** *111* (6), 3828-3857.

12. Jain, P. K.; El-Sayed, I. H.; El-Sayed, M. A., Au nanoparticles target cancer. *Nano Today* **2007,** *2* (1), 18-29.

13. Ai, B.; Yu, Y.; Möhwald, H.; Zhang, G.; Yang, B., Plasmonic films based on colloidal lithography. *Advances in Colloid and Interface Science* **2014,** *206*, 5-16.

14. Murray, C. B.; Norris, D. J.; Bawendi, M. G., Synthesis and characterization of nearly monodisperse CdE (E = sulfur, selenium, tellurium) semiconductor nanocrystallites. *Journal of the American Chemical Society* **1993,** *115* (19), 8706-8715.

15. Gaponik, N.; Hickey, S. G.; Dorfs, D.; Rogach, A. L.; Eychmuller, A., Progress in the light emission of colloidal semiconductor nanocrystals. *Small* **2010,** *6* (13), 1364-78.

16. Brus, L., Electronic wave functions in semiconductor clusters: experiment and theory. *The Journal of Physical Chemistry* **1986,** *90* (12), 2555-2560.

17. Ekimov, A. I.; Efros, A. L.; Onushchenko, A. A., Quantum size effect in semiconductor microcrystals. *Solid State Communications* **1985,** *56* (11), 921-924.

18. Etgar, L.; Moehl, T.; Gabriel, S.; Hickey, S. G.; Eychmüller, A.; Grätzel, M., Light Energy Conversion by Mesoscopic PbS Quantum Dots/TiO2 Heterojunction Solar Cells. *ACS Nano* **2012,** *6* (4), 3092-3099.

19. Kim, T.-H.; Cho, K.-S.; Lee, E. K.; Lee, S. J.; Chae, J.; Kim, J. W.; Kim, D. H.; Kwon, J.-Y.; Amaratunga, G.; Lee, S. Y.; Choi, B. L.; Kuk, Y.; Kim, J. M.; Kim, K., Full-colour quantum dot displays fabricated by transfer printing. *Nature Photonics* **2011,** *5* (3), 176-182.

20. Zhuo, S.; Shao, M.; Lee, S.-T., Upconversion and Downconversion Fluorescent Graphene Quantum Dots: Ultrasonic Preparation and Photocatalysis. *ACS Nano* **2012,** *6* (2), 1059-1064.

21. Nasilowski, M.; Mahler, B.; Lhuillier, E.; Ithurria, S.; Dubertret, B., Two-Dimensional Colloidal Nanocrystals. *Chemical reviews* **2016,** *116* (18), 10934-10982.

22. Grzelczak, M.; Vermant, J.; Furst, E. M.; Liz-Marzán, L. M., Directed self-assembly of nanoparticles. *ACS nano* **2010,** *4* (7), 3591-3605.

23. Whitesides, G. M.; Grzybowski, B., Self-assembly at all scales. *Science* **2002,** *295* (5564), 2418-2421.
24. Steiner, A. M.; Mayer, M.; Schletz, D.; Wolf, D.; Formanek, P.; Hübner, R.; Dulle, M.; Förster, S.; König, T. A.; Fery, A., Silver Particles with Rhombicuboctahedral Shape and Effective Isotropic Interactions with Light. *Chemistry of Materials* **2019,** *31* (8), 2822-2827.
25. König, T. A. F.; Santer, S., Stretching and distortion of a photosensitive polymer film by surface plasmon generated near fields in the vicinity of a nanometer sized metal pin hole. *Nanotechnology* **2012,** *23* (15), 155301.
26. Goßler, F. G.; Steiner, A. M.; Stroyuk, O.; Raevskaya, A.; König, T. A. F., Active Plasmonic Colloid-to-Film Coupled Cavities for Tailored Light-Matter Interactions. *J. Phys. Chem. C* **2019,** *accepted*.
27. Schnepf, M. J.; Mayer, M.; Kuttner, C.; Tebbe, M.; Wolf, D.; Dulle, M.; Altantzis, T.; Formanek, P.; Förster, S.; Bals, S.; König, T. A. F.; Fery, A., Nanorattles with tailored electric field enhancement. *Nanoscale* **2017,** *9* (27), 9376-9385.
28. Steiner, A. M.; Mayer, M.; Seuss, M.; Kuttner, C.; König, T. A. F.; Fery, A., Macroscopic Strain-induced Transition from Quasi-infinite Gold Nanoparticle Chains to Defined Plasmonic Oligomers. *ACS Nano* **2016,** *submitted*.
29. Hanske, C.; Tebbe, M.; Kuttner, C.; Bieber, V.; Tsukruk, V. V.; Chanana, M.; König, T. A. F.; Fery, A., Strongly coupled plasmonic modes on macroscopic areas via template-assisted colloidal self-assembly. *Nano Lett.* **2014,** *14* (12), 6863-71.
30. Gupta, V.; Probst, P. T.; Goßler, F. R.; Steiner, A. M.; Schubert, J.; Brasse, Y.; König, T. A. F.; Fery, A., Mechanotunable Surface Lattice Resonances in the Visible Optical Range by Soft Lithography Templates and Directed Self-Assembly. *ACS applied materials & interfaces* **2019,** *11* (31), 28189-28196.
31. Mayer, M.; Schnepf, M. J.; König, T. A. F.; Fery, A., Colloidal Self-Assembly Concepts for Plasmonic Metasurfaces. *Advanced Optical Materials* **2019,** *7* (1), 1800564.
32. Klinkova, A.; Therien-Aubin, H.; Ahmed, A.; Nykypanchuk, D.; Choueiri, R. M.; Gagnon, B.; Muntyanu, A.; Gang, O.; Walker, G. C.; Kumacheva, E., Structural and optical properties of self-assembled chains of plasmonic nanocubes. *Nano letters* **2014,** *14* (11), 6314-21.
33. Barrow, S. J.; Rossouw, D.; Funston, A. M.; Botton, G. A.; Mulvaney, P., Mapping bright and dark modes in gold nanoparticle chains using electron energy loss spectroscopy. *Nano letters* **2014,** *14* (7), 3799-3808.
34. Murray, C. B.; Kagan, C. R.; Bawendi, M. G., Self-Organization of CdSe Nanocrystallites into Three-Dimensional Quantum Dot Superlattices. *Science* **1995,** *270* (5240), 1335-1338.
35. Kalsin, A. M.; Fialkowski, M.; Paszewski, M.; Smoukov, S. K.; Bishop, K. J. M.; Grzybowski, B. A., Electrostatic Self-Assembly of Binary Nanoparticle Crystals with a Diamond-Like Lattice. *Science* **2006,** *312* (5772), 420-424.
36. Redl, F. X.; Cho, K. S.; Murray, C. B.; O'Brien, S., Three-dimensional binary superlattices of magnetic nanocrystals and semiconductor quantum dots. *Nature* **2003,** *423* (6943), 968-971.
37. Rose, A.; Hoang, T. B.; McGuire, F.; Mock, J. J.; Ciraci, C.; Smith, D. R.; Mikkelsen, M. H., Control of radiative processes using tunable plasmonic nanopatch antennas. *Nano letters* **2014,** *14* (8), 4797-802.
38. Hanske, C.; Müller, M. B.; Bieber, V.; Tebbe, M.; Jessl, S.; Wittemann, A.; Fery, A., The role of substrate wettability in nanoparticle transfer from wrinkled elastomers: fundamentals and application toward hierarchical patterning. *Langmuir : the ACS journal of surfaces and colloids* **2012,** *28* (49), 16745-16750.
39. Zhang, H.; Cadusch, J.; Kinnear, C.; James, T.; Roberts, A.; Mulvaney, P., Direct assembly of large area nanoparticle arrays. *ACS nano* **2018,** *12* (8), 7529-7537.
40. Flauraud, V.; Mastrangeli, M.; Bernasconi, G. D.; Butet, J.; Alexander, D. T.; Shahrabi, E.; Martin, O. J.; Brugger, J., Nanoscale topographical control of capillary assembly of nanoparticles. *Nature nanotechnology* **2017,** *12* (1), 73-80.
41. Kraus, T.; Malaquin, L.; Schmid, H.; Riess, W.; Spencer, N. D.; Wolf, H., Nanoparticle printing with single-particle resolution. *Nat. Nano.* **2007,** *2* (9), 570-576.

42. (a) Müller, M. B.; Kuttner, C.; König, T. A. F.; Tsukruk, V. V.; Förster, S.; Karg, M.; Fery, A., Plasmonic Library Based on Substrate-Supported Gradiential Plasmonic Arrays. *ACS Nano* **2014,** *8* (9), 9410-9421; (b) Volk, K.; Fritzgerald, J. P. S.; Ruckdeschel, P.; Retsch, M.; König, T. A. F.; Karg, M., Reversible tuning of surface lattice resonances in self-assembled hybrid monolayers. *Adv. Mat.* **2016,** *submitted*.

43. (a) Nepal, D.; Onses, M. S.; Park, K.; Jespersen, M.; Thode, C. J.; Nealey, P. F.; Vaia, R. A., Control over Position, Orientation, and Spacing of Arrays of Gold Nanorods Using Chemically Nanopatterned Surfaces and Tailored Particle–Particle–Surface Interactions. *ACS Nano* **2012,** *6* (6), 5693-5701; (b) Pretzl, M.; Schweikart, A.; Hanske, C.; Chiche, A.; Zettl, U.; Horn, A.; Böker, A.; Fery, A., A lithography-free pathway for chemical microstructuring of macromolecules from aqueous solution based on wrinkling. *Langmuir : the ACS journal of surfaces and colloids* **2008,** *24* (22), 12748-12753.

44. (a) Liu, Z.; Chang, T.; Huang, H.; He, T., Gold nanoparticle arrays assembled on the reconstructed surface of block copolymer thin films. *RSC advances* **2013,** *3* (43), 20464-20470; (b) Sanwaria, S.; Singh, S.; Horechyy, A.; Formanek, P.; Stamm, M.; Srivastava, R.; Nandan, B., Multifunctional core–shell polymer–inorganic hybrid nanofibers prepared via block copolymer self-assembly. *RSC Advances* **2015,** *5* (109), 89861-89868.

45. Schweikart, A.; Fery, A., Controlled wrinkling as a novel method for the fabrication of patterned surfaces. *Microchimica Acta* **2009,** *165* (3-4), 249-263.

46. Rey, A.; Billardon, G.; Lörtscher, E.; Moth-Poulsen, K.; Stuhr-Hansen, N.; Wolf, H.; Bjørnholm, T.; Stemmer, A.; Riel, H., Deterministic assembly of linear gold nanorod chains as a platform for nanoscale applications. *Nanoscale* **2013,** *5* (18), 8680-8688.

47. Ni, S.; Leemann, J.; Wolf, H.; Isa, L., Insights into mechanisms of capillary assembly. *Farad. Discuss.* **2015,** *181*, 225-42.

48. Tebbe, M.; Mayer, M.; Glatz, B. A.; Hanske, C.; Probst, P. T.; Muller, M. B.; Karg, M.; Chanana, M.; König, T. A. F.; Kuttner, C.; Fery, A., Optically anisotropic substrates via wrinkle-assisted convective assembly of gold nanorods on macroscopic areas. *Faraday Disc.* **2015,** *181*, 243-60.

49. Juodėnas, M.; Tamulevičius, T.; Henzie, J.; Erts, D.; Tamulevičius, S., Surface Lattice Resonances in Self-Assembled Arrays of Monodisperse Ag Cuboctahedra. *ACS Nano* **2019,** *13* (8), 9038-9047.

50. Mätzler, C., MATLAB functions for Mie scattering and absorption, version 2. *IAP Res. Rep* **2002,** *8* (1), 9.

51. Inc., L. https://www.lumerical.com/products/.

52. Ghosh, S. K.; Pal, T., Interparticle coupling effect on the surface plasmon resonance of gold nanoparticles: from theory to applications. *Chemical reviews* **2007,** *107* (11), 4797-4862.

53. Myroshnychenko, V.; Rodriguez-Fernandez, J.; Pastoriza-Santos, I.; Funston, A. M.; Novo, C.; Mulvaney, P.; Liz-Marzán, L. M.; De Abajo, F. J. G., Modelling the optical response of gold nanoparticles. *Chemical Society reviews* **2008,** *37* (9), 1792-1805.

54. Wang, L.; Ng, R. J. H.; Safari Dinachali, S.; Jalali, M.; Yu, Y.; Yang, J. K. W., Large Area Plasmonic Color Palettes with Expanded Gamut Using Colloidal Self-Assembly. *ACS Photonics* **2016,** *3* (4), 627-633.

55. Karg, M.; König, T. A. F.; Retsch, M.; Stelling, C.; Reichstein, P. M.; Honold, T.; Thelakkat, M.; Fery, A., Colloidal self-assembly concepts for light management in photovoltaics. *Mater. Today* **2015,** *18* (4), 185-205.

56. Romo-Herrera, J. M.; Alvarez-Puebla, R. A.; Liz-Marzan, L. M., Controlled assembly of plasmonic colloidal nanoparticle clusters. *Nanoscale* **2011,** *3* (4), 1304-15.

57. König, T. A. F.; Ledin, P. A.; Russell, M.; Geldmeier, J. A.; Mahmoud, M. A.; El-Sayed, M. A.; Tsukruk, V. V., Silver nanocube aggregation gradient materials in search for total internal reflection with high phase sensitivity. *Nanoscale* **2015,** *7* (12), 5230-9.

58. König, T. A. F.; Ledin, P. A.; Kerszulis, J.; Mahmoud, M. A.; El-Sayed, M. A.; Reynolds, J. R.; Tsukruk, V. V., Electrically Tunable Plasmonic Behavior of Nanocube–Polymer Nanomaterials Induced by a Redox-Active Electrochromic Polymer. *ACS Nano* **2014,** *8* (6), 6182-6192.

59. (a) Prodan, E.; Radloff, C.; Halas, N. J.; Nordlander, P., A hybridization model for the plasmon response of complex nanostructures. *science* **2003,** *302* (5644), 419-422; (b) Nordlander, P.; Oubre, C.; Prodan, E.; Li, K.; Stockman, M. I., Plasmon Hybridization in Nanoparticle Dimers. *Nano letters* **2004,** *4* (5), 899-903; (c) Zhang, S.; Bao, K.; Halas, N. J.; Xu, H.; Nordlander, P., Substrate-induced Fano resonances of a plasmonic nanocube: a route to increased-sensitivity localized surface plasmon resonance sensors revealed. *Nano Lett.* **2011,** *11* (4), 1657-63.

60. König, T. A. F.; Kodiyath, R.; Combs, Z. A.; Mahmoud, M. A.; El-Sayed, M. A.; Tsukruk, V. V., Silver Nanocube Aggregates in Cylindrical Pores for Higher Refractive Index Plasmonic Sensing. *Part. Part. Syst. Charact.* **2014,** *31* (2), 274-283.

61. Atorf, B.; Funck, T.; Hegmann, T.; Kempter, S.; Liedl, T.; Martens, K.; Mühlenbernd, H.; Zentgraf, T.; Zhang, B.; Kitzerow, H., Liquid crystals and precious metal: from nanoparticle dispersions to functional plasmonic nanostructures. *Liquid Crystals* **2017,** *44* (12-13), 1929-1947.

62. Špačková, B.; Wrobel, P.; Bocková, M.; Homola, J., Optical biosensors based on plasmonic nanostructures: a review. *Proceedings of the IEEE* **2016,** *104* (12), 2380-2408.

63. Mayer, M.; Scarabelli, L.; March, K.; Altantzis, T.; Tebbe, M.; Kociak, M.; Bals, S.; García de Abajo, F. J.; Fery, A.; Liz-Marzán, L. M., Controlled living nanowire growth: precise control over the morphology and optical properties of AgAuAg bimetallic nanowires. *Nano letters* **2015,** *15* (8), 5427-5437.

64. Khlopin, D.; Laux, F.; Wardley, W. P.; Martin, J.; Wurtz, G. A.; Plain, J.; Bonod, N.; Zayats, A. V.; Dickson, W.; Gérard, D., Lattice modes and plasmonic linewidth engineering in gold and aluminum nanoparticle arrays. *JOSA B* **2017,** *34* (3), 691-700.

65. (a) Martin-Moreno, L.; Garcia-Vidal, F.; Lezec, H.; Pellerin, K.; Thio, T.; Pendry, J.; Ebbesen, T., Theory of extraordinary optical transmission through subwavelength hole arrays. *Physical review letters* **2001,** *86* (6), 1114; (b) Barnes, W. L.; Dereux, A.; Ebbesen, T. W., Surface plasmon subwavelength optics. *nature* **2003,** *424* (6950), 824-830.

66. Stelling, C.; Singh, C. R.; Karg, M.; König, T. A. F.; Thelakkat, M.; Retsch, M., Plasmonic nanomeshes: their ambivalent role as transparent electrodes in organic solar cells. *Scientific Reports* **2017,** *7* (1), 42530.

67. Zhang, J.; Li, Y.; Zhang, X.; Yang, B., Colloidal self-assembly meets nanofabrication: From two-dimensional colloidal crystals to nanostructure arrays. *Advanced materials* **2010,** *22* (38), 4249-4269.

68. Lee, J. H.; Koh, C. Y.; Singer, J. P.; Jeon, S. J.; Maldovan, M.; Stein, O.; Thomas, E. L., 25th anniversary article: ordered polymer structures for the engineering of photons and phonons. *Adv Mater* **2014,** *26* (4), 532-69.

69. Mayer, M.; Tebbe, M.; Kuttner, C.; Schnepf, M. J.; König, T. A. F.; Fery, A., Template-assisted colloidal self-assembly of macroscopic magnetic metasurfaces. *Faraday discussions* **2016**.

70. (a) Schnepf, M. J.; Brasse, Y.; Goßler, F. G.; Steiner, A. M.; Obermeier, J.; Lippitz, M.; Fery, A.; König, T. A. F., Single Particle Spectroscopy of Radiative Processes in Colloid-to-Film-Coupled Nanoantennas. *Zeitschrift für Physikalische Chemie* **2018,** *232* (9-11), 1593-1606; (b) Goßler, F. R.; Steiner, A. M.; Stroyuk, O.; Raevskaya, A.; König, T. A. F., Active Plasmonic Colloid-to-Film-Coupled Cavities for Tailored Light–Matter Interactions. *The Journal of Physical Chemistry C* **2019,** *123* (11), 6745-6752.

71. Mayer, M.; Potapov, P. L.; Pohl, D.; Steiner, A. M.; Schultz, J.; Rellinghaus, B.; Lubk, A.; König, T. A. F.; Fery, A., Direct Observation of Plasmon Band Formation and Delocalization in Quasi-Infinite Nanoparticle Chains. *Nano letters* **2019,** *19* (6), 3854-3862.

72. Sarkar, S.; Gupta, V.; Kumar, M.; Schubert, J.; Probst, P. T.; Joseph, J.; König, T. A. F., Hybridized Guided-Mode Resonances via Colloidal Plasmonic Self-Assembled Grating. *ACS applied materials & interfaces* **2019,** *11* (14), 13752-13760.

73. (a) Magnozzi, M.; Brasse, Y.; König, T. A. F.; Bisio, F.; Bittrich, E.; Fery, A.; Canepa, M., Plasmonics of Au/Polymer Core/Shell Nanocomposites for Thermoresponsive Hybrid Metasurfaces. *ACS Applied Nano Materials* **2020,** *3* (2), 1674-1682; (b) Köhn Serrano, M. S.; König, T. A. F.; Haataja, J. S.; Löbling, T. I.; Schmalz, H.; Agarwal, S.; Fery, A.; Greiner, A., Self-Organization of Gold

Nanoparticle Assemblies with 3D Spatial Order and Their External Stimuli Responsiveness. *Macromolecular Rapid Communications* **2016,** *37* (3), 215-220.

74. (a) Yadavalli, N. S.; König, T.; Santer, S., Selective mass transport of azobenzene-containing photosensitive films towards or away from the light intensity. *Journal of the Society for Information Display* **2015,** *23* (4), 154-162; (b) König, T.; Papke, T.; Kopyshev, A.; Santer, S., Atomic force microscopy nanolithography: fabrication of metallic nano-slits using silicon nitride tips. *J. Mater. Sci.* **2013,** *48* (10), 3863-3869; (c) König, T. A. F.; Tsukruk, V. V.; Santer, S., Controlled topography change of subdiffraction structures based on photosensitive polymer films induced by surface plasmon polaritons. *ACS Appl. Mater. Interfaces* **2013,** *5* (13), 6009-16; (d) König, T.; Yadavalli, N. S.; Santer, S., Near-Field Induced Reversible Structuring of Photosensitive Polymer Films: Gold Versus Silver Nano-antennas. *Plasmonics* **2012,** *7* (3), 535-542; (e) König, T. A. F.; Nataraja Sekhar, Y.; Santer, S., Surface plasmon nanolithography: impact of dynamically varying near-field boundary conditions at the air–polymer interface. *J. Mater. Chem.* **2012,** *22* (13), 5945; (f) König, T. A. F.; Santer, S., Visualization of surface plasmon interference by imprinting intensity patterns on a photosensitive polymer. *Nanotechnology* **2012,** *23* (48), 485304; (g) König, T. A. F.; Goldenberg, L. M.; Kulikovska, O.; Kulikovsky, L.; Stumpe, J.; Santer, S., Reversible structuring of photosensitive polymer films by surface plasmon near field radiation. *Soft Mat.* **2011,** *7* (9), 4174.

75. Gür, F. N.; McPolin, C. P. T.; Raza, S.; Mayer, M.; Roth, D. J.; Steiner, A. M.; Löffler, M.; Fery, A.; Brongersma, M. L.; Zayats, A. V.; König, T. A. F.; Schmidt, T. L., DNA-Assembled Plasmonic Waveguides for Nanoscale Light Propagation to a Fluorescent Nanodiamond. *Nano Lett.* **2018,** *18* (11), 7323-7329.

76. Wang, S.; Wang, X.-Y.; Li, B.; Chen, H.-Z.; Wang, Y.-L.; Dai, L.; Oulton, R. F.; Ma, R.-M., Unusual scaling laws for plasmonic nanolasers beyond the diffraction limit. *Nature communications* **2017,** *8* (1), 1889.

77. Santhosh, K.; Bitton, O.; Chuntonov, L.; Haran, G., Vacuum Rabi splitting in a plasmonic cavity at the single quantum emitter limit. *Nature communications* **2016,** *7*, ncomms11823.

78. Solis Jr, D.; Willingham, B.; Nauert, S. L.; Slaughter, L. S.; Olson, J.; Swanglap, P.; Paul, A.; Chang, W.-S.; Link, S., Electromagnetic energy transport in nanoparticle chains via dark plasmon modes. *Nano letters* **2012,** *12* (3), 1349-1353.

79. Wang, D.; Wang, W.; Knudson, M. P.; Schatz, G. C.; Odom, T. W., Structural Engineering in Plasmon Nanolasers. *Chemical reviews* **2018,** *118* (6), 2865-2881.

80. (a) Viktor, G. V., The electrodynamics of substances with simultaneously negative values of epsilon and mu? *Phys. Usp.* **1968,** *10* (4), 509; (b) Shelby, R. A.; Smith, D. R.; Schultz, S., Experimental Verification of a Negative Index of Refraction. *Science* **2001,** *292* (5514), 77-79; (c) Pendry, J. B., Negative refraction. *Contemporary Physics* **2004,** *45* (3), 191-202.

81. Fang, N.; Lee, H.; Sun, C.; Zhang, X., Sub–Diffraction-Limited Optical Imaging with a Silver Superlens. *Science* **2005,** *308* (5721), 534-537.

82. (a) Ni, X.; Wong, Z. J.; Mrejen, M.; Wang, Y.; Zhang, X., An ultrathin invisibility skin cloak for visible light. *Science* **2015,** *349* (6254), 1310-1314; (b) Ergin, T.; Stenger, N.; Brenner, P.; Pendry, J. B.; Wegener, M., Three-Dimensional Invisibility Cloak at Optical Wavelengths. *Science* **2010,** *328* (5976), 337-339; (c) Pendry, J. B.; Schurig, D.; Smith, D. R., Controlling Electromagnetic Fields. *Science* **2006,** *312* (5781), 1780-1782.

83. Rogach, A.; Susha, A.; Caruso, F.; Sukhorukov, G.; Kornowski, A.; Kershaw, S.; Möhwald, H.; Eychmüller, A.; Weller, H., Nano-and Microengineering: 3-d colloidal photonic crystals prepared from sub-µm-sized polystyrene latex spheres pre-coated with luminescent polyelectrolyte/nanocrystal shells. *Advanced Materials* **2000,** *12* (5), 333-337.

84. Gupta, V. Mechanotunable Hybrid Plasmonic Systems. Technical University Dresden, 2020.

85. Goßler, F. G. Spectroscopic Properties of Self-Assembled Plasmonic and Semiconductive Nanocrystals. Technical University Dresden, 2020.

86. Schnepf, M. J. Coherent energy transfer between fluorophores and plasmonic nanostructures as a basis for colloidal metasurfaces. Technical University Dresden, 2020.

87. Sarkar, S. Optical realization and fabrication of photonic metamaterial structures. Indian Institute of Technology Delhi, 2020.

88. Mehlhorn, B. Untersuchung der photonischen Eigenschaften von selbstassemblierten Quantenpunktemittern mittels templategestützter Anordnung. Technische Universität Dresden, 2019.

89. Kumar, M. Guided modes using directed self-assembly of plasmonic nanoparticles for the application in light harvesting. Indian Institute of Technology Delhi, 2018.

90. Gour, J. Nanoparticle Grating by Directed Self-Assembly for Hot Electron Injection. Indian Institute of Technology Delhi, 2019.

91. Kularia, M. Plasmonic nanoparticle self-assembly on an fibre end face. Indian Institute of Technology Delhi, 2020.

92. Mayer, M. From Single Colloidal Particles to Coupled Plasmonic Systems. Technical University Dresden, 2019.

3   Single colloidal cavities

3.1   Nanorattles with tailored electric field enhancement

Nanorattles with tailored electric field enhancement

Max J. Schnepf, Martin Mayer, Christian Kuttner, Moritz Tebbe, Daniel Wolf, Martin Dulle, Thomas Altantzis, Petr Formanek, Stephan Förster, Sara Bals, **Tobias A. F. König*** and Andreas Fery*,

*corresponding authors

Author contribution statement

MS and MM carried out the experiments and have contributed equally. **TK** encouraged MS and MM to investigate the simulation methods and optical spectroscopy methods as well as supervised the execution and findings of this work. CK and MT contributed through synthesis and concept development. DW and PF contributed through their transmission electron microscopy method. MD and SF contributed through their small-angle scattering technique. The authors TA and SB contributed through their transmission electron microscopy and electron spectroscopy methods. The authors **TK** and AF made a significant contribution to the conception and design of the work. Through the simulation methods and optical spectroscopy methods, the author **TK** made a significant contribution to the acquisition, analysis and interpretation of the data. All authors provided critical feedback and helped shape the research, analysis and manuscript.

Check for updates

Nanorattles with tailored electric field enhancement†

Max J. Schnepf,‡[a] Martin Mayer,‡[a,b] Christian Kuttner, [a,b] Moritz Tebbe, §[c] Daniel Wolf,[d] Martin Dulle,[e] Thomas Altantzis,[f] Petr Formanek,[a] Stephan Förster,[e] Sara Bals,[f] Tobias A. F. König *[a,b] and Andreas Fery*[a,b,g]

Nanorattles are metallic core–shell particles with core and shell separated by a dielectric spacer. These nanorattles have been identified as a promising class of nanoparticles, due to their extraordinary high electric-field enhancement inside the cavity. Limiting factors are reproducibility and loss of axial symmetry owing to the movable metal core; movement of the core results in fluctuation of the nanocavity dimensions and commensurate variations in enhancement factor. We present a novel synthetic approach for the robust fixation of the central gold rod within a well-defined box, which results in an axisymmetric nanorattle. We determine the structure of the resulting axisymmetric nanorattles by advanced transmission electron microscopy (TEM) and small-angle X-ray scattering (SAXS). Optical absorption and scattering cross-sections obtained from UV-vis-NIR spectroscopy quantitatively agree with finite-difference time-domain (FDTD) simulations based on the structural model derived from SAXS. The predictions of high and homogenous field enhancement are evidenced by scanning TEM electron energy loss spectroscopy (STEM-EELS) measurement on single-particle level. Thus, comprehensive understanding of structural and optical properties is achieved for this class of nanoparticles, paving the way for photonic applications where a defined and robust unit cell is crucial.

Introduction

After irradiation with light, collective coherent oscillation of the free electrons at noble metal nanoparticle surfaces results in an enhanced electromagnetic near-field. These intense local fields can coherently couple to adjacent metallic nanoparticles resulting in enhanced electromagnetic fields that can exceed the intensity of the exciting field by multiple orders of magnitude.[1,2] The optical response and the field enhancement can be tuned by varying the material properties, *e.g.*, type of noble metal (mostly gold or silver), particle size, particle shape and, most importantly, inter-particle spacing.[3] This optimization of the field enhancement is of vital importance in sensing applications because Raman scattering scales with the fourth power of the field strength,[4,5] and therefore, analyte sensitivity is determined by material properties.

Several strategies have been developed for creating particles with large and/or controlled field enhancement in solution. Kumacheva *et al.* used a photo-activated crosslinker to assemble gold nanorods tip-to-tip in solution, targeting advanced sensing and optoelectronic applications.[6] Side-by-side assembly was achieved by Zhang *et al.*, who developed a ligand-controlled self-assembly route based on feedback at a water/chloroform interface. In this work, the authors prepared nanorod dimers with a controlled offset to break the symmetry of light.[7] Alternatively, DNA conjugation has been used extensively for precise assembly of nanorod dimers and nanospheres in solution to induce chiral plasmonic effects.[8–10] Recently, a high-yield strategy has also been introduced, using

[a]Leibniz-Institut für Polymerforschung Dresden e.V., Institute of Physical Chemistry and Polymer Physics, Hohe Str. 6, 01069 Dresden, Germany. E-mail: fery@ipfdd.de, koenig@ipfdd.de
[b]Cluster of Excellence Center for Advancing Electronics Dresden (cfaed), Technische Universität Dresden, 01062 Dresden, Germany
[c]Physical Chemistry II, University of Bayreuth, Universitätsstr. 30, 95440 Bayreuth, Germany
[d]Helmholtz-Zentrum Dresden-Rossendorf, Bautzner Landstraße 400, 01328 Dresden, Germany
[e]Physical Chemistry I, University of Bayreuth, Universitätsstr. 30, 95440 Bayreuth, Germany
*[f]EMAT, University of Antwerp, Groenenborgerlaan 171, 2020 Antwerp, Belgium*
[g]Physical Chemistry of Polymeric Materials, Technische Universität Dresden, Hohe Str. 6, 01069 Dresden, Germany
†Electronic supplementary information (ESI) available: Further experimental details, optical data, electromagnetic simulations and detailed information about the SAXS fitting procedure. See DOI: 10.1039/c7nr02952g
‡These authors have contributed equally.
§Current address: Department of Chemistry, University of Toronto, 80 St. George Street, Toronto, M5S 3A6, Ontario, Canada.
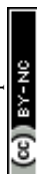
biomolecular interactions to directly fabricate colloidal assemblies with core-satellite architecture.[11,12] In many applications, however, uniform inter-particle distances and isotropic excitation conditions are essential for avoiding intensity fluctuations, and synthesis strategies targeted at improving the field enhancement homogeneity remain highly advantageous.

An alternative approach is core–shell synthesis aimed at generating field enhancement between the core and shell.[13] The group of Nam *et al.* have shown strong field enhancement using DNA-tailorable nanoparticles with ultra-small interior gap in a spherical nanoparticle system for SERS applications.[14] In order to obtain higher yield, the galvanic replacement process was then used by various groups to synthesize spherical,[13,15] cubic,[16,17] cuboidal,[18] and octahedral[19] plasmonic nanorattles, and exploit the improved sensitivity for catalytic applications and plasmonic sensors. In particular, the flat face-to-face contact at metal–insulator-metal contact points ensures larger and stronger region of field enhancement in comparison to curved particles.[5] These rattle nanoparticles, however, incorporate a freely moveable core, and the undefined core position leads to variable gap dimensions and, as a result, multiple and broad plasmonic resonances appear. These limitations can be overcome by introducing axisymmetric fixation of the inner core to the outer box using state-of-the-art synthesis methods, such as anisotropic silver overgrowth of a gold core, while suppressing side reactions[20] combined with kinetically-controlled galvanic replacement reactions.[19,21] This approach ensures a constant and well-defined gap separation over the entire colloidal ensemble.

In this contribution, we demonstrate a novel synthetic approach for axisymmetric nanorattles, comprehensive structural (TEM, SAXS) and optical (UV-vis-NIR) characterization, as well as simulations of the optical properties with the finite difference time domain (FDTD) method. Finally, we demonstrate excellent agreement between the field enhancement predicted by FDTD and EELS mapping, paving the way for applications as plasmonic particles with high intrinsic field enhancement.

Results and discussion

Synthesis and ensemble-averaged characterization *via* small-angle X-ray scattering

The synthesis of axisymmetric nanorattles consists of three steps. First, single-crystalline gold nanorods are prepared using a protocol published by Vigderman and Zubarev.[22] This synthesis utilizes the cationic surfactant cetyltrimethyl-ammonium bromide (CTAB) and silver nitrate to direct the growth of seed particles into single-crystalline gold nanorods. Hydroquinone is used as a weak reducing agent to tune the growth kinetics, resulting in a nearly 100% shape yield and high ion-to-metal conversion. To further reduce the length dispersity, purification based on depletion forces was applied.[23–25]

For this method, in dependency of an employed surfactant concentration, particle sizes and shapes can be targeted due to their different interaction areas. Thus, particles above a certain size are selectively flocculated, followed by sedimentation of those reversible flocculates. This way, the size dispersity of particle solutions can be reduced (for details, see ESI S1 and S2†). On the lateral faces of the gold nanorods, higher-index facets are exposed, while the tips feature low-index facets.[26]

Chloride ions selectively stabilize {100} facets. Consequently, in the second step, silver can be overgrown selectively on the lateral facets using cetyltrimethylammonium chloride (CTAC) as a surfactant. This yields cuboidal shells forming gold@silver cuboids with {100} facets on each of the six faces.[21,27] The controlled overgrowth relies on the deceleration of the reaction kinetics utilizing a syringe pump to suppress side reactions, *e.g.* non-selective silver overgrowth in the longitudinal direction or secondary nucleation (previously described as *living conditions*).[20] Suppression of longitudinal growth is particularly critical for the present synthesis, as uncontrolled growth leads to variations in the core/shell geometry during the next synthesis step.

In the third step, galvanic replacement is carried out on gold@silver cuboids. For this synthesis, a binary surfactant mixture of CTAC and benzylhexadecyldimethylammonium chloride (BDAC) is used to efficiently slow down the reaction kinetics. The aromatic head group of BDAC reduces the diffusion rate of complexed ions toward the stabilized metal surface.[21] Next, BDAC-complexed gold(III) chloride is continuously added at a rate below the kinetic reaction limit in order to suppress etching of the silver shell and favor galvanic replacement. During this process, gold(III) ions are reduced on the gold@silver cuboid surface forming a gold–silver alloy shell. For each reduced gold ion, three silver atoms are oxidized and removed, resulting in a cavity formed between the exterior gold–silver alloy shell and the inner gold nanorod core (eqn (1)).[19,28,29]

$$Au^{3+} + 3Ag^0 \rightarrow Au^0 + 3Ag^+ \tag{1}$$
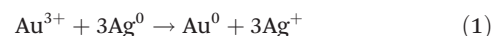
Transmission electron microscopy (TEM) images of the respective nanoparticle geometries are presented in Fig. 1. Due to the controlled nature of the silver overgrowth, gold@silver particles with a well-defined cuboidal shape and, more importantly, a negligible elongation in longitudinal direction (∼2 nm per tip) are obtained. Consequently, the nanorod core is firmly bound to the outer alloy shell after galvanic replacement and, thus, accurately positioned and fixed in the center.

In order to obtain structural information representative of the many-particle ensemble (rather than an isolated fraction as for TEM), we performed small-angle X-ray scattering (SAXS), as summarized in Fig. 2A.[12] Fig. 2B shows the scattering profiles of the intermediate colloidal dispersions (gold nanorods, gold@silver cuboids), as well as the final axisymmetric nanorattles. The scattering response reveals defined form factor minima, which provide detailed information on the size range of different hierarchical levels and indicate the high uniform-
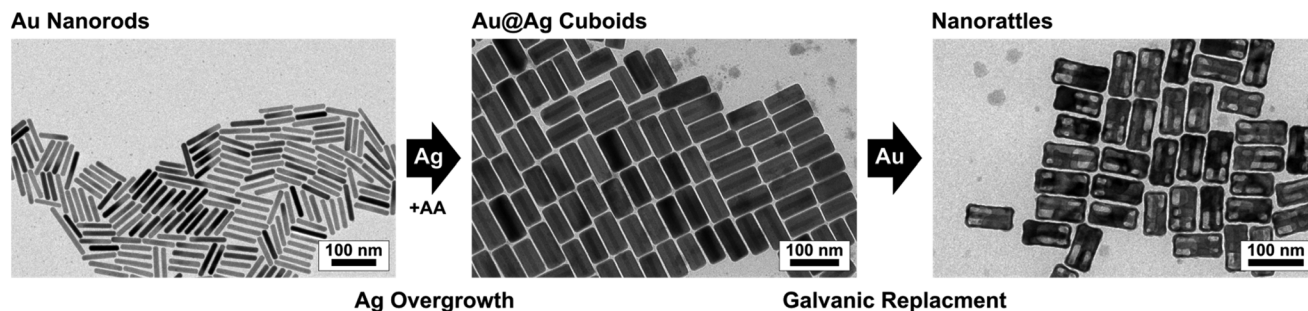
Fig. 1 Synthetic pathway toward axisymmetric nanorattles. In the TEM images, gold nanorods are overgrown with silver (gold@silver cuboids) to obtain axisymmetric nanorattles *via* subsequent galvanic replacement.

ity of the particles' sizes and shapes. Due to the complex three-dimensional structure of the cuboids and nanorattles, the scattering profiles were fitted using numerical modeling based on Debye's equation.[30] The broad parameter space (length, width, dispersity, and nanorattle wall thickness) was screened using a best fit approach, which includes the modeled scattering response of all realistic parameter combinations (for details, see ESI S3†). This comprehensive approach, based on experimental scattering response and best-fit modeling, reveals reliable morphological information concerning the quality of the plasmonic particle.

For gold nanorods, the analytical model of a cylinder (see Fig. 2B) sufficiently describes the experimental scattering response. The nanorod width (mean = 11 nm) had a narrow distribution of 3.5% and the length (mean = 68 nm) were found to exhibit no noticeable dispersity. This high uniformity can be attributed to the efficient purification method applied after synthesis (see experimental part for more details). In the plasmonics community, monodispersity for a colloidal suspension is commonly defined as dispersity below 10%,[31] which

was achieved with ease in our approach utilizing additional purification.

For the model of the three-dimensional structure of the gold@silver cuboid, the previously determined parameters of the gold nanorod were held constant, and the dimensions of the silver shell were varied. Evaluation of the SAXS data yields a width of 31.5 ± 1.6 nm and a length of 72.2 ± 5.8 nm, indicating silver tip layer and a side layer thicknesses of 2.0 nm and 10.4 nm, respectively. In comparison to previous works,[21,27] we obtained gold@silver nanoparticles of high quality (dispersity below 10%) and even more importantly, with a tip elongation of only 2 nm, which is crucial for the fixation of the core in the next synthesis step.

The nanoparticle cavities are defined by the dielectric gap between the fixed rod core and the cuboid box. SAXS analysis of the axisymmetric nanorattles (Fig. 2) provides external dimensions of 77.2 ± 3.9 nm in length and 31.5 ± 3.6 nm in width. The high sensitivity of X-ray scattering to cavity dimensions is discussed in detail in the ESI S3.† From this analysis, the size of the internal gap could be precisely determined to
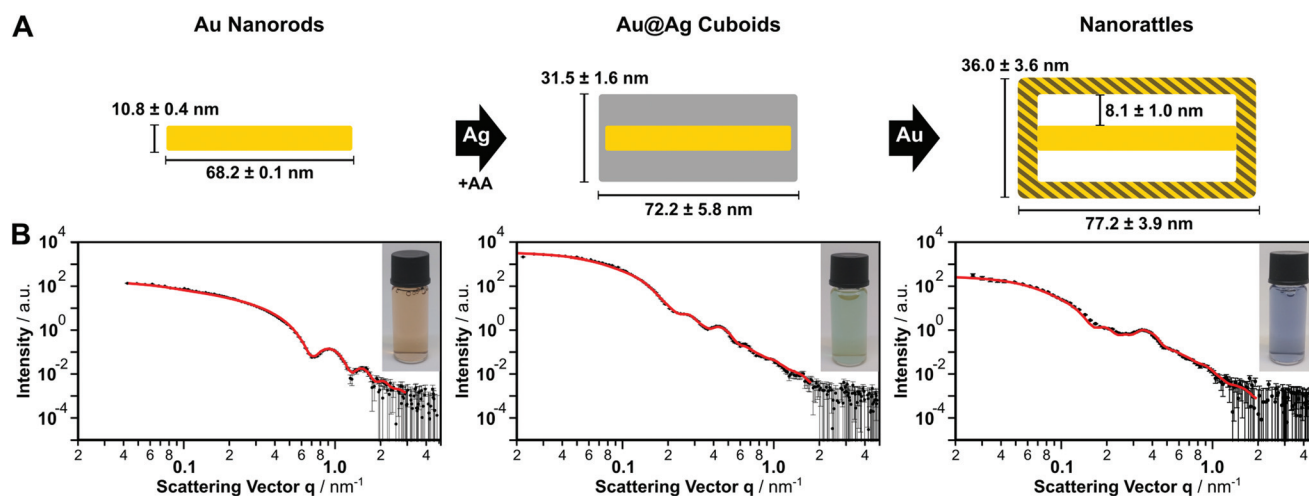

Fig. 2 Morphological characterization of the colloidal dispersion *via* small-angle X-ray scattering. (A) Schematic representation of the nanoparticle dimensions and morphology evaluated by three-dimensional modeling. The free parameters are represented by the respective data in the sketch. (B) Experimental scattering signatures (black dots) and simulations (red lines) for gold nanorods, gold@silver cuboids, and axisymmetric nanorattles.

be 8.1 ± 1.0 nm, corresponding to a shell thickness of 4.5 ± 0.5 nm at the side (long axis) and 5.5 ± 0.5 nm at the tips. A sufficient shell thickness is important to guarantee a spectral overlap between the plasmonic mode from the shell and the transversal mode from the gold nanorod core.[32] Because the galvanic replacement is initiated by the formation of a hole in the silver shell (as described in detail by Liz-Marzán et al.[19,28]), small structural defects were observed by TEM (Fig. 1). These structural defects were represented in the SAXS models by filling 9% of the cavity volume with diffuse silver scattering centers (see ESI S3F†). When considered as a whole, the SAXS measurements and models indicate that extraordinary low dispersity (<10%) was achieved, and the nanorattle cores were axisymmetrically fixed with an outstanding spatial precision below 1 nm, throughout the entire colloidal dispersion.

Plasmonic response *via* polarization-dependent UV-vis-NIR spectroscopy

We experimentally analyzed the plasmonic properties of the colloidal dispersion by extinction, absorption and scattering UV-vis-NIR spectroscopy using an integrating sphere setup (Fig. 3). In order to model the UV-vis-NIR spectroscopic response, we used the geometric sizes obtained from SAXS evaluation and calculated the optical response using a time-domain electromagnetic modeling method.

Gold nanorods exhibit one transversal dipolar mode (T1), a dominant longitudinal dipolar mode (L1), and a higher-order longitudinal mode (L2), which is in good agreement with observations from literature.[33–35] The transversal and longitudinal modes originate from excitation along the short and long axes of the nanoparticle, respectively. Importantly, an indication for high field enhancement is a dominant contribution in absorption cross section, consequently, we will distinguish between scattering and absorption. The scattering cross sections reveal that the energetically lowest longitudinal mode (L1) contributes more strongly to scattering than the energetically higher modes, which is also in good agreement

with observations from the literature.[33–35] The positions of the plasmonic modes, as well as the intensity ratios are also in good agreement with the results from electromagnetic simulations, which were based on the geometric size information revealed by SAXS modeling.

The plasmonic properties of the gold@silver cuboids are dominated by their cuboidal silver shells. Three distinct transversal modes (T1–T3) and one longitudinal dipolar mode (L1) are present in the FDTD simulations and in the experimental measurements.[21,36] The number of transversal modes is directly correlated with edge rounding and/or corner sharpness, and theoretically, five cubic modes are possible.[37] To the best of our knowledge, a maximum of three modes have been observed experimentally for edge lengths smaller than 40 nm. FDTD simulations revealed an edge rounding (defined as radius of curvature scaled by edge length) smaller than 8% (see ESI S4†). All modes show a strong contribution to absorption, except the longitudinal mode. Due to the significantly greater polarizability of silver compared to gold, the longitudinal resonance shows a stronger contribution to scattering in the NIR region.

In the case of the axisymmetric nanorattles, two transversal (T1 and T2) modes and one longitudinal (L1) are excited. During the galvanic replacement process, the cuboidal silver shell is reduced to a dielectric gap covered by a cuboidal gold box. At the same time, the ultra-thin silver layer on the tips ensures a fixed gold rod at the center. Consequently, the nanocavity can be excited between the cuboidal box and the inner gold rod. A high field enhancement is expected within the gap region, which correlates with dominant contribution of absorption cross-section. We also observe multiple transversal modes, which will be described in more detail below. The electromagnetic modeling of axisymmetric nanorattles was performed in the same manner as for core–shell and rod particles based on the morphology obtained from SAXS measurements. Here we found good agreement in the energetic mode positions, but the electromagnetic modeling underestimates the resonance broadening. In literature, this resonance broaden-
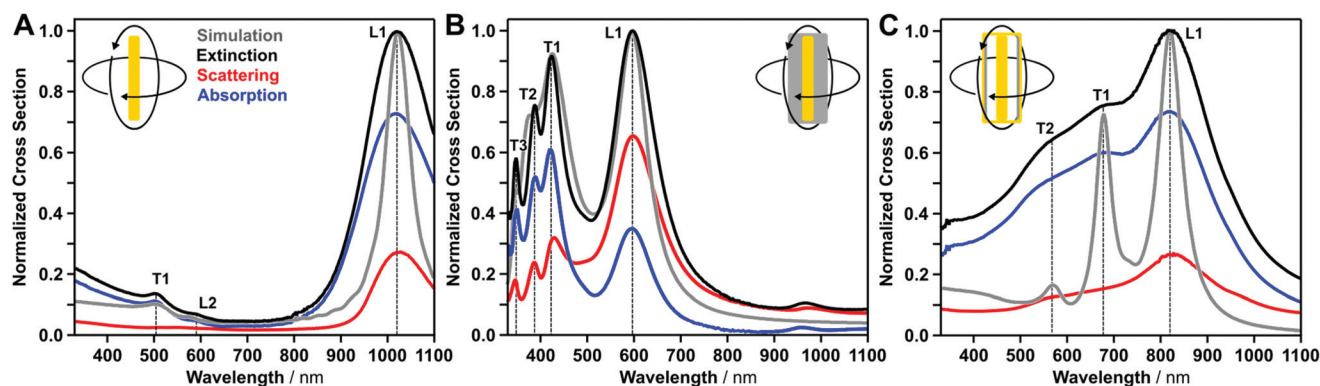

Fig. 3 Numerical simulation of the ensemble-averaged geometric model and comparison with absorption, scattering and extinction UV-vis-NIR spectroscopy. Optical response for gold nanorods (A), gold@silver cuboids (B) and axisymmetric nanorattles (C) and numerical simulations (grey line). Cross-sections were calculated based on the morphology obtained from SAXS evaluation. Schematic inset indicates the degree of freedom in the solution based measurements. Extinction (black line) is defined as sum of absorption (blue line) and scattering (red line).
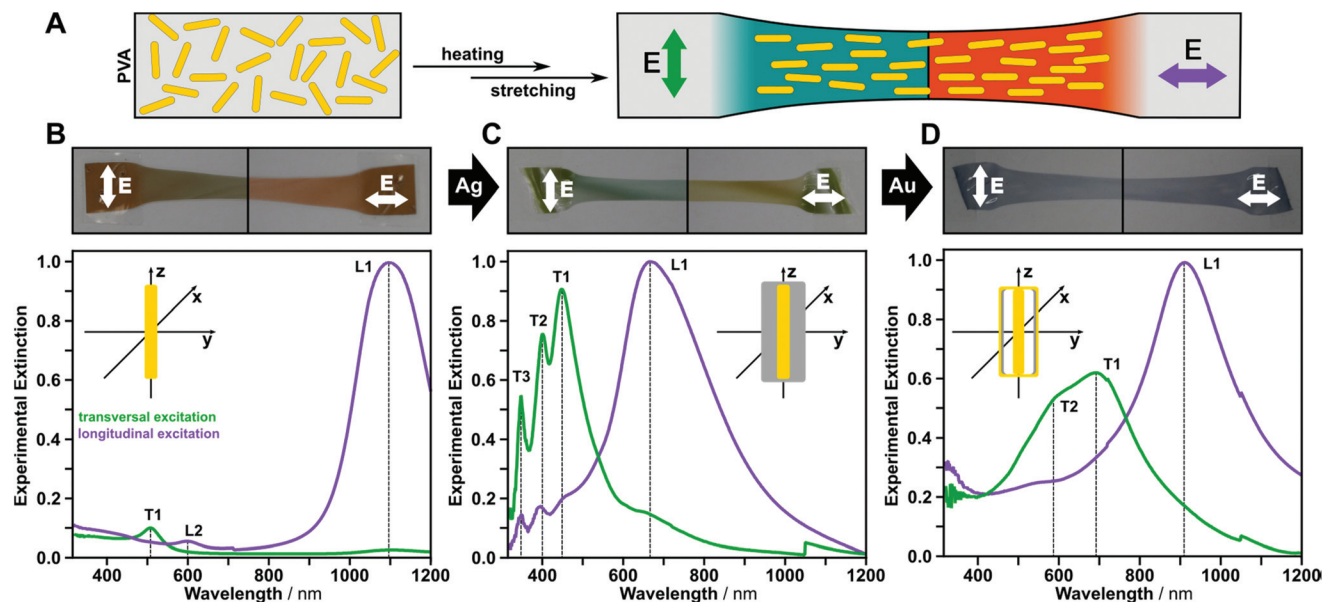
Fig. 4 Control over the anisotropic plasmonic properties by mechanical strain within a polymeric matrix. Embedding the rod-like nanoparticles in PVA matrices and subsequently stretching above the glass transition temperature results in macroscopic orientation of the anisotropic nanoparticles (schematically depicted in A). Polarization imaging and polarized UV-vis-NIR spectroscopy reveal the separate excitation of the transversal (green) and the longitudinal (purple) plasmonic modes for gold nanorods (B), gold@silver cuboids (C), and axisymmetric nanorattles (D).

ing was attributed to size and wall thickness variations.[23] In addition, broadening could also be connected to defects in the walls, however, due to the random nature of these wall defects (variation in size and position), they could not be included in the electromagnetic modeling. So far, we used conventional UV-vis-NIR spectroscopy to identify the plasmonic modes and assign transversal or longitudinal excitation based on their spectral position. In order to clarify the nature of the excitation, we conducted polarization-dependent measurements.

In order to orient the synthesized nanoparticles without electromagnetic coupling, a suspension of the surfactant-functionalized particles was mixed with a saturated aqueous polyvinyl alcohol (PVA) solution (Fig. 4).[38] Films of this suspension were prepared by evaporation of the water. The 1 mm thick films were cut into 10×50 mm² pieces, heated above the glass transition temperature ($T_g \sim 75$ °C),[39] and uniaxially stretched by 200%. The resulting shear forces acting between polymer matrix and the anisotropic nanoparticles aligned the particles along the stretching axis, and after this process, polarization dependence could easily be observed with the bare eye. We used polarized UV-vis-NIR spectroscopy to characterize the macroscopically aligned samples, and we were experimentally able to distinguish between transversal and longitudinal modes for each nanoparticle type. Fig. 4 shows color changes for gold nanorods and gold@silver cuboids in the visible wavelength range. The axisymmetric nanorattles show minor differences in color by observation with the bare eye, which is expected due to the close vicinity of the transversal nanocavity modes and the longitudinal mode in the red to NIR wavelength range. Generally, the plasmonic resonances were red-shifted with respect to their positions in aqueous solution owing to the

change of refractive index of the matrix (i.e., from water ($n = 1.33$) to PVA ($n = 1.47$ as measured by spectroscopic ellipsometry, see ESI S5† for more details)).[40]

For polarization-dependent UV-vis-NIR spectroscopy, we must define two excitation possibilities: electric field vector parallel and perpendicular to the stretching axis. Perpendicular excitation of the gold nanorods leads to a transversal mode at 510 nm (T1) only. For parallel excitation, the higher-order dipolar mode at 605 nm (L2) and the dipolar longitudinal mode at 1095 nm (L1) are observable (Fig. 4B). The measurements indicate near-perfect alignment of the gold nanorods with a dichroic ratio of 0.97 (for details see ESI†). For gold@silver cuboids, three resonances at 448 nm, 401 nm, and 348 nm (T1–3) were found during the polarization dependent measurement, corresponding to the experimentally-observed cubic modes (see also the discussion in the FDTD modelling section). For parallel excitation, only the longitudinal dipolar resonance (L1) at 670 nm was observed. For this excitation state, weak plasmonic modes were also present in the UV region, which match the cubic modes from perpendicular excitations. For the axisymmetric nanorattles, extinction along the stretching axis shows a pronounced plasmon resonance at 911 nm. For perpendicular excitation, two cavity modes (T1 at 690 nm, and T2 at 600 nm) could be clearly identified.

Near-field plasmonic properties via EELS mapping and FDTD modeling

Upon excitation, each of the particle types features distinct electromagnetic properties (Fig. 5A). The local distribution of surface charges, field enhancements, effective areas, and strengths are closely correlated with the respective particle
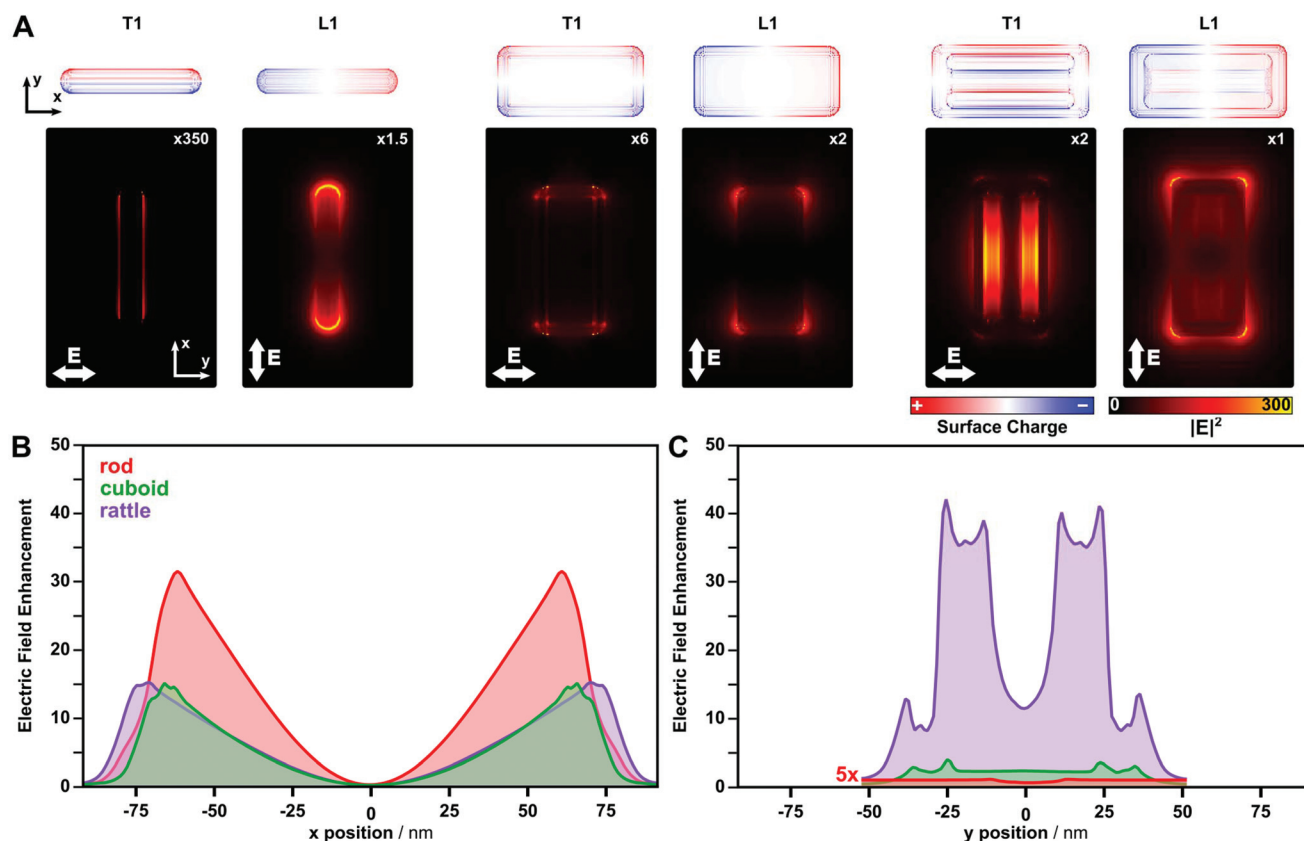
Fig. 5 Surface charge distribution and electric-field enhancement of the different plasmonic nanoparticles. (A) Nature of the plasmonic modes and integrated electric field distributions (integrated in z-direction) of the energetically lowest transversal and longitudinal plasmonic modes. The plasmonic modes were excited perpendicular and parallel to the long axes of the nanoparticles at the wavelength of the corresponding plasmonic resonance. Integrated electric field enhancement for longitudinal (B) and transversal excitation (C) (integrated in y–z and x–z, respectively, and normalized to the integrated distance and area).

shape and composition. To compare the electric field enhancements, we integrated the electric field along the beam direction and normalized these values by the integrated distance. Gold nanorods, for example, have a rather weak electric field enhancement along the cylindrical shaped rod for transversal excitation. For longitudinal excitation, the field enhancement is pronounced at the tips, as can be also identified also from the corresponding distribution of surface charges. This field concentration is increased for gold@silver cuboids as a result of the sharp edges and inclusion of plasmonically-active silver as a shell material. For axisymmetric nanorattles, a nanocavity is present and a confined electric field is observed within the dielectric cavity volume (transversal excitation). Surface charge calculations reveal the nature of the nanocavity mode. Here, the shell induces the mirror charge into the core material. These observations are in agreement with results reported in literature.[21,41] A similar nanocavity signature is obtained for the longitudinal mode, however, this signature is less pronounced due to the electrical contact between the core and the shell at the tips of the internal gold nanorods.

In order to compare and to quantify the cavity resonance with the resonances of gold nanorods and gold@silver cuboids, we integrated the electric field along the beam direc-

tion (z-axis) and lateral directions (x-axis or y-axis, respectively). Using this integration method (shown in Fig. 5), we plotted the plasmonic resonances as cross-sections corresponding to the transversal and longitudinal excitation. In these cross-section plots, two properties of the plasmonic modes could be identified: (I) the highest field enhancement occurs at the metallic–dielectric interface, and (II) the electric field decays exponentially into the dielectric material and environment. For the longitudinal cross-section (electric field vector parallel to y-axis), the field enhancement is most significant at the sharp corners. Excitations of the transversal modes (electric field vector parallel to x-axis) reveal significant differences for the various nanoparticle types. Especially for the axisymmetric nanorattles, we observed a dominant field enhancement in the gap region, which exceeds the field enhancement of the shell-environment by multiple times. More importantly, the field enhancement is even stronger than that of the longitudinal mode. In summary, these electromagnetic modeling methods present solid theoretical support for the characteristic surface charge signature and strong field enhancement factor of the cavity mode only observed for axisymmetric nanorattles.

Finally, to experimentally establish the morphological shape and field enhancement within the gap region, we ana-

lyzed the axisymmetric nanorattles by electron tomography in high-angle annular dark-field scanning transmission electron microscopy (HAADF-STEM) mode, and we supported these measurements with STEM energy dispersive X-ray spectroscopy (STEM-EDS) and STEM electron energy loss spectroscopy (STEM-EELS) mapping (Fig. 6). The investigations of the morphology (HAADF-STEM), accompanied by elemental analysis, reveal the composition of the outer shell to be an alloy of silver and gold, which is in good agreement with SAXS evaluation (details in ESI S6,† as well as literature).[28] For all analyzed nanorattles, a fixed gold rod covered by a gold box was observed. Artifacts, such as bridging between box and core were attributed to incomplete galvanic replacement and included in the SAXS evaluation. The STEM-EELS analysis of the nanorattles allowed detection of the near-field plasmonic features (Fig. 6D and ESI S7–9†). The STEM-EELS results are in good agreement with those from UV-vis-NIR spectroscopy, where three plasmonic modes could be observed. Deviations in mode positions, however, were observed and attributed to interactions with the thin carbon substrate used for EELS measurements, which is not accounted for in our simulations.[42] Further details can be found in the ESI S9.† Mapping of the near-field by EELS allows quantification of the spatial field enhancement of plasmonic modes.[43] At low energy losses (1.5 eV–2.0 eV, 620 nm–827 nm), the longitudinal dipolar mode (L1) of the nanorattle is excited. Energy losses ranging from 2.5 eV to 3.0 eV (413 nm–496 nm) identify the first-order transversal cavity mode (T1). Here, the electric field is homogeneously distributed inside the cavity. At energy losses between 3.0 eV–3.5 eV (354 nm–413 nm), the higher-order transversal mode (T2) is excited, showing a weaker field enhancement inside the cavity. The transversal response is superposed by the bridging defects between core and box. Consequently, the plasmonic properties observed on the single particle level can be transferred to the macroscopic level and *vice versa*.
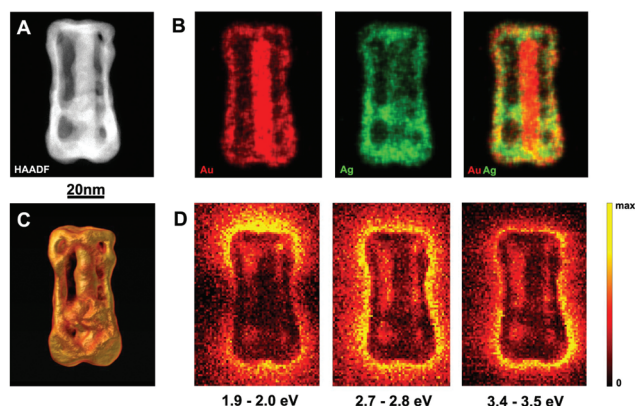

Fig. 6 Structural and electromagnetic characterization of an individual nanorattle. HAADF-STEM image of a nanorattle (A), STEM-EDS elemental maps revealing the distribution of Au and Ag in the structure (B) three-dimensional (3D) representation of the reconstructed volume of the nanorattle shown in A, (C) revealing the lateral separation between inner core and shell. STEM-EELS mappings (D) at distinct energies show electric field enhancement inside of the cavity.

Conclusion

Using a galvanic replacement process, we synthesized a nanoparticle structure where a metallic nanorod core is fixed at the small facets of a nanobox shell with defined dielectric spacer. This structure shows strong field enhancement in the particles inner cavity, which is homogenous for all particles. This field enhancement critically depends on the particle's morphology, especially on the axially-symmetric fixation of the gold nanorod to the gold nanobox and the dimensions of the box. Since our protocol allows controlling these parameters with nanoscale accuracy, the field enhancement can be efficiently tailored. For sensing and catalytic applications, a uniform wall thickness is important to ensure efficient coupling of light to the plasmonic cavity. The tailored optical properties were confirmed by comprehensive structural (TEM, SAXS) and optical (polarized UV-vis-NIR) characterization. Moreover, electromagnetic simulations were used to verify the consistency of the model and quantify the electric field enhancement. A reliable and up-scalable synthesis method of an axisymmetric nanorattle is a first step toward novel photonic *meta*-surfaces, which obtain their optical properties from the collective excitation of the assembled unit cells.[44,45] The geometric design of the unit cell is the key for such structures, which can be subsequently arranged by self-assembly to potentially exploit their collective optical effects.[46,47] Thus, our approach adds a novel element to the toolbox of plasmonic metamaterials.

Experimental

Materials

CTAB (99%) was purchased from Merck chemicals. CTAC, HAuCl$_4$·3H$_2$O (99.9%), silver nitrate (99.9999%), sodium borohydride (99%), hydroquinone (HQ, 99%), and PVA (M_w 70–100 kg mol^{-1}) were purchased from Sigma Aldrich. L-(+)-Ascorbic acid (AA, 99.5%) was purchased from Grüssing GmbH. BDAC was purchased from Molekula. All chemicals were used without further purification. All solutions, except HAuCl$_4$, were prepared immediately before use. Glassware was cleaned with aqua regia prior to use. Water was purified using a Milli-Q system (Millipore). The final resistivity was 18.2 MΩ cm.

Seed synthesis

CTAB solution (5 mL, 0.2 M) was mixed with 5 mL of an aqueous 1 mM HAuCl$_4$ solution (43.4 μL of a 0.11518 M HAuCl$_4$ solution was added to 5 mL of water). 600 μL of 0.01 M NaBH$_4$ solution was quickly added while stirring vigorously, resulting in a brownish yellow solution. Stirring was continued for 2 min, then the seed solution was kept at room temperature for up to 30 minutes until use.

Synthesis of gold nanorods

36.45 g CTAB was dissolved in 1000 mL of purified water (f.c.: 0.1 M). 4.341 mL of 0.11518 M HAuCl$_4$ solution (f.c.: 0.5 mM) and 5 mL of 0.1 M AgNO$_3$ solution were added (f.c.: 0.5 mM).

After at least 5 min, 50 mL of 0.1 M HQ solution (f.c.: 5 mM) was added while stirring. 2 min later, 24 mL of the as-prepared seed solution was added (3 batches of seed solution were mixed). Before characterization, the gold nanorod suspension was kept at 32 °C for at least 48 h.

Purification of gold nanorods

In a graduated cylinder, 11.33 g of CTAC (0.0354 mol) were dissolved in 88 mL purified water. 140 mL of the as-prepared gold nanorod dispersion was centrifuged for 30 min at 8500 rcf to decrease the volume to 12 mL. The resulting gold nanorod dispersion was mixed with the CTAC solution (f.c.: CTAC: 0.354 M, CTAB: 0.012 M). The colloidal solution was left to settle for 21 h before 95 mL of the supernatant, having a light reddish brown color, was decanted. The remaining 5 mL of the solution, containing a brown sediment, was diluted with 5 mL of Milli-Q water (f.c.: CTAC: 0.177 M, CTAB: 0.006 M). 24 h after the last agitation, the brown supernatant was separated from the brown sediment. This final sediment was used for further growth reactions.

Synthesis of gold@silver cuboids with an Ag/Au ratio of 15

35 mL of the as-prepared gold nanorod solution was centrifuged for 30 min at 8500 rcf and decanted, to reduce to volume to 5 mL. The 5 mL gold nanorod dispersion was diluted with 25 mL of a 10 mM CTAC solution. This process was repeated six times. The concentration of gold in the final solution was 0.193 mmol L^{-1} as measured utilizing the interband absorption at a wavelength of 400 nm.[33] 100 mL of this gold nanorod solution was used in the synthesis of 1 : 15 Au@Ag cuboids. Using a syringe pump with two identical syringes, 25 mL of a 0.1 M AgNO$_3$ solution and 25 mL of a 0.4 M AA solution were added to the gold nanorod solution, while it was heated to a temperature of 60 °C. The syringes were each set to deliver 250 μL h^{-1} (0.15 mol Ag per mol Au per h) in two steps of 12.5 mL each. All containers, syringes and tubes were shielded from ambient light to prevent solution degradation. The resulting deep green Au@Ag cuboid dispersions were centrifuged (35 min, 3500 rcf) and washed with a 10 mM CTAC solution.

Synthesis of nanorattle particles using a syringe pump setup

10 mL of Au@Ag cuboids with a Ag/Au ratio of 15 in CTAC were diluted with 80 mL of purified water and 10 mL of 0.1 M BDAC-solution. For a stoichiometric replacement of 40% of the silver, 30.3 mL of a 0.125 mM HAuCl$_4$-solution, containing 10 mM BDAC, were added using a syringe pump. The first two milliliters were added over the course of one hour, the remaining 28.3 mL were added over three hours. For different stoichiometric replacement percentages, the total quantity of added HAuCl$_4$ solution was varied.

Preparation of PVA films containing metal nanoparticles

7.5 g of PVA (90 kg mol^{-1}) was dissolved in 92.5 g of purified water (7.5 wt%). For each PVA film, 5 mL of the corresponding particle solution was added to 20 mL of PVA solution. After thorough mixing, the solutions were transferred into a petri dish and degassed in a desiccator under high vacuum until the solution was free of trapped air. The petri dish was then placed on a hot plate and heated to 90 °C. To slow down evaporation, the petri dish was covered with a watch glass, leaving a small gap for moisture to escape.

Electron microscopy characterization

Standard transmission electron microscopy measurements were performed with a Zeiss LEO 922 OMEGA EFTEM with an acceleration voltage of 200 kV. For TEM analysis of nanoparticles, 1 mL of nanoparticle solution was concentrated to 100 μL via centrifugation and washed twice to reduce the surfactant concentration below the critical micelle concentration. Subsequently, 4 μL of this solution was dried on 300 mesh copper grid with an approximately 3 nm carbon film.

HAADF-STEM images, electron tomography series, STEM-EDS elemental maps and STEM-EELS plasmon maps were acquired using an aberration-corrected cubed FEI Titan electron microscope operated at 120 kV and equipped with a monochromator, yielding an energy resolution of 0.12 eV. For the acquisition of the tomography series, a Fischione model 2020 single tilt tomography holder was used, and the series were acquired manually within a tilt range from −74° to +70° using a tilt increment of 2°. The reconstruction of the series was performed using the simultaneous iterative reconstruction technique (SIRT), implemented in the ASTRA toolbox.[48] For the acquisition of the STEM-EDS elemental maps, a ChemiSTEM system was used,[49] and quantification was performed using ESPIRT software. To analyze the EELS data sets, we used the EELSModel software.[50] The thickness of the C support was approximately 3 nm.

UV-vis-NIR spectroscopy

UV-vis-NIR spectra were recorded on a Cary 5000 spectrophotometer (Agilent, USA) equipped with a diffuse reflection accessory (DRA) for absorption spectroscopy and a universal measurement accessory (UMA) for polarization dependent spectroscopy. Determination of the extinction, absorption and reflection contributions was performed as described elsewhere.[12]

Small-angle X-ray scattering (SAXS)

All SAXS data reported here were measured using a "Double Ganesha AIR" (SAXSLAB, Denmark). The X-ray source of this laboratory-based system is a rotating anode (copper, MicoMax 007HF, Rigaku Corporation, Japan) providing a parallel beam at λ = 0.154 nm. The measurements were done on samples contained in 1 mm glass capillaries (Hilgenberg, code 4007610, Germany) at room temperature, and the transmitted intensity data were recorded by a position sensitive detector (PILATUS 300 K, Dectris). To cover the range of scattering vectors between 0.02–5.0 nm^{-1}, different detector positions were used. The circularly averaged data were normalized to incident beam, sample thickness and measurement time before subtraction of the solvent. All measurements were put on an absolute scale by standard less absolute intensity calibration.

Electromagnetic simulations (FDTD)

Simulations of extinction/absorbance/scattering spectra, induced magnetic and electric fields, surface charge distributions and current flow were performed using the commercial software FDTD Solutions (ver. 8.11.422) from Lumerical Solutions Inc. A total-field scattered-field source was used for the interaction with light and with a moving dipole source for the comparison with EELS measurements. For EELS simulations, the model and scripts of Nordlander and coworkers were used with a meshing of the electron trajectory in 750° × 2° nm steps.[42] For the dielectric properties of silver, a CRC approximation by Hagemann et al. was used, while for the properties of gold, data from Johnson and Christy was used.[51,52] For each material, a RMS error of 0.2 or lower was given. Two meshes were used for the simulation: for the empty space, a mesh size of 2 nm was used, while the particle was meshed with a size of 0.5 nm. To determine the field distributions, charge density and current flow, the model was simulated at the wavelengths of the absorption maxima of the corresponding plasmonic modes. Electric field enhancement distributions were integrated along the incident k-vector and the related cross-sections further integrated to the plane of incidence of the electric field of the incident light source. All simulations reached a convergence of 10^{-5} before reaching 300 fs simulation time. For the best simulation stability, the mesh area was chosen to be at least 100 nm larger than the modeled structure in all three spatial directions.

Acknowledgements

References

1 E. Hao and G. C. Schatz, J. Chem. Phys., 2003, 120, 357–366.
2 D. C. Marinica, A. K. Kazansky, P. Nordlander, J. Aizpurua and A. G. Borisov, Nano Lett., 2012, 12, 1333–1339.
3 M. Rycenga, C. M. Cobley, J. Zeng, W. Li, C. H. Moran, Q. Zhang, D. Qin and Y. Xia, Chem. Rev., 2011, 111, 3669–3712.
4 R. A. Alvarez-Puebla and L. M. Liz-Marzán, Small, 2010, 6, 604–610.
5 R. Kodiyath, S. T. Malak, Z. A. Combs, T. Koenig, M. A. Mahmoud, M. A. El-Sayed and V. V. Tsukruk, J. Mater. Chem. A, 2013, 1, 2777.
6 A. Lukach, K. Liu, H. Therien-Aubin and E. Kumacheva, J. Am. Chem. Soc., 2012, 134, 18853–18859.
7 S. Yang, X. Ni, X. Yin, B. Kante, P. Zhang, J. Zhu, Y. Wang and X. Zhang, Nat. Nanotechnol., 2014, 9, 1002–1006.
8 C. A. Mirkin, R. L. Letsinger, R. C. Mucic and J. J. Storhoff, Nature, 1996, 382, 607–609.
9 W. Ma, H. Kuang, L. Wang, L. Xu, W. S. Chang, H. Zhang, M. Sun, Y. Zhu, Y. Zhao, L. Liu, C. Xu, S. Link and N. A. Kotov, Sci. Rep., 2013, 3, 1934.
10 A. Kuzyk, R. Schreiber, Z. Fan, G. Pardatscher, E.-M. Roller, A. Hogele, F. C. Simmel, A. O. Govorov and T. Liedl, Nature, 2012, 483, 311–314.
11 S. N. Sheikholeslami, H. Alaeian, A. L. Koh and J. A. Dionne, Nano Lett., 2013, 13, 4137–4141.
12 R. P. Höller, M. Dulle, S. Thomä, M. Mayer, A. M. Steiner, S. Förster, A. Fery, C. Kuttner and M. Chanana, ACS Nano, 2016, 10, 5740–5750.
13 J. A. Fan, K. Bao, L. Sun, J. Bao, V. N. Manoharan, P. Nordlander and F. Capasso, Nano Lett., 2012, 12, 5318–5324.
14 D.-K. Lim, K.-S. Jeon, J.-H. Hwang, H. Kim, S. Kwon, Y. D. Suh and J.-M. Nam, Nat. Nanotechnol., 2011, 6, 452–460.
15 N. Gandra, C. Portz and S. Singamaneni, Adv. Mater., 2014, 26, 424–429.
16 Y. Ma, W. Li, E. C. Cho, Z. Li, T. Yu, J. Zeng, Z. Xie and Y. Xia, ACS Nano, 2010, 4, 6725–6734.
17 J.-E. Park, S. Kim, J. Son, Y. Lee and J.-M. Nam, Nano Lett., 2016, 16, 7962–7967.
18 Y. Khalavka, J. Becker and C. Sönnichsen, J. Am. Chem. Soc., 2009, 131, 1871–1875.
19 L. Polavarapu, D. Zanaga, T. Altantzis, S. Rodal-Cedeira, I. Pastoriza-Santos, J. Pérez-Juste, S. Bals and L. M. Liz-Marzán, J. Am. Chem. Soc., 2016, 138, 11453–11456.
20 M. Mayer, L. Scarabelli, K. March, T. Altantzis, M. Tebbe, M. Kociak, S. Bals, F. J. García de Abajo, A. Fery and L. M. Liz-Marzán, Nano Lett., 2015, 15, 5427–5437.
21 M. Tebbe, C. Kuttner, M. Mayer, M. Maennel, N. Pazos-Pérez, T. A. Koenig and A. Fery, J. Phys. Chem. C, 2015, 119, 9513–9523.
22 L. Vigderman and E. R. Zubarev, Chem. Mater., 2013, 25, 1450–1457.
23 K. Park, H. Koerner and R. A. Vaia, Nano Lett., 2010, 10, 1433–1439.
24 L. Scarabelli, M. Coronado-Puchau, J. J. Giner-Casares, J. Langer and L. M. Liz-Marzán, ACS Nano, 2014, 8, 5833–5842.

25 K. Nakamura, T. Oshikiri, K. Ueno, Y. Wang, Y. Kamata, Y. Kotake and H. Misawa, *J. Phys. Chem. Lett.*, 2016, **7**, 1004–1009.

26 E. Carbó-Argibay, B. Rodríguez-González, S. Gómez-Graña, A. Guerrero-Martínez, I. Pastoriza-Santos, J. Pérez-Juste and L. M. Liz-Marzán, *Angew. Chem., Int. Ed.*, 2010, **49**, 9397–9400.

27 S. Gómez-Graña, B. Goris, T. Altantzis, C. Fernández-López, E. Carbó-Argibay, A. Guerrero-Martínez, N. Almora-Barrios, N. López, I. Pastoriza-Santos, J. Pérez-Juste, S. Bals, G. Van Tendeloo and L. M. Liz-Marzán, *J. Phys. Chem. Lett.*, 2013, **4**, 2209–2216.

28 B. Goris, L. Polavarapu, S. Bals, G. Van Tendeloo and L. M. Liz-Marzán, *Nano Lett.*, 2014, **14**, 3220–3226.

29 X. Zhuo, X. Zhu, Q. Li, Z. Yang and J. Wang, *ACS Nano*, 2015, **9**, 7523–7535.

30 P. Debye, *Ann. Phys.*, 1915, **351**, 809–823.

31 N. G. Bastús, F. Merkoçi, J. Piella and V. Puntes, *Chem. Mater.*, 2014, **26**, 2836–2846.

32 Z. A. Combs, S. T. Malak, T. König, M. A. Mahmoud, J. L. Chávez, M. A. El-Sayed, N. Kelley-Loughnane and V. V. Tsukruk, *Part. Part. Syst. Charact.*, 2013, **30**, 1071–1078.

33 L. Scarabelli, A. Sanchez-Iglesias, J. Perez-Juste and L. M. Liz-Marzan, *J. Phys. Chem. Lett.*, 2015, **6**, 4270–4279.

34 X. Ye, C. Zheng, J. Chen, Y. Gao and C. B. Murray, *Nano Lett.*, 2013, **13**, 765–771.

35 B. Nikoobakht and M. A. El-Sayed, *Chem. Mater.*, 2003, **15**, 1957–1962.

36 B. A. Glatz, M. Tebbe, B. Kaoui, R. Aichele, C. Kuttner, A. E. Schedl, H. W. Schmidt, W. Zimmermann and A. Fery, *Soft Matter*, 2015, **11**, 3332–3339.

37 S. Zhang, K. Bao, N. J. Halas, H. Xu and P. Nordlander, *Nano Lett.*, 2011, **11**, 1657–1663.

38 J. Pérez-Juste, B. Rodríguez-González, P. Mulvaney and L. M. Liz-Marzán, *Adv. Funct. Mater.*, 2005, **15**, 1065–1071.

39 Z. H. Mbhele, M. G. Salemane, C. G. C. E. van Sittert, J. M. Nedeljković, V. Djoković and A. S. Luyt, *Chem. Mater.*, 2003, **15**, 5019–5024.

40 S. Mahendia, A. K. Tomar, P. K. Goyal and S. Kumar, *J. Appl. Phys.*, 2013, **113**, 073103.

41 M. Mayer, M. Tebbe, C. Kuttner, M. J. Schnepf, T. A. Konig and A. Fery, *Faraday Discuss.*, 2016, **191**, 159–176.

42 Y. Cao, A. Manjavacas, N. Large and P. Nordlander, *ACS Photonics*, 2015, **2**, 369–375.

43 A. L. Koh, K. Bao, I. Khan, W. E. Smith, G. Kothleitner, P. Nordlander, S. A. Maier and D. W. McComb, *ACS Nano*, 2009, **3**, 3015–3022.

44 W. Fan, S. Zhang, B. Minhas, K. J. Malloy and S. R. J. Brueck, *Phys. Rev. Lett.*, 2005, **94**, 033902.

45 S. P. Burgos, R. de Waele, A. Polman and H. A. Atwater, *Nat. Mater.*, 2010, **9**, 407–412.

46 S. Gómez-Graña, J. Pérez-Juste, R. A. Alvarez-Puebla, A. Guerrero-Martínez and L. M. Liz-Marzán, *Adv. Opt. Mater.*, 2013, **1**, 477–481.

47 T. Thai, Y. Zheng, S. H. Ng, H. Ohshima, M. Altissimo and U. Bach, *Nanoscale*, 2014, **6**, 6515–6520.

48 W. van Aarle, W. J. Palenstijn, J. De Beenhouwer, T. Altantzis, S. Bals, K. J. Batenburg and J. Sijbers, *Ultramicroscopy*, 2015, **157**, 35–47.

49 P. Schlossmacher, D. Klenov, B. Freitag and H. Von Harrach, *Microsc. Today*, 2010, **18**, 14–20.

50 J. Verbeeck and S. Van Aert, *Ultramicroscopy*, 2004, **101**, 207–224.

51 H. J. Hagemann, W. Gudat and C. Kunz, *J. Opt. Soc. Am.*, 1975, **65**, 742–744.

52 P. B. Johnson and R. W. Christy, *Phys. Rev. B: Solid State*, 1972, **6**, 4370–4379.

4   Colloidal -to-film coupled cavities

4.1 Template-assisted colloidal self-assembly of macroscopic magnetic metasurfaces

Template-assisted colloidal self-assembly of macroscopic magnetic metasurfaces.

Martin Mayer, Moritz Tebbe, Christian Kuttner, Max J. Schnepf, **Tobias A. F. König*** and Andreas Fery*

*corresponding authors

Author contribution statement

MM carried out the experiments. **TK** encouraged MM and MS to investigate the simulation and optical spectroscopy methods as well as supervised the execution and findings of this work. MT and CK contributed through synthesis and concept development. The authors **TK** and AF made a significant contribution to the conception and design of the work. Through the simulation methods and optical spectroscopy methods, the author **TK** made a significant contribution to the acquisition, analysis and interpretation of the data. All authors provided critical feedback and helped shape the research, analysis and manuscript.

PAPER

Template-assisted colloidal self-assembly of macroscopic magnetic metasurfaces†

Martin Mayer,[ac] Moritz Tebbe,[b] Christian Kuttner,[ac] Max J. Schnepf,[a] Tobias A. F. König*[acd] and Andreas Fery*[ace]

We demonstrate a template-assisted colloidal self-assembly approach for magnetic metasurfaces on macroscopic areas. The choice of anisotropic colloidal particle geometry, assembly pattern and metallic film is based on rational design criteria, taking advantage of mirror-charge effects for gold nanorods placed on gold film. Monodisperse gold nanorods prepared utilizing wet-chemistry are arranged with high precision on wrinkled templates to form linear array-type assemblies and subsequently transferred to a thin gold film. Due to the obtained particle-to-film distance of 1.1 nm, the plasmonic mode of the nanorod is able to couple efficiently with the supporting metallic film, giving rise to a magnetic mode in the visible spectrum (721 nm). Conventional UV-vis-NIR measurements in close correlation with electromagnetic simulations provide evidence for the presence of a magnetic resonance on the macroscopic area. The herein presented scalable lithography-free fabrication process paves the road towards colloidal functional metasurfaces with an optical response in the effective magnetic permeability.

Introduction

Recent interest in designing metamaterials focuses on the step from 3D bulk materials to 2D metasurfaces, which feature similar optical features.[1–6] Met-asurfaces are optical functional interfaces based on regular patterns of sub-wavelength repeating metaatoms (unit cells). The controlled arrangement of metaatoms allows the engineering of novel optical devices based on controlled

aLeibniz-Institut für Polymerforschung Dresden e.V., Institute of Physical Chemistry and Polymer Physics, Hohe Str. 6, 01069 Dresden, Germany. E-mail: koenig@ipfdd.de; fery@ipfdd.de
bDepartment of Physical Chemistry II, University of Bayreuth, Universitätsstr. 30, 95440 Bayreuth, Germany
cCluster of Excellence Centre for Advancing Electronics Dresden (CFAED), Technische Universität Dresden, 01062 Dresden, Germany
dTechnische Universität Dresden, Fakultät Mathematik und Naturwissenschaften, 01062 Dresden, Germany
eDepartment of Physical Chemistry of Polymeric Materials, Technische Universität Dresden, Hohe Str. 6, 01069 Dresden, Germany

reflectance,[7,8] efficient energy transport and wave guiding,[9,10] as well as perfect lensing[11] and optical magnetism.[12] For many of these applications, the main challenge is the control of the magnetic resonances in the visible optical range. The lack of magnetic response in natural optical materials[13] was first overcome by artificial magnetic resonances obtained for split-ring resonators in the micro-wave regime.[3] However for split-ring resonators, the limited scalability and saturation effects[14] deny their application in the visible optical range.

Consequently, the fabrication of nanostructures with magnetic resonances remains a challenge especially on macroscopic areas. The design of such magnetic metasurfaces needs to be rationally linked to scalable fabrication techniques of hierarchical assemblies in *quasi* 2D-resonators.[5] The incident electric-field component induces oscillating charges within the resonators and, hence, gives rise to an effective magnetic moment; this excitation is commonly referred to as a magnetic resonance.[15–17] To achieve these effects, metasurfaces have to be built with nanometre precision.[18,19] Common fabrication techniques rely on lithographic methods, like e-beam lithography or ion-beam milling, which have several drawbacks, such as losses due to poly-crystallinity and lack in resolution and scalability.[20–24] The colloidal bottom-up assembly approach, which exploits the advantages of noble metal nano-particles synthesized using wet-chemistry (*e.g.*, single-crystallinity, scalability), can provide alternatives to lithographic top-down techniques.[25–27] However, those approaches often rely on random particle deposition, which strongly limits the complexity of the prepared unit cells and the homogeneity of the obtained metasurfaces.[28–30] To boost the complexity of the fabricated metasurfaces, plasmonic nanoparticles are coupled to metallic films to form mirror charges in the emerging cavities.[8,10,31–33] Template-assisted convective self-assembly allows the design of unit cells with high complexity and in a large variety by surface-alignment of nanoparticles in well-defined orientations. Such assemblies are only limited by the scalability and spatial resolution of the directing template.[34–36]

In this work, we use a lithography-free colloidal bottom-up approach to fabricate a macroscopic magnetic metasurface. Plasmonic nanoparticles in close contact with a metallic film induce electric current loops due to mirrored charges at the substrate, which give rise to a magnetic mode. We provide theoretical explanations for the experimentally observed magnetic mode through electromagnetic modelling and conventional UV-vis-NIR spectroscopy. Anisotropic nanoparticles are used, due to the following reasons: the short axis of the nanorods is used for magnetic mode excitation and their long axes provide control over their orientation in template-assisted self-assembly. For the building block, we used tailored wet-chemical synthesis to obtain mono-disperse, gold nanorods with defined crystalline facets (flat faces). Furthermore, due to a defined spacer material we obtain a reliable particle-to-film distance. Using colloidal self-assembly, we were able to fabricate a macroscopic magnetic metasurface, which shows a clear signature of an effective magnetic permeability in the visible wavelength range. With this colloidal approach, we aim for a reliable method to make the unique manipulation of light on the macroscale possible.

Results and discussion

Design of the metasurface unit cell

One of the central prerequisites for obtaining a magnetic resonance is the induction of a circular oscillating current flow within the unit cell. This can be achieved by the efficient coupling of the surface plasmon with the electric component of the incident light.[15,37] Isolated nanoparticles in solution inherently exhibit electric modes in the form of localized surface plasmon resonances, as indicated for an exemplary dipolar-isolated mode (EM) by its surface charges (Fig. 1A, electric mode).[38] Breaking the symmetry is achieved by coupling a plasmonic nanoparticle to a substrate. The emerging modes depend strongly on the
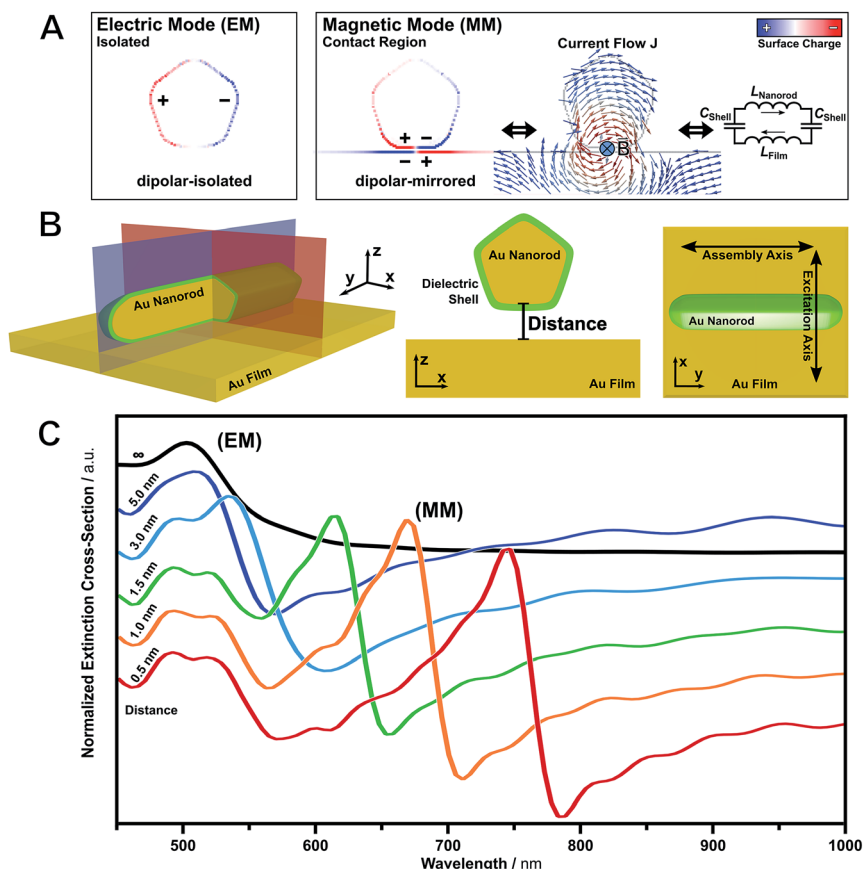

Fig. 1 Evolution of magnetic modes – from electric to magnetic resonance through metallic film-coupled plasmonic nanoparticles. (A) Surface charge pattern of an electric mode (EM), magnetic mode (MM), characteristic electric current loop (flow J) and representative inductor−capacitor (LC) model for one unit cell. (B) Schematic representation of the unit cell: gold nanorods (160 nm × 30 nm) on a 40 nm thin gold film. The short axis of the nanorod is used for the excitation by linear polarized light (transversal mode) and the long axis is used for directing the assembly process. (C) Calculated extinction cross-section at different particle-to-film distances, normalized against the bare gold film.

Faraday Discussions

substrate material, nanoparticle geometry and particle-to-film distance. In contrast to nanospheres, nanoparticles with flat faces are advantageous because of their larger contact area with the substrate, which results in narrow resonances and enhanced excitation.[39] The interaction of a nanoparticle with a dielectric substrate results in hybridized modes.[40] On the contrary, when a particle is coupled to a metallic substrate, the dipolar mode induces a mirror charge pattern at the surface of the metallic film (Fig. 1A, magnetic mode).[41–43] These mirror charges may induce an electric current loop (current density J), as calculated by electromagnetic simulations. According to Ampère's circuital law, a magnetic moment is excited.

Recently, Wang *et al.* have numerically demonstrated that magnetic modes can be represented by an inductor–capacitor (*LC*) model (Fig. 1A).[8] For film-coupled nanoparticles, the metal components act as inductors L, whereas the dielectric insulator acts as a capacitor C. Thus, the resonance wavelengths $\lambda_{(MM)}$ of the dipolar-mirrored mode (MM) can be expressed using the following equation:

$$\lambda_{(MM)} = 2\pi c \sqrt{\left(L_{nanorod} + L_{film}\right) C_{shell}/2} \tag{1}$$

However, an analytical calculation by means of eqn (1) is not straightforward, since the inductance and the capacitance depend on the curvature and geometry of the nanoparticle. Nevertheless, the model provides an intuitive description of the counter-oscillating currents in the unit cell. Consequently, a metasurface can be designed based on film-coupled nanoparticles.

We decided to design our magnetic metasurface based on film-coupled nanorods utilizing their short axes for magnetic mode excitation (transversal mode) and their long axes for providing orientational order upon self-assembly (Fig. 1B). The transversal magnetic mode is excited if the electric field component is planar with the cross-section of the unit cell (*xz*-plane, red). In contrast, the longitudinal magnetic mode, which could be excited with the electric field parallel to the long axis (*yz*-plane, blue), is significantly shifted outside the frequency range of visible light and will not be discussed further. Fig. 1B shows a schematic depiction of the proposed metasurface unit cell consisting of a nanoparticle as a building block positioned over a metallic film. The capping agent of the nanoparticle serves as a thin dielectric shell. For observation of the magnetic mode with conventional spectroscopy methods, an array of well-aligned anisotropic nanoparticles is required. For colloidal metasurface design, 1D periodic arrangements are ideal as they provide collective alignment of nanorods along their long axes. At the same time, a distance of at least five nanorod radii between the lines will suppress grating effects.[44] Tip-to-tip coupling within nanorod lines is decoupled from transversal excitation and does not interfere with the induction of the magnetic resonance.

Comprehensive numerical simulations of this unit cell clearly reveal that the spectral position of the magnetic mode can be tailored by tuning the following four parameters: (I) the dimensions and shape of the plasmonic nanoparticle; (II) the refractive index of the dielectric spacer (*e.g.*, capping agent); (III) the material of the plasmonic nanoparticle and (IV) the coupling distance between the nanoparticle surface and the substrate. These four parameters need to be precisely balanced to provide a strong magnetic resonance within the visible

spectrum. However, tuning of the first three parameters is limited by: (I) the dimension of the nanorods (approximately 30 nm in width);[45] (II) the index of refraction of the spacer material (roughly from 1.4 to 1.5 for polymeric materials);[46] and (III) the limited choice in plasmonic metals. Silver as well as gold both possess plasmonic properties in the optical range. However, even though silver features lower damping, offering narrower line-widths and higher intensities,[47,48] it is vulnerable against sulfidation and oxidation in the air.[49] Consequently, we choose gold in the present study. In contrast, the particle-to-film separation can be controlled by the capping agent and an additional spacer layer at the substrate, *e.g.*, by layer-by-layer techniques.[50] In combination, the cavity size can be tailored with nanometre precision. Taking the limited range of optimization of the nanorod morphology and the index of refraction of the building blocks into account, we will focus on the size of the nanoparticle-film cavity in order to further optimise the metasurface design.

Fig. 1C shows the extinction cross-section σ_{ext} of a nanorod at varying distances from a metallic film. The extinction spectra were normalized against the transmission (T) of the bare gold film ($\sigma_{ext} = -\log 1/T$, transparent for green light only). Owing to the transmission characteristics of gold, the extinction cross-sections show a pseudo-resonance below the interband gap of gold (<512 nm) and a pronounced increase in extinction towards lower energy. The isolated particle monomer, *i.e.* at infinite separation, shows a single plasmonic resonance (electric mode, EM). This transversal excitation corresponds to the electric mode as discussed above. Approaching the surface, the dipolar electric mode is converted to a magnetic dipolar-mirrored mode (magnetic mode, MM) and a higher-order magnetic mode. This quadrupolar-mirrored mode is further discussed in the ESI, Fig. S1.† The magnetic resonance shifts towards lower energy in comparison to the isolated electric mode. This characteristic red-shift is also known as a plasmon ruler.[51] The spectral position of the magnetic mode is particularly sensitive to distance changes even in the angstrom range. Thus, the resonance frequency may be tuned over the entire optical range. To avoid effects like quantum tunnelling, a minimum distance of 0.4 nm should be sustained.[52,53] These separations lie within the range of conventional capping agents.[54] Next, we will address the fabrication of suitable nanoparticles as building blocks.

Synthesis of well-defined building blocks

Gold nanorods possess intrinsic anisotropy in both their geometrical and optical properties. Thus, nanorods, as well as their top-down lithographic equivalents, are common building blocks in metamaterial fabrication, *e.g.*, as in the well-known double-bar setup.[15,18,55] The fabrication of hierarchical unit cells of high precision requires building blocks of well-defined size and shape (Fig. 2). High structural integrity is critical for the performance of the final system, because disorder and polydispersity in size and shape yield additional undesired resonance broadening. By using wet-chemical bottom-up synthesis, a variety of monodisperse building blocks is accessible. In particular, the control over nanoparticle size, shape, and crystallinity allows for tailored morphological and optical properties.[56,57] The penta-twinned nanorods used were prepared by seed-mediated growth based on a modified protocol by Pérez-Juste *et al.*[45,58] combined with a supplemental purification step employing depletion forces.[59,60]
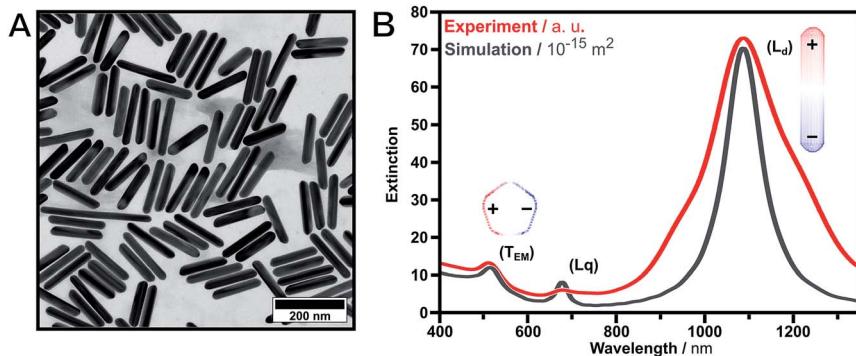
Fig. 2 Gold nanorods in solution – nature of the electric modes. (A) TEM image of the purified gold nanorods with mean dimensions of 161.0 ± 14.8 nm in length and 30.2 ± 3.7 nm in width. (B) Experimental (red) and simulated (black) extinction spectra. The gold nanorods exhibit three electric plasmon resonances, which can be attributed to dipolar transversal (T_{EM}, 512 nm), dipolar longitudinal (L_d, 1087 nm) and quadrupolar longitudinal (L_q, 680 nm) modes. The corresponding surface charges of the dipolar excitations are shown as insets.

With this method, penta-twinned gold nanorods can be produced which exhibit larger thicknesses and higher aspect ratios compared to the more commonly used single-crystalline gold nanorods.[61] Additionally, their pentagonal cross-section and their flat sides are beneficial for substrate-supported effects due to the increased interaction areas. However, owing to the use of twinned seeds only 20% of the resulting nanoparticles are nanorods with the majority being spherical and 2D by-products. These by-products need to be removed as they strongly impede the bottom-up self-assembly of hierarchical unit cells. Consequently, a supplemental purification step is required to yield narrow distributions. Efficient separation can be achieved by exploiting depletion forces with additional surfactants acting as depletants, as published recently.[59,60] Here, the effective physical parameter is the interaction area and, thus, the morphology of the nanoparticles in solution. To avoid time-consuming screening for an adequate depletant (*i.e.*, surfactant) concentration, we measured a calibration curve which allows the purification of penta-twinned gold nanorods depending on their longitudinal localized surface plasmon resonance (see ESI Fig. S2†). This purification protocol enables almost quantitative removal of spherical by-products and other morphologies. A second purification step is performed to remove longer and thinner nanorods to selectively tune and enhance the size-distribution. Fig. 2 shows a TEM image (A) and extinction spectra (B) of the synthesized and purified nanorod sample. The nanorods exhibited mean dimensions of 161.0 ± 14.8 nm in length and 30.2 ± 3.7 nm in width (for as-synthesized TEM images, UV-vis spectra and histograms of the size distribution, see ESI Fig. S2†). Consequently, the herein presented 3-step protocol is an ideal means to precisely tailor the aspect ratio of nanorods. The dipolar electric characters of the transversal (T_{EM}) and the predominant longitudinal plasmon resonance (L_d) are depicted by their surface charges in Fig. 2 (insets).

For the successful template-assisted convective assembly the wetting behaviour of the nanorods is critical. As shown recently by our group, surface chemistry
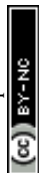
providing enhanced wettability can be adjusted using surface functionalisation with a hydrophilic protein shell.[21,55] Consequently, concentrated highly stable solutions of gold nanorods with bovine serum albumin (BSA)[21] as dielectric shells were obtained for subsequent assembly. In the dry state, the BSA layer exhibits a shell thickness below 2 nm as we have shown in previous work. Consequently, these nanoparticles match the requirements for reliable template-assisted colloidal self-assembly. In the following, we focus on the self-assembly of the nanorods into array-type structures.

Fabrication of film-coupled nanorod arrays as magnetic unit cells

Controlled colloidal self-assembly of the nanoscale building blocks into the proposed magnetic unit cell is an important step towards a macroscopic magnetic metasurface (Fig. 3). Recently, we demonstrated the precise alignment of nano-rods into well-defined 1D particle lines using template-assisted convective self-assembly employing wrinkled elastomeric substrates.[55] In the first fabrication step, the nanorods are assembled in the form of tip-to-tip arrangements within the periodic structure of the wrinkle. In order to achieve periodic macroscopic alignment in single particle lines the templates need to be homogeneous on square-centimetre scales. The dimensions of its features are crucial and need to precisely match the nanorod dimensions (i.e., width). The employed wrinkled templates are fabricated by plasma treatment of a macroscopic uniaxially stretched polydimethylsiloxane (PDMS) elastomer. The plasma treatment intro-duces a thin oxidized film at the surface. Upon strain release, periodic wrinkles are formed due to the mechanical mismatch between the substrate and the thin film.[62] The template periodicity is critical for controlling the period of the align-ment. To avoid any grating effects the periodicity was chosen to be sufficiently large (see discussion above for more details). Thus, periodicity and amplitude were tuned to values of 210 nm and 40 nm, respectively.[62] Subsequently, the amplitude was reduced to 20 nm by additional plasma post-treatment without altering the periodicity to match the dimensions of the employed gold nano-rods.[55] At the same time, the surface is hydrophilized sufficiently to enable subsequent nanoparticle assembly from aqueous solution (see plasma post-treatment calibration in the ESI Fig. S3†).

Nanorod assembly into single particle lines was achieved by dip coating. The unidirectional laminar flow promotes the orientation of the anisotropic particles along the major (long) axis. Fig. 3A displays schematically the self-assembly process. Macroscopic templates are withdrawn from a highly concentrated nanoparticle solution (2 mg mL^{-1}). During withdrawal, the nanorods are aligned into the channels by capillary forces within the confined meniscus (see Fig. 3B). Due to the confinement of the wrinkle structure, we are able to align the building blocks for a further transfer step.

In the second fabrication step, we use the wet-contact print method to transfer the pre-aligned anisotropic nanorods onto the gold film. The building blocks were transferred to a hydrophilized gold film while maintaining their orientational order. Utilizing template stripping, a surface roughness of the gold film below 1 nm was achieved. Consequently, a uniform contact between the nanorods and the supporting gold film is provided. Quantitative transfer can be achieved by wet-transfer printing of the prefilled templates and subsequent lift-off of the emptied
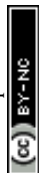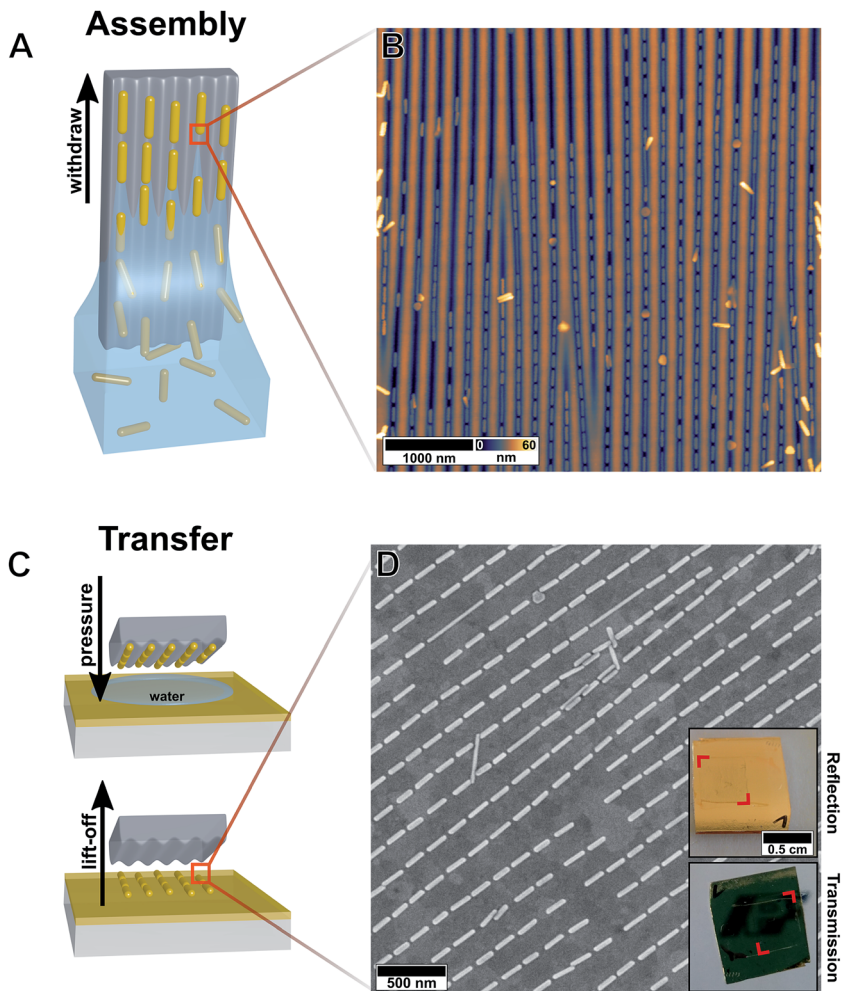
Fig. 3 Macroscopic template-assisted self-assembly using mechanical instabilities. (A) Schematic template-assisted self-assembly process by dip coating the wrinkled templates in a highly concentrated gold nanorod solution. (B) AFM image of the self-assembled array of gold nanorods in the wrinkle template. (C) Schematic transfer process using wet-contact printing and subsequent lift-off of the emptied template. (D) SEM image of the assembled structures transferred to a smooth gold film and photographs of the macroscopic substrate in reflection and transmission (upper and lower inset, respectively).

template as schematically depicted in Fig. 3C. Contrary to the transfer to other surface materials,[55] an additional adhesion promoter is not required. The combination of van der Waals interactions between the gold nanoparticles and gold film and the gold-selective binding groups of the protein shell (*e.g.*, amine, thiol) is sufficient to guarantee a complete transfer. Thus, sufficient particle–substrate spacing is given solely by the thickness of the dried shell of the stabilizing agent at the nanorod surface. The successful transfer covers an area of 5 mm × 5 mm as evidenced by SEM micrographs and macroscopic photographs (see Fig. 3D).

The quality of the assembled structures was evaluated using statistical analysis of the position and orientation of the particles with high magnification SEM images (360 individual nanorods, for further information see ESI Fig. S4†). The tip-to-tip particle spacing was determined to be 15.6 ± 5.8 nm within the lines and 209 ± 6 nm between neighbouring lines, in-line with the template periodicity. The high structural precision of the assembly was evidenced by the averaged deviation θ to the principle alignment direction $\langle \sigma_\theta \rangle$ being only $2.69°$ corresponding to a 2D-order parameter $\langle S_{2D} \rangle$ of 0.99 ($\langle S_{2D} \rangle = \langle 2 \cos^2(\theta) - 1 \rangle$). This large-yield and scalable method enabled us to fabricate a metasurface array of film-coupled nanorods on the macroscale. The following section will elucidate its optical characteristics.

Optical characterisation of film-coupled nanorod arrays

The optical properties of the macroscopic assemblies were investigated using conventional far-field UV-vis-NIR measurements. Since the magnetic resonance is dominated by absorption, spectroscopy was performed in the transmission geometry.[63] In order to allow spectroscopy in transmission, the thickness of the gold film was set to 34 nm (Fig. 3D, insets). In the visible wavelength range, the magnetic mode is excited only if the polarized light is in plane with the cross-section of the nanorod (transversal mode). Experimentally, this excitation was
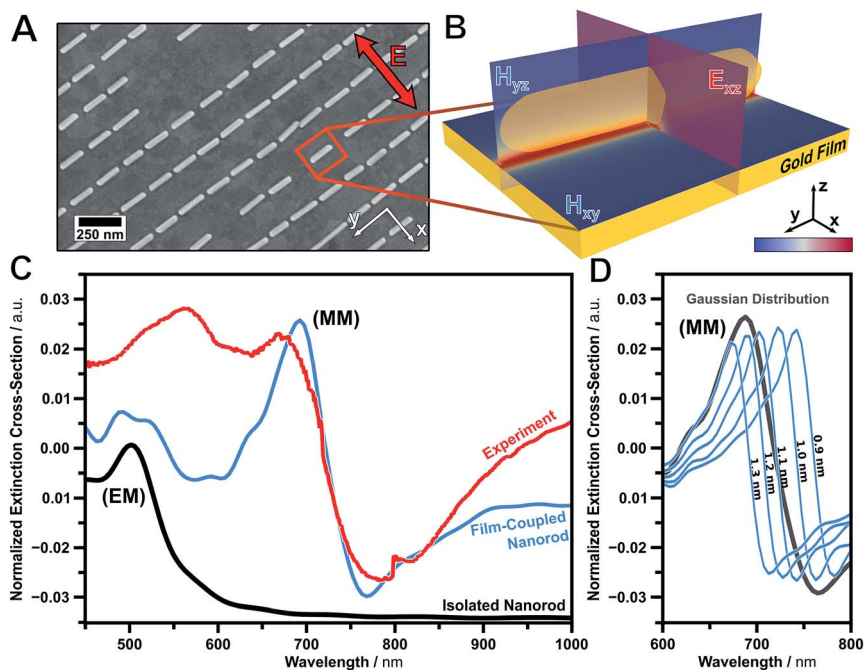

Fig. 4 Macroscopic magnetic metasurfaces. (A) SEM image of the template-assisted self-assembled array of film-coupled nanorods. (B) Simulated magnetic ($|H|^2/|H_0|^2$, coloured scale range from 1 to 4) and electric field intensity ($|E|^2/|E_0|^2$, coloured scale range from 1 to 100) of the unit cell. (C) Experimentally observed UV-vis-NIR (red) and modelled (blue) extinction spectra of the metasurface. Modelled transversal extinction spectrum of an isolated nanorod (black, not to scale). (D) Modelled extinction spectra of the magnetic mode at various particle-to-film distances (0.9 nm to 1.3 nm) and the averaged result.

performed on a spot size of 4 mm × 4 mm using polarized spectroscopy measurements. Fig. 4 shows the extinction spectrum normalized against the bare gold film.

Experimentally we observe the clear spectral signature of a magnetic mode (MM) with its peak intensity at 675 nm and point of inflexion at 721 nm (Fig. 4C). In addition, the quadrupolar-mirrored mode at 556 nm is present. The experimental observation is in excellent agreement with the modelling results of a film-coupled nanorod array (blue). The extinction cross-section of an isolated nanorod in air (transversal excitation, black) indicates the position of the initial electric mode (EM). From the position of the magnetic mode (MM), a mean particle-to-film distance of 1.1 nm was extracted. This distance is still above the quantum tunnelling limit of 0.4 nm.[53] The small deviation between the experiment and the model can be attributed to the high sensitivity towards particle-to-film distances. This influence is determined in Fig. 4D for various distances from 0.9 nm to 1.3 nm. This further emphasises the high sensitivity of the mode towards distance variations. Consequently, macroscopic magnetic substrates may be tuned over the entire visible spectrum.

Effective magnetic properties of the metasurface

To quantify the magnitude of the magnetic response of the metasurface, we modelled the effective optical properties using the S-parameter retrieval method established by D. R. Smith et $al.$[64] This method is in close analogy to the inductor–capacitor (LC) model (see eqn (1) and Fig. 5A). For this purpose, the anisotropic optical response must be calculated in the forward and backward direction (S-parameters). The model was built based on identical parameters ($i.e.$, nanorod dimensions, shell and film thickness, particle-to-film distance) to those described above.

Before we can understand the effective magnetic permeability of the unit cell, we will discuss the optical properties of the following building blocks: (I) the bare gold film and (II) the gold nanorod monomer (ESI Fig. S5†). These steps are important to prove the stability of the S-parameter method in this frequency
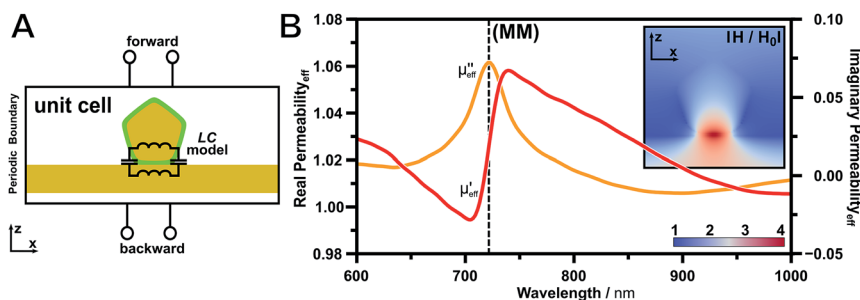

Fig. 5 Effective magnetic properties of film-coupled nanorods. (A) Schematic representation of the S-parameter retrieval method and analogy to the inductor−capacitor (LC) model. The unit cell is treated as an effective medium, since only the S-parameters are evaluated in the forward and backward direction. (B) Calculated magnetic permeability for the film-coupled nanorod revealing the presence of a magnetic resonance and related magnetic field (inset).

range. (I) The calculated effective electric permittivity of the bare gold film (40 nm thickness) agrees well with literature values (see Methods part). (II) The optical properties of the individual gold nanorod monomer are of particular interest for colloidal optical metamaterial design, because the bulk real part of the permittivity of gold is always negative. Once the metallic particle is surrounded by dielectric medium, the real part of the permittivity turns positive, which is in good agreement with the observations described in literature.[65]

Adding a film to the nanorod will result in a clear response in the complex magnetic permeability (Fig. 5B). The imaginary part of the permeability reveals the energetic location of the magnetic resonance through its characteristic peak at the point of inflexion of the extinction, whereas the real part shows the typical slope at the same energy. This relation is defined generally as the Kramers–Kronig relation, which indicates the relation between the absorption and dispersion. At the same energy, an electric response was also observed in the permittivity (ESI Fig. S5†). Consequently, the observed resonances show a mode characteristic for an electric and a magnetic resonance. This is not surprising due to the strong electromagnetic coupling of the plasmonic particle to the metallic film. We want to advise that the retrieved values below the interband gap of gold (<515 nm) should be taken with caution. In this short wavelength regime the permittivity is in the non-radiative limit for a surface plasmon resonance, which renders the response of the particle to a highly damped mode.[66] However, the signature of the magnetic mode is clearly revealed by the magnetic permeability. Consequently, the herein fabricated system represents a magnetic metasurface, which is capable of tuning the effective permeability by the induction of a magnetic moment.

Conclusion

Within this study, we developed a scalable colloidal self-assembly approach towards magnetic metasurfaces using anisotropic metal nanoparticles coupled to a supporting noble metal film. The assembly was based on a rational design strategy, which used the short axis for magnetic mode excitation and the long axis for the template-assisted self-assembly process. In particular, our approach utilizes mirror charges induced by the gold nanorods into the gold film to excite a magnetic resonance. With this approach, we were able to identify a suitable unit cell geometry: (I) anisotropic building blocks with flat faces to ensure a large contact area to the supporting substrate; (II) a suitable spacer material for a well-defined nanoscale particle-to-film distance and (III) sufficient line-to-line spacing to neglect grating effects. The building blocks are assembled through a template-assisted colloidal self-assembly technique resulting in a well-defined orientation and scalability. Applying nanoparticles with a thin homogenous dielectric shell enabled us to realize a mean coupling distance of 1.1 nm. The 2D-order parameter was determined to be close to unity (0.99) clearly proving the high potential of the employed convective self-assembly technique. Conventional UV-vis-NIR spectroscopy in close agreement with electromagnetic simulations was used to reveal the signature of the optical properties of the fabricated magnetic metasurface. The main target optical feature, the magnetic resonance, was identified at a wavelength of 721 nm. Retrieval of the effective optical properties (S-parameter method) clearly identified its presence and the magnetic mode was found in absorption as well as dispersion.

Achieving optical metasurface features on macroscopic areas requires assembly concepts that are robust in the sense that local variations are suppressed or can be tolerated. In the present study, we achieve robustness in several ways: first, the use of nanorods allows for control over orientational order by exploiting their intrinsic anisotropy (anisotropy in geometrical and optical properties), which is demonstrated by the high 2D-order parameter. In addition, line spacings (structure periodicity) that are much larger than the relevant particle length scale (in this case the particle width) grant robustness by suppressing undesired coupling between lines. Finally, the use of a defined nanoparticle coating as a spacer layer results in uniform particle-to-film distances.

In terms of functionality, these aspects allow for the extension of this concept to a functional magnetic metasurface. In particular, the high sensitivity of the film-coupled concept (sharp drop of the magnetic resonance) makes it interesting for sensing applications. For example, stimulus responsive polymers could be used as spacer layers and thus could translate configurational changes into an optically detectable response. Thus, the proposed approach can be generalized towards the colloidal fabrication of functional optical metasurfaces on a macroscopic area.

Methods

Materials

Ammonia hydroxide solution (NH_3, 25%), ascorbic acid (AA, $C_6H_8O_6$, >99%), benzyldimethylhexadecylammonium chloride (BDAC), bovine serum albumin (BSA, 98%), hydrogen peroxide (H_2O_2, 30%), hydrogen tetrachloroaurate ($HAuCl_4$, >99.9%) and sodium borohydride ($NaBH_4$, 99%) were purchased from Sigma Aldrich. 1 M sodium hydroxide (NaOH) solutions and trisodium citrate ($Na_3C_6H_5O_7$, >99%) were supplied by Grüssing. Hexadecyltrimethylammonium bromide (CTAB, 99%) was received from Merck KGaA. Hexadecyl-trimethylammonium chloride (CTAC, 99%) was supplied by Molekula. Sylgard 184 PDMS elastomer kits were purchased from Dow Corning. NOA81 UV Curing Optical Adhesive was supplied by Norland Products. Gold films were evaporated on RCA-SC1 cleaned silicon wafers. All chemicals and solvents were used as received. MilliQ-grade water (18.2 M cm, pH 8) was used as the solvent in all preparations.

Penta-twinned gold nanorod synthesis

The penta-twinned gold nanorod synthesis protocol was adopted from Pérez-Juste et al. with some recently published optimisations.[45,58]

3.5 nm sized citrate-capped gold seeds. Briefly, 20 mL of a 0.125 mM $HAuCl_4$, 0.25 mM trisodium citrate aqueous solution was prepared and stirred for 10 min at room temperature. Next, 600 μL of a freshly prepared 0.1 M $NaBH_4$ solution was added quickly under vigorous stirring. After 2 min, the stirring rate was reduced and the seeds were aged for 40 min under slow stirring at room temperature. To ensure complete removal of excessive $NaBH_4$, the solution was stirred at 40–45 °C for another 10 min.

5.5 nm sized CTAB-capped gold seeds. 8 mL of a growth solution consisting of 40 mM CTAB and 0.125 mM $HAuCl_4$ was prepared. The Au(III) was reduced to Au(I)
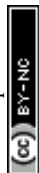
utilizing 20 μL of a 0.1 M AA solution (f.c. 0.25 mM). Then, 1333 μL of the citrate-capped gold seeds were added quickly and the solution was mixed thoroughly for 30 s using Vortex-Finger treatment. The 5.5 nm sized CTAB-capped gold seeds were aged for 3 h at 23 °C prior to the final overgrowth step.

Penta-twinned gold nanorod growth. 4 L of a growth solution containing 8 mM CTAB and 0.125 mM $HAuCl_4$ was prepared. The solution was kept at 20 °C for at least 30 min. Next, 12.5 mL of a 0.1 M AA solution (f.c. 0.313 mM) was added and gently stirred leading to the solution becoming clear within minutes. Finally, 6.67 mL of 5.5 nm sized CTAB-capped seeds were added quickly and mixed thoroughly. For the nanorod growth, the solution was kept at 20 °C overnight.

Nanorod purification

Nanorod purification was carried out in a manner analogous to the purification protocol by Scarabelli et al.[60] For penta-twinned gold nanorods of an average length and width of about 160 nm and 30 nm, respectively, the final surfactant (CTAC) concentration, determined by the calibration curve in ESI Fig. S2,† was set to 70 mM with a 25 wt% CTAC solution leading to selective flocculation and sedimentation overnight. The supernatant was discarded and the sediment containing the nanorods was redispersed in 12 mL of a 10 mM BDAC solution for the next purification step. The longer gold nanorods were slowly sedimented in a 10 mM BDAC solution over the course of 5 days. The targeted gold nanorods in the supernatant were collected and the longer nanorods in the precipitate were discarded.

Ligand exchange and functionalization

For functionalization with BSA, the BDAC concentration in 6 mL of a penta-twinned gold nanorod solution was set to 0.5 mM (correlating to the critical micelle concentration, CMC, of BDAC) by repeated centrifugation at 1400 RCF for 30 min. Directly before functionalization, the surfactant concentration was reduced below the CMC to 0.25 mM by dilution. The nanorod solution was added quickly to a 30 mL BSA solution (pH 8, 10 mg mL^{-1}) containing 0.02 wt% triso-dium citrate under sonication. After 20 min of sonication, the solution was centrifuged at 1500 RCF for 45 min and the concentrated nanorods were redis-persed in one drop of NaOH solution at pH 11 and diluted with 30 mL of BSA solution (pH 10, 1 mg mL^{-1}) containing 0.02 wt% trisodium citrate. Finally, after incubation overnight at 4 °C, the BSA-functionalized gold nanorods were washed 3 times at 1500 RCF for 45 min with NaOH solution at a pH value of 10.5 to remove excess protein. Subsequently the solution was concentrated to a gold concentra-tion of 2 mg mL^{-1}.

Wrinkle preparation for templates

Wrinkled templates with a wavelength and amplitude of approximately 210 nm and 30 nm, respectively, were produced as described elsewhere.[55] Briefly, PDMS was prepared by casting 25 g of the mixture of cross-linker and pre-polymer (1 : 5 w/w) in a balanced polystyrene dish (10 cm × 10 cm). First, the PDMS was pre-cross-linked at room temperature for 24 h and afterwards cross-linked at 80 °C for 4 h. The final PDMS was cut into 1 cm × 4.5 cm strips and individually stretched above the critical strain in a home-built stretching apparatus. Next, the
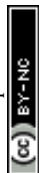
strips were plasma-treated for 1200 s in an oxygen atmosphere at 0.6–1.2 mbar and relaxed slowly after cooling to room temperature inducing wrinkle formation. The wrinkled PDMS substrates were cut into 1 cm × 0.7 cm templates. To adjust the amplitude to the desired value of 15–20 nm the substrate was post-treated with oxygen plasma at 0.6 mbar with a power of 100 W for 540 s (see calibration curve in ESI Fig. S3†). Finally, the templates were covalently fixed on plasma-activated glass strips (6 mm × 76 mm) with the wrinkles oriented parallel to the long axis of the glass slides, which later act as a fixture for the subsequent assembly process by dip-coating.

Substrates

Smooth gold film substrates were produced by template stripping. Therefore, a 34.19 ± 0.02 nm thick gold film (see also in ESI Fig. S6 and Table S1†) was evaporated on a RCA SC-1 cleaned silicon wafer without adhesive agent. Afterwards, 1.5 cm × 1.5 cm glass slides were placed on top with 3 μL of NOA81 UV Curing Optical Adhesive and cured with an approximated energy exposure of 2 J cm^{-2} from a hand-held UV light source followed by 12 h final curing at 50 °C. Finally, the glass slides were carefully stripped using a scalpel with the smooth gold film on top. The resulting gold films exhibited a root-mean-square roughness (r_{RMS}) of 0.38 nm and were spectrally transparent within an optical window between 400 nm and 750 nm.

Convective self-assembly and transfer

Template-assisted convective self-assembly of gold nanorods was performed by dip-coating as published recently by Tebbe *et al.*[55] Therefore, the wrinkled templates fixed on the glass strip were clamped into the dip-coater and moved into 1 cm × 1 cm glass cuvettes, which act as containers. Afterwards, 600 μL of the gold nanorod solution (2 mg mL^{-1}, pH 10.5, BSA-stabilized) was poured slowly into the container. Assembly is performed by withdrawing the template with a commercially available dip-coater (DC/D/LM system, KSV Instruments, Germany) at a speed of 10 μm min^{-1}. Transfer to the gold substrate was adopted from Hanske *et al.*[21] Briefly, the gold substrate was hydrophilized with oxygen plasma for 7 min (0.2 mbar, 100 Ws). The resulting hydrophilic gold substrate was wetted with 6 μL of a pH 10.5 NaOH solution and the nanorod-filled wrinkled template was pressed onto the substrate with a pressure of 140 kPa. After 5 h, the water was dried and the transfer was complete. Finally, the empty template was carefully lifted off.

Modelling and numerical simulation

A commercial-grade simulator from Lumerical Solutions, Inc. (FDTD Solutions, Version 8.11.442 on Linux x86_64) based on the finite-difference time-domain (FDTD) method was used to perform the calculations. The penta-twinned gold nanorods were modelled with a pentagonal cross section in water (constant index of refraction of 1.333) and a rounded cap to represent their true structure. Nanorod dimensions were set according to the TEM analysis (see size distributions in ESI Fig. S2D and E,† 161 nm × 30 nm) and the rods were covered with a homogeneous 3 nm layer of BSA with a fixed index of refraction of 1.48. The edge rounding and tip length were rendered to agree with the experimental UV-vis-NIR

measurements of the purified nanorod solutions (10% and 11 nm, respectively). Assemblies were modelled with optimised gold nanorods on a gold substrate in air (constant index of refraction of 1). To emulate the dried state on the gold substrate, the thickness of the BSA layer was reduced to 1.5 nm. Considering the smoothness of the gold substrate and the good agreement with the experiment, the optical roughness of the film was neglected. On the basis of the experimental data of Johnson and Christy an approximating polynomial function for the optical constants of gold is used by the FDTD software (6 coefficients, 1 imaginary weight: 0.241 RMS error).[67] Zero-conformal-variant mesh refinement with a mesh size of 0.5 nm was used for the best representation of the rounded structure and in the cavity the mesh size was reduced to 0.1 nm. All simulations reached the automatic shut-off level of 10^{-6} before reaching 300 fs of simulation time. The simulation space was restricted by perfectly matched layers for isolated nanorods as boundary conditions and by periodic boundaries for the unit cell setup. The fields were normalized against the unit cell without the nanorod but with the gold film as reference. Therefore, the presented data include only the contribution of the nanorod whereas the contribution of the gold film serves as the background. To calculate the effective optical properties of film-coupled nanorods, S-parameter extraction analysis from Lumerical Solutions Inc. was used. To retrieve the optical constants for the inhomogeneous asymmetric structure, we calculated the S11 and S22 parameters by simulating in the forward and backward source direction, respectively, at an automatic shut-off level of 10^{-7}.

Characterisation

Optical characterization of the solutions was performed in a 1 mm pathway cuvette without dilution using a Cary 5000 spectrometer (Agilent, USA) using the Cary Universal Measurement Accessory (UMA), which allowed the measurement of aqueous nanoparticle solutions in the range of 200 nm to 1850 nm. The gold substrates were measured in the transmission geometry on the Cary 5000 spectrometer (Agilent, USA) with an attached Cary Universal Measurement Accessory (UMA) at a spot size of 4 mm × 4 mm with linearly polarized light. The background was recorded on the same substrate prior tot he transfer of the gold nanorods. The spot size was fixed to the same value for UV-vis and NIR detectors resulting in slit widths of 1 nm and 4 nm, respectively.

The gold substrate was characterized using variable-angle spectroscopic ellipsometry at incident angles from 45° to 85° in 5° steps in a wavelength range from 193 nm to 1690 nm using a RC2 (J.A. Woollam Co., USA) and was fitted using the CompleteEASE software package (see ESI Fig. S6 and Table S1† for fitting parameters).

AFM measurements of all substrates (wrinkled templates, gold films, assemblies in the wrinkled templates and nanorods transferred to the gold films) were performed using a Nanoscope Dimension V (Bruker, USA), operated in the Tapping Mode™. Al-coated silicon cantilevers (OTESPA, Bruker) with a stiffness of typically 35–47.2 N m^{-1} and typical resonance frequencies of 300 kHz were utilized.

TEM measurements of the gold nanoparticles at all relevant stages of the synthesis were performed using a Zeiss 922 OMEGA EFTEM at a voltage of 120 kV. Zero-loss filtered images were recorded using a bottom mounted Ultrascan 1000
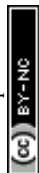
(Gatan) CCD camera system. Gatan Digital Micrograph 3.9 for GMS 1.4 software was used for image acquisition. TEM samples were concentrated and the surfactant concentration (if present) was set to the corresponding critical micelle concentration. Droplets of 5 μL were dried on a Quantifoil 300 mesh copper grid with carbon films placed on a hydrophobic film to trap the droplet during drying. For the determination of the mean particle dimensions 250 particles per sample were measured.

SEM measurements were recorded using a LEO 1530 FE-SEM (Zeiss, Germany) with in-lens and SE2 detectors using an acceleration voltage of 2–3 kV.

Acknowledgements

References

1 A. V. Kildishev, A. Boltasseva and V. M. Shalaev, *Science*, 2013, **339**, 1289.

2 J. B. Pendry, *Phys. Rev. Lett.*, 2000, **85**, 3966–3969.

3 J. B. Pendry, A. J. Holden, D. J. Robbins and W. J. Stewart, *IEEE Trans. Microwave Theory Tech.*, 1999, **47**, 2075–2084.

4 D. R. Smith, W. J. Padilla, D. C. Vier, S. C. Nemat-Nasser and S. Schultz, *Phys. Rev. Lett.*, 2000, **84**, 4184–4187.

5 N. Yu and F. Capasso, *Nat. Mater.*, 2014, **13**, 139–150.

6 S. P. Burgos, R. de Waele, A. Polman and H. A. Atwater, *Nat. Mater.*, 2010, **9**, 407–412.

7 G. M. Akselrod, T. Ming, C. Argyropoulos, T. B. Hoang, Y. Lin, X. Ling, D. R. Smith, J. Kong and M. H. Mikkelsen, *Nano Lett.*, 2015, **15**, 3578–3584.

8 H. Wang, K. O'Dea and L. Wang, *Opt. Lett.*, 2014, **39**, 1457–1460.

9 A. Rose, T. B. Hoang, F. McGuire, J. J. Mock, C. Ciracì, D. R. Smith and M. H. Mikkelsen, *Nano Lett.*, 2014, **14**, 4797–4802.

10 J. B. Lassiter, F. McGuire, J. J. Mock, C. Ciracì, R. T. Hill, B. J. Wiley, A. Chilkoti and D. R. Smith, *Nano Lett.*, 2013, **13**, 5866–5872.

11 S. Kawata, A. Ono and P. Verma, *Nat. Photonics*, 2008, **2**, 438–442.

12 M. Kataja, T. K. Hakala, A. Julku, M. J. Huttunen, S. van Dijken and P. Torma, *Nat. Commun.*, 2015, **6**, 1–8.

13 A. Alù and N. Engheta, *Opt. Express*, 2009, **17**, 5723–5730.

14 J. Zhou, T. Koschny, M. Kafesaki, E. N. Economou, J. B. Pendry and C. M. Soukoulis, *Phys. Rev. Lett.*, 2005, **95**, 223902.

15 G. Dolling, C. Enkrich, M. Wegener, J. F. Zhou, C. M. Soukoulis and S. Linden, *Opt. Lett.*, 2005, **30**, 3198–3200.

16 C. M. Soukoulis and M. Wegener, *Nat. Photonics*, 2011, **5**, 523–530.

17 D. Lin, P. Fan, E. Hasman and M. L. Brongersma, *Science*, 2014, **345**, 298–302.

18 Z.-G. Dong, H. Liu, M.-X. Xu, T. Li, S.-M. Wang, S.-N. Zhu and X. Zhang, *Opt. Express*, 2010, **18**, 18229–18234.

19 N. I. Zheludev, *Science*, 2010, **328**, 582–583.

20 N. Meinzer, W. L. Barnes and I. R. Hooper, *Nat. Photonics*, 2014, **8**, 889–898.

21 C. Hanske, M. Tebbe, C. Kuttner, V. Bieber, V. V. Tsukruk, M. Chanana, T. A. F. König and A. Fery, *Nano Lett.*, 2014, **14**, 6863–6871.

22 H. Ditlbacher, A. Hohenau, D. Wagner, U. Kreibig, M. Rogers, F. Hofer, F. R. Aussenegg and J. R. Krenn, *Phys. Rev. Lett.*, 2005, **95**, 257403.

23 B. J. Wiley, D. J. Lipomi, J. Bao, F. Capasso and G. M. Whitesides, *Nano Lett.*, 2008, **8**, 3023–3028.

24 G. V. Naik, V. M. Shalaev and A. Boltasseva, *Adv. Mater.*, 2013, **25**, 3264–3294.

25 J.-S. Huang, V. Callegari, P. Geisler, C. Brüning, J. Kern, J. C. Prangsma, X. Wu, T. Feichtner, J. Ziegler, P. Weinmann, M. Kamp, A. Forchel, P. Biagioni, U. Sennhauser and B. Hecht, *Nat. Commun.*, 2010, **1**, 150.

26 Y. Cui, M. T. Björk, J. A. Liddle, C. Sönnichsen, B. Boussert and A. P. Alivisatos, *Nano Lett.*, 2004, **4**, 1093–1098.

27 Z. Li, S. Butun and K. Aydin, *ACS Photonics*, 2014, **1**, 228–234.

28 M. J. Rozin, D. A. Rosen, T. J. Dill and A. R. Tao, *Nat. Commun.*, 2015, **6**, 1–7.

29 W. Chen, M. Tymchenko, P. Gopalan, X. Ye, Y. Wu, M. Zhang, C. B. Murray, A. Alu and C. R. Kagan, *Nano Lett.*, 2015, **15**, 5254–5260.

30 G. M. Akselrod, J. Huang, T. B. Hoang, P. T. Bowen, L. Su, D. R. Smith and M. H. Mikkelsen, *Adv. Mater.*, 2015, **27**, 8028–8034.

31 H. Chen, T. Ming, S. Zhang, Z. Jin, B. Yang and J. Wang, *ACS Nano*, 2011, **5**, 4865–4877.

32 H. Chen, L. Shao, T. Ming, K. C. Woo, Y. C. Man, J. Wang and H.-Q. Lin, *ACS Nano*, 2011, **5**, 6754–6763.

33 T. Maurer, P.-M. Adam and G. Lévêque, *Nanophotonics*, 2015, **4**, 363–382.

34 A. Rey, G. Billardon, E. Lortscher, K. Moth-Poulsen, N. Stuhr-Hansen, H. Wolf, T. Bjornholm, A. Stemmer and H. Riel, *Nanoscale*, 2013, **5**, 8680–8688.

35 S. Ni, J. Leemann, H. Wolf and L. Isa, *Faraday Discuss.*, 2015, **181**, 225–242.

36 X. Zhou, Y. Zhou, J. C. Ku, C. Zhang and C. A. Mirkin, *ACS Nano*, 2014, **8**, 1511–1516.

37 A. Vallecchi, M. Albani and F. Capolino, *Opt. Express*, 2011, **19**, 2754–2772.

38 C. F. Bohren and D. R. Huffman, in *Absorption and Scattering of Light by Small Particles*, Wiley-VCH Verlag GmbH, 2007, ch. 12, pp. 325–380, DOI: 10.1002/9783527618156.

39 T. König, R. Kodiyath, Z. A. Combs, M. A. Mahmoud, M. A. El-Sayed and V. V. Tsukruk, *Part. Part. Syst. Charact.*, 2014, **31**, 274–283.

40 S. Zhang, K. Bao, N. J. Halas, H. Xu and P. Nordlander, *Nano Lett.*, 2011, **11**, 1657–1663.

41 G. Lévêque and O. J. F. Martin, *Opt. Express*, 2006, **14**, 9971–9981.

42 A. Pors and S. I. Bozhevolnyi, *Opt. Express*, 2013, **21**, 27438–27451.

43 D. E. Gómez, Z. Q. Teo, M. Altissimo, T. J. Davis, S. Earl and A. Roberts, *Nano Lett.*, 2013, **13**, 3722–3728.

44 M. B. Müller, C. Kuttner, T. A. F. König, V. V. Tsukruk, S. Förster, M. Karg and A. Fery, *ACS Nano*, 2014, **8**, 9410–9421.

45 M. Mayer, L. Scarabelli, K. March, T. Altantzis, M. Tebbe, M. Kociak, S. Bals, F. J. García de Abajo, A. Fery and L. M. Liz-Marzán, *Nano Lett.*, 2015, **15**, 5427–5437.

46 J. E. Mark, *Polymer Data Handbook*, Oxford University Press, 2009.
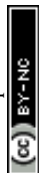
47 N. Dmitruk, S. Malynych, I. Moroz and V. Kurlyak, *Semicond. Phys., Quantum Electron. Optoelectron.*, 2010, **13**, 369–373.

48 J. Becker, I. Zins, A. Jakab, Y. Khalavka, O. Schubert and C. Sönnichsen, *Nano Lett.*, 2008, **8**, 1719–1723.

49 J. L. Elechiguerra, L. Larios-Lopez, C. Liu, D. Garcia-Gutierrez, A. Camacho-Bragado and M. J. Yacaman, *Chem. Mater.*, 2005, **17**, 6042–6052.

50 G. Decher, *Science*, 1997, **277**, 1232–1237.

51 P. K. Jain, W. Huang and M. A. El-Sayed, *Nano Lett.*, 2007, **7**, 2080–2088.

52 L. Yang, H. Wang, Y. Fang and Z. Li, *ACS Nano*, 2016, **10**, 1580–1588.

53 J. A. Scholl, A. Garcia-Etxarri, G. Aguirregabiria, R. Esteban, T. C. Narayan, A. L. Koh, J. Aizpurua and J. A. Dionne, *ACS Nano*, 2016, **10**, 1346–1354.

54 C. Kuttner, M. Chanana, M. Karg and A. Fery, in *Macromolecular Self-Assembly*, ed. L. Billon, O. V. Borisov, Wiley-VCH, 2016.

55 M. Tebbe, M. Mayer, B. A. Glatz, C. Hanske, P. T. Probst, M. B. Muller, M. Karg, M. Chanana, T. A. F. Konig, C. Kuttner and A. Fery, *Faraday Discuss.*, 2015, **181**, 243–260.

56 E. C. Dreaden, A. M. Alkilany, X. Huang, C. J. Murphy and M. A. El-Sayed, *Chem. Soc. Rev.*, 2012, **41**, 2740–2779.

57 Y. Xia, Y. Xiong, B. Lim and S. E. Skrabalak, *Angew. Chem., Int. Ed.*, 2009, **48**, 60–103.

58 J. Pérez-Juste, L. M. Liz-Marzán, S. Carnie, D. Y. C. Chan and P. Mulvaney, *Adv. Funct. Mater.*, 2004, **14**, 571–579.

59 K. Park, H. Koerner and R. A. Vaia, *Nano Lett.*, 2010, **10**, 1433–1439.

60 L. Scarabelli, M. Coronado-Puchau, J. J. Giner-Casares, J. Langer and L. M. Liz-Marzán, *ACS Nano*, 2014, **8**, 5833–5842.

61 L. Scarabelli, A. Sánchez-Iglesias, J. Pérez-Juste and L. M. Liz-Marzán, *J. Phys. Chem. Lett.*, 2015, **6**, 4270–4279.

62 B. A. Glatz, M. Tebbe, B. Kaoui, R. Aichele, C. Kuttner, A. E. Schedl, H.-W. Schmidt, W. Zimmermann and A. Fery, *Soft Matter*, 2015, **11**, 3332–3339.

63 U. K. Chettiar, A. V. Kildishev, T. A. Klar and V. M. Shalaev, *Opt. Express*, 2006, **14**, 7872–7877.

64 D. R. Smith, D. C. Vier, T. Koschny and C. M. Soukoulis, *Phys. Rev. E: Stat., Nonlinear, Soft Matter Phys.*, 2005, **71**, 036617.

65 C. Rockstuhl, F. Lederer, C. Etrich, T. Pertsch and T. Scharf, *Phys. Rev. Lett.*, 2007, **99**, 017401.

66 M. Tebbe, C. Kuttner, M. Mayer, M. Maennel, N. Pazos-Perez, T. A. F. König and A. Fery, *J. Phys. Chem. C*, 2015, **119**, 9513–9523.

67 P. B. Johnson and R. W. Christy, *Phys. Rev. B: Solid State*, 1972, **6**, 4370–4379.

4.2 Single particle spectroscopy of radiative processes in colloid-to-film-coupled nanoantennas

Single particle spectroscopy of radiative processes in colloid-to-film-coupled nanoantennas

Max J Schnepf, Yannic Brasse, Fabian R Goßler, Anja Maria Steiner, Julian Obermeier, Markus Lippitz, Andreas Fery* and **Tobias A.F. König***

*corresponding authors

Author contribution statement

MS and YB carried out the experiments and have contributed equally to the paper. **TK** encouraged MS, YB and FG to investigate the simulation, fabrication and optical spectroscopy methods as well as supervised the execution and findings of this work. AS contributed through synthesis of the particles. JO and ML contributed through their single photon spectroscopy method. The authors **TK** and AF made a significant contribution to the conception and design of the work. Through the simulation, fabrication and optical spectroscopy methods, the author **TK** made a significant contribution to the acquisition, analysis and interpretation of the data. All authors provided critical feedback and helped shape the research, analysis and manuscript.

Max J. Schnepf[a], Yannic Brasse[a], Fabian R. Goßler,
Anja Maria Steiner, Julian Obermeier, Markus Lippitz,
Andreas Fery* and Tobias A.F. König*

Single Particle Spectroscopy of Radiative Processes in Colloid-to-Film-Coupled Nanoantennas

Abstract: We present a fluorescent emitter (rhodamine B) coupled to a dielectric or metallic interface as well as a metallic cavity to study their radiative decay processes. Supported by finite-difference time-domain (FDTD) simulations, we correlate the non-radiative and radiative decay rates with the absorption and scattering cross section efficiencies, respectively. On a single particle level, we use atomic force microscopy (AFM), scanning electron microscopy (SEM), scattering spectroscopy, fluorescence life time imaging (FLIM) and time-correlated single photon counting (TCSPC) to evaluate the enhanced fluorescence decay at the same location. With this study, we show a colloidal gain material, which can be integrated into lattices using existing directed self-assembled methods to study their coherent energy transfer.

---

[a]**Max J. Schnepf and Yannic Brasse:** These authors contributed equally.
***Corresponding authors: Andreas Fery,** Leibniz Institute of Polymer Research (IPF), Institute of Physical Chemistry and Polymer Physics, Hohe Str. 6, 01069 Dresden, Germany; Cluster of Excellence Center for Advancing Electronics Dresden (CFAED), Technische Universität Dresden, Dresden, Germany; and Physical Chemistry of Polymeric Materials, Technische Universität Dresden, Dresden, Germany, e-mail: fery@ipfdd.de; and **Tobias A.F. König,** Leibniz Institute of Polymer Research (IPF), Institute of Physical Chemistry and Polymer Physics, Hohe Str. 6, 01069 Dresden, Germany; and Cluster of Excellence Center for Advancing Electronics Dresden (CFAED), Technische Universität Dresden, Dresden, Germany, e-mail: koenig@ipfdd.de
Max J. Schnepf and Anja Maria Steiner: Leibniz Institute of Polymer Research (IPF), Institute of Physical Chemistry and Polymer Physics, Hohe Str. 6, 01069 Dresden, Germany
Yannic Brasse and Fabian R. Goßler: Leibniz Institute of Polymer Research (IPF), Institute of Physical Chemistry and Polymer Physics, Hohe Str. 6, 01069 Dresden, Germany; and Cluster of Excellence Center for Advancing Electronics Dresden (CFAED), Technische Universität Dresden, Dresden, Germany
Julian Obermeier and Markus Lippitz: Lehrstuhl Experimentalphysik III, Department of Physics, University Bayreuth, Universitätsstraße 30, 95447 Bayreuth, Germany

1 Introduction

For the next generation of information and sensing technology, nanoscaled systems with high emission rates and short decay times must be integrated cost-efficiently into scalable optical platforms. Quantum emitters such as fluorophores or quantum dots adjacent to metallic particles are attractive candidates for controlling and increasing the excitation and decay rates [1–4]. Increasing the decay rate, for instance, reduces the probability of photobleaching. This results in more cycles of excitation and emission, as well as improved detection limits by enhanced emission rates [3, 5]. Pioneering work from Lakowicz et al. [6] studied the enhancement and shortening of the life time using single-stranded oligonucleotides to assemble silver particles in proximity to fluorophores. Later, this relationship was investigated as a function of the distance between two metallic particles sandwiching a fluorophore [7]. The spectral overlap between the localized surface plasmon resonance (LSPR) of the metallic particles and the fluorescence emission results in energy transfer due to near field interactions [8–10]. Thus, rational design of the plasmonic nanostructure is desired for optimization of these interactions in respect of the fluorescent decay rates. Wet chemical synthesis of metallic particles in colloidal systems features the required optical tunability and their directed self-assembly solves the bottleneck of scalability [11, 12]. Using a particle-to-film coupled (nanoantenna) setup, Smith et al. [13] have shown that the limiting factor is not the metallic loss, but rather the intrinsic nonlocality of the dielectric response. However, it is still a matter of debate whether the radiation efficiency is low or the emission is not observable in the far field [14]. Patched nanoantenna concepts introduced by Smith were applied by the Mikkelsen group [15]. They tuned the distance between silver nanocubes and a metallic film to show enhancement of the spontaneous emission rate due to the defined cavity. However, to unravel the mechanism of spontaneous emission in metallic systems, the Mikkelsen group noted that suitable, reliable and precise tuning of the plasmon resonance is required.

By hybridizing colloidal plasmonic antennas with fluorophores, we demonstrate enhancement of spontaneous emission and significant increase of decay rates. Matching our experimental setup, we used modeling methods to correlate the cross-section efficiency with the fluorescence enhancement and the decay

rates. In comparison to top-down lithographic methods, the colloidal synthesis and metallic film-coupled cavities are an inherently inexpensive and flexible platform for large-scale applications such as quantum information systems and ultralow-power switches.

2 Experimental

2.1 Particle synthesis

Fluorescence-labeled silane was produced by stirring a mixture of 6.0 mg rhodamine B isothiocyanate (11 μmol) and 17.72 μL 3-aminopropyltriethoxysilane (102 μmol) in 2 mL ethanol overnight. The synthesis of fluorescence-labeled silica particles is based on a modified protocol of the Stöber synthesis [16, 17]. One hundred and twenty-three milliliter ethanol, 10.9 mL ammonium hydroxide solution (NH_4OH, 28–30%) and the labeled silane solution were added to a 500 mL three-necked flask equipped with a reflux condenser. Five milliliter tetraethoxy orthosilicate (TEOS, 22.56 mmol) in 20 mL ethanol were preheated and added to the three-necked flask at 50 °C under vigorous magnetic stirring. The stirring speed was reduced after 30 s, and the mixture was left for reaction overnight. The product was centrifuged at 8500 relative centrifugal force (RCF) for 30 min and redispersed in ethanol. Washing was repeated three times. The resulting particle size of 102.0 ± 9.8 nm was determined via transmission electron microscopy (TEM) statistics by evaluating the diameters of at least 100 particles.

Hexadecyltrimethylammonium chloride capped spherical gold nanoparticles were synthesized in a seeded growth process, as previously described [18]. The resulting particles had a size of 78.6 ± 3.3 nm as determined by (TEM) statistics (at least 100 particles). An aqueous dispersion of these particles (0.66 mg gold) was centrifuged four times at 300 RCF for 30 min and redispersed in 10 mL of 1.1 mM hexadecyltrimethylammonium bromide aqueous solution. Prefunctionalization was conducted in a 25 mL glass vial under magnetic stirring at 30 °C by adding 1 μL of 3-mercapto trimethoxysilane, and 20 μL of NaOH (0.1 M) 3 h later. After 24 h of reaction time, the product was centrifuged as described above. Overcoating was initiated by adding 20 μL NaOH (0.1 M) to the particle dispersion in a glass vial under magnetic stirring at 30 °C. Forty minutes later, 10 μL of TEOS and 4 μL of the fluorescence-labeled silane solution (as described above) were added and left to react for 72 h. The final product was purified as described above. The doped silica shell thickness was quantified to be 4.0 ± 0.5 nm as determined by TEM statistics (at least 100 particles).

2.2 Substrate preparation

Smooth gold film substrates were produced by template stripping. A 34.2 ± 0.1 nm thick gold film was evaporated on an RCA SC1 cleaned [19] silicon wafer without adhesive layer. Afterwards, 1.5 cm $\times$ 1.5 cm glass slides were placed on top with 3 µL of NOA81 UV Curing Optical Adhesive and cured with an approximate energy exposure of 2 J/cm^2 from a hand-held UV light source followed by 12 h thermal curing at 50 °C. Finally, the glass slides were carefully stripped from the wafer using a scalpel, leaving the smooth gold film situated on top. The resulting gold films exhibited a root-mean-square (RMS) roughness of 0.4 nm and were spectrally transparent within a 400–750 nm optical window. Particle deposition was conducted via spin coating of 60 µL diluted particle dispersion several weeks after synthesis on both glass slides and gold coated glass at 2000 rpm for 2 min.

2.3 Characterization

Particles were analyzed by TEM using a Libra 120 (Carl Zeiss AG) operated with an acceleration voltage of 120 kV. Sizes were evaluated for at least 100 particles per sample. Scanning electron microscopy images were recorded on a NEON 40 (Carl Zeiss AG) microscope with an Everhart-Thornley detector.

Fluorescence life time images and time correlated single photon counting (TCSPC) measurements were acquired with an inverted confocal scanning microscope (MicroTime 200, PicoQuant, Germany) with a 100× air objective (UPLFLN, NA 0.9, Olympus, Japan), resulting in a focused laser spot with a diameter of 340 ± 4 nm for the laser configuration used. For excitation, a picosecond pulsed laser diode head (LDH-D-C-510, PicoQuant, Germany) with a center wavelength of 506 nm and a pulse width of 110 ps (full width at half maximum, FWHM), driven at repetition rates of 20, 30, and 40 MHz. For fluorescence collection, a dichroic mirror (ZT405-442/510rpc-UF3, Chroma, USA), a long pass filter with a cut-off below 519 nm (FF01-519/LP, Semrock, USA) and a single photon counting module (SPCM-AQRH, Excelitas, USA) were used. For evaluation of fluorescence life time images and TCSPC evaluation, SymphoTime 64 2.1 was used. Fluorescence life time images were recorded at 0.2 µW excitation power (before objective) and a dwell time of 2 ms per pixel. Single particle TCSPC experiments were performed at 0.2 µW excitation power (before objective) and a measurement time of 60 s. The instrument response function (IRF) was collected at the same excitation conditions but in the absence of the 519 nm long pass filter and with 2 s integration time to reach similar counts as the fluorescent TCSPC measurements.

To obtain fluorescence spectra, the sample was excited by an optical para-metric oscillator (APE OPO PP Auto FAN) with a center wavelength of 519 nm (15 nW excitation power) through an Olympus MPlanFLN 100× 0.9 BDP objective in reflection. The excitation and fluorescence signals were then separated with a dichroic mirror (RT532rdc-UF1, Chroma, USA). Residual energy at the excitation wavelength was removed with a long pass filter (532 LP Edge Basic, Semrock, USA). The spectra were acquired with a Princeton Instruments Iso-Plane SCT320 spectrograph (150 g/mm grating, blaze 500 nm, center wavelength 700 nm) equipped with a PIXIS 400 eXcelon charged-coupled device (CCD) camera (Princeton Instruments). The spectra were corrected by subtracting dark spectra (i.e. spectra recorded without laser excitation).

Single particle scattering spectroscopy was conducted on a Nikon Ti-U inverted microscope in transmission mode. The microscope was equipped with an IsoPlane-160 spectrometer and a PIXIS: 256 CCD camera (Princeton Instruments). Measurements were performed with a darkfield condenser (air, NA 0.8–0.95) and a 60× air objective (CFI S Plan Fluor ELWD, NA 0.7, Nikon, Japan) under illumination with a 100 W halogen lamp. Spectra with 383 nm bandwidth were recorded for 30 s at 600 nm and 750 nm center wavelengths. These spectra were corrected by subtraction of the CCD's dark current and division by a reference spectrum (white light scattering) for polystyrene nanoparticles (hydrodynamic diameter $D_h = 450$ nm).

2.4 FDTD simulations

A commercial-grade simulator based on the finite-difference time-domain (FDTD) method was used to perform the calculations (Lumerical FDTD, version 8.16) [20]. For the simulation of the optical response, a total-field scattered-field source was used and the frequency points were set to be half the wavelength span. Monitor boxes (transmission monitors in all three principle directions) were used to obtain the optical responses of the system as well as the dipole power. For the dielectric properties of gold, data from Johnson and Christy was fitted using six coefficients with a RMS error of 0.2 [21]. For the silica shell, we chose a fixed refractive index of 1.4. The mesh size was set to 1 nm for the optical response simulations, and an additional mesh overlay of 0.5 nm was applied for calculations of the dipole and the induced fields. To determine the electric field and surface charge density, we simulated the model at the plasmonic mode frequency. In order to calculate the Purcell factor P and radiative decays, we used a dipole source with emission wavelengths between 400 nm and 800 nm and obtained P by the dipole source. All simulations reached an auto-shutoff of at least 10^{-7} before reaching 300 fs

simulation time. For the best simulation stability, the mesh area was chosen to be at least 100 nm larger than the existing structure in all three principal directions.

3 Results and discussion

We use the concept of a gold nanoparticle coupled to a metallic film, separated by a fluorophore-labeled spacer material (Figure 1a). The system consists of the following colloidal building blocks (details in Experimental part): (1) The silica
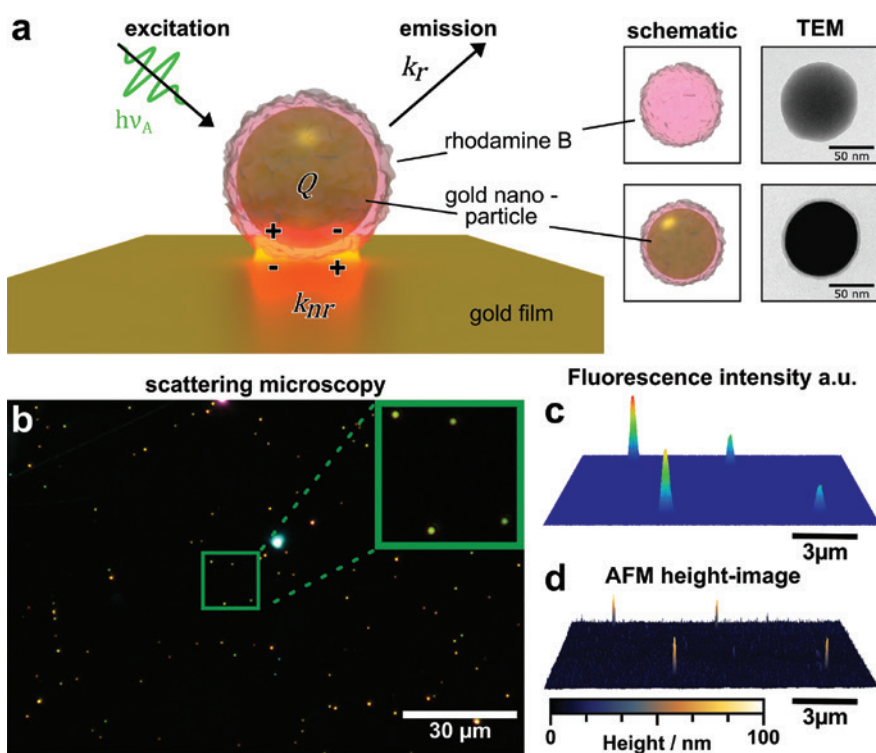

Fig. 1: Concept of colloidal plasmonic nanoantenna for single particle spectroscopy: (a) Schematic depiction of the particle-to-film coupled nanocavity consisting of the colloidal building blocks (4 nm rhodamine B labeled silica shell and 79 nm gold nanoparticle core) on a gold film acting as a plasmonic mirror. Pulsed laser excitation at 506 nm induces rhodamine B emission at 580 nm, which energetically couples to the small mode volume between particle and film. The mode volume is highlighted by the red color. (b) Scattering microscopy image of multiple core-shell particles on a gold film (green and orange color). (c) Fluorescence life time image and (d) atomic force microscopy (AFM) image of a selected area in (b).

particle or shell, labeled with rhodamine B acting as a gain material. (2) The gold nanoparticle (78.6 ± 3.3 nm via TEM), which acts as a nanoantenna due to the generation of LSPR upon interaction with incident light. (3) The gold film acting as a plasmonic mirror, in which opposing surface charges are induced. In the combination of these building blocks, the silica shell acts as a defined dielectric spacer of 4 nm building a plano-convex mode volume. We designed the fluorophore-plasmonic system to feature overlap between the radiation spectrum of rhodamine B and the cavity resonance (see Supporting Information Figures S1 and S2). Spherical particles were used because they are available with lowest size- and shape-dispersity and therefore can form robust nanocavities [18]. In order to describe our nanoantenna system, a convenient expression of the relationship between non-radiative (k_{nr}) and radiative decay (k_r) is given by the definitions of quantum efficiency ($QE_0 = k_r\tau_0$) and fluorescence life time ($\tau_0 = (k_r + k_{nr})^{-1}$). In the case of a fluorophore in vicinity of a metallic surface (index m) the definition for quantum efficiency and fluorescence life time can be extended by introducing an altered radiative decay rate $k_{m,r}$ as well as an additional non-radiative decay rate $k_{m,nr}$ thus becoming $QE_0 = (k_{m,r})\tau_m$ and $\tau_m = (k_{m,r} + k_{m,nr} + k_{nr})^{-1}$ [22]. In a classical fluorophore system, the values for quantum efficiency and life time are coupled to each other. When the quantum efficiency is decreasing, lifetime is also decreasing and vice versa. Once a metallic interface is available, other combinations may occur, such as high quantum efficiency at short life times. As we will later show in detail, these fluorescence parameters are related to the extinction (defined as sum of scattering and absorption) cross section efficiency. The cross section efficiency is defined as cross section scaled by the area of the scattering object (metallic nanoparticle). Thus, by controlling the extinction cross section efficiency (by changing cavity size, particle size or geometry for instance), the fluorescence parameters can be influenced. The particle-to-film coupled resonance was quantified by scattering spectroscopy (see Figure S5) and is correlated with fluorescent decay (Figure 3) as well as emission spectroscopy (Figure 2 and Figure S5).

Plasmonic resonances are sensitive to particle size, shape or surrounding media, which has already been discussed in literature [23]. The sensitivity is defined as the change of wavelength (plasmonic resonance) scaled by changes of an optical parameter [24]. As an example, the colloid-to-film-coupled system is four times more sensitive to changes in particle-to-film distance as compared to changes in particle size (see Figure S3 for more details). Therefore, we suspect that the slight color changes shown in Figure 1b are predominantly governed by variations in the particle-to-film distance. These changes are reflected in the scattering spectra shown in Figure S5. For instance, the particle in the top right of the inset is red-shifted by 10–15 nm in comparison to the other particles. The particle-to-film distance is affected by two major variables. First, it is influenced by the stabilizing surfactant
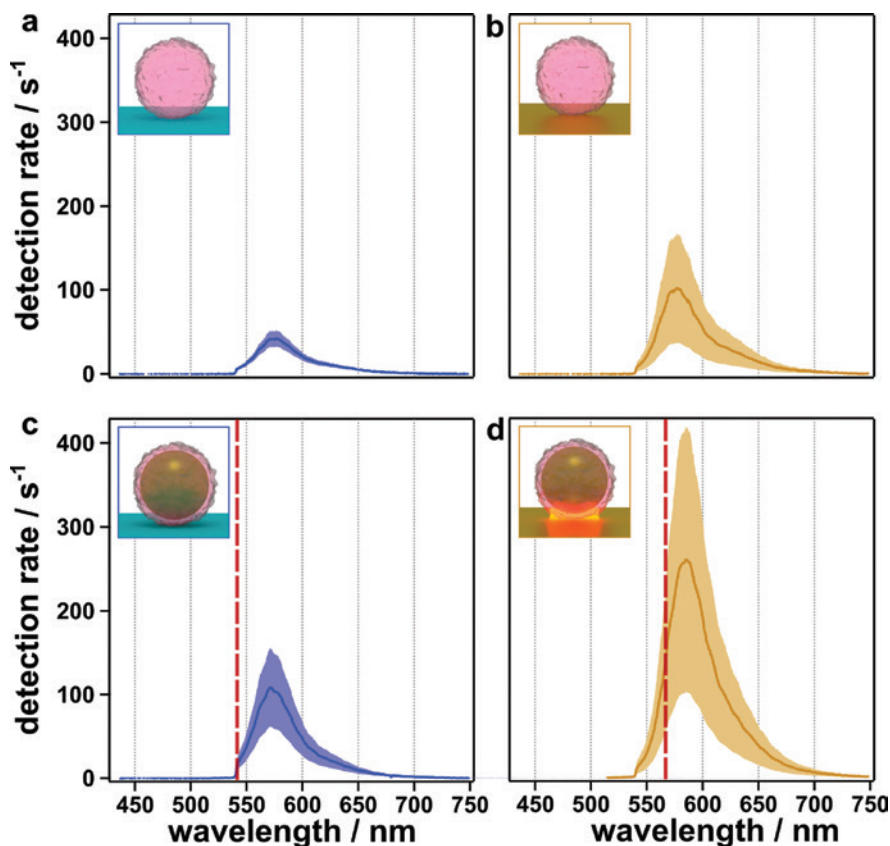
Fig. 2: Fluorescence emission spectroscopy of the colloidal building blocks and various fluorophore-plasmonic systems: Detection rates averaged over four fluorescence emission spectra (solid line) of rhodamine B labeled silica particles on (a) glass substrate ('reference' setup) and (b) gold film ('film' setup) including the respective standard deviation (filled region). Fluorescence response of a plasmonic-core and rhodamine B-shell system coupled to (c) glass substrate ('particle' setup) and (d) gold film ('cavity' setup). Cavity resonance (maximum in scattering intensity) is indicated by the red dashed line in each panel.

and capillary forces acting during the drying process. Second, it is determined by the silica shell thickness (4.0±0.5 nm via TEM), which is adjusted through our chemical overgrowth process. Using this colloidal building block approach, we are able to fabricate a robust and reproducible fluorophore-plasmonic system to quantify the extinction efficiency as well as the radiative processes at the same location.

In order to study the fluorescence emission spectroscopically, we excite the fluorophore-plasmonic system with a 506 nm pulsed laser in a confocal setup (details in Experimental part). In Figure 2, we compare the relative fluorescence

detection rates from our individual building blocks and combinations thereof as follows: (a) rhodamine B-functionalized silica particle on a dielectric film as reference system (abbreviated as 'reference' setup), (b) rhodamine B-functionalized silica particle coupled to metallic gold film (denoted as 'film' setup), (c) plasmonic-core and rhodamine B doped-shell coupled to dielectric film (denoted as 'particle' setup) and (d) core-shell nanoparticle coupled to metallic film (denoted as 'cavity' setup). We observed that the detected rate doubles when one metallic interface is available ('film' setup: factor 2.4, 'particle' setup: factor 2.6), and once a second metallic interface is available (i.e. the 'cavity' setup), the fluorescence intensity doubles again (factor 5.9 in comparison to the 'reference' setup). In the case of the 'reference' setup, fluorescence intensity is linear proportional to the particle volume, i.e. the amount of emitters. For the 'film' setup the relation is more complex since particles with a diameter of 102 ± 10 nm have regions which are strongly influenced by the gold-film and regions of almost no influence. It has to be taken into account that the effective number of fluorescent emitters is significantly reduced in the core-shell systems (excluded Volume of the plasmonic core). Normalizing for the amount of fluorophore per particle (see Table S1), the fluorescence intensity of the 'cavity' setup is calculated to increase by a factor of 38 in respect to the 'reference'. Commensurately, the standard deviation of the fluorescence intensity increases by factors of 6 and 18 as one and two metallic interfaces are available, respectively. Considering the increased sensitivity of the plasmonic systems, this increase of standard deviation is reasonable (see earlier discussions and Figure S3). The quality factor, which is defined by the full width at half maximum of the resonance peak scaled by the frequency, remains unaffected for all setups. The averaged quality factor for all setups is $\langle Q_{em} \rangle = 15.9 \pm 0.4$. The continuity of the quality factor suggests that no inelastic processes (such as Raman-scattering) are involved.

For space and time correlated studies, the same fluorophore-plasmonic systems have been studied using fluorescence life time imaging (FLIM) methods and atomic force microscopy (AFM) (Figure 3, and S5 as well as S4 and S10 for a second correlated location) to ensure that single particles are observed. Similar to the previously introduced confocal fluorescence emission spectroscopy, we investigated the fluorescent decay of several 'particle' and 'cavity' setups. The life time is studied using a pulsed laser at 506 nm with a time-correlated single photon counting (TCSPC) method (details in Experimental part).

TCSPC reveals a difference in fluorescence life time when one or two metallic interfaces are available. For the 'particle' setup two decay times were observed: A fast ($\tau_A < 80$ ps) and a slow decay time ($\tau_B = 3.6 \pm 0.1$ ns). Comparing these decay times with the instrument response function and the background, respectively, we essentially observe a superposition of an unresolvable fast decay time and a fluorescence decay time of unbound rhodamine B. The decay time of 3.6 ns in the
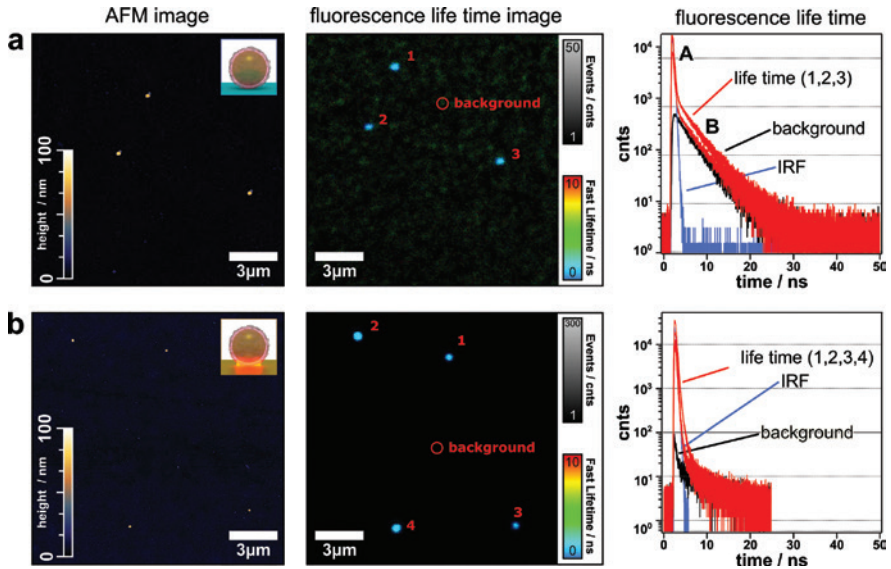
Fig. 3: Fluorescence life time characterization of the 'particle' and 'cavity' setup: AFM image (left), fluorescence life time image (middle) and life time (right) for (a) the 'particle' setup and (b) the 'cavity' setup. Fluorescence life time decay is shown for the highlighted positions in the AFM/fluorescence images (red) and background (black). The instrument response function (IRF) is plotted in blue color.

background is in agreement with the life time which we measured in the 'reference' setup (see Figure S13).

It should be noted, that we illuminate a spot size of 340 nm in diameter. TCSPC detection counts of multiple 'particle' and 'cavity' setups vary by 26% and 44% (see histogram in Figure S6), respectively. This behavior was also observed in the intensity of the emission spectra and can be attributed to the sensitivity of the fluorophore-plasmonic system.

At the 'cavity' setup, we observe a rapid decay ($\tau < 80$ ps) in fluorescence life time for all measured positions (Figure 3b). This characteristic decay matches the instrument response function and the background signal, but for the latter case with several orders of magnitude less intensity. Therefore, the lifetime cannot be specified, except for noting that it is faster than 80 ps. Similar to the observation by fluorescence emission spectroscopy, the detected TCSPC counts almost triple (factor 2.7) when a second metallic interface is available [22, 25].

We used FDTD simulations to describe the radiative processes of the fluorophore-plasmonic system. First, to study the interaction of light (plane wave source) with the various systems, we use the absorption and scattering cross section efficiency (Figure 4a). We observe that the absorption is about four times

greater than of the scattering cross section, which is reasonable for the applied particle size and particle-to-film distance [26]. The observed peaks and shoulders correlate with the corresponding plasmonic modes, namely a dipole resonance (for the 'particle' setup) as well as a lower and a higher order dipolar cavity resonance (in the 'cavity' setup). We used surface charge calculations to identify the cavity modes (see Figure S7). The extinction cross section of the 'film' setup corresponds to the typical absorbance of a gold film [21].

As a second step, we used the Jablonski diagram to correlate the calculated extinction cross section efficiency with the radiative process (Figure 4b) [27]. We start from a classical fluorophore system and expand the Jablonski diagram to our fluorophore-plasmonic system. In the setup without metal ('reference' setup), the excited fluorophore decays with a non-radiative decay rate (k_{nr}) and a radiative decay rate (k_r), respectively. Once a metallic interface is added to the system, the absorption and scattering cross section efficiency results in an increased coupling rate (arrow thickness represent increased coupling rates) and an increased decay rate ($k_{m,r}$). This behavior is reasonable due to the fluorophore induced plasmon oscillations, which result in an increased radiation to the far field [28].

Third, we used FDTD simulations with a dipole source to distinguish between the non-radiative and radiative decay rates of the fluorophore-plasmonic system (Figure 4c). For all setups, the dipole source is located inside the cavity with an electric field vector perpendicular to the film. To fully explain the radiative processes, we chose a dipole source with an excitation wavelength between 400 nm and 800 nm as well as a -sweep of 40 narrow-bandwidth dipole sources with center wavelengths covering the same wavelength domain (Figure S11). The ideal case of a dipole orientation perpendicular to the cavity was assumed for the decay rates to obtain the highest coupling interactions for each system. Additional positions and orientations of the fluorophore are shown in Figure S12. In all setups, we observe the radiative process altered by the metallic interfaces. For the 'cavity' setup, the absorption at the plasmonic resonances correlates with the non-radiative decay. The same signature is observed for the scattering cross section and the radiative decay, which is increased significantly compared to the "particle" (120-fold) and the "film" setup (530-fold). It is also notable that for the uncoupled systems, the radiative decay rates correlate directly with the corresponding plasmon resonance position. However, In the cavity system, the radiative decay rate enhancement is redshifted by 50 nm in respect to the plasmon resonance. More available metallic interfaces result in higher absorption/non-radiative decay and higher scattering/radiative decay. Based on the calculations for non-radiative and radiative decay rates, we can comprehend the reduction of life time, which is defined as the inverse sum of non-radiative and radiative decay rates (see Figure S8). Thus, the quantitative resolution of the enhanced TCSPC signal of the "cavity" system is an intrinsic
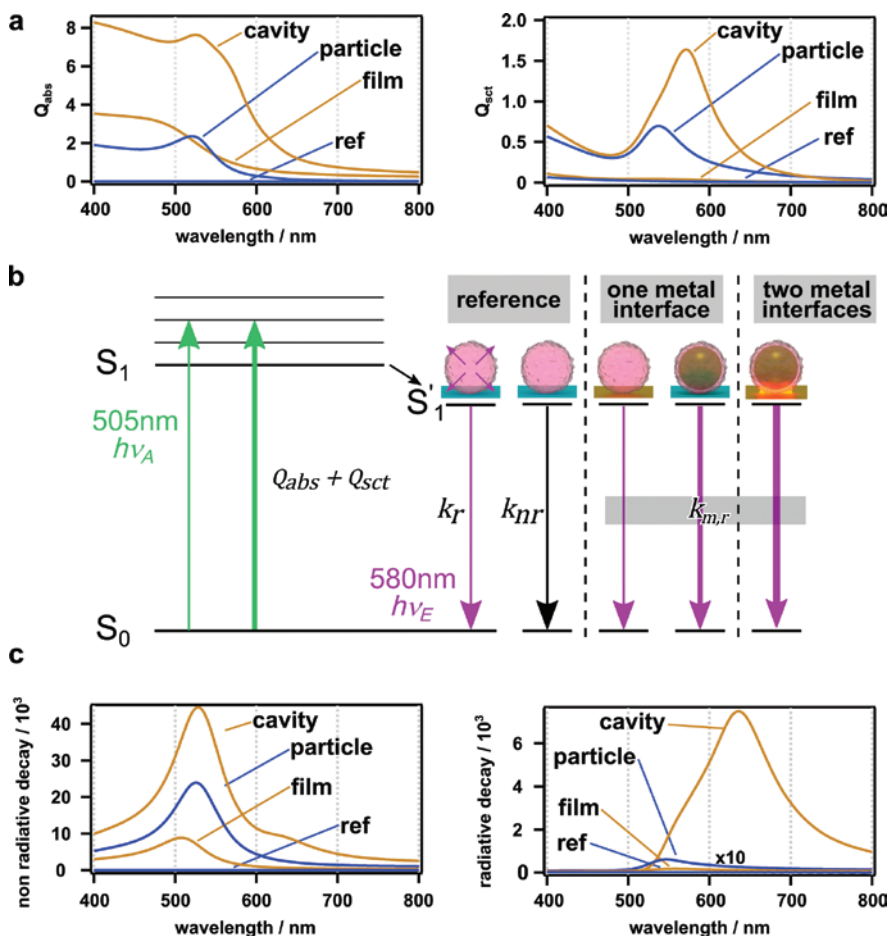
Fig. 4: Radiative processes of colloidal film-coupled nanoantennas supported by FDTD simulations and Jablonski diagram: (a) FDTD simulated absorption and scattering cross-section efficiency (Q) for various systems. (b) Jablonski diagram including fluorophore absorption ($h\nu_A$), absorption and scattering cross section efficiency (Q) from ground state (S_0) to excited states (S_1) and radiative, non-radiative decay rates (k) as well as additional decay rate k_m for various metallic setups. (c) Simulated non-radiative and radiative decay rates for various setups. Labels for the colloidal building blocks and systems: rhodamine B particle on a dielectric film ('reference' setup), rhodamine B coupled to metallic film ('film'), plasmonic-core and rhodamine B-shell coupled to dielectric film ('particle') and metallic film ('cavity').

problem occurring for evaluating coupled emitters. For future investigations on these systems, fluorophores specifically designed for long life times [22] as well as new generations of quantum dot emitters [25] could be employed. In this figure we plotted also the quantum efficiency to show that in a fluorophore-plasmonic

system the life time is shortened while the quantum efficiency is increased. For application where coherent coupling is crucial, we also determined the Purcell factor, which shows an enhanced spontaneous emission ($P_{\text{cavity}} \approx 40{,}000$ and $P_{\text{particle}} \approx 20{,}000$) at the plasmonic cavity resonance wavelength.

4 Conclusion

In this work, we compared four different colloid-based systems to study their radiative processes, namely, a classical fluorophore system, two systems with one metallic interface and one system with two metallic interfaces. The observed trend is that the absorption cross section, as well as the non-radiative decay increased as soon as a metallic interface was available. The same signature was observed for the scattering cross section and radiative decay. Moreover, the emission rate doubled upon addition of a second metallic interface to the system. In the growing field of energy transfer studies between quantum emitter and plasmonic particles, rational design parameters are crucial to study their weak and strong coupling properties. With this study it is possible to conclude from the extinction cross section of a plasmonic system on their radiative processes when a quantum emitter is available. Moreover, we have shown a colloidal gain material, which can be integrated cost efficiently in existing self-assembled plasmonic lattices to study their coherent energy transfer [29–31].

References

1. K. J. Russell, T.-L. Liu, S. Cui, E. L. Hu, Nat. Photonics **6** (2012) 459.
2. G. M. Akselrod, C. Argyropoulos, T. B. Hoang, C. Ciracì, C. Fang, J. Huang, D. R. Smith, M. H. Mikkelsen, Nat. Photonics **8** (2014) 835.

3. P. Anger, P. Bharadwaj, L. Novotny, Phys. Rev. Lett. **96** (2006) 113002.

4. H. Li, C.-Y. Chen, X. Wei, W. Qiang, Z. Li, Q. Cheng, D. Xu, Anal. Chem. **84** (2012) 8656.

5. Q.-C. Sun, H. Mundoor, J. C. Ribot, V. Singh, I. I. Smalyukh, P. Nagpal, Nano Lett. **14** (2014) 101.

6. J. Zhang, Y. Fu, M. H. Chowdhury, J. R. Lakowicz, Nano Lett. **7** (2007) 2101.

7. A. Bek, R. Jansen, M. Ringler, S. Mayilo, T. A. Klar, J. Feldmann, Nano Lett. **8** (2008) 485.

8. K. Matsuzaki, S. Vassant, H. W. Liu, A. Dutschke, B. Hoffmann, X. Chen, S. Christiansen, M. R. Buck, J. A. Hollingsworth, S. Götzinger, V. Sandoghdar, Sci. Rep. **7** (2017) 42307.

9. R. Chikkaraddy, B. de Nijs, F. Benz, S. J. Barrow, O. A. Scherman, E. Rosta, A. Demetriadou, P. Fox, O. Hess, J. J. Baumberg, Nature **535** (2016) 127.

10. R. Chikkaraddy, V. A. Turek, N. Kongsuwan, F. Benz, C. Carnegie, T. van de Goor, B. de Nijs, A. Demetriadou, O. Hess, U. F. Keyser, J. J. Baumberg, Nano Lett. **18** (2017) 405.

11. M. Rycenga, C. M. Cobley, J. Zeng, W. Li, C. H. Moran, Q. Zhang, D. Qin, Y. Xia, Chem. Rev. **111** (2011) 3669.

12. M. Grzelczak, J. Vermant, E. M. Furst, L. M. Liz-Marzán, ACS Nano **4** (2010) 3591.

13. C. Ciracì, R. T. Hill, J. J. Mock, Y. Urzhumov, A. I. Fernández-Domínguez, S. A. Maier, J. B. Pendry, A. Chilkoti, D. R. Smith, Science **337** (2012) 1072.

14. J. Yang, R. Faggiani, P. Lalanne, Nanoscale Horiz. **1** (2016) 11.

15. A. Rose, T. B. Hoang, F. McGuire, J. J. Mock, C. Ciracì, D. R. Smith, M. H. Mikkelsen, Nano Lett. **14** (2014) 4797.

16. W. Stöber, A. Fink, J. Colloid Interface Sci. **26** (1968) 62.

17. A. Rauh, M. Rey, L. Barbera, M. Zanini, M. Karg, L. Isa, Soft Matter **13** (2017) 158.

18. A. M. Steiner, M. Mayer, M. Seuss, S. Nikolov, K. D. Harris, A. Alexeev, C. Kuttner, T. A. F. König, A. Fery, ACS Nano **11** (2017) 8871.

19. W. Kern, D. A. Puotinen, RCA Rev. **31** (1970) 187.

20. Lumerical Inc. http://www.lumerical.com/tcad-products/fdtd/. Accessed March 29, 2018.

21. P. B. Johnson, R. W. Christy, Phys. Rev. B **6** (1972) 4370.

22. T. Soller, M. Ringler, M. Wunderlich, T. A. Klar, J. Feldmann, H. P. Josel, Y. Markert, A. Nichtl, K. Kürzinger, Nano Lett. **7** (2007) 1941.

23. Y. Sonnefraud, A. Leen Koh, D. W. McComb, S. A. Maier, Laser Photonics Rev. **6** (2012) 277.

24. A. Steinbrück, O. Stranik, A. Csaki, W. Fritzsche, Anal. Bioanal. Chem. **401** (2011) 1241.

25. A. Raevskaya, V. Lesnyak, D. Haubold, V. Dzhagan, O. Stroyuk, N. Gaponik, D. R. T. Zahn, A. Eychmüller, J. Phys. Chem. C **121** (2017) 9032.

26. V. Myroshnychenko, J. Rodríguez-Fernández, I. Pastoriza-Santos, A. M. Funston, C. Novo, P. Mulvaney, L. M. Liz-Marzán, F. García de Abajo, J. Chem. Soc. Rev. **37** (2008) 1792.

27. A. Jablonski, Nature **131** (1933) 839.

28. J. R. Lakowicz, Y. Fu, Laser Photonics Rev. **3** (2009) 221.

29. M. Mayer, M. Tebbe, C. Kuttner, M. J. Schnepf, T. A. König, A. Fery, Faraday Discuss. **191** (2016) 159.

30. Y. Brasse, M. B. Müller, M. Karg, C. Kuttner, T. A. F. König, A. Fery, ACS Appl. Mater. Interfaces **10** (2018) 3133.

31. K. Volk, J. P. S. Fitzgerald, P. Ruckdeschel, M. Retsch, T. A. F. König, M. Karg, Adv. Opt. Mater. **5** (2017) 1600971.

4.3 Active plasmonic colloid-to-film coupled cavities for tailored light-matter interactions

Active Plasmonic Colloid-to-Film-Coupled Cavities for Tailored Light–Matter Interactions

Fabian R. Goßler, Anja Maria Steiner, Oleksandr Stroyuk, Alexandra Raevskaya and **Tobias A.F. König***

*corresponding author

Author contribution statement

FG carried out the experiments. **TK** encouraged FG to investigate the simulation, fabrication and optical spectroscopy methods as well as supervised the execution and findings of this work. AS contributed through synthesis of the metallic nanoparticles. OS and AR contributed through synthesis of the semiconductive nanoparticles. **TK** made a significant contribution to the conception and design of the work. Through the simulation, fabrication and optical spectroscopy methods, the author **TK** made a significant contribution to the acquisition, analysis and interpretation of the data. All authors provided critical feedback and helped shape the research, analysis and manuscript.

Active Plasmonic Colloid-to-Film-Coupled Cavities for Tailored Light−Matter Interactions

Fabian R. Goßler,[†,‡] Anja Maria Steiner,[†,‡] Oleksandr Stroyuk,[§,∥] Alexandra Raevskaya,[§,∥] and Tobias A. F. König*[,†,‡] [ID]

[†]Leibniz-Institut für Polymerforschung Dresden e.V., Institute for Physical Chemistry and Polymer Physics, Hohe Str. 6, 01069 Dresden, Germany

[‡]Cluster of Excellence Centre for Advancing Electronics Dresden and [§]Physical Chemistry, TU Dresden, 01069 Dresden, Germany

[∥]L.V. Pysarzhevsky Institute of Physical Chemistry, National Academy of Sciences of Ukraine, 01030 Kiev, Ukraine

S *Supporting Information*

ABSTRACT: For large-scale fabrication of optical circuits, tailored subwavelength structures are required to modulate the refractive index. Here, we introduce a colloid-to-film-coupled nanocavity whose refractive index can be tailored by various materials, shapes, and cavity volumes. With this colloidal nanocavity setup, the refractive index can be adjusted over a wide visible wavelength range. For many nanophotonic applications, specific values for the extinction coefficient are crucial to achieve optical loss and gain. We employed bottom-up self-assembly techniques to sandwich optically active ternary metal-chalcogenides between a metallic mirror and plasmonic colloids. The spectral overlap between the cavity resonance and the broadband emitter makes it possible to study the tunable radiative properties statistically. For flat cavity geometries of silver nanocubes with sub-10 nm metallic gap, we found a fluorescence enhancement factor beyond 1000 for 100 cavities and a 112 meV Rabi splitting. In addition, we used gold spheres to extend the refractive index range. By this easily scalable colloidal nanocavity setup, gain and loss building blocks are now available, thereby leading to new generation of optical devices.
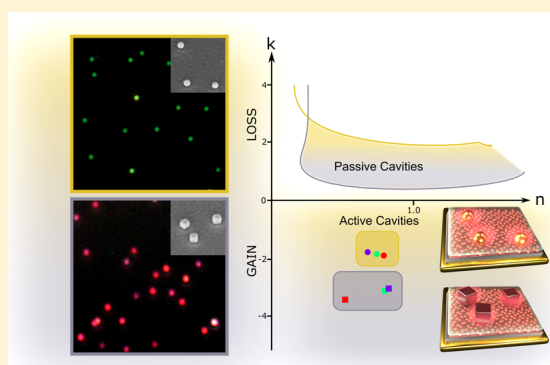
INTRODUCTION

Plasmonic cavity-coupled emitters are highly appealing systems to study light−matter interactions due to their strong and confined nearfield enhancement upon excitation.[1] Such systems have proven to be promising candidates for tailoring photonic properties at exceptionally small mode volumes.[2,3] Recently, colloidal approaches have been introduced to continue this development by incorporating the emitting material (molecular excitons or quantum dots (QDs)) using host−guest chemistry,[4] simple immersion techniques,[5] or polyelectrolyte multilayers.[6] The fast energy transfer between excitonic quantum emitters and the cavity system leads to hybridized light−matter states provided that the plasmon−exciton coupling is sufficient.[7,8] To exploit these sub-wavelength-scale phenomena for applications like optical circuits and calculations, the refractive index (RI) ($\tilde{n} = n + ik$) of the structure itself must be modulated.[9] Most computational metastructures are based on alternating the real part of the refractive index through implementation of different dielectric materials. In these periodic arrangements, the materials are chosen such that the index contrast in the real part n is maximized, whereas the imaginary part k is minimized to reduce losses.[10] These conditions are often met using ordered polymer structures.[11] However, a high refractive index contrast with a spatial variation below the diffraction limit is desirable for application in transformation optics,[12] such as cloaking,[13] field concentration,[14] and perfect absorbers.[15] To achieve this, plasmonic nanostructures can be used instead of dielectric materials. The material refractive index contrast can be increased significantly if a noble metal ($n < 1$ due to free electrons) is used instead of a dielectric material ($n \sim 1.4$). When noble metals are used, greater absorptive losses are generally encountered, but these losses are not overly problematic because the plasmonic structures feature much higher coupling interactions than dielectric structures.[16] In other words, the imaginary index can be also used as a material contrast property. This is shown in the recent developments in the field of passive parity-time metamaterials, where contrasts in both n and k are utilized to provide a unidirectional light propagation.[17] If optically active materials like molecular excitons or quantum dots are now coupled to such structures, k can be further modulated to become negative (single-mode lasing).[18] These active parity-time metamaterials might be an important step toward next-generation optical applications on a subwavelength scale.[18]

Here, we study the radiative properties for a set of colloid-to-film-coupled cavities as determined by their composition. We combine a well-defined self-assembled monolayer (SAM) of thiolates with a polymeric film formed using layer-by-layer deposition methods to achieve a homogeneous and emitting spacer layer of various thicknesses. Gold spheres and silver cubes are used as plasmonic colloids, and ternary metal-chalcogenide quantum dots with a long photoluminescence (PL) lifetime (100 ns) and broad emission range (full width at half-maximum (FWHM) = 304 meV) are chosen as the optically active material. By using a combination of surface and optical characterization methods, we can establish the presence of light−matter interactions and study the optical properties statistically. An improvement in electromagnetic simulation methods allows us to calculate the effective refractive index for each system. This quantification combined with self-assembly makes the colloid-to-film-coupled cavities potentially useful for the next generation of optical circuits.

EXPERIMENTAL METHODS

Substrate Preparation. A gold film with a thickness of 50 nm was evaporated onto a clean glass slide (Menzel) using physical vapor deposition (HEX-L by Korvus Technology Ltd, Newington, U.K.). The gold layer thickness was validated using spectroscopic ellipsometry (J.A. Woollam, RC2 Ellipsometer) to be 50 nm. The substrate was then incubated in a 1 mM solution of (11-mercaptoundecyl)-N,N,N-trimethylam-97 monium bromide (MUTAB) (Sigma Aldrich) to form a positively charged self-assembled monolayer. The thickness was determined to be 1.5 nm using spectroscopic ellipsometry. A monolayer of thioglycolic acid (TGA) functionalized silver−indium−sulfide (AgInS) quantum dots was assembled by placing the sample into an aqueous QD dispersion for 30 min at room temperature. The formation of a homogeneous layer of AgInS QDs was verified using fluorescence lifetime imaging (FLIM) and atomic force microscopy (AFM). An additional polymeric spacer was applied by (repeatedly) dip-coating the sample into (alternating) solutions of poly(allylamine hydrochloride) (PAH) (0.1 mg/mL; 0.5 mM NaCl) and poly(styrene sulfonate) (PSS) (0.1 mg/mL; 0.5 mM NaCl) each for 60 s. Between each layer-by-layer assembly step, the sample was rinsed with ultrapure water (Merck Millipore) for 30 s. Each PAH/PSS monolayer is estimated to be 1−2 nm in thickness, as measured by ellipsometry. The metallic nanoparticles were applied by drop-casting onto the substrate for 30 s, followed by rinsing with purified water and nitrogen drying.

Dark-Field Measurements. Single-particle scattering spectroscopy was done with a Nikon Ti-U inverted microscope in transmission mode. The data were recorded using an IsoPlane-160 spectrometer and a PIXIS: 256 charge-coupled device camera (Princeton Instruments). Measurements were performed with a dark-field condenser (air, NA 0.8−0.95) and a 60× air objective (CFI S Plan Fluor ELWD, NA 0.7, Nikon, Japan) under illumination by an Energetiq EQ-99 laser-driven light source. The measured spectra were corrected by subtracting the dark current at the detector and normalizing against the white light scattering spectrum of a polystyrene particle solution.

Time-Resolved Fluorescence Measurements. Fluorescence lifetime images and time-correlated single-photon counting (TCSPC) data were measured with an inverted confocal scanning microscope (MT200, PicoQuant) incorporating a 100× air objective (UPLFLN, NA 0.9, Olympus, Japan).

Diode lasers with 405 and 506 nm central wavelengths (LDH-405; LDH-510) and 1−5 MHz repetition rates were used for excitation. The signal was guided through a long pass filter with a cutoff below 519 nm (FF01-519/LP, Semrock) and detected with a SPCM-AQRH single-photon counting module (Excelitas).

Photoluminescence (PL) Measurements. The spectrum of the AgInS QD monolayer was detected with an Andor SR 163 Spectrograph during continuous exposure with a 405 nm diode laser (LDH-405). The background correction was done by dark current measurement.

Synthesis of Plasmonic Nanoparticles. Hexadecyltrimethylammonium chloride (CTAC) capped gold nanopheres were synthesized by a seed-mediated growth process, as described by Steiner et al.[19]

Briefly, the particles were synthesized in three steps. First, tetrachloroauric acid (HAuCl$_4$) was reduced by sodium borohydride (NaBH$_4$) in the presence of hexadecyltrimethylammonium bromide. The obtained 2 nm single-crystalline seeds were successively grown up within the next two steps to receive spherical particles of about 70 nm. For the growing process, HAuCl$_4$, CTAC, and ascorbic acid serve as Au precursor, stabilizing agent, and reductant, respectively. To ensure kinetic control, a syringe pump was used in the last step.

CTAC-capped silver nanocubes were synthesized by a living silver overgrowth of gold nanospheres, as recently published by Mayer et al.[20]

Synthesis of Quantum Dots. AIS/ZnS core/shell QDs were prepared in aqueous alkaline solutions as described in detail in recent literature.[21,22] Briefly, core AIS QDs were formed via the interaction between sodium sulfide and a mixture of Ag(I) and In(III) complexes with thioglycolic acid (TGA). The reaction was performed in deionized (DI) water at 96−98 °C in the presence of ammonia and was complete in 60 min. A ZnS shell was subsequently formed over the AIS cores by the addition of a Zn(II)−TGA complex. In this step, the colloidal solution remained at 96−98 °C for additional 10 min. The AIS/ZnS QDs were then precipitated by introducing an excessive amount of 2-propanol separating the precipitate from the supernatant by centrifugation and redispersing in pure DI water. The procedure yields stable colloidal AIS/ZnS solutions with a molar Ag(I) concentration of up to 0.1 M. The atomic ratio of metals in the final AIS/ZnS QDs was kept at Ag/In/Zn = 1:4:8.

Finite-Difference Time-Domain (FDTD) Simulations. A commercial-grade simulator based on the finite-difference time-domain (FDTD) method was used to perform the calculations (Lumerical FDTD, version 8.16).[23] To simulate the optical response, a total-field scattered-field source was used, and the frequency points were set to be half the wavelength span. We used perfectly matched the layer boundary conditions (BC) in all principal directions with a linearly polarized plane wave source ($\lambda = 300-800$ nm). Monitor boxes were used to obtain the optical responses of the system. For the dielectric properties of gold and silver, data from Johnson and Christy[24] and CRC[25] were fitted using six coefficients for gold and five for silver. Both fits had an root-mean-square (RMS) error of 0.2. For simulating the coupling interactions, we added a Lorentz Oscillator to resemble the optically active layer inside the cavity. All simulations reached an auto-shut-off of at least 10^{-5} before reaching 300 fs simulation time. For the best simulation stability, the mesh area was chosen to be at least 100 nm larger than the existing structure in all three principal directions. For the simulation of the coupling interactions, we employed a Lorentz
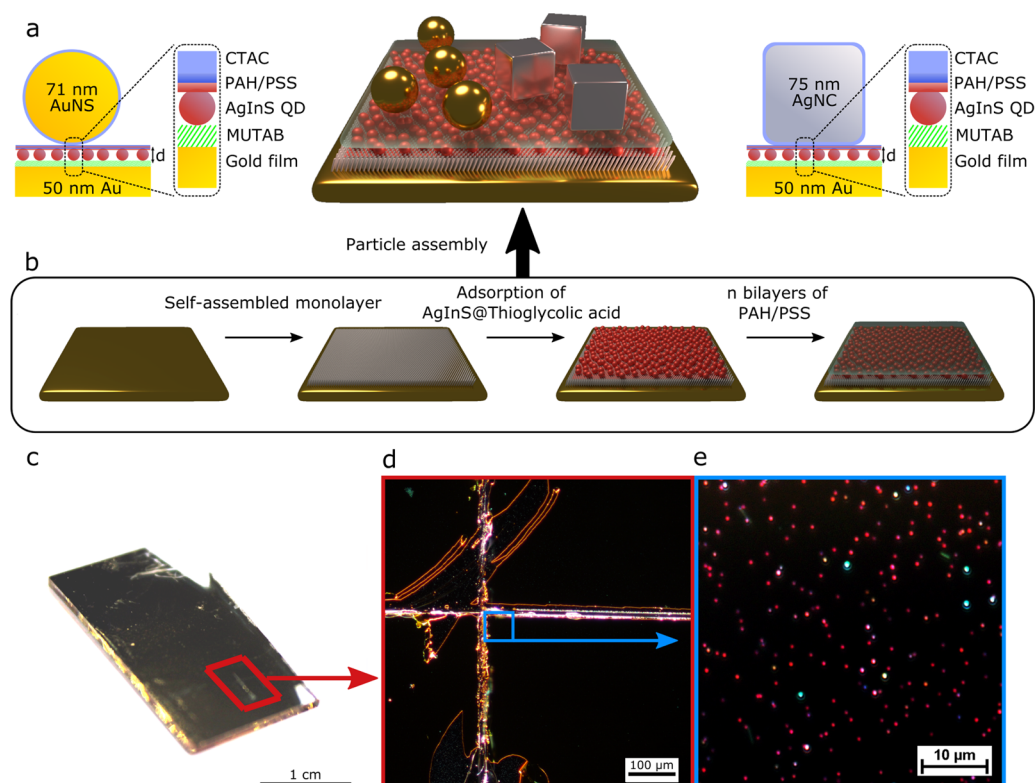
Figure 1. Setup of the macroscopic colloid-to-film-coupled nanosystem: (a) schematic description of the colloid-to-film nanocavity for a gold nanosphere (left) and a silver nanocube (right) coupled to a gold film with ternary metal-chalcogenide quantum dots sandwiched between colloid and film. (b) Fabrication steps required to form the uniform emitting spacer layer. (c) A photograph of an as-prepared substrate containing self-assembled cavities. (d) Dark-field microscopy image of the sample in (c) with two engraved orientation lines. (e) Dark-field microscopy image of the area marked in (d) showing colloid-to-film-coupled nanocavities.

model layer inside the cavity spacing. For effective refractive index calculations, the FDTD S-parameter extraction analysis was used.[26] To retrieve the optical constants for the inhomogeneous asymmetric structure, we calculated the optical response in the forward (S12/S22) and reverse (S11/S21) directions. For these simulations, the automatic shut-off level was adjusted to 10^{-7}. For all simulations with and without dipoles (to simulate a dipole-free situation, the dipole amplitude was set to 1/10), we ensured that the electromagnetic fields propagated as a plane wave (uniform fields) by introducing an electric field monitor at a sufficient distance from the structure (1 μm). We used periodic BCs in plane, a perfectly matched layer BC in the beam direction and a linearly polarized plane wave source (λ = 300−800 nm). The simulation setup was placed in the center of the FDTD simulation surrounded by air (n = 1). Metamaterial span as well as metamaterial center was set to the colloid-to-film-coupled setup accordingly.

■ RESULTS AND DISCUSSION

The fabrication of our colloidal nanocavities starts with a self-assembled monolayer of (11-mercaptoundecyl)-*N,N,N*-trimethylammonium bromide that is adsorbed on a gold film as a 1.5 nm layer (see Figure 1). This method proved to be suitable for the bottom-up self-assembly, since thiolate-based self-assembled monolayers SAMs on gold are easy to generate and offer ordered monolayers on a macroscopic scale.[27−29] Therefore, the surface charge is uniformly distributed and allows the negatively charged silver−indium−sulfide (AgInS) particles (3 nm) to be adsorbed in a homogeneous monolayer. We get a homogeneously distributed monolayer of emitters with an estimated quantum

dot density of 6.5×10^{12} emitters per cm^2 (Figure S1). To tune the distance between the metallic surfaces and ensure a homogeneous surface, additional polymer spacing was applied using the well-known layer-by-layer assembly method involving PAH and PSS.[30,31] Thus, the distance between the metal surfaces was adjusted by including different amounts of polyelectrolyte bilayers. Uniform coverage and low surface roughness of the spacing-emitter layer was verified via atomic force microscopy (AFM, Figure S2), scanning electron microscopy (SEM, Figure S3), and FLIM measurements (Figure S4). By AFM, an RMS surface roughness of 2.045 nm was measured on a 15×15 μm^2 area, and a uniform fluorescence emission signal was detected. The plasmonic colloids were then applied using drop-casting. For the CTAC surfactant layer surrounding the nanoparticles, we estimated a thickness of 2 nm from simulations. The final cavity spacing d is therefore made up of the thiolate SAM (1.5 nm), AgInS QDs (3 nm), a variable PAH/PSS multilayer, and a surfactant around the particles (2 nm). To ensure that the cavities were built from single particles, further SEM measurements and dark-field microscopy were employed to study the prepared substrates (Figures S5 and S6). This combination of self-assembled monolayers and colloidal building blocks makes it possible to manufacture a variety of stable cavity systems featuring different spacings and geometries with low fabrication efforts. A complementary and statistical study on their radiative properties is now possible.

Figure 2 shows a general evaluation of the different cavity designs chosen to cover a broad range of cavity resonances and light−matter interactions. For quantitative information about the single cavities and their exciton-coupling, single-particle
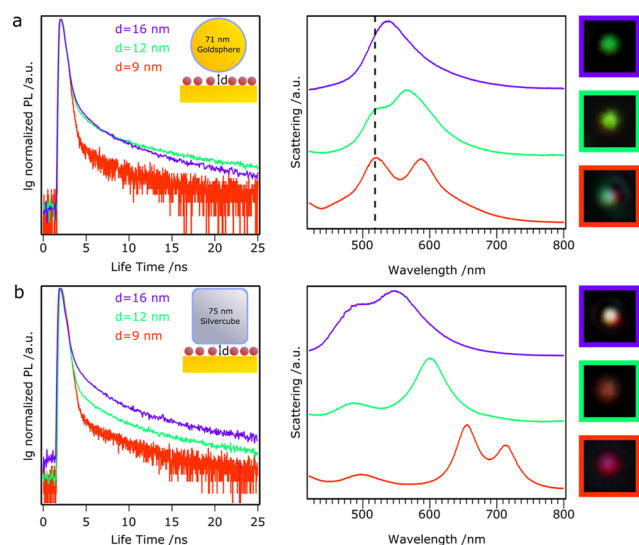
Figure 2. Spectroscopic properties of various colloid-to-film-coupled setups: time-correlated single-photon counting, scattering spectroscopy, and dark-field imaging of (a) gold spheres and (b) silver cubes coupled to a gold film with 9 nm (red), 12 nm (green), and 16 nm (purple) cavity spacing. The dashed line in (a) marks the gold film scattering.

scattering spectroscopy and TCSPC were used to directly access the optical properties of the colloid-to-film-coupled cavities. The TCSPC decay rate measurements of gold spheres and silver cubes were highly sensitive to the particle-to-film distance d. For gold spheres with 12 and 16 nm spacings, similar TCSPC curves

were obtained, whereas the 9 nm cavity led to a significantly enhanced decay rate. Silver cubes offer a greater degree of decay rate changes as a clear trend toward shorter lifetimes was detected for decreasing particle-to-film distances. This effect becomes more comprehensive when the single cavity scattering spectra are taken into account. Both particle systems show coupling interactions with the gold mirror as expressed through a spectral redshift. The silver cubes show a large sensitivity $\frac{\Delta\lambda}{\Delta d}$ of 23.7, whereas the gold spheres were less sensitive at 7.1. The higher sensitivity of the cube setup is dominated by the edge geometry rather than the material properties of silver (Figure S7). This relationship is also observable through dark-field microscopy as shown in Figure 2. Whereas only minor changes of the color of the cavity scattering cross section are visible for the sphere-to-film geometry, a more pronounced color variation takes place for the cube-to-film systems. The pronounced peak at 520 nm in the sphere-to-gold film system is caused by scattering of the gold film and not visible in the cube-to-gold film geometry due to the much higher scattering intensity of the silver cubes compared to gold spheres. The most significant observation is the Rabi splitting of the cavity resonance for the sub-10 nm cube-to-gold film gap. This mode hybridization is a signature that light−matter interactions between the plasmonic and the excitonic systems are becoming strong enough to overcome the energetic losses of the resonator. Since light−matter interactions are necessary for optical gain, we further investigated the optical properties of this particular 9 nm silver cube cavity setup.

To evaluate the suitability of the cube-to-gold-film-coupled cavities for tasks that demand strong plasmon−exciton
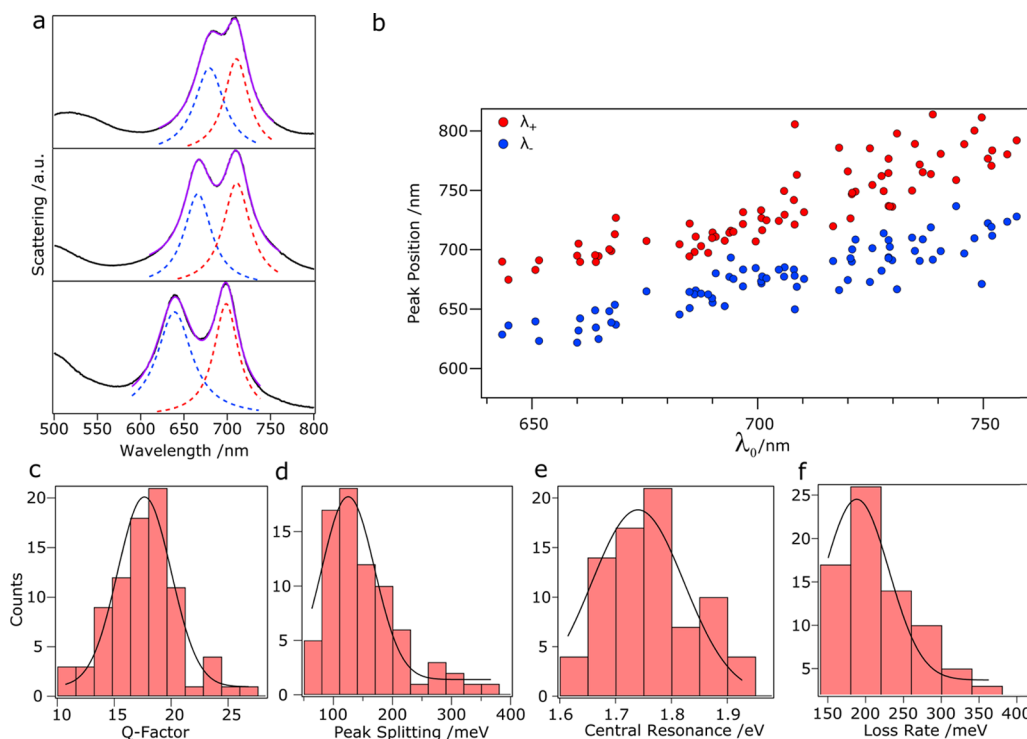

Figure 3. Statistical evaluation of silver cube nanocavities at 9 nm spacing: (a) dark-field scattering spectra of three representative nanocavities. The solid black line shows the measured scattering response. The blue and red dashed lines show the individual Lorentzian fits and the purple solid lines show the combined fits. (b) Peak position of the hybridized modes with respect to the estimated cavity resonance λ_0. (c−f) Histogram plots and Gaussian fits (black lines) of (c) Q-factor, (d) peak splitting, (e) cavity resonance, and (f) loss rate. Seventy-seven nanocavities were studied statistically.
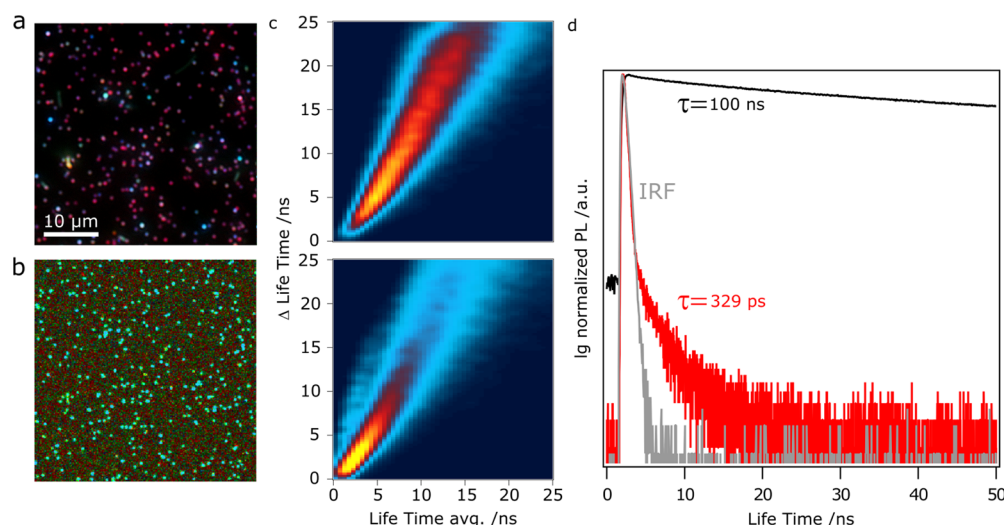
Figure 4. Dark-field spectroscopy and time-correlated single-photon counting in cube-to-film-coupled cavities: (a) dark-field scattering image of silver cube nanocavities at 9 nm spacing. (b) Fluorescence events (gray scale) and fluorescence lifetime (color scale) image of the corresponding cavities in (a). (c) Lifetime pattern images of quantum dot monolayers without (top) and with (bottom) silver cubes. (d) Normalized photoluminescence (PL) measurements of the ensemble of quantum dots on glass (black) and a single cavity (red). The instrument response function is shown in gray.

interactions, we need to quantify the occurring losses γ as well as the coupling strength g. Another point of interest is the quality factor Q, which is a measure of the energetic losses with respect to the resonance wavelength of an optical resonator. Our colloidal approach enables statistical measurements of the optical properties of single cavities by dark-field scattering spectroscopy. The required parameters can directly be extracted from the resulting spectra, since γ is the spectral FWHM, whereas g is given by the distance between the hybridized plasmon peaks.[32] This can be understood by applying a coupled-oscillator model

$$\omega_{\pm} = \frac{1}{2}(\omega_{cav} + \omega_0) \pm \sqrt{g^2 + \frac{\delta^2}{4}} \tag{1}$$

where $\omega_{\pm}$ is the frequency of the hybrid modes, ω_{cav} is the cavity frequency, ω_0 is the emitter frequency, g is the coupling strength, and δ is the detuning between cavity and emitter resonance. As Figure 3 shows, we evaluated 77 cube-to-film-coupled cavities and extracted the desired parameters using Lorentzian functions (Figure 3a). To visualize the optical range in which our cavities are operational, we also obtained the estimated cavity wavelength λ_0 for each spectrum (Figure 3b) by using an additional Lorentzian fit. We found the mean quality factor of the 9 nm cube system to be 16.9 ± 0.2, whereas typical plasmonic cavities have Q-factors between 5 and 10, although similarly high Q-factors were reported for different cavity geometries.[16,32] The statistical analysis of coupling strength gives a normal distribution with a mean value of 111.5 ± 5.2 meV, which is of the same order of magnitude as published in literature recently.[7] The variations of the coupling strengths are affected by several parameters. On the one hand, the absolute position of the emitters is crucial. Cube-to-metallic-film-coupled cavities induce large field enhancements near the edges of the cubes and lower field strengths in the center. Varying positions of the AgInS particles in each cavity will therefore lead to different levels of interaction. On the other hand, the number of emitters N also affects the cavity coupling.[33,34] For the cube-to-film geometry, we have an estimated N of 360 emitters per cavity (Figure S1). The estimated average central wavelength of the

coupling cavities is found to be 720 nm (1.72 ± 0.01 eV), which matches the emission from the AgInS QD monolayer (Figure S8). The mean losses of the cavities are found to be 177.5 ± 6.5 meV. Although the loss surpasses the coupling strength in general, we can still observe plasmonic mode hybridization, which is usually associated with strong plasmon−exciton coupling. Latter is defined by $2g > \gamma$, which is only the case for several of the detected cavities (Figure S9). The statistical evaluation shows that the cavities feature stable conditions concerning their light−matter interactions. Together with the scalable manufacturing process, they can be employed in macroscopic applications in the future.

One of the most promising ways to employ plasmonic cavities is their impact on the emitters' decay channels. Due to the QDs' close proximity to the metal surfaces, the excitable states of the quantum dots are altered, leading to both faster radiative and nonradiative decays.[35] Since the increase in radiative decay rates generally exceeds that of the nonradiative channels, the overall quantum efficiency of the QD emission improves significantly. This gives rise to photoluminescence enhancement, which results in a strong increase in emission. Figure 4a shows a dark-field microscopy image of the cube-to-gold-film-coupled cavities sandwiching the AgInS QD monolayer, verifying the presence of a cube-to-gold-film-coupled nanocavities. Figure 4b shows the same area as a FLIM, in which the contrast resembles the photoluminescence intensity and the color indicates the lifetime. A strong increase in the emission intensity can be detected at each cavity. To quantitatively analyze the photoluminescence enhancement, we determined the enhancement factor (EF), which is defined as

$$EF = \frac{I_{cav} A_{fit}}{I_{bkg} A_{cav}} \tag{2}$$

I_{cav} is the emission intensity of the cavity, I_{bkg} is the intensity of the AgInS QD monolayer outside the cavity, A_{fit} is the area of the enhanced region, and A_{cav} is the estimated area of the cavity. The data were extracted from each cavity by applying a two-dimensional Gaussian fit, in which I_{cav} describes the amplitude, I_{bkg} the baseline, and A_{fit} the FWHM of the fit. A_{cav} was assumed

to be 75×75 nm². A statistical evaluation of 100 cavities gives an EF of 1002 ± 48 for the cube-to-gold-film-coupled nanocavities.

For application in devices like optical circuits, it is necessary to modulate the decay rates of the emitters in a controlled fashion. Since the lifetime is inversely proportional to the decay rate, a decrease is to be expected for plasmonically enhanced fluorescence. TCSPC was employed to further quantify the radiative decay properties of the cavities. Whereas uncoupled AgInS emitters show an estimated average lifetime of 100 ns, the metal-enhanced photoluminescent system shows a drastically decreased lifetime of about 330 ps (Figure 4d), which is nearly indistinguishable from the instrument response function for most of the measured photons. Both the improved emission and the enhanced exciton decay indicate a strong interaction between plasmonic and excitonic components of the system. To study the macroscopic changes in emission behavior for cube-to-gold-film-coupled cavities, we employed a lifetime pattern analysis of FLIM measurements that provides information about the general lifetime distributions of a measured surface. Figure 4c shows the lifetime pattern of an AgInS QD monolayer on gold without (top) and with (bottom) plasmonic colloids. Although only about 2.5% of the surface is affected by the plasmonic cavities, we observed strong confinement of the lifetime distribution at high decay rates. This shows that our colloidal approach is suitable for the large-scale modulation of the radiative properties in enhancement and lifetime.

Since complementary experimental findings have pointed toward the presence of significant plasmon−exciton coupling in our cavity systems, their actual suitability as optical loss and gain materials was studied using FDTD simulations. The correspondence between refractive index and spatial location is crucial for applications such as transformation optics or nonreciprocal light propagations. We used the *S*-parameter method to determine the refractive index of our colloid-to-film-coupled cavity, which was calculated for an area of 300×300 nm² (see Figure 5). For this, the colloidal cavity was excited in both forward and backward directions, from which a transfer matrix with four elements was determined (*S*-matrix). Together with the size and position of the cavity, the effective refractive index was calculated. The first step in FDTD *S*-parameter calculations is the comparison of the results with values from literature (see also Figure S10). The comparison of the bulk refractive index values for gold[24] and silver[25] also indicates the total range in which the index of the gold/silver colloidal cavity can be modulated. Starting with a gold sphere as colloid, the imaginary refractive index/extinction coefficient (k) could be changed significantly (60%) with respect to the literature values for gold, whereas the real refractive index (n) changes only slightly (10%). These complex index values correspond to earlier published data that were used to quantify a colloidal magnetic metasurface.[36,37] Loops are observed in the index modulation diagrams for silver cubes, and these loops vary as the cavity spacing is adjusted. This effect is attributed to the flat cavity geometry, which causes a clear and strong cavity resonance between 600 and 750 nm. The loops in the index diagram of Figure 6 are to be interpreted as resonances (Lorentz oscillation). These resonances result in a peak in the real part of the refractive index, whereas the imaginary part is similar to a derivative of the peak. Figure S9 shows the real and imaginary parts of the refractive index with respect to wavelength. Given the resonance form, the same real refractive index can occur at different wavelengths. The same applies to the imaginary part. It
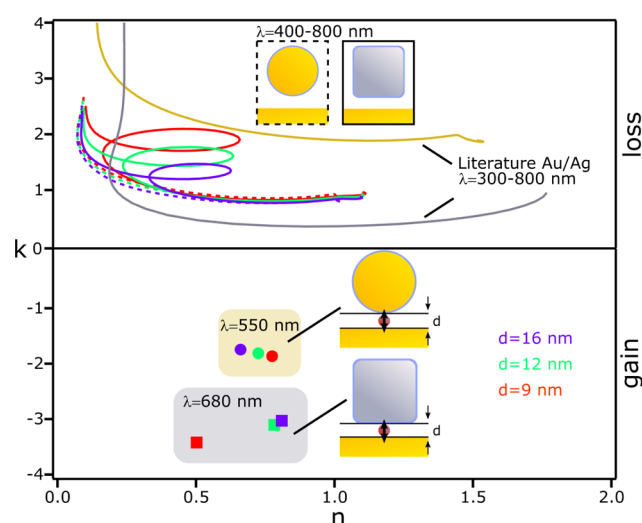

Figure 5. Index modulation diagram of a set of colloid-to-film-coupled nanocavities: literature values for the bulk gold and silver material are plotted between 300 and 800 nm in gold and gray, respectively. The *S*-parameter method is used to simulate the refractive indices from 400 to 800 nm for spherical gold (dashed line) and cubic silver (solid line) cavities at various dielectric spacings (9, 12, and 16 nm, color scheme inset). A dipole source was chosen to emulate the emitting material at 550 nm for the spherical cavity and at 680 nm for the cubic cavity.
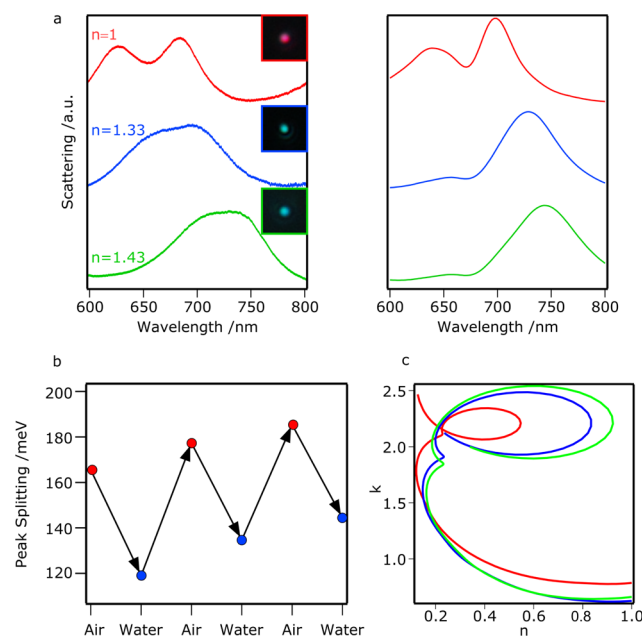

Figure 6. Cyclical change in the refractive index environment: (a) measured (left) and simulated (right) scattering responses of a nanocavity in different dielectric media, including air (red), water (blue), and ethylene glycol (green). (b) Reversible switching of plasmon mode hybridization by alternating the environment. (c) *S*-matrix calculations of the effective refractive index of the cavity structure for different ambient conditions.

follows that the loop tip can be interpreted as a resonance peak and the loop width is proportional to the FWHM of the resonance. Figure S11 describes the physical meaning of the resonances by plotting the refractive index as permittivity and permeability. An electrical mode is defined as a peak in the imaginary part of the permittivity and a magnetic mode is defined as a peak in the imaginary part of the permeability.[37−39]

From this it can be concluded that at spherical cavities only a magnetic mode is present and at cubic cavities electrical as well as magnetic properties occur. Depending on the excitation wavelength or cavity spacing, the real index can be changed by a factor of 2−3 and the imaginary index by 50−56% with respect to the values for bulk gold. With this scalable colloidal approach, the refractive index can be modulated in the range of metallodielectric materials.[10] Beyond this range, the imaginary index can become negative, whereas the real index remains unchanged by introducing an emitter within the colloidal cavity. We simulated the presence of a quantum emitter by introducing a single-wavelength dipole source whose electric field vector is perpendicular to the metallic surfaces. With this approach, we were able to determine the complex index for the sphere-to-gold film cavity at 550 nm and for the cube-to-gold film cavity at 680 nm. Consequently, with these colloid-to-film-coupled nanocavities, one can create an alternating imaginary index profile with periodic loss and gain regions.

Beyond optical computing, plasmonic systems are also highly sensitive to changes in their environments. Therefore, their optical response can be further altered by changing the parameters like the ambient RI. To study how the light−matter interactions respond when the cavity resonance is changed, we varied the dielectric environment of the system from air ($n = 1$) to water ($n = 1.33$) and to ethylene glycol ($n = 1.43$). Figure 6 shows the scattering signals for these different ambient conditions, both in experiments and simulations. Whereas pronounced splitting is observed in air, reduced splitting is observed if the surrounding medium is changed to water or ethylene glycol. If a sample is immersed in water and dried afterward, the original peak splitting is recovered. As it is plotted in Figure 6b, this RI modulation can be cycled. We also calculated the effective refractive index using the FDTD S-parameter method. With this method, we also observed that the ambient refractive index changes the effective index to the same extent. Thus, using various colloidal cavities (Figure 5) and refractive index environments (Figure 6), we can change the real and imaginary parts of the cavity response independently.

CONCLUSIONS

We have demonstrated the ability to tailor refractive index on a sub-wavelength scale for a set of nanocavities using spectroscopic and electromagnetic simulation methods. To ensure cost-effective fabrication on a large scale, we employed a self-assembled monolayer of thiolates and polyelectrolytes to tailor the cavity properties. This method allows us to statistically quantify the spectroscopic properties of the colloid-to-film-coupled cavities with and without embedded emitters and could be extended to create different emitter densities by using varying thiolates in the future. The resonance position and shape could be adjusted over a wide visible spectral range by introducing different colloidal materials, shapes and cavity spacings. The plasmon−exciton interaction, as a measure of the coupling strength, was confirmed by scattering spectroscopy, fluorescence lifetime measurements, and reversible refractive index sensing. The coupling strength also correlated with the effective refractive index shown by the FDTD S-parameter method. Thus, by changing the colloidal cavity parameters, the real and imaginary parts of the refractive index could be selectively and independently changed. The accurate determination of optical constants is an important step in the design of photonic nanostructures. The low-cost and scalable fabrication of tailor-made nanocavities can therefore lead to new generation of optical circuits and light modulators.

ASSOCIATED CONTENT

Supporting Information

The Supporting Information is available free of charge on the ACS Publications website at DOI: 10.1021/acs.jpcc.8b12566.

UV−vis spectrum and density calculation for the AgInS monolayer; AFM, SEM, transmission electron microscopy (TEM), and additional dark-field and FLIM measurements of the studied samples; PL spectra of AgInS QDs both as a monolayer and in solution; exemplary scattering spectrum for determining coupling strength and losses in a cavity; additional FDTD simulations (PDF)

AUTHOR INFORMATION

Corresponding Author

*E-mail: koenig@ipfdd.de.

ORCID

Tobias A. F. König: 0000-0002-8852-8752

Notes

The authors declare no competing financial interest.

ACKNOWLEDGMENTS

REFERENCES

(1) Ciracì, C.; Hill, R. T.; Mock, J. J.; Urzhumov, Y.; Fernández-Domínguez, A. I.; Maier, S. A.; Pendry, J. B.; Chilkoti, A.; Smith, D. R. Probing the Ultimate Limits of Plasmonic Enhancement. *Science* **2012**, *337*, 1072−1074.

(2) Giannini, V.; Fernández-Domínguez, A. I.; Heck, S. C.; Maier, S. A. Plasmonic Nanoantennas: Fundamentals and Their Use in Controlling the Radiative Properties of Nanoemitters. *Chem. Rev.* **2011**, *111*, 3888−3912.

(3) Park, J.-E.; Jung, Y.; Kim, M.; Nam, J.-M. Quantitative Nanoplasmonics. *ACS Cent. Sci.* **2018**, *4*, 1303−1314.

(4) Chikkaraddy, R.; de Nijs, B.; Benz, F.; Barrow, S. J.; Scherman, O. A.; Rosta, E.; Demetriadou, A.; Fox, P.; Hess, O.; Baumberg, J. J. Single-Molecule Strong Coupling at Room Temperature in Plasmonic Nanocavities. *Nature* **2016**, *535*, 127−130.

(5) Chen, X.; Chen, Y.-H.; Qin, J.; Zhao, D.; Ding, B.; Blaikie, R. J.; Qiu, M. Mode Modification of Plasmonic Gap Resonances Induced by Strong Coupling with Molecular Excitons. *Nano Lett.* **2017**, *17*, 3246−3251.

(6) Akselrod, G. M.; Argyropoulos, C.; Hoang, T. B.; Ciracì, C.; Fang, C.; Huang, J.; Smith, D. R.; Mikkelsen, M. H. Probing the Mechanisms of Large Purcell Enhancement in Plasmonic Nanoantennas. *Nat. Photonics* **2014**, *8*, 835−840.

(7) Han, X.; Wang, K.; Xing, X.; Wang, M.; Lu, P. Rabi Splitting in a Plasmonic Nanocavity Coupled to a WS_2 Monolayer at Room Temperature. *ACS Photonics* **2018**, *5*, 3970−3976.

(8) Sugimoto, H.; Yashima, S.; Fujii, M. Hybridized Plasmonic Gap Mode of Gold Nanorod on Mirror Nanoantenna for Spectrally Tailored Fluorescence Enhancement. *ACS Photonics* **2018**, *5*, 3421−3427.

(9) Silva, A.; Monticone, F.; Castaldi, G.; Galdi, V.; Alù, A.; Engheta, N. Performing Mathematical Operations with Metamaterials. *Science* **2014**, *343*, 160−163.

(10) Lee, J.-H.; Koh, C. Y.; Singer, J. P.; Jeon, S.-J.; Maldovan, M.; Stein, O.; Thomas, E. L. 25th Anniversary Article: Ordered Polymer Structures for the Engineering of Photons and Phonons. *Adv. Mater.* **2014**, *26*, 532−569.

(11) Jiang, P.; Ostojic, G. N.; Narat, R.; Mittleman, D. M.; Colvin, V. L. The Fabrication and Bandgap Engineering of Photonic Multilayers. *Adv. Mater.* **2001**, *13*, 389−393.

(12) Chen, H.; Chan, C. T.; Sheng, P. Transformation Optics and Metamaterials. *Nat. Mater.* **2010**, *9*, 387−396.

(13) Ergin, T.; Stenger, N.; Brenner, P.; Pendry, J. B.; Wegener, M. Three-Dimensional Invisibility Cloak at Optical Wavelengths. *Science* **2010**, *328*, 337−339.

(14) Schuller, J. A.; Barnard, E. S.; Cai, W.; Jun, Y. C.; White, J. S.; Brongersma, M. L. Plasmonics for Extreme Light Concentration and Manipulation. *Nat. Mater.* **2010**, *9*, 193−204.

(15) Liu, N.; Mesch, M.; Weiss, T.; Hentschel, M.; Giessen, H. Infrared Perfect Absorber and Its Application As Plasmonic Sensor. *Nano Lett.* **2010**, *10*, 2342−2348.

(16) Hugall, J. T.; Singh, A.; van Hulst, N. F. Plasmonic Cavity Coupling. *ACS Photonics* **2018**, *5*, 43−53.

(17) Feng, L.; Xu, Y.-L.; Fegadolli, W. S.; Lu, M.-H.; Oliveira, J. E. B.; Almeida, V. R.; Chen, Y.-F.; Scherer, A. Experimental Demonstration of a Unidirectional Reflectionless Parity-Time Metamaterial at Optical Frequencies. *Nat. Mater.* **2012**, *12*, 108−113.

(18) Feng, L.; Wong, Z. J.; Ma, R.-M.; Wang, Y.; Zhang, X. Single-Mode Laser by Parity-Time Symmetry Breaking. *Science* **2014**, *346*, 972−975.

(19) Steiner, A. M.; Mayer, M.; Seuss, M.; Nikolov, S.; Harris, K. D.; Alexeev, A.; Kuttner, C.; König, T. A. F.; Fery, A. Macroscopic Strain-Induced Transition from Quasi-infinite Gold Nanoparticle Chains to Defined Plasmonic Oligomers. *ACS Nano* **2017**, *11*, 8871−8880.

(20) Mayer, M.; Steiner, A. M.; Röder, F.; Formanek, P.; König, T. A. F.; Fery, A. Aqueous Gold Overgrowth of Silver Nanoparticles: Merging the Plasmonic Properties of Silver with the Functionality of Gold. *Angew. Chem., Int. Ed.* **2017**, *56*, 15866−15870.

(21) Raevskaya, A.; Lesnyak, V.; Haubold, D.; Dzhagan, V.; Stroyuk, O.; Gaponik, N.; Zahn, D. R. T.; Eychmüller, A. A Fine Size Selection of Brightly Luminescent Water-Soluble Ag−In−S and Ag−In−S/ZnS Quantum Dots. *J. Chem. Phys. C* **2017**, *121*, 9032−9042.

(22) Stroyuk, O.; Raevskaya, A.; Spranger, F.; Selyshchev, O.; Dzhagan, V.; Schulze, S.; Zahn, D. R. T.; Eychmüller, A. Origin and Dynamics of Highly Efficient Broadband Photoluminescence of Aqueous Glutathione-Capped Size-Selected Ag−In−S Quantum Dots. *J. Phys. Chem. C* **2018**, *122*, 13648−13658.

(23) FDTD Solutions; Lumerical Inc.. https://www.lumerical.com/products/fdtd-solutions/ (accessed Feb 10, 2019).

(24) Johnson, P. B.; Christy, R. W. Optical Constants of the Noble Metals. *Phys. Rev. B* **1972**, *6*, 4370−4379.

(25) Hagemann, H. J.; Gudat, W.; Kunz, C. Optical Constants from the Far Infrared to the X-Ray Region: Mg, Al, Cu, Ag, Au, Bi, C, and Al2O3. *J. Opt. Soc. Am.* **1975**, *65*, 742−744.

(26) Smith, D. R.; Vier, D. C.; Koschny, T.; Soukoulis, C. M. Electromagnetic Parameter Retrieval from Inhomogeneous Metamaterials. *Phys. Rev. E* **2005**, *71*, No. 036617.

(27) Bain, C. D.; Evall, J.; Whitesides, G. M. Formation of Monolayers by the Coadsorption of Thiols on Gold: Variation in the Head Group, Tail Group, and Solvent. *J. Am. Chem. Soc.* **1989**, *111*, 7155−7164.

(28) Love, J. C.; Estroff, L. A.; Kriebel, J. K.; Nuzzo, R. G.; Whitesides, G. M. Self-Assembled Monolayers of Thiolates on Metals as a Form of Nanotechnology. *Chem. Rev.* **2005**, *105*, 1103−1170.

(29) Reynaud, C. A.; Duché, D.; Le Rouzo, J.; Nasser, A.; Nony, L.; Pourcin, F.; Margeat, O.; Ackermann, J.; Berginc, G.; Nijhuis, C. A.; et al. Enhancing Reproducibility and Nonlocal Effects in Film-Coupled Nanoantennas. *Adv. Opt. Mater.* **2018**, *6*, No. 1801177.

(30) Decher, G. Fuzzy Nanoassemblies: Toward Layered Polymeric Multicomposites. *Science* **1997**, *277*, 1232−1237.

(31) Izquierdo, A.; Ono, S. S.; Voegel, J. C.; Schaaf, P.; Decher, G. Dipping versus Spraying: Exploring the Deposition Conditions for Speeding Up Layer-by-Layer Assembly. *Langmuir* **2005**, *21*, 7558−7567.

(32) Zengin, G.; Wersäll, M.; Nilsson, S.; Antosiewicz, T. J.; Käll, M.; Shegai, T. Realizing Strong Light-Matter Interactions Between Single-Nanoparticle Plasmons and Molecular Excitons at Ambient Conditions. *Phys. Rev. Lett.* **2015**, *114*, No. 157401.

(33) Törmä, P.; Barnes, W. L. Strong Coupling Between Surface Plasmon Polaritons and Emitters: A Review. *Rep. Prog. Phys.* **2015**, *78*, No. 013901.

(34) Hoang, T. B.; Akselrod, G. M.; Argyropoulos, C.; Huang, J.; Smith, D. R.; Mikkelsen, M. H. Ultrafast Spontaneous Emission Source Using Plasmonic Nanoantennas. *Nat. Commun.* **2015**, *6*, No. 7788.

(35) Schnepf Max, J.; Brasse, Y.; Goßler Fabian, R.; Steiner Anja, M.; Obermeier, J.; Lippitz, M.; Fery, A.; König Tobias, A. F. Single Particle Spectroscopy of Radiative Processes in Colloid-to-Film-Coupled Nanoantennas. *Z. Phys. Chem.* **2018**, *232*, 1593−1606.

(36) Mayer, M.; Tebbe, M.; Kuttner, C.; Schnepf, M. J.; König, T. A. F.; Fery, A. Template-Assisted Colloidal Self-Assembly of Macroscopic Magnetic Metasurfaces. *Faraday Discuss.* **2016**, *191*, 159−176.

(37) Brasse, Y.; Müller, M. B.; Karg, M.; Kuttner, C.; König, T. A. F.; Fery, A. Magnetic and Electric Resonances in Particle-to-Film-Coupled Functional Nanostructures. *ACS Appl. Mater. Interfaces* **2018**, *10*, 3133−3141.

(38) Dolling, G.; Enkrich, C.; Wegener, M.; Zhou, J. F.; Soukoulis, C. M.; Linden, S. Cut-Wire Pairs and Plate Pairs as Magnetic Atoms for Optical Metamaterials. *Opt. Lett.* **2005**, *30*, 3198−3200.

(39) Mayer, M.; Schnepf, M. J.; König, T. A. F.; Fery, A. Colloidal Self-Assembly Concepts for Plasmonic Metasurfaces. *Adv. Opt. Mater.* **2019**, *7*, No. 1800564.

5   Colloidal polymers

5.1   Direct observation of plasmon band formation and delocalization in quasi-infinite nanoparticle chains

Direct observation of plasmon band formation and delocalization in quasi-infinite nanoparticle chains

Martin Mayer, Pavel L Potapov, Darius Pohl, Anja Maria Steiner, Johannes Schultz, Bernd Rellinghaus, Axel Lubk,* **Tobias A.F. König*** and Andreas Fery*

*corresponding authors

Author contribution statement

MM carried out the experiments. **TK** encouraged MM and AS to investigate the numerical simulation, fabrication and optical spectroscopy methods as well as supervised the execution and findings of this work. PP, JS and AL contributed through their analytical simulations, transmission electron microscopy and electron spectroscopy methods. DP and BR contributed through their transmission electron microscopy method. AS contributed through synthesis of the metallic nanoparticles. AL, **TK** and AF made a significant contribution to the conception and design of the work. Through the simulation, fabrication and optical spectroscopy methods, the author **TK** made a significant contribution to the acquisition, analysis and interpretation of the data. All authors provided critical feedback and helped shape the research, analysis and manuscript.

Direct Observation of Plasmon Band Formation and Delocalization in Quasi-Infinite Nanoparticle Chains

Martin Mayer,[†,§] Pavel L. Potapov,[⊥] Darius Pohl,[§,#,‖] Anja Maria Steiner,[†,§] Johannes Schultz,[⊥] Bernd Rellinghaus,[§,#,‖] Axel Lubk,*[,⊥] Tobias A. F. König,*[,†,§] and Andreas Fery*[,†,§,‡]

[†]Institute of Physical Chemistry and Polymer Physics and [‡]Department of Physical Chemistry of Polymeric Materials, Leibniz-Institut für Polymerforschung Dresden e.V., Hohe Strasse 6, 01069 Dresden, Germany

[§]Cluster of Excellence Center for Advancing Electronics Dresden (cfaed) and [‖]Dresden Center for Nanoanalysis, Technische Universität Dresden, D-01062 Dresden, Germany

[⊥]Institute for Solid State Research and [#]Institute for Metallic Materials, Leibniz-Institut für Festkörper und Werkstoffforschung, Helmholtzstrasse 20, 01069 Dresden, Germany

S *Supporting Information*

ABSTRACT: Chains of metallic nanoparticles sustain strongly confined surface plasmons with relatively low dielectric losses. To exploit these properties in applications, such as waveguides, the fabrication of long chains of low disorder and a thorough understanding of the plasmon-mode properties, such as dispersion relations, are indispensable. Here, we use a wrinkled template for directed self-assembly to assemble chains of gold nanoparticles. With this up-scalable method, chain lengths from two particles (140 nm) to 20 particles (1500 nm) and beyond can be fabricated. Electron energy-loss spectroscopy supported by boundary element simulations, finite-difference time-domain, and a simplified dipole coupling model reveal the evolution of a band of plasmonic waveguide modes from degenerated single-particle modes in detail. In striking difference from plasmonic rod-like structures, the plasmon band is confined in excitation energy, which allows light manipulations below the diffraction limit. The non-degenerated surface plasmon modes show suppressed radiative losses for efficient energy propagation over a distance of 1500 nm.

KEYWORDS: *Surface plasmons, nanoparticle, plasmonic polymer, template-assisted self-assembly, electron-energy loss spectroscopy*
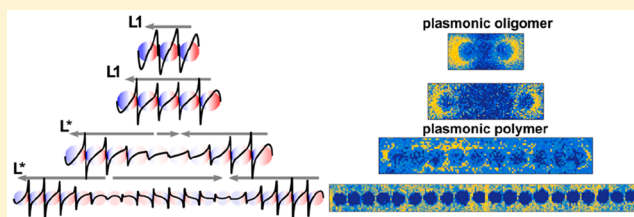
Localized surface plasmon resonances (LSPR) are self-sustaining resonances appearing when delocalized conduction-band electrons of a metal are confined within a nanoparticle.[1,2] Plasmonic resonances are characterized by strong and localized electromagnetic field enhancement, which is strongly sensitive to the geometry and composition of the nanoparticle and the environment.[3] This makes them attractive for a wide range of applications, in which sub-wavelength control of electromagnetic fields from the infrared to ultraviolet range is crucial.[4] In particular, long metallic nanoparticle chains have been proposed for plasmonic waveguiding,[5] i.e., photonic transport confined to the submicron and, hence, subwavelength length scale, which is difficult to realize with optical devices.[6,7] In this length scale, plasmonic waveguides open up new strategies for signal transport due to their strong confinement and the high signal speed. It has been predicted through analytical and numerical studies that regular nanoparticle chains support plasmon modes with distinct dispersion relations and, hence, signal transmission velocities depending on the geometric parameters of the chain.[8] More recently, geometric modifications of the monopartite chain prototype, such as bipartite chains or zig-zag chains, are predicted to feature more

complicated band structures, including plasmonic band gaps as well as topological edge states.[9]

For the realization of such waveguides and the experimental proof of the predicted effects, however, energy dissipation in the metal and precise positional control of the metallic nanoparticles are still bottlenecks. In particular, the intrinsic losses of the employed metals limit the overall performance of plasmonic waveguides.[10] However, smart assembly, resulting in finely tuned particle coupling, can further lower the dissipation. For example, Liedl et al. recently showed low-dissipative and ultrafast energy propagation at a bimetallic chain with three 40 nm particles.[11] Various colloidal techniques, such as DNA origami[12] or self-assembly by chemical linkers,[13] are available to assemble noble metal nanoparticles into chains. In principle, infinitely long particle chains can be fabricated with these techniques; however, trade-offs in particle spacing, particle size, or linear geometry must be accepted. In recent years, masks have been used for colloidal self-assembly to overcome the size limitation, which results into long-range energy transfer, even
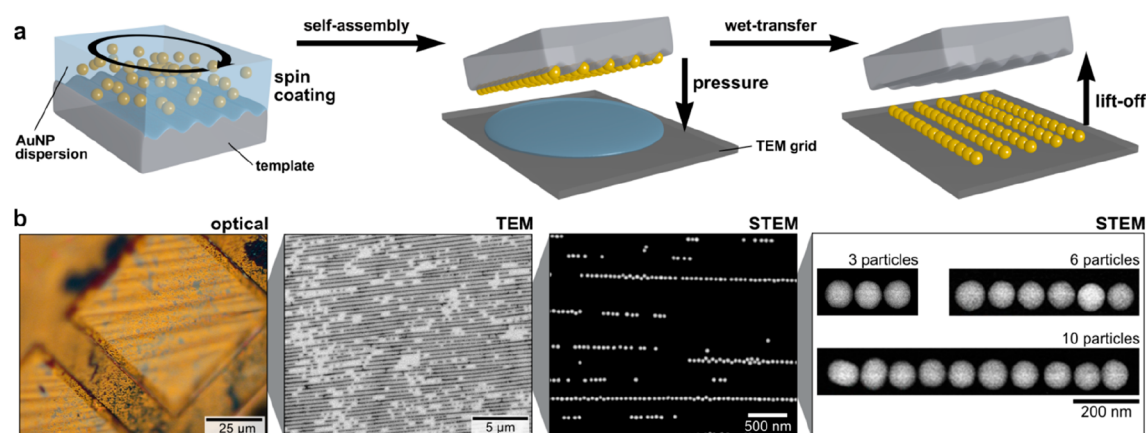
Figure 1. Large-area template-assisted self-assembly of various chain lengths and wet transfer for spectroscopic (EELS) studies. (a) Schematic template-assisted colloidal self-assembly via spin coating followed by wet-transfer printing on a TEM grid. (b) A microscope image and (S)TEM images and selective details (3, 6, and 10 particle chains) of the transferred gold particle chains.
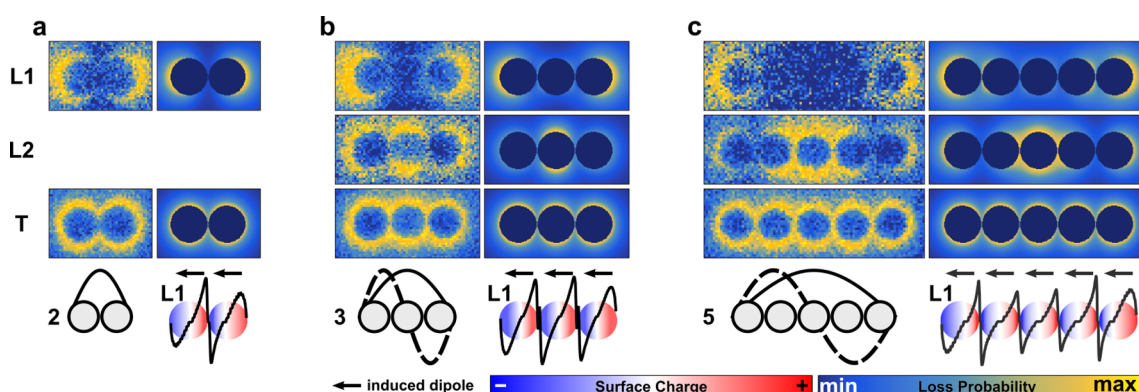

Figure 2. Theoretical and experimental plasmonic modes of a (a) dimer, (b) trimer, and (c) pentamer. Schematic descriptions, integrated surface charge images, and plots (black line) as well as corresponding dipole moments for simulated surface charge plots for the most-dominant longitudinal modes. Experimental and simulated EELS maps of longitudinal and transversal modes.

around a micrometer-sized corner.[14] It has been shown that above a rather undefined chain length, the so-called "infinite chain limit", the longitudinal plasmonic modes converge to a nonzero asymptotic energy.[15,16] Consequently, the plasmonic response above this lengths differs from shorter chains because of the discrete nature of the chain and the finite coupling strength.[17] To make it easier to distinguish between them, chains above the infinite chain limit are referred to plasmonic polymers, whereas shorter chains are called plasmonic oligomers, in close analogy to organic polymer synthesis.[8,12]

Although the energy transport is principally improved by dark modes, which suffer significantly less from radiation losses than the bright ones, it is still a matter of debate whether those dark modes are responsible for the transport.[18] Recently, methods for visualizing localized plasmons on the nanometer scale have emerged. These methods involve transmission electron microscopy (TEM) combined with electron energy-loss spectroscopy (EELS) with high-energy resolution, which is now readily available in dedicated monochromated TEM instruments. Examples of successful application of TEM and EELS methods includes mapping LSPR modes in metallic nanocubes,[19] nanorods,[20−22] and nanospheres.[23,24]

In this Letter, we fabricated long regular nanoparticle chains, which allow for individual probing of local fields. By comprehensive spatially resolved electron energy loss studies, the plasmonic response is characterized. Here, we will

particularly address the transition from individual single particle modes to plasmonic bands in quasi-infinite long chains, which has not been directly observed previously. Robust excitation of the plasmonic waveguide modes relies on recent developments in our groups: single crystalline wet-chemical synthesis[25] and template-assisted colloidal self-assembly[26] as well as improved EELS characterization in the TEM[27] and electromagnetic modeling.[18]

Template-assisted colloidal self-assembly (Figure 1) was used to fabricate colloidal nanoparticle chains (particle diameter of 70 nm) on micrometer-scale carbon-coated TEM grids.[26,28,29] Because high optical quality, reproducibility, and narrow size distributions are crucial parameters, single-crystalline spherical gold nanoparticles (AuNSp) were synthesized by seed-mediated growth, which comply with these requirements.[30,31] The highly linear assembly of these gold spheres into wrinkled elastomeric templates results in closely packed chains with a homogeneous spacing of <2 nm.[26,31] The obtained interparticle distance relies, in this case, only on the well-defined thickness of the employed dielectric spacer, i.e., in this case, on the protein shell.[26] The resulting spacing can also be seen in the TEM images in Figure 1b. The directed self-assembly process followed by wet-contact printing on the target structure (TEM grid) is outlined in Figure 1a. Transfer to a TEM grid allows the spectroscopic study of the coherent plasmonic coupling in chains of different lengths (Figure 1b) while maintaining the good filling rate (defined by

chains per area) and close packing of the nanoparticles within chains. To obtain close-packed chains with varying lengths and a slightly reduced density of chains on the sample, the pH of the colloidal nanoparticle solution was slightly reduced, as described in the experimental section. Thus, such assemblies mark the perfect test system to study the effects of various particle lengths with comparable properties in a combinatorial approach.

The following investigates the transition from plasmonic monomer to polymer (i.e., beyond the infinite chain limit) in detail. Figure 2 shows plasmonic oligomers consisting of a number of nanoparticles well-below the infinite chain limit. The plasmonic properties for such short particle chains with up to five particles have been studied extensively by Mulvaney et al.[24] EELS in the TEM is nowadays a common approach to spatially image plasmons. In this method, the energy loss of a focused electron beam upon crossing the electric field of a plasmon (excited by the evanescent field of the very same electron) is spectroscopically mapped.

For short particle chains, several plasmon modes can be observed in the EELS maps and spectra (see also Figure S4). By directly comparing experimentally observed maps of energy loss with the electromagnetic simulations, the nature of the induced coupling interactions can be elucidated. This comparison allows for the identification of the plasmonic modes by their corresponding surface charges. Starting from a single particle (Figure S2), the addition of a second particle (forming a dimer, Figure 2a) induces hybridization.[32] Hence, the longitudinal modes split into a symmetric (L2) and antisymmetric (L1) one with higher and lower energy, respectively, compared to the fundamental (transversal) mode.[15,24] The maps of energy-loss and the derived surface charges reveal the lower energy antisymmetric mode. The higher-energy L2 mode is not unambiguously detectable because of its lower interaction with the electron beam (see below for details) and its larger damping by interband transitions.

By forming a trimer (Figure 2b), the L1 mode shifts further to lower energies. Additionally, the next order longitudinal L2 mode, with a node in the central particle, can be discerned from the transversal and L1 mode. The mutual cancellation of induced dipoles generates a net dipole moment of zero (even numbers of surface charge waves) rendering this L2 mode dark (i.e., non-radiatively interacting with photons). The higher-energy L3 mode above the transversal mode is again damped by interband transitions. As the number of particles increases to five particles, the energetically lowest mode (L1) approaches the infinite chain limit already (see Figure 2c). However, the induced longitudinal modes L1 and L2 can still be discerned, and the surface charge waves cover the complete length of the chain.

By exciting such particle chains with an electromagnetic field, e.g., a light wave or the evanescent field of a focused electron beam, collective localized surface plasmons are induced in the particle chain. The induced electron density oscillation results in a localized dipole moment of the single particles (defined by surface charges). At large interparticle distances, these oscillations do not couple and are energetically degenerate. When the interparticle distance is decreased far below the excitation wavelength, the localized dipole moments of the single particles couple, lifting the degeneracy. By extension, higher-order multipole moments also couple, which becomes increasingly important at small particle distances. The following shows that the principal plasmonic behavior of nanoparticle chains can be well-described on the dipolar coupling level. In

particular the dipoles oriented along the chain axis strongly couple coherently leading to a set of distinguishable longitudinal modes (Figure 3).
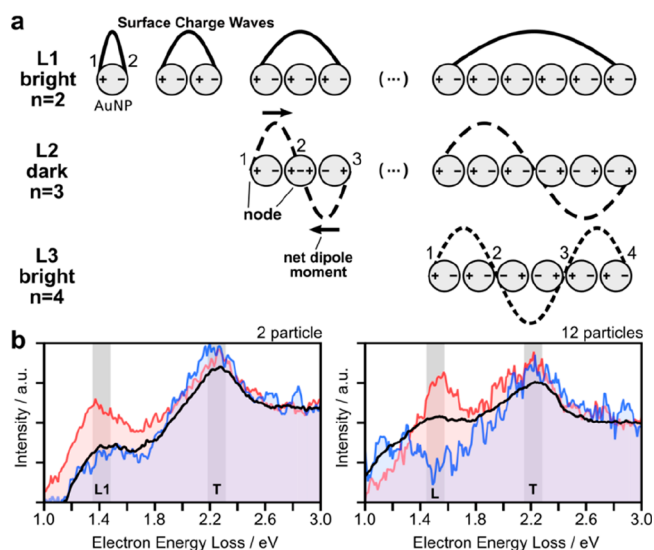

Figure 3. Definitions of the longitudinal plasmonic modes and their spectroscopic response. (a) Schematic descriptions of the plasmonic modes along the geometric axis by surface charge ($\pm$), dipole moment (black line), net-dipole moment, node, and surface charge wave (schematically representing the polarization field of the respective plasmonic modes). (b) Selected electron energy loss spectra (EELS) for 2 and 12 particles. The blue and red lines show the EELS response averaged over 10−40 pixels, and the black line represents the values averaged over all spectra of the scanned map.

Therefore, similar to the electron-wave function in a diatomic molecule, the energetically lowest coherent plasmonic mode in a plasmonic dimer (L1 at 1.4 eV/885 nm) is an antisymmetric bonding mode (Figure 3b). For longer chains, several harmonics of the longitudinal mode can be excited (see also Figure 3a), which are defined by the number of nodes (n). In this context, a node is defined by a zero dipole moment at a specific chain position and the longitudinal modes (Lm) are indexed by $m = n + 1$.[24] Using this definition, bright modes (nonzero overall dipole moment) occur at odd m and dark modes (zero overall dipole moment) at even m, respectively. Figure 3b exemplarily shows two selected EEL spectra for chains with 2 and 12 particles. In contrast to rod like structures,[33] the excitation energy of the L1 mode in long chains converges at low energies, described as the infinite chain limit.[16] In literature, this limit is typically defined somewhere between 8 and 12 particles (see also a spectral visualization in Figure S1).[15,16] In contrast, nanoparticle dipole moments, perpendicular to the chain axis, couple only weakly, resulting in (almost) degenerate transversal modes (marked as T at 2.2 eV/560 nm).

Approaching the infinite chain limit, the intensity of the fundamental longitudinal mode L1 shifts further to smaller energies and gradually vanishes (Figure 4). Electromagnetic simulations reveal that this decrease can be ascribed to an increased damping due to intraband transitions (see Figure S7 for respective spectra). Above L2, the L3 mode becomes observable as identified by the number of nodes ($n = 4$).

When increasing the number of particles in a chain beyond the infinite chain limit, it becomes increasingly difficult or even impossible to discern pure Lm modes (Figures 5 and S5 for the
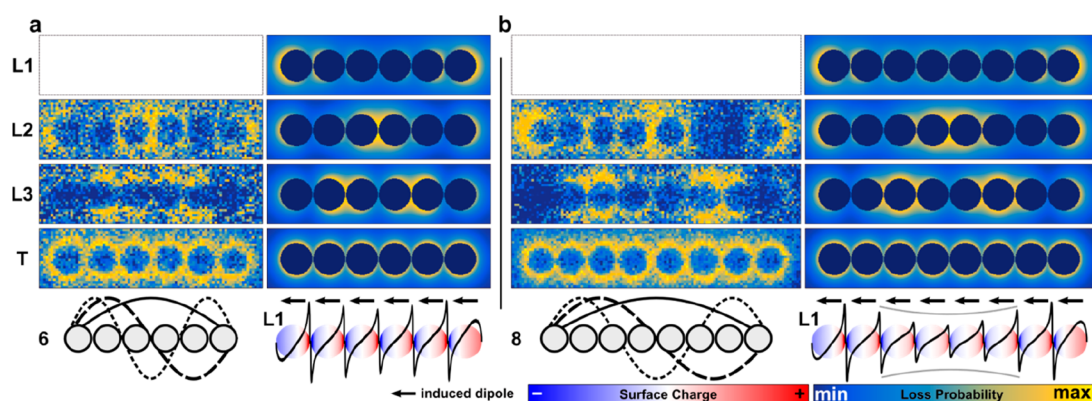
Figure 4. Particle chain length approaching the infinite chain limit. Schematic description, simulated surface charge plots of the lowest-order L1 mode, and maps of energy loss for all resolvable plasmonic modes (panels a and b, 6 and 8 particles, respectively; experimental results are shown on the left and simulated results on the right; the intensity of L1 was experientially below the detection limit).
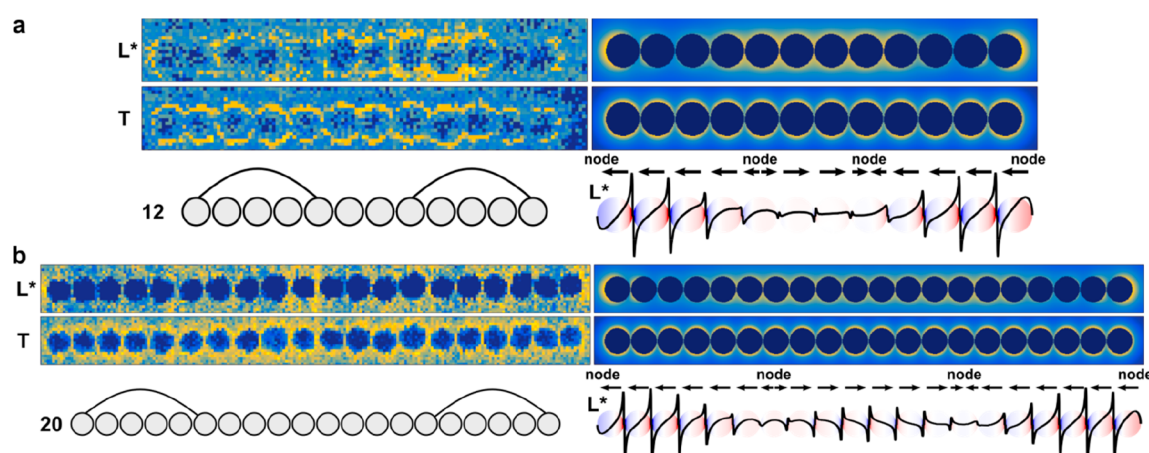

Figure 5. Particle chains beyond the infinite chain limit. Schemes, simulated surface charge plots, and maps of energy loss for all selected plasmonic modes (panels a and b show 12 and 20 particles, respectively; experimental results are shown on the left, and simulated results are shown on the right). Note the localized increase of field strength around the small kink of the chain in panel a at the ninth particle of the chain.

maps of 10 and 15 particles) because more modes occupy the same spectral region. Indeed, instead of spectrally well-separated longitudinal modes, distinguished by their node number, a broad band of surface plasmon modes emerges (denoted by L*). This L* mode is characterized by two broad nodes close to the edge and a large maximum in between. The impact of the band formation on the surface charges is summarized in Figure S6. The longest studied chain covers a distance of almost 1.5 μm, although there are much longer chains on the TEM grid (>30 particles) available. However, those particles tend to contain a certain degree of disorder, such as non-colinear alignment, distance variations, etc. These irregularities increasingly influence the mode formation by giving rise to localization effects, as was already visible in Figure 5a (see below for a more-detailed discussion of this effect).

Figure 6a summarizes the evolution of the excitation energy upon the transition from plasmonic oligomers to plasmonic polymers by plotting their peak position as a function of the chain length *j*. Significant scattering of the mode energies is observable, which is predominantly due to slight variations (disorder) of the observed chains. For instance, examining the L1 mode of the dimer, the latter consists of "kissing" spheres (Figure 2a), thus leading to an enhanced interaction and, hence, energy shift. The transversal mode is independent from the chain length within the error of the measurement. This indicates

small coupling interactions between transversal dipoles and, hence, the degeneracy of the corresponding single particle oscillations. In contrast, more longitudinal modes, separated in energy, appear with increasing chain length. Their energy decreases as the number of particles increases, approaching a lower boundary in the infinite chain limit. Eventually, the longitudinal modes energetically approach each other for plasmonic polymers and superimpose (i.e., degenerate) due to their finite lifetimes and, hence, energy widths (Figure 6b). Consequently, they cannot be discerned anymore (Figure 5), forming an effective L* mode. This degenerated L* mode is defined by its characteristic in-phase excitation at the chain ends and its characteristic superposition of multiple harmonic longitudinal modes in the central region. In the simplified sketch in Figure 6b, the transition from isolated modes to the superimposed L* mode is visualized by an oscillating wave model.

The behavior of long particle chains differs from the reported plasmonic properties of long metallic rods, which support high-order harmonics with well-distinguishable energies.[20,21] To understand the plasmonics of long nanoparticle chains, simple coupled dipole models[8,9] have been used in the past (see Downing et al.[34] for a more elaborate quantum description). Accordingly, nanoparticle chains may be approximated by an assembly of discrete individual dipoles P_i for each particle (of
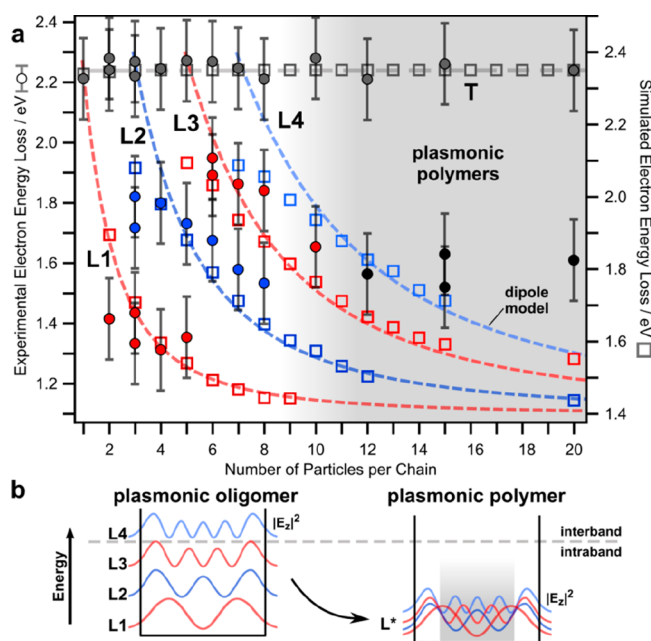
Figure 6. Study showing the transition from plasmonic oligomers to plasmonic polymers. (a) Experimental EELS (filled circles) and BEM simulated (hollow squares) energies of the various longitudinal modes as a function of particle length. Dashed lines show the results of the coupled dipole model. (b) Schematic description for the formation of the merged longitudinal plasmonic modes L* beyond the infinite chain limit.

index i). These dipoles couple with their neighbors by dipole−dipole interaction facilitated by the electric field propagator G_{ij} (see section S1 of the Supporting Information for an explicit expression of the propagator), as described by the following self-consistent polarization model:

$$P_i(\omega) = \alpha(\omega)\left(E_{ext}(\omega) + \sum_{j\neq i} G_{ij}(\omega)P_j(\omega)\right) \tag{1}$$

Here, α denotes the (isotropic) single sphere polarizability and E_{ext} the external electric field associated with, e.g., the electron beam. A plasmonic mode occurs at the poles of $(\alpha^{-1} - G)^{-1}$ (with $G \equiv \{G_{ij}\}$), which can be found by searching the zeros of $\det(1 - \alpha(\omega)G(\omega))$. However, $\alpha(\omega)G(\omega)$ is generally non-Hermitian due to retardation and loss (i.e., the complex nature of α), and α is a nonlinear function in the complex plane. Therefore, exact zeros (i.e., exact resonances) generally do not exist and maximal responses to external fields occur at the minima of the determinant in the complex plane ω, i.e., at frequencies with imaginary part accounting for the finite lifetime of the plasmon mode. The above model is a simplified version of the more general multiple elastic scattering of multipole expansions model (MESME),[35] which has been previously used to simulate SPR in nanoparticle chains.[36] Indeed, the small interparticle distance also leads to significant quadrupole and even higher-order multipole interactions. Especially, the short distance interaction between nearest neighbors is increased in comparison to the simple dipole interaction model.

Here, the simple structure of the dipole model is exploited to analytically discuss several aspects of the long chain limit, not accessible by a full-scale numerical solution of Maxwell equation. First of all, by evaluating the eigenvalue problem $\overline{G}P(\omega) = a\omega P(\omega)$ (see section S1 in the Supporting Information), eq 1 admits

analytical solutions for the mode structure in arbitrary chain lengths, if the interaction to nearest neighbors (i.e. $j = i \pm 1$) is restricted, the inverse polarizability in the considered energy loss regime (i.e. $\alpha^{-1} \approx a\omega$) is linearized, and a ω-averaged propagator (i.e., $G(\omega) \approx \overline{G}$) is used. In particular, the longitudinal mode energies are given by $\omega_l = \omega_0 - 2G_{xx}\cos\left(\frac{l\pi}{n+1}\right)$, $l\epsilon\{1, ..., n\}$, with n denoting the number of particles. The corresponding polarizations read $P_{xj,l} = \sin\left(\frac{lj\pi}{n+1}\right)$, $l\epsilon\{1, ..., n\}$, with j being the particle index. Inserting the dipole field propagator and employing a polarizability derived from the dielectric function of gold,[37] the transverse mode is, however, too high in energy at 2.5 eV, and the energy band is too narrow (0.5 eV) compared to the experiment. To obtain the band widths in reasonable agreement with the experimental results (i.e., approximately that of taking higher-order multipole interactions into account), the coupling parameters were adapted to $G_{xx} \approx 800$ THz (3.3 eV/375 nm) for the dipole aligned along the chain (see Figure 6a). An indirect proof for the existence of higher-order multipole couplings is provided by the full-scale numerical solution of Maxwell's equation, which correctly reproduced the bandwidth. The energy shift can be explained by the interaction with the carbon substrate. The latter acts as a reflecting half-plane for the electric field of the plasmon mode, introducing a second propagator (see section S1 in the Supporting Information for an explicit expression):

$$P_i(\omega) = \alpha(\omega)\left(E_{ext}(\omega) + \sum_{j\neq i} G_{ij}(\omega)P_j(\omega) + \sum_{j} G_{ij}^{ref}(\omega)P_j(\omega)\right) \tag{2}$$

Primarily, the reflected partial wave directly acts back on the emitting particle, giving rise to an additional self-interaction term $\alpha(\omega)G_{ii}^{ref}(\omega)P_i(\omega)$. This term leads to a renormalization of the polarization and, hence, to plasmon energy according to:

$$P_i(\omega) = \frac{\alpha(\omega)}{1 - \alpha(\omega)G_{ii}^{ref}(\omega)}\left(E_{ext}(\omega) + \sum_{j\neq i} G_{ij}(\omega)P_j(\omega)\right) \tag{3}$$

Numerical calculations using the dielectric function of carbon and the geometry of the gold particles show that this effect is sufficient to explain the red shift of approximately 0.2 eV (see also ref 38). In the full-scale solution of the Maxwell equations, an effective medium approach was employed to reproduce the red shift. Considering the various involved approximations, the agreement among full-scale simulations, the dipole model, and the experimental results is rather good (see Figure 6a). The remaining differences to the experimental observed energies are ascribed to long-range coupling of the reflected wave (not included in our models) and deviations from the idealized geometry in the experiment, such as fluctuations in distance, shape, alignment, surface, etc. The latter can be subsumed under disorder effects. While the accurate description of disorder effects requires elaborate perturbation and renormalization schemes (for example, see ref 39 for a treatment within the self-consistent theory of Anderson localization), it is has been established that disorder in 1D systems always tends to localize the wave field with a characteristic exponential damping $|E| \approx \exp(|x - x_0|/\xi(\eta))$ depending on the disorder strength η.[40] Upon close inspection of the investigated long chains, indeed, the localized excitations are close to geometric perturbations of

the chain (e.g., close to the kink in Figure 5a); however, a larger sample base would be required to further elaborate this effect.

Next, the infinite chain limit is discussed using the discrete dipole model. The dipole coupling model describes analytically the formation of a continuous band of longitudinal modes with a dispersion relation (wave vector q) $\omega(q) = \omega_0 - 2G_{xx}\cos qd$ in the infinite chain limit (d denotes the interparticle distance). However, due to the finite energy resolution and the finite lifetime (energy width) of the plasmon modes, only a supposition of harmonics can be excited (L* mode). Thus, the highest group velocity $v_{max} = [\partial\omega/\partial q]_{max} \approx 0.4\ c$ is reached around $q = 2\pi/4d$, which corresponds to longitudinal plasmon modes close to the energy of the (nondispersive) transverse mode. The group velocities decrease toward the longer wavelengths (and, therefore, lower excitation energies). Consequently, the group velocity and hence, the transport in the transversal mode is almost zero as the coupling $G_{yy,zz}$ between the transverse dipoles is very small. Finally, the analytical expressions for the net dipole moment are $p_x(q) = \frac{1}{qd}(1 - \cos qL)$ of the q-dependent modes (chain length of L), which is a measure for the optical coupling strength of individual modes (e.g., optically dark modes have a net moment zero). Accordingly, dark modes appear whenever $q = 2\pi n/L$, and the largest net dipole moment is realized in the long wavelength limit $q \to 0$. Furthermore, from the analytical band dispersion, the plasmonic density of states can be computed according to

$$\text{DOS}(\omega) = 2\frac{dq(\omega)}{d\omega} = \left(G_{xx}d\sqrt{1 - \left(\frac{\omega - \omega_0}{2G_{xx}}\right)^2}\right)^{-1}$$

which also grows toward smaller excitation energies (more generally toward the band edge, which coincides the band minimum in this case). Consequently, we may conclude that the optical coupling ($\sim p \times \text{DOS}$) is maximal for lower excitation energies, where it is eventually bounded by increasing losses.

Thus, treating more complicated chains (e.g., with multipartite basis) including beyond-nearest neighbor interactions requires numerical schemes. However, for periodic arrangements such as the long chain, the use of Bloch's theorem greatly facilitates their implementation (see section S1 in the Supporting Information). In that case, eq 1 reads as;

$$c_{a\mu}(q, \omega) = \sum_{b\nu} D_{a\mu}^{b\nu}(q, \omega)c_{b\nu}(q, \omega) \tag{4}$$

with $c_{a\mu}$ (nanoparticle index in unit cell a and Cartesian index μ) denoting the excitation coefficients of the Bloch waves $P_{a\mu} = c_{a\mu}(q,\omega)e^{iqxn}$ and $D_{a\mu}^{b\nu}$ a dynamical coupling matrix. This formulation has been recently used to compute topological effects in Su−Schrieffer−Heeger model chains.[41]

To highlight the substantial importance of the degenerated L* mode in the plasmonics of linear particle chains, its impact on energy transport along such chains is briefly studied in the following. These considerations will also shine light on an important consequence of the non-Hermiticity (i.e., lossy) nature of the plasmonic system by providing a characteristic length scale for the coherent coupling of the plasmonic modes. Plasmonic waveguiding is chosen because it is typically described as one of the most promising applications for linear particle chains.[11,18,42] Furthermore, the effect is dominated by near-field effects. As it has been suggested earlier, the previously

observed degenerated modes have suppressed radiative losses, which may be further tuned by higher multipole order near field coupling terms (beyond dipole).[8,43−45] Finite-difference time-domain (FDTD) electromagnetic modeling were employed to quantify the energy transport properties (Figure 7).
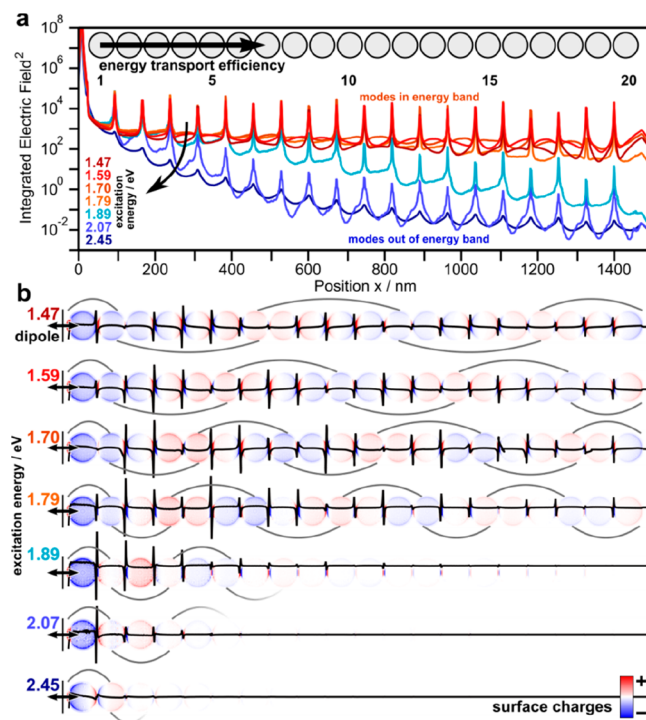

Figure 7. Energy-transport properties of plasmonic polymers (consisting of 20 nanoparticles). (a) Integrated electric field along the particle chain in respect to various dipole energies. (b) Corresponding integrated surface charge images (red−blue color scale) and surface charge waves (black line).

As a simplified waveguiding experiment, a dipole source at one end of the particle chain is used as source. Figure 7a visualizes the energy transport efficiency along the chain for all excitable modes by the integrated electric field (red indicating within and blue indicating out of the energy band).

The energetically highest mode (transversal, 2.42 eV, dark blue) exhibits a double exponential decay resulting in a theoretical damping factor of −1.83 dB/50 nm. Longitudinal waveguiding modes above 1.8 eV (i.e., not yet merged with the energy band) perform similar to a fast decay of the transported energy (blue; for the spectral overlap of the individual longitudinal modes, see Figure S8b). On the contrary, degenerated modes overlapping with the energy band support efficient waveguiding with damping factors as low as −0.26 dB/50 nm (for an excitation energy of 1.59 eV). For very small energies, however, the damping factor increases again. This behavior is consistent with previous studies[8] and can be explained by an optimal balance of group velocity (increasing toward higher energies) and radiative losses (decreasing toward high energies) in the sub-radiant level above the super-radiant L1. In comparison to a comparable DNA-assembled waveguide, which is below the infinite chain limit, the herein observed damping is lower by a factor of 3.[18]

Table 1 lists the properties of the supported waveguiding modes as well as the integrated electric fields E^2 at the first and last particle for each mode (necessary to calculate the damping

Table 1. Plasmonic Waveguide Properties of Different Plasmonic Modes (Transverse Mode: 2.42 eV and Longitudinal Modes: >2.42 eV; Effective Mode Size Describes the Radial Drop of the Integrated E^2 perpendicular to the Particle Chains to $1/e^2$)

excitation energy, eV	2.42	2.07	1.89	1.79	1.70	1.59	1.47
integrated E_0^2 ($x_0 = 0$ nm)	1071	1513	1925	1758	1679	1519	1171
integrated E_N^2 ($x_N = 1380$ nm)	<0.01	<0.01	0.06	28	218	284	114
damping in decibels per 1380 nm	−50.4	−56.2	−45.0	−17.9	−8.8	−7.2	−10.1
damping in decibels per 50 nm	−1.83	−2.04	−1.63	−0.65	−0.32	−0.26	−0.37
effective mode energy, eV	8.86	4.43	4.13	2.82	2.58	2.07	1.70
effective mode size, nm	137	141	145	173	198	229	261

factor). The induced surface charge waves (Figure 7b) propagate with an effective energy along the particle chain, as visualized by the respective length of the wave package. The energy propagation for a selected mode (1.59 eV) is highlighted in Video S1. Finally, the mode size perpendicular to the particle chains (energy E^2 at $1/e^2$ of the cross-section) is critical for practical applications to avoid cross-talk between neighboring waveguides. The mode size for degenerated modes is below 300 nm, while for the non-degenerated modes, it is 140 nm. However, in the real system, disorder effects produce an additional localization (see the discussion above), which may further increase the damping factor.

In summary, we directly observed the formation of hybridized plasmonic modes on linear nanoparticle chains as a function of the chain length ranging from one nanoparticle to the infinite chain limit. Plasmonic oligomers and polymers have been fabricated by template-assisted colloidal self-assembly yielding highly ordered chains with low disorder. Electron energy-loss spectroscopy and theoretical modeling allowed us to characterize the plasmonic mode transition between short chains (plasmonic oligomers) and long chains (plasmonic polymers). Plasmonic oligomers show well-separated, non-degenerated longitudinal modes and degenerated transverse modes. Beyond roughly 10 particles, a band of longitudinal modes eventually emerges. This band exhibits a degenerated plasmonic waveguide mode signature with a large dispersion, which makes it suitable for long distance energy transport in the optimal band region. Theoretical simulations of the waveguiding performance suggest that the L* mode with a mode wavelength of 730 nm is able to transport energy with a damping of −0.26 dB/50 nm at a mode cross-section size of 260 nm. Our findings pave the way for further exploitation of plasmonic nanoparticle chains as waveguides and photonic devices. For example, the waveguide mode can be intervened at each contact point by inserting materials such as fluorescent emitters[46] and organic[47] or smart polymers[48] to further modulate and enhance the radiative properties of the plasmonic waveguide.[49] Of particular interest is the coupling at end points of the chain, which sustain particular edge states that may be tuned by complex chain geometries (e.g., bipartite chains). Furthermore, the presented approach opens up new possibilities to study combinatorically the plasmonics of multimetallic chains or chains with multiply particle morphologies within one chain.

Methods. *Synthesis, Template-Assisted Colloidal Self-Assembly, and Wet Transfer to Carbon-Coated TEM Grids.* The synthesis of single-crystalline spherical gold nanoparticles with a diameter of 70.5 ± 1.2 nm was accomplished by a three-step seed-mediated growth approach and template-assisted self-assembly into wrinkled PDMS templates via spin-coating of protein (BSA) coated particle solutions (12 mg/mL [Au^0]) as published elsewhere.[31] The pH of the nanoparticle solution was

adjusted to pH 10 to produce closely packed particle lines in incompletely filled templates.

Transfer in the grooves of the template assembled particle chains was performed by wet-contact printing. The 3 nm carbon-film coated TEM grid (copper, 300 square meshes) was incubated in PEI solution (1 mg/mL, 1800 g/mol, linear) for 1 h and subsequently washed with purified water (Milli-Q-grade, 18.2 MΩ cm at 25 °C). For the transfer, a 2 μL water droplet (pH 10) was placed on the TEM grid, the particle-filled PDMS stamp was pressed onto the grid with a constant pressure of 100 kPa, and the grid was left to dry under environmental conditions (23 °C, 55% relative humidity). After drying (4 h), the stamp was carefully removed, leaving the nanoparticle chains on the carbon film of the grid.

STEM EELS Characterization. STEM scanning and EELS spectrum-imaging was performed in the probe-corrected Titan^3 operating at 300 kV. The microscope was equipped with a Tridiem energy filter and a Wien monochromator operating in the accelerating mode, which ensured the energy resolution of 100−120 meV. EELS was performed under the convergence angle of 22 mrad and the collection angle of 8 mrad with the energy dispersion of 0.01 eV per channel. The spectrum images were acquired with a beam current 200 pA and dwell time 25 ms. For each chain of gold particles, 4−7 runs of spectrum-imaging were performed followed by the summation of the data cubes with accounting for the spatial drift between runs. The obtained spectra were corrected for the energy instabilities, and the zero-loss peak was then removed by using the reference profile collected in a separate run without any sample object. An example of spectra treatment is shown in Figure S3. Finally, the distinct peaks in the low-loss region of spectra were recognized and their energy positions and magnitude were fitted using the nonlinear least-squares procedure. The integrated area under each fitted peak was plotted as a function of the beam position giving rise to maps of the probability for plasmon excitation, i.e., maps of energy-loss.

Electromagnetic Simulations. Simulations of electron energy loss spectra and mappings were performed using the Matlab MNPBEM13 toolbox,[50] which is based on the boundary element method (BEM) by García de Abajo.[51] Each sphere of the chain was approximated by triangulation (400 vertices per particle). The dimensions and positions of the gold nanospheres were selected according to the experimental size (70.5 ± 1.2 nm) and spaced with a distance of 1.5 nm. The dielectric properties of gold were taken from Johnson and Christy.[37] An effective medium of $n = 1.2$ is selected to emulate the air−substrate interface. The energy of the simulated electron beam was set to the experimental accelerating voltage of the TEM (300 kV). For each particle chain several spectra were evaluated in the energy range from 1−3 eV at different (not overlapping) electron-beam positions to ensure excitation of all possible plasmonic modes EELS mappings were performed at selected

energy levels and were simulated by 1.5 nm meshing of the electron beam. The respective spectra are summarized in Figure S7.

For energy-transfer and waveguiding simulations, a commercial-grade simulator based on the finite-difference time-domain (FDTD) method was used to perform the calculations (Lumerical Inc., Canada, version 8.16).[52] For the broadband and single-mode excitation for energy transport, a dipole source for the specific wavelength range (short pulse length of 3 fs; $E \approx$ 1−4 eV; $\lambda = 300-1300$ nm; see spectra in Figure S8a) and single wavelength to probe individual modes (long pulse length of 18 fs) was used with a distance of 15 nm to the first particle, respectively. To extract the exact peak positions from the spectra, the internal multipeak-fitting function of IGOR Pro 7 (WaveMetrics) was used. The mode size of the modes was defined by integrating of E^2 along the particle line and radially defining the $1/e^2$ decay of the E^2 field. For the FDTD simulations, the same refractive index data, nanoparticle dimension, inter particle distance, and materials constants were used as in the BEM simulations. Perfectly matched layers in all principal directions as boundary conditions, zero-conformal-variant mesh refinement, and an isotropic mesh overwrite region of 1 nm were used. All simulations reached the auto shut-off level of 10^{-5} before reaching 150 fs of simulation time.

■ ASSOCIATED CONTENT

Ⓢ Supporting Information

The Supporting Information is available free of charge on the ACS Publications website at DOI: 10.1021/acs.nano-lett.9b01031.

> Additional simulations, additional EELS maps, experimental EELS spectra including data treatment, and a detailed description of the discrete dipole model (PDF)
> A movie showing the electric field during energy propagation along a particle chain (MPG)

■ AUTHOR INFORMATION

Corresponding Authors
*E-mail: a.lubk@ifw-dresden.de.
*E-mail: koenig@ipfdd.de.
*E-mail: fery@ipfdd.de.

ORCID Ⓘ
Martin Mayer: 0000-0003-4013-1892
Tobias A. F. König: 0000-0002-8852-8752
Andreas Fery: 0000-0001-6692-3762

Notes
The authors declare no competing financial interest.

■ ACKNOWLEDGMENTS

■ REFERENCES

(1) Willets, K. A.; Van Duyne, R. P. *Annu. Rev. Phys. Chem.* **2007**, *58*, 267−297.
(2) Khurgin, J. B. *Nat. Nanotechnol.* **2015**, *10*, 2−6.
(3) Mayer, K. M.; Hafner, J. H. *Chem. Rev.* **2011**, *111*, 3828−3857.
(4) Rycenga, M.; Cobley, C. M.; Zeng, J.; Li, W.; Moran, C. H.; Zhang, Q.; Qin, D.; Xia, Y. *Chem. Rev.* **2011**, *111*, 3669−3712.
(5) Brongersma, M. L.; Hartman, J. W.; Atwater, H. A. *Phys. Rev. B: Condens. Matter Mater. Phys.* **2000**, *62*, R16356−R16359.
(6) Krenn, J. R. *Nat. Mater.* **2003**, *2*, 210−211.
(7) Vetrone, F.; Rosei, F. *Science* **2017**, *357*, 452−453.
(8) Willingham, B.; Link, S. *Opt. Express* **2011**, *19*, 6450.
(9) Gómez, D. E.; Hwang, Y.; Lin, J.; Davis, T. J.; Roberts, A. *ACS Photonics* **2017**, *4*, 1607−1614.
(10) Khurgin, J. B. *Nat. Nanotechnol.* **2015**, *10*, 2.
(11) Roller, E.-M.; Besteiro, L. V.; Pupp, C.; Khorashad, L. K.; Govorov, A. O.; Liedl, T. *Nat. Phys.* **2017**, *13*, 761−765.
(12) Tan, S. J.; Campolongo, M. J.; Luo, D.; Cheng, W. *Nat. Nanotechnol.* **2011**, *6*, 268−276.
(13) Klinkova, A.; Choueiri, R. M.; Kumacheva, E. *Chem. Soc. Rev.* **2014**, *43*, 3976.
(14) Solis, D.; Paul, A.; Olson, J.; Slaughter, L. S.; Swanglap, P.; Chang, W.-S.; Link, S. *Nano Lett.* **2013**, *13*, 4779−4784.
(15) Barrow, S. J.; Funston, A. M.; Gómez, D. E.; Davis, T. J.; Mulvaney, P. *Nano Lett.* **2011**, *11*, 4180−4187.
(16) Slaughter, L. S.; Wang, L.-Y.; Willingham, B. A.; Olson, J. M.; Swanglap, P.; Dominguez-Medina, S.; Link, S. *Nanoscale* **2014**, *6*, 11451−11461.
(17) Maier, S. A.; Kik, P. G.; Atwater, H. A. *Appl. Phys. Lett.* **2002**, *81*, 1714−1716.
(18) Gür, F. N.; McPolin, C. P. T.; Raza, S.; Mayer, M.; Roth, D. J.; Steiner, A. M.; Löffler, M.; Fery, A.; Brongersma, M. L.; Zayats, A. V.; König, T. A. F.; Schmidt, T. L. *Nano Lett.* **2018**, *18*, 7323−7329.
(19) Nicoletti, O.; de la Peña, F.; Leary, R. K.; Holland, D. J.; Ducati, C.; Midgley, P. A. *Nature* **2013**, *502*, 80.
(20) Collins, S. M.; Nicoletti, O.; Rossouw, D.; Ostasevicius, T.; Midgley, P. A. *Phys. Rev. B: Condens. Matter Mater. Phys.* **2014**, *90*, 155419.
(21) Rossouw, D.; Couillard, M.; Vickery, J.; Kumacheva, E.; Botton, G. A. *Nano Lett.* **2011**, *11*, 1499−504.
(22) Schaffer, B.; Riegler, K.; Kothleitner, G.; Grogger, W.; Hofer, F. *Micron* **2009**, *40*, 269−273.
(23) Barrow, S. J.; Collins, S. M.; Rossouw, D.; Funston, A. M.; Botton, G. A.; Midgley, P. A.; Mulvaney, P. *ACS Nano* **2016**, *10*, 8552−8563.
(24) Barrow, S. J.; Rossouw, D.; Funston, A. M.; Botton, G. A.; Mulvaney, P. *Nano Lett.* **2014**, *14*, 3799−3808.
(25) Mayer, M.; Steiner, A. M.; Röder, F.; Formanek, P.; König, T. A. F.; Fery, A. *Angew. Chem., Int. Ed.* **2017**, *56*, 15866−15870.
(26) Hanske, C.; Tebbe, M.; Kuttner, C.; Bieber, V.; Tsukruk, V. V.; Chanana, M.; Konig, T. A. F.; Fery, A. *Nano Lett.* **2014**, *14*, 6863−6871.
(27) Krehl, J.; Guzzinati, G.; Schultz, J.; Potapov, P.; Pohl, D.; Martin, J.; Verbeeck, J.; Fery, A.; Büchner, B.; Lubk, A. *Nat. Commun.* **2018**, *9*, 9.
(28) Tebbe, M.; Mayer, M.; Glatz, B. A.; Hanske, C.; Probst, P. T.; Müller, M. B.; Karg, M.; Chanana, M.; König, T. A. F.; Kuttner, C.; Fery, A. *Faraday Discuss.* **2015**, *181*, 243−260.
(29) Mayer, M.; Tebbe, M.; Kuttner, C.; Schnepf, M. J.; König, T. A. F.; Fery, A. *Faraday Discuss.* **2016**, *191*, 159−176.
(30) Zheng, Y.; Zhong, X.; Li, Z.; Xia, Y. *Part. Part. Syst. Char.* **2014**, *31*, 266−273.
(31) Steiner, A. M.; Mayer, M.; Seuss, M.; Nikolov, S.; Harris, K. D.; Alexeev, A.; Kuttner, C.; Konig, T. A. F.; Fery, A. *ACS Nano* **2017**, *11*, 8871−8880.
(32) Nordlander, P.; Oubre, C.; Prodan, E.; Li, K.; Stockman, M. I. *Nano Lett.* **2004**, *4*, 899−903.
(33) Mayer, M.; Scarabelli, L.; March, K.; Altantzis, T.; Tebbe, M.; Kociak, M.; Bals, S.; García de Abajo, F. J.; Fery, A.; Liz-Marzán, L. M. *Nano Lett.* **2015**, *15*, 5427−5437.
(34) Downing, C. A.; Weick, G. *Phys. Rev. B: Condens. Matter Mater. Phys.* **2017**, *95*, 125426.
(35) García de Abajo, F. J. *Phys. Rev. Lett.* **1999**, *82*, 2776−2779.
(36) Cai, W.; Sainidou, R.; Xu, J.; Polman, A.; García de Abajo, F. J. *Nano Lett.* **2009**, *9*, 1176−1181.

(37) Johnson, P. B.; Christy, R. W. *Phys. Rev. B* **1972**, *6*, 4370−4379.

(38) Waxenegger, J.; Trügler, A.; Hohenester, U. *Comput. Phys. Commun.* **2015**, *193*, 138−150.

(39) Lubatsch, A.; Kroha, J.; Busch, K. *Phys. Rev. B: Condens. Matter Mater. Phys.* **2005**, *71*, 184201.

(40) Mott, N. F.; Twose, W. D. *Adv. Phys.* **1961**, *10*, 107−163.

(41) Pocock, S. R.; Xiao, X.; Huidobro, P. A.; Giannini, V. *ACS Photonics* **2018**, *5*, 2271−2279.

(42) Lal, S.; Link, S.; Halas, N. J. *Nat. Photonics* **2007**, *1*, 641.

(43) Choquette, J. J.; Marzlin, K.-P.; Sanders, B. C. *Phys. Rev. A: At., Mol., Opt. Phys.* **2010**, *82*, 82.

(44) Stockman, M. I.; Faleev, S. V.; Bergman, D. J. *Phys. Rev. Lett.* **2001**, *87*, 87.

(45) Ropers, C.; Park, D. J.; Stibenz, G.; Steinmeyer, G.; Kim, J.; Kim, D. S.; Lienau, C. *Phys. Rev. Lett.* **2005**, *94*, 94.

(46) Schnepf, M. J.; Brasse, Y.; Goßler, F. R.; Steiner, A. M.; Obermeier, J.; Lippitz, M.; Fery, A.; König, T. A. F. *Z. Phys. Chem.* **2018**, *232*, 1593−1606.

(47) Stelling, C.; Singh, C. R.; Karg, M.; König, T. A. F.; Thelakkat, M.; Retsch, M. *Sci. Rep.* **2017**, *7*, 7.

(48) Volk, K.; Fitzgerald, J. P. S.; Ruckdeschel, P.; Retsch, M.; König, T. A. F.; Karg, M. *Adv. Opt. Mater.* **2017**, *5*, 1600971.

(49) Mayer, M.; Schnepf, M. J.; König, T. A. F.; Fery, A. *Adv. Opt. Mater.* **2019**, *7*, 1800564.

(50) Hohenester, U.; Trügler, A. *Comput. Phys. Commun.* **2012**, *183*, 370−381.

(51) García de Abajo, F. J.; Aizpurua, J. *Phys. Rev. B: Condens. Matter Mater. Phys.* **1997**, *56*, 15873−15884.

(52) Lumerical Inc. Lumerical hompage. https://www.lumerical.com/products/fdtd/ (accessed January, 2019).

6   Colloidal lattice

6.1   Hybridized guided-node resonances via colloidal plasmonic self-assembled grating

Hybridized Guided-Mode Resonances via Colloidal Plasmonic Self-Assembled Grating

Swagato Sarkar, Vaibhav Gupta, Mohit Kumar, Jonas Schubert, Patrick T Probst, Joby Joseph and **Tobias A.F. König***

*corresponding author

Author contribution statement

SS, VG and MK carried out the experiments. **TK** encouraged SS, VG, MK and PP to investigate the simulation, fabrication and optical spectroscopy methods as well as supervised the execution and findings of this work. JS and PP contributed through their synthesis and self-assembly methods. JJ and **TK** made a significant contribution to the conception and design of the work. Through the simulation, fabrication and optical spectroscopy methods, the author **TK** made a significant contribution to the acquisition, analysis and interpretation of the data. All authors provided critical feedback and helped shape the research, analysis and manuscript.

Hybridized Guided-Mode Resonances via Colloidal Plasmonic Self-Assembled Grating

Swagato Sarkar,[†,‡] Vaibhav Gupta,[†] Mohit Kumar,[†,‡] Jonas Schubert,[†] Patrick T. Probst,[†] Joby Joseph,[‡] and Tobias A.F. König*,[†,§]

[†]Institute for Physical Chemistry and Polymer Physics, Leibniz-Institut für Polymerforschung Dresden e.V. (IPF), Hohe Str. 6, 01069 Dresden, Germany

[‡]Photonics Research Lab, Department of Physics, Indian Institute of Technology Delhi, 110016 New Delhi, India

[§]Cluster of Excellence Center for Advancing Electronics Dresden (cfaed), Technische Universität Dresden, 01062 Dresden, Germany

Ⓢ *Supporting Information*

ABSTRACT: For many photonic applications, it is important to confine light of a specific wavelength at a certain volume of interest at low losses. So far, it is only possible to use the polarized light perpendicular to the solid grid lines to excite waveguide—plasmon polaritons in a waveguide-supported hybrid structure. In our work, we use a plasmonic grating fabricated by colloidal self-assembly and an ultrathin injection layer to guide the resonant modes selectively. We use gold nanoparticles self-assembled in a linear template on a titanium dioxide (TiO₂) layer to study the dispersion relation with conventional ultraviolet—visible—near-infrared spectroscopic methods. Supported with finite-difference in time-domain simulations, we identify the optical band gaps as hybridized modes: plasmonic and photonic resonances. Compared to metallic grids, the observation range of hybridized guided modes can now be extended to modes along the nanoparticle chain lines. With future applications in energy conversion and optical filters employing these cost-efficient and upscalable directed self-assembly methods, we discuss also the application in refractive index sensing of the particle-based hybridized guided modes.

KEYWORDS: guided-mode resonance, localized surface plasmon resonance, template-assisted colloidal self-assembly, grating, plasmonic hybridization
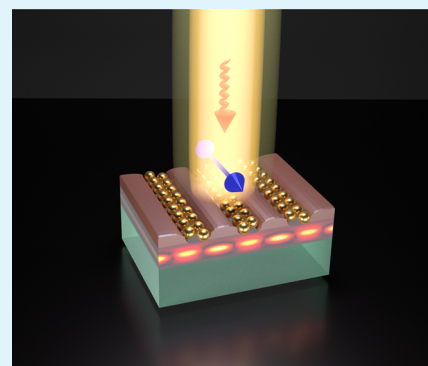
INTRODUCTION

Optical antennas are the key to confine light energy into a target structure and vice versa.[1] Plasmonic nanoparticles (NPs), in particular, are suitable for collecting light energy into a nanometer-sized volume via oscillation of the free electrons at the particle surface (localized surface plasmon resonance, LSPR) and converting the energy into a current, that is, light harvesting.[2] Thus, efficient light concentration and hot carrier extraction have led to diverse applications such as photocatalysis,[3] photovoltaics,[4] and photodetection.[5] Plasmonic NP chains are of special interest as they can excite modes with suppressed radiative losses.[6,7] When a chain is formed from individual NPs, the excited plasmon mode for incident polarization along the chain direction shifts to a lower energy (super-radiant mode) until a certain group velocity of the collective plasmon mode is reached.[8] This collective plasmon mode along with all higher energy modes can be imagined analogously to a mechanical string vibration model or nondegenerated modes as in quantum mechanics. In theory of plasmonic chains, these energetic higher modes (subradiant) have lower propagation losses than the super-radiant mode.[9] Recent research topics have focused on the study of these subradiant modes for possible applications in optical sensing,[10] subdiffraction energy transport,[11,12] and plasmonic NP gratings.[13]

However, these NP chain-based plasmonic grating resonant (PGR) modes still have radiative damping, and their resonance wavelength varies greatly because of size and particle spacing.[13] By incorporating thin-film layers, plasmon modes can be extracted by phase-matching conditions and guided within these layers following the properties of a grating waveguide-based guided-mode resonant[14,15] (GMR) structure. Such waveguide—plasmon polaritons have been intensively studied and can be used to investigate strong coupling,[16−18] to demonstrate light generation,[19] and to show filter properties with high optical transmission.[20] All these properties benefit from the hybridized coupling (Fano resonance) of a narrow (waveguide mode) and a broad (plasmonic mode) oscillation.[21] In most of the cases, these hybrid structures are fabricated using an electron beam and contact lithography

followed by physical vapor deposition, sol−gel approach, and a chemical etching step which results in a limited array of polycrystalline NPs that suffer from increased damping. Recent developments in directed self-assembly can solve this bottleneck to realize large-scale assembly of monocrystalline NPs at a reasonable price.[22] In particular, the combination of rapid top-down laser interference lithography (LIL) template and bottom-up template-assisted self-assembly (TASA) methods allow the freedom to assemble NPs in various two-dimensional structures.[23] Consequently, development in self-assembly makes it possible to access the plasmon modes along the NP line selectively. Generally, the NP-based pure plasmonic resonance mechanisms are extremely responsive to the change in the surrounding media and thus have significantly contributed toward the fabrication of highly sensitive refractive index[24] (RI) as well as biological sensors.[25,26] As broader PGR (super- and subradiant) modes with a larger full width at half-maximum (fwhm) have a higher radiative loss, Q-factor (inversely proportional to fwhm) remains significantly low for their application in the field of sensing. By coupling the plasmonic features to the high "Q" photonic modes (with smaller fwhm) of a dielectric GMR structure, one can increase the sensitivity of the so-obtained hybridized photonic modes as compared to the pure photonic (GMR) case while maintaining the sharpness and "quality".

In this work, we have applied plasmonic grating, that is, the NP lines (fabricated by LIL and TASA) directly to the waveguide (TiO$_2$ layer) to save the process steps in constructing the hybridized geometry. A previous work from our group has demonstrated plasmonic studies of NP lines formed by template-assisted colloidal self-assembly, followed by a printing transfer to the target substrate.[13] Here, we save ourselves from the transfer step by assembling the particles directly into the GMR structure. However, this step is not trivial as the surface chemistry of the particles and the substrate required for an efficient assembly now had to be adjusted to the LIL-fabricated GMR structure. Moreover, this effective fabrication step was not possible in the previous work as those substrates were made by mechanical instability (wrinkling) followed by assembly through spin-coating. For the current work, we have used LIL and convective self-assembly toward the fabrication of the hybrid optoplasmonic structures which till now are limited by "e-beam" fabrication techniques.[16,17] The grating period and waveguide thickness are chosen accordingly to obtain a phase match to favor coupling between the GMR and PGR modes. Experimental and theoretical spectroscopic methods with polarizations both parallel and perpendicular to the chain direction are used to study the plasmonic NP−waveguide polaritons on the centimeter scale. With this simple, cost-efficient, and upscalable fabrication method, we are able to discuss the complete hybrid nature of the resulting modes and show their application as opto-plasmonic RI sensors.[27]

EXPERIMENTAL SECTION

Fabrication of Dielectric GMR Structure. TiO$_2$ films are deposited on glass substrates (2.5 × 2.5 cm^2) using electron beam evaporation (LAB 500 evaporator, Leybold Optics GmbH) at a rate of 2 Å/s up to a layer thickness of 200 nm. They are divided into individual smaller pieces and spin-coated with the negative photoresist ma-N 405 diluted with ma-T 1050 (MicroChem) in a 1:1 ratio. Optimized spin parameters of 6000 rpm, acceleration of 2000 rpm/s, and a total spin time of 33 s produced a thin film of 150 nm thickness, as confirmed by spectroscopic ellipsometry (RC2-DI, J.A. Woollam

Co., Inc.). The coated substrates are further exposed to LIL to obtain a photoresist grating.

Gold Particle Synthesis. Spherical gold NPs with 88 ± 12 nm diameter are synthesized via a colloidal seeded growth process according to the procedure of Bastús et al.[28] Citrate-stabilized NPs are coated with bovine serum albumin (BSA) prepared according to already published methods.[29] Briefly, 40 mL of the NP solution is added to 4 mL of 1 mg/mL BSA solution with 1 wt % sodium citrate at pH 9. The solution is allowed to incubate overnight. After fourfold centrifugation, the NPs are analyzed with UV−vis spectroscopy and transmission electron microscopy. The NP size of 88 nm is determined by a statistical analysis of 50 particles.

Directed Self-Assembly. The fabricated dielectric GMR sample is UV flood-exposed (UV-15 S/L, Herolab) at 254 nm for 10 min and subsequently hard-baked at 120 °C for 4 min on a hot plate to reduce the swelling and leaching out of the photoresist while in contact with the slightly alkaline particle solution. Oxygen plasma treatment (30 s, 0.2 mbar, 80 W, Flecto 10, Plasma Technology) *prior* to the convective assembly experiment[30] creates good wettability of the substrate that is fixed to a motorized translation stage (PLS-85, Physik Instrumente). A cleaned glass slide (Menzel) is mounted above the GMR sample at a distance of 0.5 mm, and 25 μL of NP solution (0.5 mg/mL gold, pH 9) is placed in between the gap. The elevated pH value ensures a strong negative surface charge of the protein coating (−30 mV)[29] to provide electrostatic stabilization of the colloidal suspension. A constant linear motion at the rate of 1 μm/s is imparted to the stage through a computerized software system to recede the contact line in a direction parallel to the channels. The stage temperature is set to 14 K above dew point to control the evaporation rate at the meniscus that drives the transport of NPs toward the three-phase contact line. Lateral confinement by the channel geometry and a vertical one determined by the thickness of the liquid film inside the channels enables the selective crystallization of particles into double (dimer) lines together with the help of attractive capillary forces that arise during drying.

UV−Vis−NIR Spectroscopy. An ultraviolet−visible−near-infra-red (UV−vis−NIR) spectrophotometer (Cary 5000, Agilent Technologies) in transmission geometry is used for recording optical responses corresponding to a broad range of 400−2400 nm. A rotatable polarizer is used to investigate the effect of both polarizations, s-pol (transverse electric, TE) and p-pol (transverse magnetic, TM), where the electric fields are out-of-plane and in-plane to the plane of incidence, respectively.

Finite-Difference in Time-Domain Simulations. A commercial-grade simulator based on the finite-difference in time-domain (FDTD) method is used to perform the calculations (Lumerical FDTD,[31] version 8.16). For the simulation of the optical response, a plane wave source is used and the frequency points are set equal to that of the wavelength span. Monitor boxes (transmission monitors kept normal to the substrate) are used to obtain the optical responses of the systems. For the dielectric properties of gold, data from Palik[32] are fitted using six coefficients with a root-mean-square error of 0.2. For the photoresist, TiO$_2$ layer, and glass substrate, the optical constants are fitted by using the experimentally obtained values through spectroscopic ellipsometry that are available in Supporting Information T1 (see Figure S1). The mesh size in the FDTD region is set to auto-nonuniform with a minimum mesh size of 0.25 nm and an additional mesh overlay of 2 nm applied over the arranged particle geometry. Periodic boundary conditions are applied for X and Z directions with perfectly matching layers along the Y direction.

RI Sensing. Deuterium oxide of 99.9% purity (D$_2$O), commonly known as heavy water, is used as an initial surrounding medium which is altered with a solution (0.3 g/mL) of sodium chloride (NaCl) in D$_2$O to slightly increase RI and observe the characteristic spectral change. The RI of pure water and salt solution are initially measured using a digital multiple wavelength refractometer DSR-L (Schmidt + Haensch) and used for the calculation of the sensitivity of different resonant geometries.
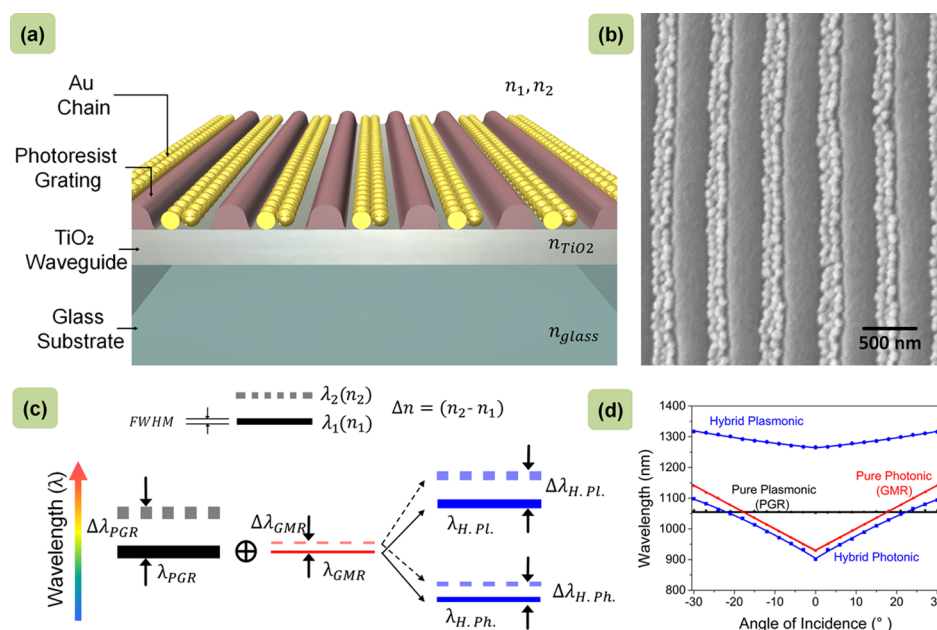
Figure 1. Concept and optical properties of plasmonic self-assembled GMR structure. (a) Plasmonic NP grating self-assembled inside a photoresist template on a TiO_2 waveguide. (b) SEM image of the plasmonic NP grating showing gold NPs within the photoresist grating channels. (c) Schematic illustrating the formation of two hybridized states: plasmonic (H. Pl.) and photonic (H. Ph.) along with the effect of RI variation (n_1 to n_2). The sensitivity ($S = \Delta\lambda/\Delta n$) and FOM (= S/fwhm) can be obtained from the distance between the solid and dashed lines ($\Delta\lambda$) and line thickness (fwhm), respectively. (d) Dispersion relation for pure photonic (guided-mode resonance), pure plasmonic (plasmonic grating resonance), and their hybridized modes obtained experimentally in air through an AOI scan with polarization along particle chains.
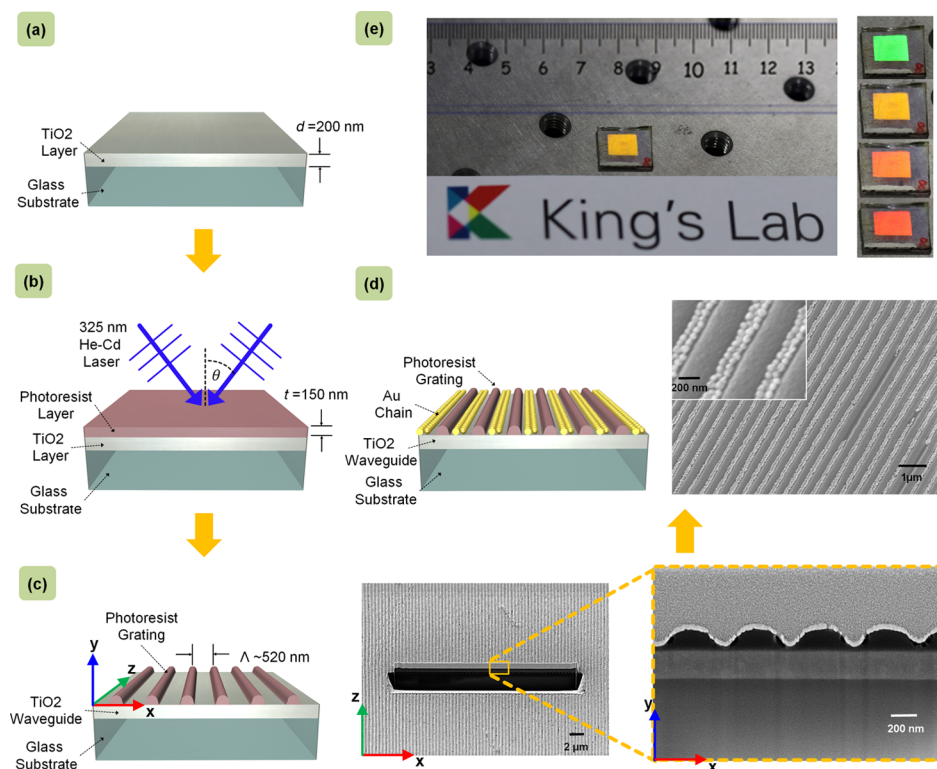

Figure 2. Fabrication of the hybrid optoplasmonic structure: (a) deposition of 200 nm TiO_2 layer onto the glass substrate by electron beam physical vapor deposition. (b) Spin-coating of negative photoresist and LIL using a He−Cd laser. (c) Formation of a GMR structure with a 520 nm periodic photoresist grating. Focused ion beam (FIB) cut reveals grating channels in a magnified view. (d) Directed self-assembly of gold NPs (88 nm in diameter) by the controlled evaporation of particle dispersion (convective self-assembly). An SEM image of the final structure with a magnified view in the inset shows dimer particle chain arrangement within grating channels. (e) Photograph of the fabricated sample on an optical table. Different first-order diffracted wavelengths (colors) at various AOIs appear on reflections from ordinary white room-light source.
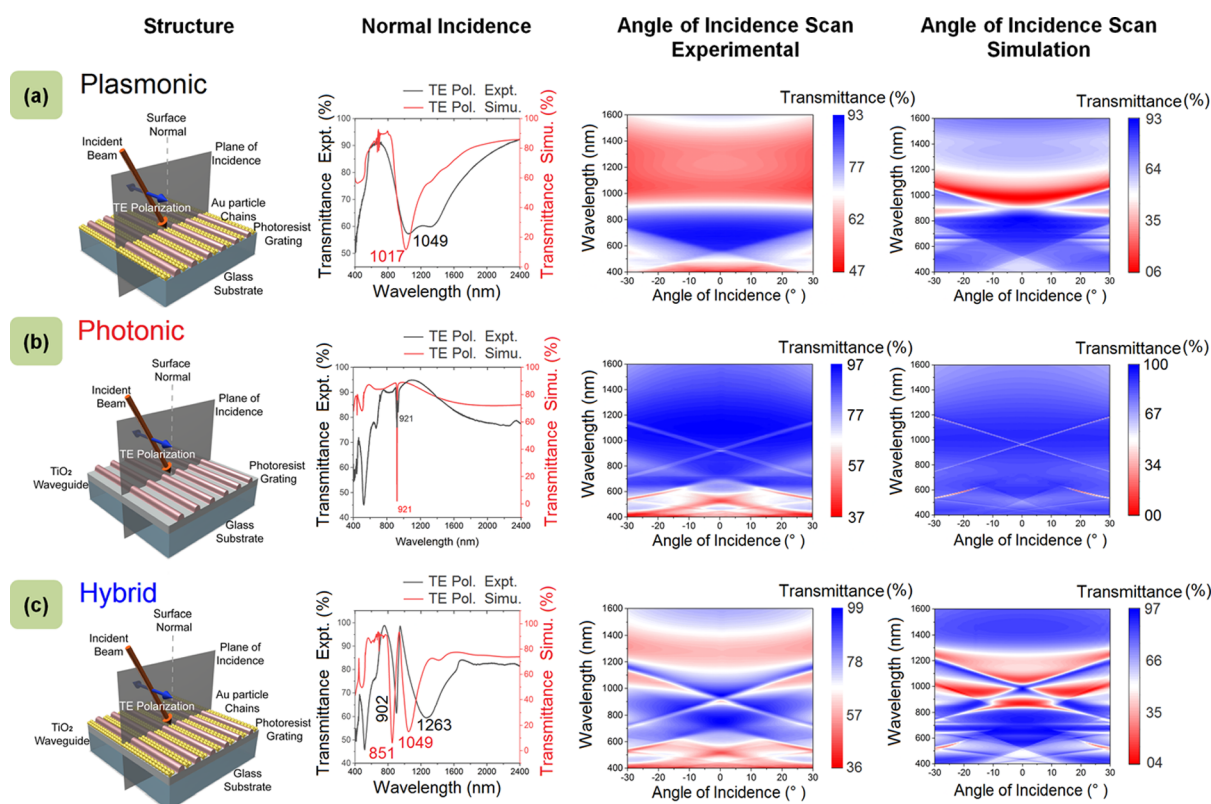
Figure 3. Comparison of optical properties of three different structures in TE mode: (a) plasmonic dimer lines of gold NPs with 520 nm periodicity supported by photoresist gratings on a glass substrate. Both experiment and simulation studies show a broad particle resonance around 1000 nm for excitation with TE polarization along the chain directions. Variation of the incidence angle experimentally exhibits a constant broad dip which is also supported by simulations. (b) Dielectric GMR structure with a photoresist grating (of periodicity 520 nm and thickness 150 nm) on a TiO$_2$ waveguide (of 200 nm thickness) and a glass substrate. Experimental as well as simulation studies observe transmission dip at 921 nm for normal incidence, whereas splitting of modes occurs on varying the AOI. (c) Hybrid plasmonic–dielectric resonant structure with gold NP dimer lines filled within the grating lines of a dielectric GMR. At normal incidence, two hybrid modes are excited at different wavelengths. Scanning of the incidence angle reveals the interaction of the broad plasmonic mode with the photonic GMR mode at higher angles, as observed from both experimental and simulation data.

RESULTS AND DISCUSSION

Figure 1a shows a schematic illustration of the hybrid optoplasmonic structure composed of a plasmonic NP grating and a dielectric GMR structure. This GMR structure is a photoresist grating (periodicity, Λ = 520 nm, and thickness, t = 150 nm) on a titanium dioxide (TiO$_2$) waveguide layer (thickness, d = 200 nm) supported by a glass substrate which forms a resonance between a diffracted and a waveguided mode. More discussion on the GMR structure can be found in Supporting Information T2. Figure 1b shows a scanning electron microscopy (SEM) image of the fabricated hybrid structure in top view. Figure 1c explains the interplay of the pure states into the formation of the hybridized states and their effect on RI variation. The top bars, solid and dotted, denote wavelengths corresponding to the initial (n_1) and final (n_2) indices, respectively. The thickness of the solid bar is used to represent "fwhm" of the resonance mechanism in general instead of referring to each of the individual cases. Sensitivity (S) is generally defined as the rate of change ($\Delta\lambda$) of resonant wavelength (λ_R) in response to change (Δn) in the surrounding index (n_1 to n_2). A plasmonic (PGR) mode with higher "S" and broader "fwhm" couples with the photonic (GMR) mode of relatively lesser "S" and smaller "fwhm" to produce hybrid photonic (H. Ph.) and hybrid plasmonic (H. Pl.) states. Apart from sensitivity, another factor that decides

the quality of sensing is the figure of merit[33] (FOM), which can be defined as the ratio between "S" and "fwhm". As smaller "fwhm" results in sharper curves with better measurement resolution, this is desired in all practical sensors apart from high "S" to maintain a high "FOM". Thus, as shown in the schematic, the hybridized photonic mode (H. Ph.) can have an enhancement in "S" because of the coupling of plasmonic features while still maintaining lower "fwhm" to have a decent "FOM". Figure 1d shows the dispersion relation for these pure and hybrid states obtained by plotting the resonant dip wavelength of experimentally observed transmission spectra as a function of the angle of incidence (AOI) in the case of parallel polarization. For both of the pure and hybrid photonic modes, the introduction of oblique incidence lifts the degeneracy of normal incidence through mode splitting; the split resonant dips corresponding to the higher wavelengths are plotted only in this figure. More detailed analysis of the dispersion studies has been elucidated further in this discussion.

Figure 2 describes the overall fabrication procedure of the desired hybrid geometry, which is a combination of top-down and bottom-up approaches in producing the dielectric GMR structure and plasmonic NP grating, respectively. The details of the Lloyd mirror-based LIL setup corresponding to Figure 2b are given in Supporting Information T3 (schematic in Figure S3). Once the photoresist grating of the GMR structure

is formed, the grating channels are filled with synthesized gold NPs through the process of directed self-assembly (TASA). Supporting Information T4 includes more about the TASA setup with a schematic in Figure S4. A movie clip of particle assembly recorded in real time by using an optical microscope in reflection mode is also provided in the Supporting Information (Video V1) that can provide a direct insight into the assembly process. Thus, one can observe a fast filling process of gold NP arrangement in chains over a large area which may be considered superior in comparison to the electron beam deposition techniques. Although grating homogeneity was lacking over a large scale that resulted in partial filling of some grating channels, the overall characteristics remain maintained when compared to the simulative study of ideal homogeneous chains and are discussed in the following sections. Figure 2d shows the finalized structure with an SEM image exhibiting efficient filling of photoresist channels with gold NPs. The magnified view in the inset supports the formation of dimer chains, which is considered during all simulative analyses throughout this report. Thus, our method, in contrast to e-beam techniques provides not only cost efficiency and large area fabrication, but also a plausible effort toward bringing in both the physical and chemical communities to a single productive platform. Moreover, plasmonic NP chains have been directly assembled in different designated geometries for studying both pure and hybrid states. The non-necessity of any molded template and transfer mechanism, unlike previous study,[13] has indeed made the whole fabrication process even simpler.

To have a thorough analysis of the fabricated hybrid structure, its optical characteristics in contrast to its constituent pure photonic and plasmonic counterparts are investigated to full extent. Although the "photonic" term is associated with the case of a dielectric GMR structure, "plasmonic" can be referred to a gold NP grating self-assembled directly on a separate photoresist-patterned glass substrate without any waveguide layer. Figure 3a presents studies on such plasmonic blocks excited in parallel polarization, that is, the TE case with respect to the plane of incidence lying normal to the grating lines (shown in the figure). Under normal incidence in air, the experimental spectroscopic data exhibit collective plasmonic resonances around 1049 nm as a broad transmission dip that well-agrees with previously reported findings[13] and can be identified as the super-radiant mode. For a better understanding of the associated resonance, a simulation model with similar geometry of gold NP dimer chains on a photoresist-patterned glass substrate is considered using FDTD methods, with the specifications given in the Experimental Section. The deviation between the experimental and theoretical transmittance values can be attributed to the nonideal cases of finite chain length along with the missing particles in reality as compared to the modeled ideal case of infinitely chained close-packed structures. Further, studies under the variation of AOI are performed. As the polarization (TE) is fixed parallel to the chain orientation, varying the incident angle keeps the incident electric field intact, thus producing similar transmission spectra over −30° to 30°. The transmittance values as a function of wavelength and incident angle obtained experimentally as well as through simulation are provided in Figure 3a that correspond to the dispersion relation. The effects of polarization perpendicular to the grating lines (TM) are also explored via experiment as well as simulation and presented in Figure S5a of Supporting Information T5. It can be observed

that plasmonic bands are formed around 530 nm corresponding to a single NP resonant dip.

Next, in Figure 3b, dielectric GMR with a photoresist grating and TiO_2 waveguide on a glass substrate is studied for optical characterization as well as for comparison with the final hybrid structure. The experimental and simulation transmission spectra match well with a periodicity of 520 nm, waveguide thickness of 200 nm, and a grating amplitude of 150 nm. For normal incidence in air, both the graphs produce a transmission dip at 921 nm for TE polarization, that is, parallel to the grating. However, in contrast to the simulation, the resonant dip in the experimental curve has a shorter depth because of the lesser diffraction efficiency of the fabricated grating. This can be caused by the nonuniformities like the variation in duty cycle (the ratio between the ridge width and the period of grating) and depth over large area unlike the ideal uniform case of simulation. As the incident angle is varied from 0° toward ±30°, we observe a similar splitting of the resonant mode into nondegenerate[14] modes. The purpose of these AOI scans is to observe the effect of the red-shifted order interplaying with the plasmonic band in the final hybrid optoplasmonic structure. Figure S5b of Supporting Information T5 shows similar GMR optical characteristics in the TM mode with a resonant wavelength around 870 nm under normal incidence.

Finally, Figure 3c shows the case of a hybrid structure achieved through the combination of the fabrication processes discussed in this report with 150 nm grating thickness, 520 nm grating periodicity, and 200 nm TiO_2 waveguide layer supported on a glass substrate. The normal incidence spectrum obtained experimentally (black curve) in air contains two resonant dips: the broader one around 1263 nm as a hybrid plasmonic resonant mode along with a sharper hybrid photonic mode at 902 nm corresponding to the GMR phenomenon. The simulation results (red curve) similarly show the presence of both hybrid plasmonic and photonic resonances at 1049 and 851 nm, respectively. The experimentally obtained GMR transmittance dip (photonic) is enhanced in the hybridized photonic state at 902 nm because of the effect of coupling. As AOI is increased from 0° toward ±30°, one of the photonic modes (red-shifted) starts interplaying more with the constant plasmonic band as their spectral positions get closer. Thus, at larger angles, more of the plasmonic features are induced to the photonic mode through an easy exchange of energy, making both the hybrid modes broad as seen from the figure. The simulation results of the AOI scan in Figure 3c also agree to this experimentally observed fact. This hybridization, however, is strictly a feature of the TE modes as no such case is obtained for the TM mode, confirmed by Figure S5c of Supporting Information T5. This is because of the fact that for the TE case, the GMR sharp resonance falls on the left shoulder of the broad PGR mode at normal incidence providing a fair chance of the coupling mechanism. For the TM case (see Figure S5), the plasmonic resonances near 530 nm are the effective contributions of single NPs. As located far away from the photonic resonances (around 870 nm), nonoverlapping of these modes results in noncoupling, making the TE excitation case the only possible way of hybridization. This is contradictory to the case of well-known waveguide–plasmonic structures[16,17] consisting of metallic bar-based grating where plasmonic modes are only excited in the TM polarization, whereas the TE case produces only a grating-like response.[34] To compare our plasmonic grating of NP chains with metallic
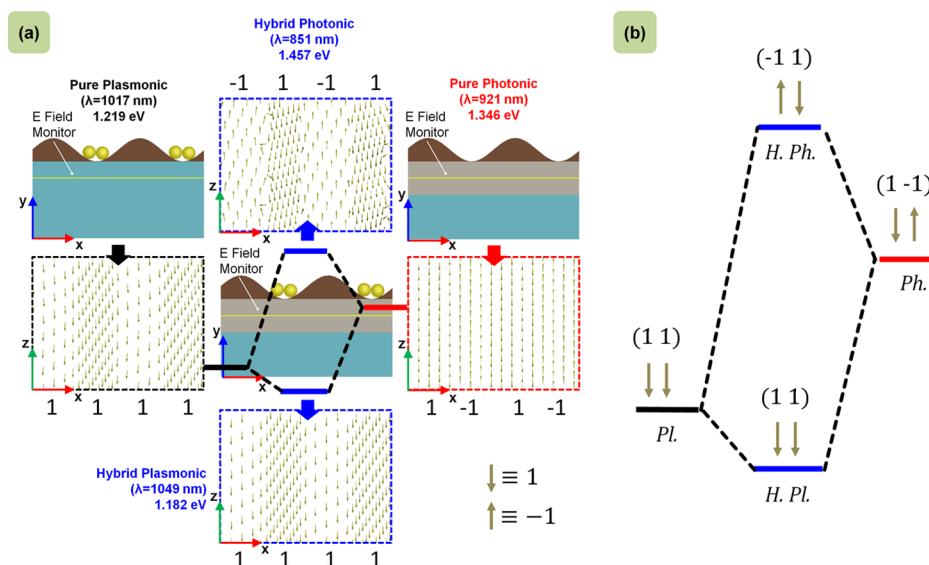
Figure 4. Hybridization model of the plasmonic NP GMR grating by FDTD simulations. (a) Pure plasmonic and photonic modes are excited at PGR (1017 nm) and GMR (921 nm) wavelengths, respectively, in their corresponding setups. Hybridized modes are also excited at their respective resonant wavelengths (851 and 1049 nm) in the hybridized setup. The electric field vector maps (*xz*-plane) are plotted for all the resonant setups below the grating (fixed *y*-position). (b) With the vector direction definition downward ($\downarrow \equiv +1$) and upward ($\uparrow \equiv -1$), the plasmonic NP GMR hybridization model can be represented schematically.
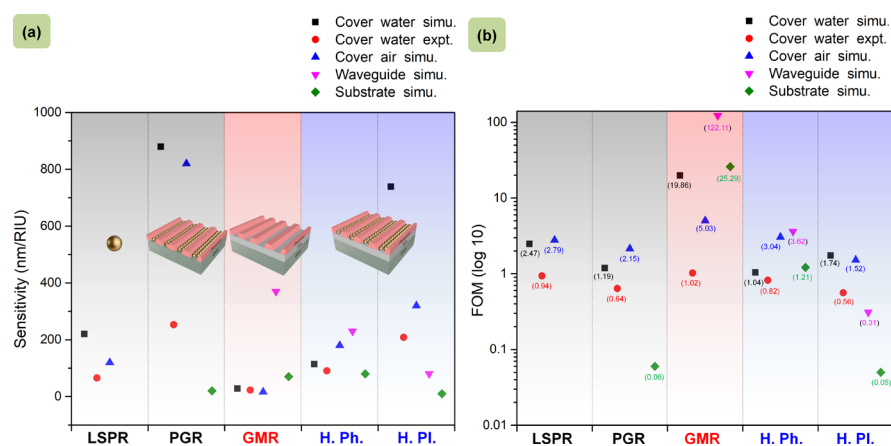
Figure 5. Studies on sensing performance of different resonant geometries: (a) comparison of sensitivity (S) and (b) FOM of different resonance configurations obtained via simulation and experiment.

bars, a similar dimension of the grating in the hybrid optoplasmonic geometry for both the polarizations is studied and shown in Figure S6 of Supporting Information T6. This points out that unlike our case, TM excitation instead of TE is indeed required to bring in the hybridization for these types of waveguide–plasmonic structures.

To justify the proper coining of the photonic/plasmonic terms to the observed hybrid modes, the various resonance conditions are studied through simulation by investigating the electric field ($\vec{E}$) distribution at resonant wavelengths for all of the pure and hybrid structures. Figure 4a shows the different geometries used in simulative studies with the E-field monitors placed below the grating–waveguide/substrate interface. The electric field vectors obtained in these monitors clearly show the basic notion of hybridization in terms of alignment of field vectors for the cases of pure and hybridized geometries. From a simplified model, as shown in Figure 4b, we can write a system of equations to understand the effect of superposition of the

pure states |Ph.⟩ and |Pl.⟩ to produce the hybridized ones |H. Ph.⟩ and |H. Pl.⟩, which is

$$\frac{1}{2}\begin{bmatrix} -\text{Pl.} & -\text{Ph.} \\ \text{Ph.} & \text{Pl.} \end{bmatrix}\begin{bmatrix} |\text{Ph.}\rangle \\ |\text{Pl.}\rangle \end{bmatrix} = \begin{bmatrix} |\text{H. Ph.}\rangle \\ |\text{H. Pl.}\rangle \end{bmatrix} \tag{1}$$

The operators (1 1 and 1 −1 for Pl. and Ph., respectively) used here are identical to the basic states to understand the influence onto one another. The hybridized plasmonic state |H. Pl.⟩ can definitely be identified for its similarity of alignment corresponding to the pure state |Pl.⟩. The mixing of states in hybridization can also be idealized from the spatial distribution of electric field ($\vec{E}$) that exhibits the resultant hybridized states as the superposition of the pure ones. The field profiles for all the planes of interest can be found in Figure S7 of Supporting Information T7. The similarities in the E-field profiles of the hybridized states to that of the pure counterparts give an initial impression which is further exploited through the vector plot in Figure 4a at our chosen

layer of interest. The use of matrix notation in explaining plasmonic lattice resonances[35] through a similar hybridization model, previously, included a rigorous mathematical calculation based on dipole–dipole interactions. We, in our hybridization model, have realized the orientations of electric field vectors as a distinctive feature to construct the matrix that can relate the hybridized states to the pure states. This simple yet supportive notation can also be implied on nanoscaled geometries revealing the hybridization of plasmonic dipolar and quadrupolar modes[36] and thus bear significant importance toward the generalization of the plasmonic hybridization model.

A detailed study on the RI sensing behavior of these pure and hybrid resonant states has been carried out to imply the importance of the hybridized modes using pure water and salt solution. Supporting Information T8 contains RI data (Figure S8) corresponding to the liquids used. For simulation, these RI data are incorporated into the simulation model as surrounding media to obtain spectral feedback for the different resonant geometries. For the experimental realization, three separate custom-made poly(dimethylsiloxane) cuvettes with distinct samples operating in PGR, GMR, and hybrid modes are introduced to the spectrophotometer, and sensing measurements are performed in response to pure D_2O and salt solution. For a comparative isolated particle LSPR measurement, gold NP solutions in glass cuvettes with different suspension media (pure D_2O and salt solution) are used. Supporting Information T9 contains the sensing data for both the simulation and experiment (spectra in Figure S9) of all the resonant geometries with water as a cover medium. Sensitivity (S) and FOM are calculated for the corresponding resonant line shapes and are tabulated in Table S1 of the same section. Figure 5a,b contains the S and FOM values for these cases of water as a cover medium. However, the GMR structure in simulation (cover water simu.) shows a slight deviation from its resonance condition, which can be identified through the oscillations in the transmission spectra (in Figure S9) along with the extreme sharp resonance dip that resulted in high FOM. It is assumed that the associated parameters of the GMR model are meant for operating with the background FDTD index = 1.0, which is the case of air, and have been studied so far in terms of transmittance spectra for different resonance geometries. Hence, a separate study is carried out in FDTD simulation where the background indices are varied from 1.0 to 1.1 for calculating S and FOM and are presented in Supporting Information T10 (Figure S10a) for all the resonant geometries. These are shown in Figure 5 as "cover air simu." data points. An increase in sensitivity for the hybrid photonic (H. Ph.) state as compared to the pure photonic state (GMR) is evident with a reasonable FOM. There is a certain mismatch in the "S" values between simulation and experiment for the cases of plasmonic (both pure and hybrid) modes, which is due to the nonconsideration of the protein coatings around the NPs in the simulation. These coatings, in reality, have affected the experimental plasmonic sensitivity and can be eliminated out in future by physical means like plasma cleaning or heat treatment. The photonic modes (both pure and hybrid) remain unaffected, showing matching values for experiment and simulation.

In particular, the fabricated GMR structure operating in the pure photonic state itself has a lower value ($S_{avg} \approx 22$ nm/RIU) as compared to conventional GMR RI sensors operating in a wavelength-interrogation scheme, which is now increased to a higher value ($S_{avg} \approx 128$ nm/RIU) because of the inclusion of the plasmonic features. "S_{avg}" is calculated over the three measurement cases of cover index variation, as shown in Figure 5.

The use of plasmonic NP grating in contrast to single NPs for plasmonic coupling has also affected the degree of enhancement as PGR ($S_{avg} \approx 650$ nm/RIU) shows a surprisingly high sensitivity than the single-particle LSPR ($S_{avg} \approx 135$ nm/RIU). This is also the reason behind obtaining high FOM values despite having a low Q factor ($Q = \lambda_R/fwhm$). This has been explained in our earlier publication[37] as an amplification because of plasmon–plasmon coupling in metallic NPs separated at nanometric distances that showed similar enhancements in RI sensitivity over orders of magnitude. Thus, the choice of PGR modes for the coupling of a highly sensitive plasmonic resonant mechanism into the modes of a relatively lower sensitive dielectric GMR structure is surely justified toward attaining an increased sensitivity. In fact, the reason behind getting a high sensitivity of the PGR mode in comparison to that of GMR as a response to the change in the cover medium can be understood from the electric field distribution for the different resonance mechanisms, as shown in Figure S7 of Supporting Information T7. As we have investigated the change in the cover index, the PGR modes that are located mainly around the particles in the cover region responded effectively to this index variation and resulted in higher S values. On the other hand, the GMR modes that are localized mostly within the waveguide can have the evanescent fields only to sense the change in the cover which resulted in lower sensitivity. The sensitivity of the pure photonic GMR mode can be increased by rigorous optimization of the constituting parameters which however is not the current focus of this article. Rather, we have discussed the possibilities of enhancement of sensitivity by coupling the plasmonic features into the GMR structure. While considering the sensitivity of the hybridized modes, one can locate the field distribution of the hybridized photonic (H. Ph.) modes mostly within the waveguide, whereas the hybridized plasmonic (H. Pl.) modes are localized around the particles that lie in the cover region. Thus, a change in cover medium has resulted in a higher sensitivity of H. Pl. as compared to H. Ph. However, the sensitivity of this H. Pl. mode is lower than that of PGR (pure plasmonic) because of the admixing of GMR features. Nonetheless, the H. Ph. sensitivity is better as compared to GMR, with the FOM values higher than that in PGR (which was our target), and is expected to be even higher if the constituent photonic mode (GMR) itself has a higher sensitivity value.

To prove the influence of the pure modes on the hybrid ones, we have extended our discussion on sensitivity with two simulation cases of index variation by changing the waveguide and substrate indices separately. As the GMR mode (pure photonic) is localized within the waveguide, we have obtained high S values for the case of waveguide index variation. The H. Ph. also being located within the waveguide has shown a higher sensitivity value with a higher FOM than the case of cover index variation (dataset "cover air simu.") which, yet, is lower than GMR sensitivity because of the admixing of the PGR modes. PGR that was previously sensitive to the cover region now shows lesser sensitivity and lower FOM on the change of medium, that is the substrate index, for the case of pure plasmonic mode. Correspondingly the H. Pl. located mainly in the cover region is now less sensitive to this waveguide index

change. Supporting Information T10 contains details of this study with the corresponding plots in Figure S10b. Figure 5 contains the data set "waveguide simu." that shows S and FOM for the variation of the medium indices. We have also performed a separate study to back up the conclusion where we have changed the substrate index of all the cases (dataset "substrate simu." in Figure 5). The pure photonic (GMR) and the hybrid photonic (H. Ph.) being located in the waveguide, nearer to the substrate, result in certain sensitivity which however is lesser than the case of the waveguide index variation (waveguide simu.). The pure plasmonic (PGR) and hybrid plasmonic (H. Pl.) modes being away from the substrate show much lesser values of S. Figure S10c of Supporting Information T10 contains the associated plots. The calculated values of S and FOM from the plots in Figure S10 are tabulated in Table S2 of the same section which provides a comparative analysis of the sensitivity of the different resonance geometries for different regions of the resonating structures.

Thus, we can conclude that the sensitivity of the hybridized states is solely dependent on that of the pure states and the medium these pure states are sensitive to. With a proper optimization and choice of these pure states, one can tune between the sensitivity and FOM over a wide spectral range. Thus, a pre-optimized GMR device with an improved "S" (optimization of duty cycle and index contrast) can surely have a further enhanced sensitivity as well as a higher FOM (FOM = S/fwhm) in the hybrid photonic mode as long as the resonant wavelength overlaps with the plasmonic resonance.

CONCLUSIONS

In summary, we have demonstrated a new method of combining top-down (LIL) and bottom-up (colloidal synthesis and TASA) approaches for the successful fabrication of hybrid plasmonic–photonic geometry over a large centimeter-scale area. The fabricated structure with a proper choice of design parameters supports coupling of the plasmonic radiant modes of gold NP grating to the photonic modes of TiO_2-based GMR under normal incidence; this results in the formation of hybridized states that can be tuned by varying AOI. The hybridized structure is optically characterized in comparison to its constituent resonant geometries along with an in-depth study of these resonances through numerical simulations to understand the coupling of two resonances. On the basis of the electric field plots, a matrix transfer model is also established that can be applied in general to similar cases of coupling of different resonances. With a system completely new in the field of modal strong coupling, we have realized its potential application in RI sensing where the sensitivity of a GMR device can further be enhanced via admixing of plasmonic signatures without much loss of the resolution. Furthermore, these hybrid structures can set up a new paradigm in the field of strongly coupled systems leading to plasmonic hot electron generation and thus can find application in solar energy harvesting, photovoltaics, photocatalysis, and many others.

ASSOCIATED CONTENT

Ⓢ Supporting Information

The Supporting Information is available free of charge on the ACS Publications website at DOI: 10.1021/acsami.8b20535.

Real-time video of directed self-assembly of particles under an optical microscope (AVI)

Optical constants of TiO_2, ma-N 405 photoresist, and glass substrate measured from spectroscopic ellipsometry; concepts of a GMR structure; LIL using Lloyd's mirror setup; directed self-assembly for the arrangement of particles; optical characteristics of the different resonant geometries in TM mode; comparison of plasmonic bars with similar dimensions in hybrid geometry; electric field plots at resonance for different cross sections; RI measurement for sensing; spectra for sensing measurements with water as a cover medium; and spectra for sensing measurements with air as a cover medium (PDF)

AUTHOR INFORMATION

Corresponding Author
*E-mail: koenig@ipfdd.de.

ORCID Ⓘ
Jonas Schubert: 0000-0002-5728-9779
Tobias A.F. König: 0000-0002-8852-8752

Author Contributions
S.S. has performed the experiments and software-based simulations. S.S. and T.A.F.K. have written the manuscript. S.S., V.G., and M.K. have fabricated the sample. V.G. and M.K. have performed the characterization. J.S. has synthesized the NPs. P.T.P. has operated the assembly process. J.S., P.T.P., and J.J. have contributed to correcting and modifying the manuscript. T.A.F.K. and J.J. have conceived the idea. T.A.F.K. has supervised the whole work. All authors have reviewed and contributed to the final manuscript.

Notes
The authors declare no competing financial interest.

REFERENCES

(1) Novotny, L.; Van Hulst, N. Antennas for Light. *Nat. Photonics* **2011**, *5*, 83–90.

(2) Knight, M. W.; Sobhani, H.; Nordlander, P.; Halas, N. J. Photodetection with Active Optical Antennas. *Science* **2011**, *332*, 702–704.

(3) Zhang, X.; Chen, Y. L.; Liu, R.-S.; Tsai, D. P. Plasmonic Photocatalysis. *Rep. Prog. Phys.* **2013**, *76*, 046401.

(4) Atwater, H. A.; Polman, A. Plasmonics for Improved Photovoltaic Devices. *Nat. Mater.* **2010**, *9*, 205–213.

(5) Chalabi, H.; Schoen, D.; Brongersma, M. L. Hot-Electron Photodetection with a Plasmonic Nanostripe Antenna. *Nano Lett.* **2014**, *14*, 1374–1380.

(6) Stockman, M. I.; Faleev, S. V.; Bergman, D. J. Localization Versus Delocalization of Surface Plasmons in Nanosystems: Can One State Have Both Characteristics? *Phys. Rev. Lett.* **2001**, *87*, 167401.

(7) Choquette, J.J.; Marzlin, K.-P.; Sanders, B. Superradiance, Subradiance, and Suppressed Superradiance of Dipoles Near A Metal Interface. *Phys. Rev. A* **2010**, *82*, 023827.

(8) Maier, S. A.; Kik, P. G.; Atwater, H. A. Observation of Coupled Plasmon-Polariton Modes in Au Nanoparticle Chain Waveguides of Different Lengths: Estimation of Waveguide Loss. *Appl. Phys. Lett.* **2002**, *81*, 1714−1716.

(9) Willingham, B.; Link, S. Energy Transport in Metal Nanoparticle Chains via Sub-Radiant Plasmon Modes. *Opt. Express* **2011**, *19*, 6450−6461.

(10) Polavarapu, L.; Pérez-Juste, J.; Xu, Q.-H.; Liz-Marzán, L. M. Optical Sensing of Biological, Chemical and Ionic Species Through Aggregation of Plasmonic Nanoparticles. *J. Mater. Chem. C* **2014**, *2*, 7460−7476.

(11) Solis, D., Jr.; Willingham, B.; Nauert, S. L.; Slaughter, L. S.; Olson, J.; Swanglap, P.; Paul, A.; Chang, W.-S.; Link, S. Electromagnetic Energy Transport in Nanoparticle Chains Via Dark Plasmon Modes. *Nano Lett.* **2012**, *12*, 1349−1353.

(12) Gür, F. N.; McPolin, C. P. T.; Raza, S.; Mayer, M.; Roth, D. J.; Steiner, A. M.; Löffler, M.; Fery, A.; Brongersma, M. L.; Zayats, A. V. DNA-Assembled Plasmonic Waveguides for Nanoscale Light Propagation to a Fluorescent Nanodiamond. *Nano Lett.* **2018**, *18*, 7323.

(13) Hanske, C.; Tebbe, M.; Kuttner, C.; Bieber, V.; Tsukruk, V. V.; Chanana, M.; König, T. A. F.; Fery, A. Strongly Coupled Plasmonic Modes on Macroscopic Areas via Template-Assisted Colloidal Self-Assembly. *Nano Lett.* **2014**, *14*, 6863−6871.

(14) Wang, S. S.; Magnusson, R. Theory and Applications of Guided-Mode Resonance Filters. *Appl. Opt.* **1993**, *32*, 2606−2613.

(15) Liu, Z. S.; Tibuleac, S.; Shin, D.; Young, P. P.; Magnusson, R. High-Efficiency Guided-Mode Resonance Filter. *Opt. Lett.* **1998**, *23*, 1556−1558.

(16) Christ, A.; Tikhodeev, S.; Gippius, N.; Kuhl, J.; Giessen, H. Waveguide-plasmon Polaritons: Strong Coupling of Photonic and Electronic Resonances in a Metallic Photonic Crystal Slab. *Phys. Rev. Lett.* **2003**, *91*, 183901.

(17) Zeng, P.; Cadusch, J.; Chakraborty, D.; Smith, T. A.; Roberts, A.; Sader, J. E.; Davis, T. J.; Gómez, D. E. Photoinduced Electron Transfer in the Strong Coupling Regime: Waveguide-Plasmon Polaritons. *Nano Lett.* **2016**, *16*, 2651−2656.

(18) Liu, J.-N.; Huang, Q.; Liu, K.-K.; Singamaneni, S.; Cunningham, B. T. Nanoantenna-Microcavity Hybrids with Highly Cooperative Plasmonic-Photonic Coupling. *Nano Lett.* **2017**, *17*, 7569−7577.

(19) Rodriguez, S. R. K.; Murai, S.; Verschuuren, M. A.; Rivas, J. G. Light-Emitting Waveguide-plasmon Polaritons. *Phys. Rev. Lett.* **2012**, *109*, 166803.

(20) Sakat, E.; Vincent, G.; Ghenuche, P.; Bardou, N.; Collin, S.; Pardo, F.; Pelouard, J.-L.; Haïdar, R. Guided Mode Resonance in Subwavelength Metallodielectric Free-Standing Grating for Bandpass Filtering. *Opt. Lett.* **2011**, *36*, 3054−3056.

(21) Klein, M. W.; Tritschler, T.; Wegener, M.; Linden, S. Lineshape of Harmonic Generation by Metallic Nanoparticles and Metallic Photonic Crystal Slabs. *Phys. Rev. B: Condens. Matter Mater. Phys.* **2005**, *72*, 115113.

(22) Grzelczak, M.; Vermant, J.; Furst, E. M.; Liz-Marzán, L. M. Directed Self-Assembly of Nanoparticles. *ACS Nano* **2010**, *4*, 3591−3605.

(23) Mayer, M.; Schnepf, M. J.; König, T. A. F.; Fery, A. Colloidal Self-Assembly Concepts for Plasmonic Metasurfaces. *Adv. Opt. Mater.* **2019**, *7*, 1800564.

(24) Mayer, K. M.; Hafner, J. H. Localized Surface Plasmon Resonance Sensors. *Chem. Rev.* **2011**, *111*, 3828−3857.

(25) Brolo, A. G. Plasmonics for Future Biosensors. *Nat. Photonics* **2012**, *6*, 709−713.

(26) Farka, Z.; Juřík, T.; Kovář, D.; Trnková, L.; Skládal, P. Nanoparticle-Based Immunochemical Biosensors and Assays: Recent Advances and Challenges. *Chem. Rev.* **2017**, *117*, 9973−10042.

(27) Xavier, J.; Vincent, S.; Meder, F.; Vollmer, F. Advances in optoplasmonic sensors—combining optical nano/microcavities and photonic crystals with plasmonic nanostructures and nanoparticles. *Nanophotonics* **2018**, *7*, 1−38.

(28) Bastús, N. G.; Comenge, J.; Puntes, V. Kinetically Controlled Seeded Growth Synthesis of Citrate-Stabilized Gold Nanoparticles of Up to 200 nm: Size Focusing versus Ostwald Ripening. *Langmuir* **2011**, *27*, 11098−11105.

(29) Dewald, I.; Isakin, O.; Schubert, J.; Kraus, T.; Chanana, M. Protein Identity and Environmental Parameters Determine the Final Physicochemical Properties of Protein-Coated Metal Nanoparticles. *J. Phys. Chem. C* **2015**, *119*, 25482−25492.

(30) Malaquin, L.; Kraus, T.; Schmid, H.; Delamarche, E.; Wolf, H. Controlled Particle Placement through Convective and Capillary Assembly. *Langmuir* **2007**, *23*, 11513−11521.

(31) Lumerical Inc. http://www.lumerical.com/tcad-products/fdtd/.

(32) Smith, D. Y.; Shiles, E.; Inokuti, M.; Palik, E. The Optical Properties of Metallic Aluminum. *Handbook of Optical Constants of Solids*, 1985; Vol. 1, pp 369−406.

(33) Otte, M. A.; Sepúlveda, B.; Ni, W.; Juste, J. P.; Liz-Marzán, L. M.; Lechuga, L. M. Identification of the Optimal Spectral Region for Plasmonic and Nanoplasmonic Sensing. *ACS Nano* **2009**, *4*, 349−357.

(34) Schider, G.; Krenn, J. R.; Gotschy, W.; Lamprecht, B.; Ditlbacher, H.; Leitner, A.; Aussenegg, F. R. Optical Properties of Ag and Au Nanowire Gratings. *J. Appl. Phys.* **2001**, *90*, 3825−3830.

(35) Baur, S.; Sanders, S.; Manjavacas, A. Hybridization of Lattice Resonances. *ACS Nano* **2018**, *12*, 1618−1629.

(36) Zhang, S.; Bao, K.; Halas, N. J.; Xu, H.; Nordlander, P. Substrate-Induced Fano Resonances of a Plasmonic Nanocube: A Route to Increased-Sensitivity Localized Surface Plasmon Resonance Sensors Revealed. *Nano Lett.* **2011**, *11*, 1657−1663.

(37) König, T.; Kodiyath, R.; Combs, Z. A.; Mahmoud, M. A.; El-Sayed, M. A.; Tsukruk, V. V. Silver Nanocube Aggregates in Cylindrical Pores for Higher Refractive Index Plasmonic Sensing. *Part. Part. Syst. Charact.* **2014**, *31*, 274−283.

6.2 Mechanotunable surface lattice resonances in the visible optical range by soft lithography templates and directed self-assembly

Mechanotunable surface lattice resonances in the visible optical range by soft lithography templates and directed self-assembly

Vaibhav Gupta, Patrick T Probst, Fabian R Goßler, Anja Maria Steiner, Jonas Schubert, Yannic Brasse, **Tobias A.F. König*** and Andreas Fery

Author contribution statement

VG and PP carried out the experiments and have contributed equally to the work. **TK** encouraged VG, PP, FG and AS to investigate the simulation, fabrication and optical spectroscopy methods as well as supervised the execution and findings of this work. JS and PP contributed through their synthesis and self-assembly methods. **TK** and AF made a significant contribution to the conception and design of the work. Through the simulation, fabrication and optical spectroscopy methods, the author **TK** made a significant contribution to the acquisition, analysis and interpretation of the data. All authors provided critical feedback and helped shape the research, analysis and manuscript.

Mechanotunable Surface Lattice Resonances in the Visible Optical Range by Soft Lithography Templates and Directed Self-Assembly

Vaibhav Gupta,[†,‖] Patrick T. Probst,[†,‡,‖] Fabian R. Goßler,[†] Anja Maria Steiner,[†] Jonas Schubert,[†,‡,§] Yannic Brasse,[†,‡] Tobias A. F. König,*[,†,‡] and Andreas Fery*[,†,‡,§]

†Institute for Physical Chemistry and Polymer Physics, Leibniz-Institut für Polymerforschung Dresden e.V., Hohe Str. 6, 01069 Dresden, Germany

‡Cluster of Excellence Center for Advancing Electronics Dresden (cfaed) and §Physical Chemistry of Polymeric Materials, Technische Universität Dresden, 01069 Dresden, Germany

Ⓢ *Supporting Information*

ABSTRACT: We demonstrate a novel colloidal self-assembly approach toward obtaining mechanically tunable, cost-efficient, and low-loss plasmonic nanostructures that show pronounced optical anisotropy upon mechanical deformation. Soft lithography and template-assisted colloidal self-assembly are used to fabricate a stretchable periodic square lattice of gold nanoparticles on macroscopic areas. We stress the impact of particle size distribution on the resulting optical properties. To this end, lattices of narrowly distributed particles (~2% standard deviation in diameter) are compared with those composed of polydisperse ones (~14% standard deviation). The enhanced particle quality sharpens the collective surface lattice resonances by 40% to achieve a full width at half-maximum as low as 16 nm. This high optical quality approaches the theoretical limit for this system, as revealed by electromagnetic simulations. One hundred stretching cycles demonstrate a reversible transformation from a square to a rectangular lattice, accompanied by polarization-dependent optical properties. On the basis of these findings we envisage the potential applications as strain sensors and mechanically tunable filters.

KEYWORDS: stretchable optics, strain-sensing, surface lattice resonance, Bragg reflector, template-assisted self-assembly
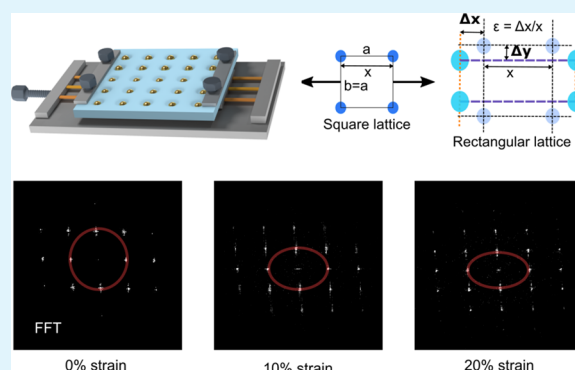
INTRODUCTION

Plasmonic resonances of metallic nanoparticles are of broad interest because of their strong interaction with light and their energy confinement at sub-wavelength scales. Light interaction induces collective oscillation of free electrons commonly known as localized surface plasmon resonance (LSPR). Spectral properties of such modes can be engineered by varying the nanoparticle composition, size or shape, and the surrounding refractive index.[1] For photonic and optical applications, it is desirable to achieve high optical quality and wide optical tunability simultaneously. The quality factor is defined by the ratio of the resonance wavelength to the resonance width. One effective approach toward obtaining high optical quality is the interference between a plasmon mode and a Bragg grating mode, also known as symmetry breaking or Fano resonance.[2,3] The arising surface lattice resonance (SLR) yields coherence to the system by confining the high electromagnetic field in the lattice plane.[4] Whereas typical LSPR exhibits a full width at half-maximum (fwhm) of >80 nm, for SLR the spectral width is drastically reduced, down to 1−2 nm.[5]

In order to steer this lattice plasmonic resonance to the visible wavelength (λ), an energetic overlap between the Bragg mode and the particle plasmon resonance is necessary. In the first order and at normal incidence, the mode occurs at λn (n as environmental refractive index).[6] To cover the entire visible area, the size of the particles and the lattice periodicity must be adjusted accordingly.[7] Such SLR response in the visible wavelength range was demonstrated for a lattice of aluminum rectangles fabricated by electron beam lithography.[8] In those examples, lithography methods were employed, which require masks and etching processes. Thus, fabrication becomes costly and highly energy-consumptive. Colloidal self-assembly can be a more cost-efficient and ecofriendly alternative, and renders SLR on cm² areas easily accessible. For example, non-close hexagonally packed particle arrays supporting SLR can be readily generated by floating plasmonic core−shell nanoparticles at the water−air interface.[9] In this system, the temperature-induced change in the refractive index of the
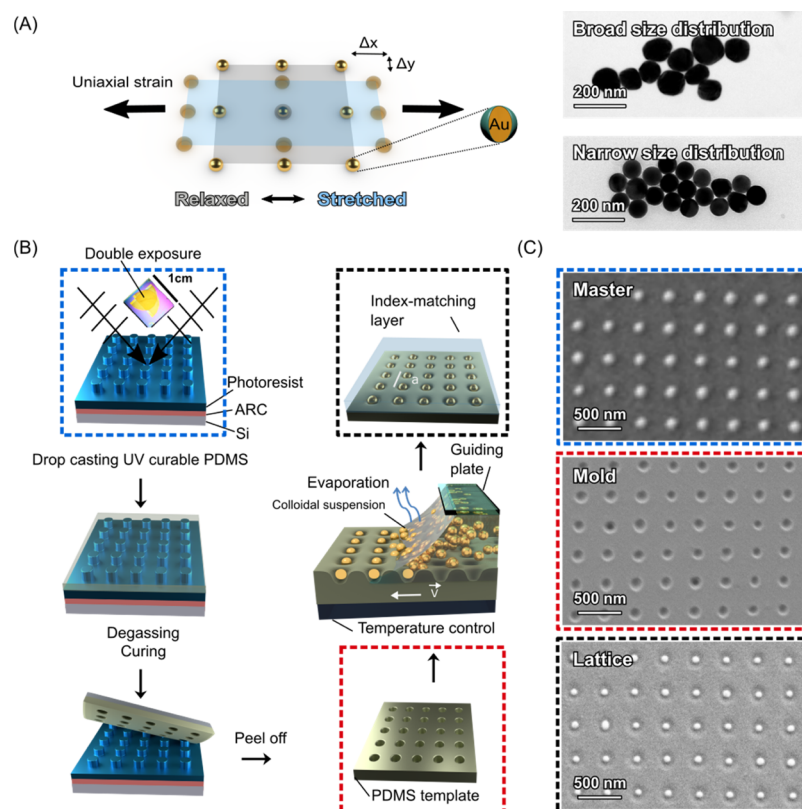
Figure 1. Soft lithography template fabrication for directed self-assembly. (A) Scheme of a stretchable 2D plasmonic lattice under uniaxial strain. Corresponding TEM images of two particle systems with broad and narrow particle size distribution. (B) Scheme represents the fabrication of a stretchable 2D lattice using a combination of LIL, soft molding, and directed self-assembly of plasmonic nanoparticles. ARC: anti-reflective coating. (C) SEM images of the fabricated nanopillars master, nanoholes array, and 2D plasmonic lattice (narrow size distribution). Dashed frames in pictorial representation correspond to the SEM image.

hydrogel shell additionally allows a reversible 50 nm shift of the hybridized mode with a line width of 50 nm.

Recently, mechanical deformation of plasmonic arrays sparked research interest as an alternative stimulus for spectral tuning.[5] Odom and co-workers showed that optimum conditions for lasing can be achieved by mechanical tuning.[10] As well, we showed in earlier work that colloidal linear particle assembly can be split into plasmonic oligomers, resulting in strain sensitivity and potential applications in sensing.[11] The colloidal approach is particularly well suited for creating mechanically tunable assemblies as particles can be directly transferred to the target substrate or embedded in elastomers. For precise strain-induced tuning of optical properties, it is mandatory to address specific lattice orientations consistently over the whole substrate. Therefore, defect-free templates molded from electron beam masters are commonly used in capillarity-assisted particle assembly of two-dimensional (2D) lattices.[12,13] Porous anodic alumina[14] or laser interference lithography (LIL)[15] can be a better scalable alternative. In contrast, hexagonal assemblies produced template-free at the water−air or liquid−liquid interface suffer from differently oriented domains. The variation in strain-induced lattice deformation from domain to domain would lead to a broad averaged SLR peak.

In this work, we combine the top-down method soft lithography and the bottom-up method template-assisted self-assembly (TASA) as facile and scalable fabrication methods to generate a mechanically tunable SLR. Flexible nature of the metasurface can overcome the optical cavity design limitation

by creating real-time tunable high-quality mode. To design the collective optical properties for the visible wavelength regime, we use electromagnetic finite element simulations. After realizing the square lattice of gold nanospheres assembled inside an elastomeric template, the sharp spectral features, modulated by mechanical stresses, are quantified using conventional UV−vis spectroscopy. Both our theoretical and experimental results stress the importance of particle size polydispersity for the quality of the collective SLR mode. Our approach of flexible and tunable high-quality plasmonic lattice paves the way for cost-effective next-generation optical and photonic devices.

■ RESULTS AND DISCUSSION

We discuss a 2D square plasmonic lattice embedded in polydimethylsiloxane (PDMS) that shows a dynamic tuning of lattice constants under mechanical deformation. Because of a Poisson's ratio (which is the negative of the ratio of transverse to axial strain) of 0.5, stretching in the x-direction results in a reduction in the y-direction.[11] Consequently, applying a uniaxial strain transforms the system from a square to a rectangular lattice (Figure 1A). Generally, a non-stretched plasmonic square lattice enables coupling between single-particle LSPR and degenerate 2D Bragg diffraction to produce two hybridized modes.[16] Upon deformation into a rectangular lattice, two different Bragg modes (along the x- and y-directions) arise, which interact with the LSPR and allow switchable hybrid modes with polarization dependence.[10]
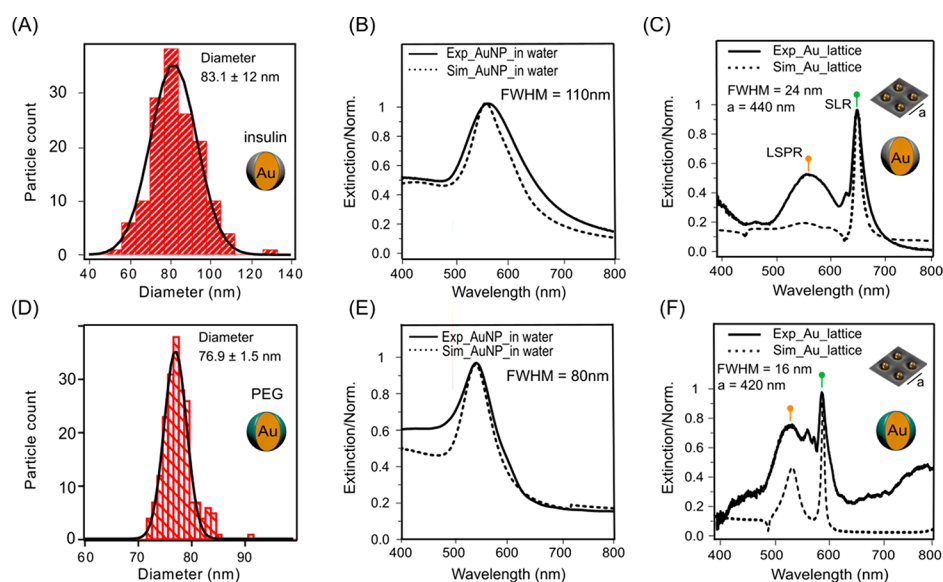
Figure 2. From various colloidal particle systems to SLR. (A,D) Size distribution of broadly/narrowly distributed gold nanoparticles coated with insulin and PEG, respectively. (B,E) Corresponding experimental and simulated extinction spectra in water. (C,F) Simulated and measured extinction of a 2D plasmonic lattice at periodicity (a = 440 nm) for a broad case and (a = 420 nm) for a narrow case. To reflect the particle polydispersity, the simulated spectra were averaged for different particle diameters.

In order to obtain high-quality modes, it is vital to maintain energetic stability and order in the system.[17,18] To achieve those essentials, we followed a soft lithography fabrication approach to create a square lattice of well-defined periodicity over cm^2 areas (Figure 1B). This method starts with a double LIL exposure to fabricate the nanopillar master on a photoresist-coated silicon wafer. Negative replication by a soft lithography molding step produces a nanohole structure (nanohole array from UV-curable PDMS). More details about the LIL setup are shown in Supporting Information Text T1 and Figure S1. This flexible template was used for capillarity-assisted assembly to align the colloidal plasmonic nanoparticles in a 2D square lattice. Briefly, a droplet of nanoparticle suspension was dragged across the topographical template. The hole dimensions were chosen (120 nm diameter and ∼70 nm depth, see also Figure S2) such that only one particle fits into it. A high filling rate can be achieved at the same time (see Figure 1C).[13] At the receding meniscus, the particles concentrate facilitated by evaporation-driven convection. This local accumulation reduces the Brownian motion of nanoparticles and thereby increases the probability of particles being deposited inside the features. Net repulsive particle−substrate interaction and good colloidal stabilization of particles provided by surface modification prevent random sequential adsorption to the substrate and irreversible aggregation, respectively. Precise tuning of contact angle and surface tension balances the components of the capillary force at the meniscus acting parallel and normal to the substrate to drag the gold nanoparticles along and only allow deposition where they feel a sidewall of the topographical features counteracting this motion (more details are in Supporting Information Text T2).[19] As a big advantage of this assembly method, the assembly area is only limited by template size and reservoir of colloidal particle solution. It was already demonstrated that the latter limitation can be overcome by a continuous microfluidic feed of suspension.[20]

To investigate the influence of particle size distribution on SLR quality, square lattices of two different particle systems

were fabricated: one with a broad particle size distribution and one with a narrow size distribution that shows an eightfold smaller standard deviation (Figure 2A,D). Citrate- and surfactant-stabilized synthesis routes were used to produce broad and narrow size distributions, respectively (see the Experimental Section for more details). The low-molecular-weight ligands from syntheses were exchanged against insulin and polyethylene glycol (PEG) to demonstrate the tolerance of the employed assembly technique concerning different surface chemistries. Indeed, the achieved filling rates are comparable, being 81 and 79%, respectively, as evaluated from 150 × 150 μm^2 scanning electron microscopy (SEM) images (more details are in Supporting Information Text T4). The good periodic order of the plasmonic grating was characterized employing the radial distribution function as evaluated from SEM (more details are in Supporting Information Text T5). Moreover, the utilized coatings provide good biocompatibility and help integration in biomedical sensing applications.[21,22] For technical reasons the broad particle size distribution particles were arranged in a 440 nm and the narrow particle size distribution particles were assembled in a 420 nm square lattice. Finally, the plasmonic lattice was index-matched by spin-coating an ultraviolet (UV) curable PDMS layer. Embedding of particles leads to the same wavelength for the wavefront propagation in substrate and superstrate, which enhances the in-plane coupling of the SLR.

The spectra of single particles with LSPR at 560 nm (broad) and 540 nm (narrow) in aqueous solution were reproduced by finite-difference time-domain (FDTD) simulations (Figure 2B,E). A summary of optical properties resulting from the two particle distributions is presented in Supporting Information Table S1. To reflect the particle polydispersity, the simulated data for the broad size distribution were averaged over several spectra of varying particle size. Because of the periodic arrangement, the nanoparticles couple with each other coherently and an SLR mode arises for both particle kinds (Figure 2C,F). A detailed explanation of SLR is given in Supporting Information T3. However, with narrowly dis-
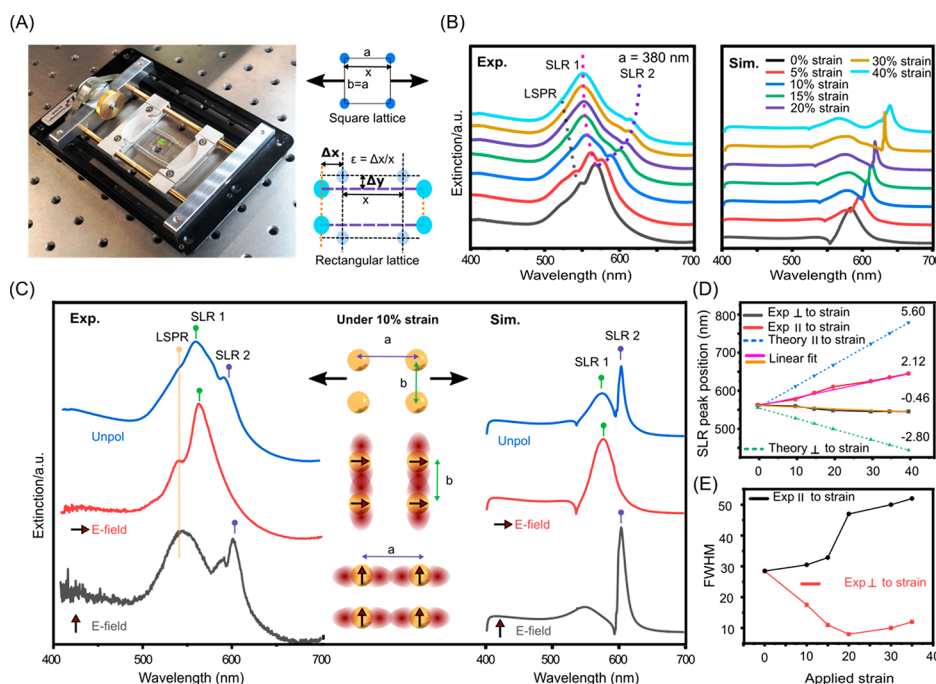
Figure 3. Mechanotunable SLR. (A) Photograph of the stretching device with a clamped sample in the center and schematic of the square lattice under uniaxial strain. (B) Experimental and simulated spectra of the gold nanoparticle lattice under various strains (considering partial force transfer in simulations). (C) Experimental and simulated polarization-dependent selective reading of the lattice resonance modes. (D) Comparison between theoretically expected (100% force transfer) and experimentally obtained SLR peak positions. (E) fwhm of the SLR peaks for various strains.

tributed particles (Figure 2F), the fwhm is reduced from 24 to 16 nm (Q-factor $\lambda/\Delta\lambda$ from 27 to 36) as compared to more polydisperse particles (Figure 2C). This highlights the importance of particle quality, as expected from the corresponding simulated spectra (Figure 2C,F). Note that the mode structure is nicely reproduced by simulations for the narrow size distribution (Figure 2F), whereas the LSPR is only weakly reproduced for the broader case (Figure 2C). The larger size distribution and scattering cross section result in a broad LSPR that is less pronounced as compared to the SLR peak. It is important to mention that in simulations an infinite lattice is considered, whereas an experiment averaging over a 12 mm^2 area reflects variations in particle coverage. Therefore, the ratio of SLR to LSPR extinction is larger in simulations as compared to experiments. We also performed the mean square error (MSE) calculations. The MSE is defined as the average squared difference of the normalized extinction values between the simulation data and what is measured experimentally. The MSE value in the case of broadly distributed gold nanoparticle lattice SLR is 0.11 and for the narrow size distribution it is 0.13. This leads to the fact that experimental spectra match nearly perfectly with simulations. The small oscillation between LSPR and SLR represents the Rayleigh anomaly. This is the wavelength where diffraction turns from being evanescent to radiative.[6] In general, a larger period (440 nm) is expected to produce a narrower SLR as compared to 420 nm because of less overlap with plasmonic losses. The fact that the narrowly distributed particles show a smaller fwhm even for a less optimal 420 nm lattice emphasizes the benefits of mono-disperse building blocks. Please note that despite the different synthesis routes used, both particle types are monocrystalline and consequently show comparable plasmonic damping. Furthermore, insulin and PEG coating of particles produce a

similar dielectric environment as both represent organic ligands.

In order to modulate the SLR mode at normal incidence, we benefit from the flexible nature of the UV-PDMS substrate (Figure 3). We discuss here the mechanical tunability only with the narrow particle size distribution particles and compared two different periodicities, 420 and 380 nm. Stretching experiments for broadly distributed particles at a periodicity of 440 nm are provided in Supporting Information S7. The lattice constant of our particle array can be varied in situ by straining the substrate uniaxially. Because of its centimeter square dimensions, the optical properties of the final plasmonic lattice could be studied using conventional UV−vis spectroscopy with a beam size of 3 × 4 mm^2. Figure 3A shows the photograph of a home-built stretching device. Increasing the strain gradually from 0 to 40% transforms the square lattice into a rectangular one with lattice constant a (along the applied strain direction) and b (along the perpendicular direction). Two different lattice constants in the x- and y-directions result in two different SLR modes. Because of the strain-induced non-degeneration, one of the SLR shifts toward higher wavelengths (violet color marker in Figure 3B), whereas the other one is blue-shifted (pink color marker) for unpolarized light illumination. We found that the macroscopically applied strain was only partially transferred to the lattice (more details below). Therefore, the simulated spectra displayed in the right panel of Figure 3B were calculated for the effective lattice constraints as derived from the experimental spectra. The experimentally observed spectral shifts are in good agreement with FDTD simulations. In general, SLR1 is broader as compared to SLR2 because of the reduced plasmonic damping of gold for larger wavelengths in the visible wavelength range.[7] Moreover, the Q-factor of SLR is
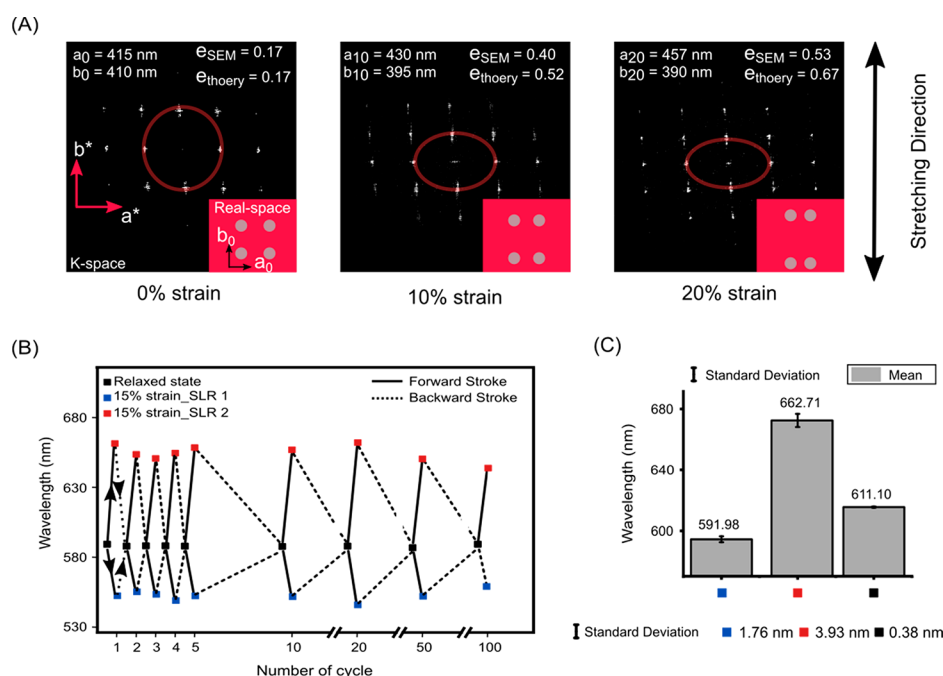
Figure 4. Evaluation of strain transfer. (A) 2D fast Fourier transform (FFT) of 0, 10, and 20% strain SEM images. a_i, b_i and a_i^* b_i^* are the lattice constants in real space and k-space respectively, with i giving the applied strain in percent. (B) Stretch and relax cycles of a plasmonic lattice ($a = 420$ nm) plotted against SLR peaks for 15% strain. (C) Mean value and standard deviation in SLR peak positions are shown for relaxed and stretched cases. Abbreviation e represents the ellipticity of the ellipse.

an interplay between the single particle scattering cross section and the Bragg mode. The low-quality SLR1 shows a significant overlap with the broad LSPR mode for all applied strains. In contrast, the overlap of SLR2 gradually decreases when red-shifting with increasing strain. A strain of 30% (20% in experiments, Figure 3E) represents an optimal balance between LSPR and Bragg modes. The reduced overlap accompanied with less plasmonic character produces a very sharp peak SLR2. When increasing the strain further, SLR2 moves out of the scattering cross section of the single particle, leading to peak broadening. This optimization by adjustment of periodicities of the lattice is explained theoretically in Supporting Information Text T3.

The two different SLR modes in rectangular lattices can be studied in more detail when using linearly polarized excitation, as depicted in Figure 3C for a 10% strain. Note that the SLR induced by polarization in the x-direction is at lower wavelengths as compared to the y-excitation. At first glance, this is counterintuitive as the periodicity in the x-direction is larger. However, this can be understood by considering every plasmonic particle as a dipole antenna. This effect is highlighted in the schematic illustration in Figure 3C. Excitation along the x-axis induces electron oscillations in the parallel orientation for each particle. Yet, these dipoles radiate the scattered light mainly perpendicular to the dipole moment. This concludes that the surface lattice mode always propagates normal to the incident E-field direction. Or, in other words, for an asymmetric lattice, the SLR mode is defined by the lattice constant which is normal to the incident polarization.[23]

As mentioned before, we see a deviation between macroscopically applied strain and effective deformation of the lattice. Figure 3D compares the strain-induced experimental peak shifts with the theoretical values (considering 100% transfer of applied strain and Poisson's ratio of 0.5). SLR1 is

modulated by strain parallel to the stretching direction, whereas the shift in SLR2 reflects the perpendicular strain. The comparison between the slopes (linear fit) of the strain-dependent SLR position for theory and experiment gives a measure for partial strain transfer. The ratio between slopes gives 37.8% transfer parallel to the stretching direction and 16.4% in the perpendicular direction (ratio of perpendicular/parallel 0.43). This is in good agreement with the in situ stretching results in dark-field microscopy (Supporting Information Figure S8). We attribute the partial transfer of strain to the creep of the polymer chains and deformation of the clamped region when applying a macroscopic strain. It is important to emphasize that the optical quality can be changed by the stretching (Figure 3E). In general, one of the resonance peaks undergoes a red shift, whereas the other one is blue-shifted under successively increased strain. As compared to a relaxed state, the coupling strength between LSPR and Bragg modes decreases under strain for the red-shifted SLR modes (narrow fwhm in the case of 30% strain). The blue-shifted SLR successively becomes broader in terms of line width (fwhm) because of increased overlap with the single particle scattering cross section that leads to more plasmonic losses. Depending on the application aspect, this gives freedom in terms of fwhm selection.

The optical analysis shows that the applied macroscopic strain can only be converted by about 38 and 16%. In order to justify this relationship, we have carried out SEM measurements of the strained samples (Figure 4). These measurements were performed for a plasmonic lattice constant of 420 nm. SEM images were analyzed with 2D FFT for 0, 10, and 20% strain. Evaluated lattice constants (a, b) in parallel and perpendicular with respect to the real space strain direction (black arrow) are shown in Figure 4A. In the relaxed state, the FFT shows that the lattice itself is not perfectly square. During the LIL fabrication, the samples are illuminated twice and

mechanically rotated 90°. Inaccuracies in the rotation can lead to a deviation in the lattice pattern. We compared the eccentricity values from theory and SEM to understand the deviation of the ellipse from being circular. Eccentricity values show a clear trend that UV-PDMS grating was stretched but the force transfer on to the particle grating was partial. In the case of 20% strain, the lattice constant in the strain direction changes from 415 to 457 nm. This translates to a 50% strain transfer as compared to theoretical values. Similarly, for perpendicular to the strain direction, only 24% of the strain was transferred. Finally, the stretching inside the SEM confirms that there is moderate force transferred from the macroscopic scale to the nanometer lattice deformation scale. The force cannot be implemented one to one probably because of the clamp holder. To stretch the PDMS, the material is squeezed at the clamp holder with an unrecognized force, which can cause the mismatch. Note that the deviation between SEM and optical spectrum data could also be because of the absence of the index matching layer during the SEM measurement. Nonuniform embedding leads to less frictional forces and more degree of freedom in terms of particle motion.

In order to confirm the robustness of the elastomeric plasmonic lattice, the sample was stretched and relaxed 100 times and the bright-field spectrum was measured after each cycle (Figure 4B). The maximum strain was kept to a constant value of 15% for all the cycles. The black color dots (relaxed state) in Figure 4B show that UV-PDMS recovers even after 100 cycles with a standard deviation of only 0.38 nm, as summarized in Figure 4C. The deviation in the values for SLR1 (blue dots) and SLR2 (red dots) is higher as compared to the relaxed state. This can be correlated with the manual handling of the stretching device.

■ CONCLUSIONS

In conclusion, we discussed the assembly of ordered nanoparticle arrays that show a narrow and mechanically tunable SLR over 100 cycles of deformations. The assembly relies on directed self-assembly of colloidal nanoparticles in templates formed by soft lithography. We showed the arrangement with broad/narrow particle size distribution and discussed their influence on the optical quality. The real-time mechanical tuning and accessibility of non-degenerated SLR modes hold great potential for plasmonic lasing,[24] biosensing,[25] or colorimetric sensors.[8] We show that the optical properties of the system change dramatically upon applying strain, as the array changes from a square lattice to a rectangular lattice. Importantly, the optical quality is not lost upon straining the system and the SLR peaks can be shifted over a wavelength range of 70 nm. Moreover, the uniaxially strained lattice opens up the possibility for introducing optical anisotropy. This scalable system with monocrystalline nanoparticle building blocks provides a platform to curb the rigid nature of optical systems and offers versatile plasmon mode engineering within flexible electronics. Finally, the rational design framework established also allows for extending the approach to supracolloidal structure (clusters, hetero-clusters, etc.).

■ EXPERIMENTAL SECTION

Template Fabrication. Nanopillars with various periodicities and diameters were fabricated with LIL using Lloyd's mirror setup. Further experimental details can be found in Supporting Information Text T1. A cleaned silicon wafer substrate (2.54 cm × 2.54 cm) was first spin-coated with a back antireflection coating AZ BARLi II (70 nm in thickness). Further, a layer (214 nm thickness) of AZ MIR 701 14cp (Micro Chemicals GmbH) positive resist, 1 to 1 ratio diluted with ethyl L-lactate, was spin-coated (6000 rpm, 60 s) on top. The sample was exposed twice to the laser with 90° sample rotation. A wet chemical development process was used to etch the exposed resist in order to fabricate the pillars (master structures). The sample was immersed in AZ 726 MIF developer (Micro Chemicals GmbH) for 30 s followed by gentle rinsing with water and nitrogen drying. Soft lithography was employed to fabricate elastic molds of the as-prepared periodic nanostructures using silicone rubber PDMS, called UV-PDMS. We used two-component KER-4690 photo-curable PDMS (Shin Etsu & Micro Resist Technology GmbH) with a 1 to 1 mixing ratio. The mixture was stirred for 30 min through the magnetic stirring process and degassed for 20 min. The blend was drop-casted on the substrate, degassed again, and cured with a 365 nm UV lamp for 30 min. After the peel-off process possible remains of the photoresist were removed by rinsing with ethanol and drying with nitrogen.

Nanoparticle Synthesis. *Particle Synthesis of Broad Size Distribution.* Citrate-stabilized nanoparticles were prepared via seed-mediated growth synthesis.[26] The protein coating was prepared according to earlier published methods.[27−29] Briefly, 40 mL of the nanoparticle solution was added to a 4 mL 1 mg mL^{-1} insulin solution with 1% wt sodium citrate at pH 9 to generate the desired protein coating. The solution was allowed to incubate overnight. After fourfold centrifugation, the nanoparticles were analyzed with UV−vis and Libra 120 transmission electron microscopy (TEM). The nanoparticle size of 83.1 ± 12.2 nm was determined by statistical analysis of 150 particles.

Particle Synthesis of Narrow Size Distribution. Spherical gold nanoparticles capped by hexadecyltrimethylammonium chloride were synthesized by a seed-mediated growth process.[11] The resulting particles had a size of 76.9 ± 1.5 nm as determined by (TEM) statistics (at least 100 particles). Briefly, the PEG-stabilized particles were synthesized in three steps. First, so-called Wulff seeds are produced by reducing tetrachloroauric acid (HAuCl$_4$) with sodiumborohydrate (NaBH$_4$) in the presence of hexadecyltrimethylammonium bromide (CtaB). The obtained 2 nm large and single-crystalline particles are successively grown by two further synthesis steps until they reach the desired particle size. During the growing process, HAuCl$_4$, ascorbic acid, and CtaC serve as the Au precursor, reductant, and stabilizing agent. In order to guarantee kinetic control and thus control over the particle shape, a syringe pump system is used for the last growing step. The resulting particles were purified by centrifuge washing and set to a surfactant concentration of 2 mM. For the self-assembly step, a ligand exchange was performed from CtaC to PEG-6k-SH.[30]

Template-Assisted Colloidal Self-Assembly. Prior to the assembly experiment, the microscopy glass slide (Menzel) was hydrophobized via gas-phase deposition of trichloro(1*H*,1*H*,2*H*,2*H*-perfluorooctyl)silane (448931, Sigma-Aldrich) at 60 °C for 3 h. Using a custom-made setup, 15 μL nanoparticle suspension [0.5 mg mL^{-1} gold, 0.25 mM sodium dodecyl sulfate, 0.025 wt % Triton X-45 (Sigma-Aldrich)] was confined between the template and the stationary glass slide (gap ≈ 500 μm) and the patterned substrate was withdrawn underneath the droplet at a speed of 1 μm s^{-1} by a motorized translational stage (PLS-85, Physik Instrumente). Whereas the surfactants added tune surface tension and contact angle to enable selective deposition of the particles,[19] the elevated solution pH value (pH 9) in the case of insulin coating ensures colloidal stability by electrostatic repulsion. The experiment was carried at 12 K above dew point. Further experimental details can be found in Supporting Information Text T2. Prior to optical characterization, the samples were index-matched by spin-coating UV-curable PDMS at 2000 rpm for 60 s.

UV−Vis−NIR Spectroscopy. Optical spectra were measured on a Cary 5000 spectrometer (Agilent, USA) using the Cary universal measurement accessory. The spot size was fixed to 3 × 4 mm^2 for UV−vis and NIR detectors. All the dispersion spectra were measured

by rotating the sample plane by keeping the plane of incidence constant.

Bright-Field Imaging. Images of the self-assembled nanostructures were captured by a Nikon Eclipse LV100ND microscope using a bright-field reflection microscopy setup. The surface was illuminated by a halogen light source (12 V, 50 W) focused by a 5× objective lens. Images were taken by a Nikon DS-Fi2 5.24-megapixel charge coupled device (CCD) camera and analyzed by Nikon imaging (NIS-Elements) software. Unpolarized light was used for all the images.

Bright-Field Spectroscopy. Spectroscopy under strain was performed with a home-built stretching device on a transmission microscope (Nikon Ti-U). The microscope was equipped with an IsoPlane-160 spectrometer and a PIXIS: 256 CCD camera (Princeton Instruments). The light beam (100 W halogen lamp) was focused with a bright-field condenser (Ti-C-LWD) and collected with a 60× air objective (CFI S Plan Fluor ELWD, NA 0.7). Spectra with 383 nm bandwidths were taken at 600 and 750 nm center wavelength for 0.5 s (New Technologies and Consulting/Harald Giessen, NT&C software). All spectra were corrected by subtraction of the CCD's dark current and normalized by a reference spectrum, which was recorded in an area without particles.

Spectroscopic Ellipsometry. RC2-D dual rotating compensator ellipsometer, ex situ with automated tip and tilt alignment stage from J.A. Woollam Ellipsometer Solutions was used for refractive index measurements. Further, measured data were fitted with Complete Ease software via the Cauchy substrate model.

FDTD Simulations. We have used a commercial software package for performing FDTD simulations (Lumerical FDTD, version 8.16).[31] For the simulation of the optical response, a plane wave source was used and the frequency points were set to be half the wavelength span. Two-dimensional (2D) frequency-domain field and power monitors (transmission and reflection monitors in the direction parallel to the lattice plane) were used to obtain the optical responses of the system. For the dielectric properties of gold, data from Johnson and Christy were fitted using six coefficients with an rms error of 0.2.[32] The refractive index of the substrate (UV-PDMS) was measured via spectroscopic ellipsometry (Figure S6). In order to determine the electric field and surface charge density, we simulated the model at the LSPR and hybrid mode (SLR) frequencies. Periodic boundary conditions were used for square plasmonic lattice simulations in the lattice plane direction. For stretching, periodicities of the lattice in both the directions were increased based on the tabulated Poisson's ratio. All simulations reached an auto-shutoff of at least 10^{-7}. For the best simulation stability, the mesh area was chosen to be at least 100 nm larger than the existing structure in the lattice plane direction.

Atomic Force Microscopy. For evaluating the topography of photoresist masters and PDMS molds, atomic force microscopy (AFM) height images were measured using a Dimension 3100 NanoScope V (Bruker, USA) operated in tapping mode. Stiff cantilevers (40 N m^{-1}, 300 kHz, Tap300, Budget Sensors, and Bulgaria) were employed.

Scanning Electron Microscopy. A NEON 40 FIB-SEM workstation (Carl Zeiss Microscopy GmbH, Oberkochen, Germany) operated at accelerating voltage (electron high tension) of 1 kV was used for capturing scanning electron micrographs.

■ ASSOCIATED CONTENT

Ⓢ Supporting Information

The Supporting Information is available free of charge on the ACS Publications website at DOI: 10.1021/acsami.9b08871.

> Details on LIL, AFM of templates, TASA, hybridization model of SLR, comparison of quality factor, determination of fill factor, characterization of spacial order, mechano-tunability, in situ dark-field microscopy, and refractive index evaluation (PDF)

■ AUTHOR INFORMATION

Corresponding Authors
*E-mail: koenig@ipfdd.de (T.A.F.K.).
*E-mail: fery@ipfdd.de (A.F.).

ORCID ⊚
Jonas Schubert: 0000-0002-5728-9779
Tobias A. F. König: 0000-0002-8852-8752
Andreas Fery: 0000-0001-6692-3762

Author Contributions
‖Equal contribution: V.G., P.T.P.

Notes
The authors declare no competing financial interest.

■ REFERENCES

(1) Rycenga, M.; Cobley, C. M.; Zeng, J.; Li, W.; Moran, C. H.; Zhang, Q.; Qin, D.; Xia, Y. Controlling the Synthesis and Assembly of Silver Nanostructures for Plasmonic Applications. *Chem. Rev.* **2011**, *111*, 3669−3712.

(2) Chu, Y.; Schonbrun, E.; Yang, T.; Crozier, K. B. Experimental Observation of Narrow Surface Plasmon Resonances in Gold Nanoparticle Arrays. *Appl. Phys. Lett.* **2008**, *93*, 181108.

(3) Luk'Yanchuk, B.; Zheludev, N. I.; Maier, S. A.; Halas, N. J.; Nordlander, P.; Giessen, H.; Chong, C. T. The Fano Resonance in Plasmonic Nanostructures and Metamaterials. *Nat. Mater.* **2010**, *9*, 707−715.

(4) Wang, W.; Ramezani, M.; Väkeväinen, A. I.; Törmä, P.; Rivas, J. G.; Odom, T. W. The Rich Photonic World of Plasmonic Nanoparticle Arrays. *Mater. Today* **2018**, *21*, 303−314.

(5) Kravets, V. G.; Kabashin, A. V.; Barnes, W. L.; Grigorenko, A. N. Plasmonic Surface Lattice Resonances: A Review of Properties and Applications. *Chem. Rev.* **2018**, *118*, 5912−5951.

(6) Hessel, A.; Oliner, A. A. A New Theory of Wood's Anomalies on Optical Gratings. *Appl. Opt.* **1965**, *4*, 1275−1297.

(7) Mayer, M.; Schnepf, M. J.; König, T. A. F.; Fery, A. Colloidal Self-Assembly Concepts for Plasmonic Metasurfaces. *Adv. Opt. Mater.* **2019**, *7*, 1800564.

(8) Tseng, M. L.; Yang, J.; Semmlinger, M.; Zhang, C.; Nordlander, P.; Halas, N. J. Two-Dimensional Active Tuning of an Aluminum Plasmonic Array for Full-Spectrum Response. *Nano Lett.* **2017**, *17*, 6034−6039.

(9) Volk, K.; Fitzgerald, J. P. S.; Ruckdeschel, P.; Retsch, M.; König, T. A. F.; Karg, M. Reversible Tuning of Visible Wavelength Surface Lattice Resonances in Self-Assembled Hybrid Monolayers. *Adv. Opt. Mater.* **2017**, *5*, 1600971.

(10) Yang, A.; Hryn, A. J.; Bourgeois, M. R.; Lee, W.-K.; Hu, J.; Schatz, G. C.; Odom, T. W. Programmable and Reversible Plasmon Mode Engineering. *Proc. Natl. Acad. Sci. U.S.A.* **2016**, *113*, 14201−14206.

(11) Steiner, A. M.; Mayer, M.; Seuss, M.; Nikolov, S.; Harris, K. D.; Alexeev, A.; Kuttner, C.; König, T. A. F.; Fery, A. Macroscopic Strain-Induced Transition from Quasi-Infinite Gold Nanoparticle Chains to Defined Plasmonic Oligomers. *ACS Nano* **2017**, *11*, 8871−8880.

(12) Kraus, T.; Malaquin, L.; Schmid, H.; Riess, W.; Spencer, N. D.; Wolf, H. Nanoparticle Printing with Single-Particle Resolution. *Nat. Nanotechnol.* **2007**, *2*, 570−576.

(13) Ni, S.; Wolf, H.; Isa, L. Programmable Assembly of Hybrid Nanoclusters. *Langmuir* **2018**, *34*, 2481−2488.

(14) Jiang, W.; Ma, Y.; Zhao, J.; Li, L.; Xu, Y.; Guo, H.; Song, L.; Chen, Z.; Zhang, Y. Robust Assembly of Colloidal Nanoparticles for Controlled-Reflectance Surface Construction. *ACS Appl. Mater. Interfaces* **2019**, *11*, 23773−23779.

(15) Sarkar, S.; Gupta, V.; Kumar, M.; Schubert, J.; Probst, P. T.; Joseph, J.; König, T. A. F. Hybridized Guided-Mode Resonances via Colloidal Plasmonic Self-Assembled Grating. *ACS Appl. Mater. Interfaces* **2019**, *11*, 13752−13760.

(16) Khlopin, D.; Laux, F.; Wardley, W. P.; Martin, J.; Wurtz, G. A.; Plain, J.; Bonod, N.; Zayats, A. V.; Dickson, W.; Gérard, D. Lattice Modes and Plasmonic Linewidth Engineering in Gold and Aluminum Nanoparticle Arrays. *J. Opt. Soc. Am. B* **2017**, *34*, 691.

(17) Auguié, B.; Barnes, W. L. Collective Resonances in Gold Nanoparticle Arrays. *Phys. Rev. Lett.* **2008**, *101*, 143902.

(18) Auguié, B.; Barnes, W. L. Diffractive Coupling in Gold Nanoparticle Arrays and the Effect of Disorder. *Opt. Lett.* **2009**, *34*, 401−403.

(19) Ni, S.; Leemann, J.; Wolf, H.; Isa, L. Insights into Mechanisms of Capillary Assembly. *Faraday Discuss.* **2015**, *181*, 225−242.

(20) Ni, S.; Klein, M. J. K.; Spencer, N. D.; Wolf, H. Capillary Assembly of Cross-Gradient Particle Arrays Using a Microfluidic Chip. *Microelectron. Eng.* **2015**, *141*, 12−16.

(21) Chanana, M.; RiveraGil, P.; Correa-Duarte, M. A.; Liz-Marzán, L. M.; Parak, W. J. Physicochemical Properties of Protein-Coated Gold Nanoparticles in Biological Fluids and Cells before and after Proteolytic Digestion. *Angew. Chem., Int. Ed.* **2013**, *52*, 4179−4183.

(22) Lowe, S.; O'Brien-Simpson, N. M.; Connal, L. A. Antibiofouling Polymer Interfaces: Poly(Ethylene Glycol) and Other Promising Candidates. *Polym. Chem.* **2015**, *6*, 198−212.

(23) Humphrey, A. D.; Barnes, W. L. Plasmonic surface lattice resonances on arrays of different lattice symmetry. *Phys. Rev. B: Condens. Matter Mater. Phys.* **2014**, *90*, 075404.

(24) Wang, D.; Bourgeois, M. R.; Lee, W.-K.; Li, R.; Trivedi, D.; Knudson, M. P.; Wang, W.; Schatz, G. C.; Odom, T. W. Stretchable Nanolasing from Hybrid Quadrupole Plasmons. *Nano Lett.* **2018**, *18*, 4549−4555.

(25) Danilov, A.; Tselikov, G.; Wu, F.; Kravets, V. G.; Ozerov, I.; Bedu, F.; Grigorenko, A. N.; Kabashin, A. V. Ultra-Narrow Surface Lattice Resonances in Plasmonic Metamaterial Arrays for Biosensing Applications. *Biosens. Bioelectron.* **2018**, *104*, 102−112.

(26) Bastús, N. G.; Comenge, J.; Puntes, V. Kinetically Controlled Seeded Growth Synthesis of Citrate-Stabilized Gold Nanoparticles of up to 200 nm: Size Focusing versus Ostwald Ripening. *Langmuir* **2011**, *27*, 11098−11105.

(27) Strozyk, M. S.; Chanana, M.; Pastoriza-Santos, I.; Pérez-Juste, J.; Liz-Marzán, L. M. Protein/Polymer-Based Dual-Responsive Gold Nanoparticles with pH-Dependent Thermal Sensitivity. *Adv. Funct. Mater.* **2012**, *22*, 1436−1444.

(28) Dewald, I.; Isakin, O.; Schubert, J.; Kraus, T.; Chanana, M. Protein Identity and Environmental Parameters Determine the Final Physicochemical Properties of Protein-Coated Metal Nanoparticles. *J. Phys. Chem. C* **2015**, *119*, 25482−25492.

(29) Höller, R. P. M.; Dulle, M.; Thomä, S.; Mayer, M.; Steiner, A. M.; Förster, S.; Fery, A.; Kuttner, C.; Chanana, M. Protein-Assisted Assembly of Modular 3D Plasmonic Raspberry-like Core/Satellite Nanoclusters: Correlation of Structure and Optical Properties. *ACS Nano* **2016**, *10*, 5740−5750.

(30) Matricardi, C.; Hanske, C.; Garcia-Pomar, J. L.; Langer, J.; Mihi, A.; Liz-Marzán, L. M. Gold Nanoparticle Plasmonic Super-lattices as Surface-Enhanced Raman Spectroscopy Substrates. *ACS Nano* **2018**, *12*, 8531−8539.

(31) Lumerical Inc. Lumerical https://www.lumerical.com/products/fdtd-solutions/ (accessed Feb 10, 2019).

(32) Johnson, P. B.; Christy, R. W. Optical Constants of the Noble Metals. *Phys. Rev. B: Solid State* **1972**, *6*, 4370.

6.3   Tunable Circular Dichroism by Photoluminescent Moiré Gratings

Tunable Circular Dichroism by Photoluminescent Moiré Gratings

Olha Aftenieva, Max J. Schnepf, Börge Mehlhorn and Tobias A. F. König*

*corresponding author

Author contribution statement

OA and MS carried out the experiments and contributed equally to the work. **TK** encouraged OA, MS and BM to investigate the simulation, fabrication and optical spectroscopy methods as well as supervised the execution ad findings of this work. **TK** made a significant contribution to the conception and design of the work. Through the simulation, fabrication and optical spectroscopy methods, the author **TK** made a significant contribution to the acquisition, analysis and interpretation of the data. All authors provided critical feedback and helped shape the research, analysis and manuscript.

Tunable Circular Dichroism by Photoluminescent Moiré Gratings

Olha Aftenieva, Max Schnepf, Börge Mehlhorn, and Tobias A. F. König*

In nanophotonics, there is a current demand for ultrathin, flexible nanostructures that are simultaneously easily tunable, demonstrate a high contrast, and have a strong response in photoluminescent polarization. In this work, the template-assisted self-assembly of water-dispersed colloidal core–shell quantum dots into 1D light-emitting sub-micrometer gratings on a flexible substrate is demonstrated. Combining such structures with a light-absorbing metallic counterpart by simple stacking at various angles results in a tunable Moiré pattern with strong lateral contrast. Furthermore, a combination with an identical emitter-based grating leads to a chiroptical effect with a remarkably high degree of polarization of 0.72. Such a structure demonstrates direct circular polarized photoluminescence, for the first time, without a need for an additional chiral template as an intermediary. The suggested approach allows for reproducible, large-area manufacturing at reasonable costs and is of potential use for chiroptical sensors, photonic circuit applications, or preventing counterfeit.

1. Introduction

A Moiré effect occurs when repetitive structures such as gratings are superimposed against each other with a relative difference in lattice constant or in-plane rotation angle.[1] By tuning these parameters, Moiré pattern can be accurately controlled and applied for measuring strain deformation,[2] precise alignment in optical security labels,[3] and biosensors.[4] In addition, configurations with the Moiré effect show more optical features than their primary components.[5] Formation of Moiré pattern can be realized through interference,[5,6] block copolymer,[7]

nanosphere,[8] or imprinting lithography.[9] These approaches result in large-area quasicrystal patterns, being, however, permanently inscribed in the medium and, thus, hindering the tunability of optical properties. An alternative strategy implies separate manufacturing of periodic structural components and generating a Moiré interference by bringing them into close contact. The simplest periodic structures to consider are 1D gratings that, when stacked at various angles, result in two-and-a-half-dimensional chiral metasurface. Such structures demonstrate strong circular dichroism (CD). With crossed gold gratings, one could achieve CD, characterized through the degree of polarization, of 0.3.[10] When using aluminum helically stacked lattices, the abovementioned effect was 2.5 times stronger and observed over the entire visible and near-infrared wavelengths range.[11] By taking advantage of the surface lattice resonance from the metal nanoparticle arrangements, one can reach comparable effect strength.[12] Such metal-based chiral structures, however, suffer from the non-radiative ohmic losses that limits their usage to the absorption-based applications.

To exploit the chiroptical effect for the light generation, one has to introduce a light-emitting component. Colloidal quantum dots (QDs) appear to be the optimal candidates, featuring broadband absorption, size- and material-controllable emission wavelength, high quantum yields, and photostability.[13,14] To directly induce the circularly polarized photoluminescence, two principal strategies have been suggested: through connecting chiral ligands to the QDs surface[15] or by combining achiral QDs with chiral plasmonic metasurfaces. The first approach resulted in relatively weak induced chirality and required elaborate surface modifications. On the contrary, combination with chiral metal nanostructures enabled strong circularly polarized emission. For this, the CD response of the template should match either absorption[16] or emission bands of the QDs.[17]

The necessity to have a chiral plasmonic template with inherent energy losses and quenching effects hinders such light-emitting metasurfaces from practical applications. On the contrary, assembling emitters into chiral structures directly enables loss-free polarized photoluminescence. On this notion, special care must be taken about the optical performance. To avoid significant quenching of the photoluminescence for closely packed QDs,[18] one can utilize the core–shell QDs, where the distance between the emitting centers is defined by the shell thickness.[19] Moreover, to match multiple virtual hybridization

O. Aftenieva, Dr. M. Schnepf, B. Mehlhorn, Dr. T. A. F. König
Leibniz Institute for Polymer Research Dresden e.V.
Hohe Straße 6, 01069 Dresden, Germany
B. Mehlhorn
Leibniz Institute for Solid State and Materials Research Dresden e.V.
Helmholtzstraße 20, 01069 Dresden, Germany
Dr. T. A. F. König
Center for Advancing Electronics Dresden (cfaed)
Technische Universität Dresden
01062 Dresden, Germany
E-mail: koenig@ipfdd.de

The ORCID identification number(s) for the author(s) of this article can be found under https://doi.org/10.1002/adom.202001280.

**ADVANCED
SCIENCE NEWS**
www.advancedsciencenews.com

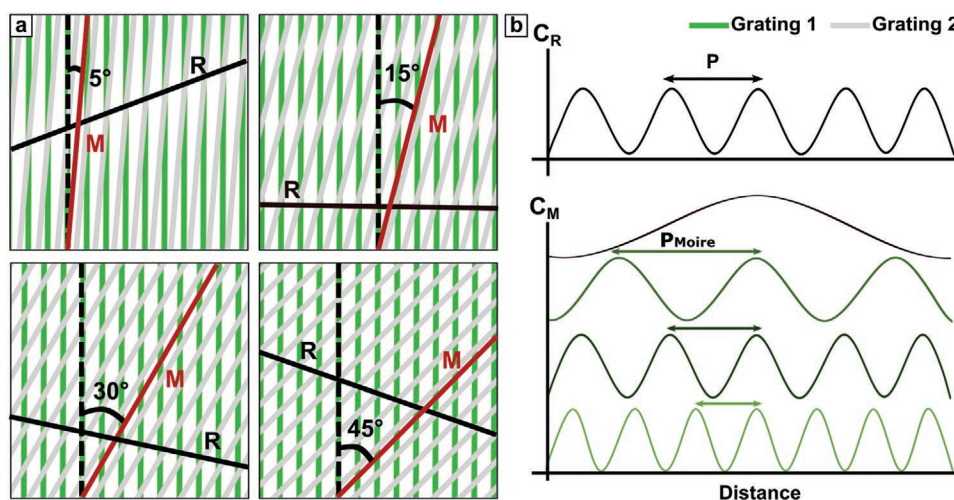**ADVANCED
OPTICAL
MATERIALS**
www.advopticalmat.de

Figure 1. Exemplary interference patterns and their characterization. a) Moiré patterns generated by two superimposed gratings (as shown with green and gray lines) with equal periodicities at various orientation angles. b) Contrast profile plots along principal directions (*M*: crossing the Moiré interference lines; *R*: parallel to them).

states created by the Moiré pattern and observe a chiral response over a large wavelength span, it might be beneficial to employ emitters with broadband absorption, as well as emission, spectra.[16,20]

Until now, production of periodic light-emitting structures with the features on the scale of the emitter wavelength remained to be challenging, and the direct arrangement of emitters into chiral structures providing a pure circular-polarized light-emitting device has not been demonstrated. Template stripping [20,21] and electron beam lithography [22] techniques potentially allow for high-resolution patterning, being, however, cost-inefficient and not applicable for large-area manufacturing. To produce patterned emitter-based structures on a centimeter-scale area, simple casting, Langmuir–Blodgett deposition, dip coating, inkjet printing, or photopatterning could be applied. However, these methods mostly result in films without sufficient uniformity and control over the film thickness.[23–25] As an alternative, one can employ contact printing techniques[26–29] to create periodic micrometer-sized structures on a centimeter scale through the confinement self-assembly of nanocrystals just by using a structured stamp. However, due to the generally poor cohesion of quantum emitters and the strong influence of artifacts on the wetting behavior, it remains a difficult task to assemble quantum emitters into a sub-micrometer grating.

To overcome this challenge, one has to adjust the surface properties of the stamping template, and utilize particles with a size much smaller than the gap. The latter is easily fulfilled for the QDs that are few nanometers in diameter. To allow the water-based colloidal solution to fill the gaps in the structured template, the contact angle must be sufficiently decreased through the surface activation. The stability of colloidal QDs in an aqueous solution is ensured, in this case, by thioglycolic acid (TGA) through the electrostatic repulsion of carboxylic groups,[30] that additionally promote stronger adhesion of QDs to the substrate than to the stamping template. Then, during drying, van der Waals forces cause a strong cohesion between the particles. Overall, the abovementioned printing technique creates emitter-based sub-micrometer metasurfaces that can be

utilized for multiple photonic applications, including band edge and near-infrared lasing,[21,26] photodetection,[27,28] fabrication of light-emitting diodes,[31] security labels,[32] parity-time symmetric gain–loss systems, where the high contrast is required together with an ability to change the phase shift of the contributing components, or for generating a polarized light source.

In this work, the optical effects induced by superposition of two 1D gratings, comprised of photoluminescent semiconductor material or a metal, were explored. Their fabrication with a low-effort lithography-based approach gives a competitive advantage among other high-resolution techniques. Both gratings were produced on a centimeter-scale area: the metal component was introduced on a rigid substrate through the metal vapor deposition, and the emitter-based grating was printed by the soft-lithographic method on a flexible substrate, to ensure close contact between the structures. A simple stacking and relative in-plane twisting of those 1D grids enabled the robust appearance of fluorescent Moiré patterns that demonstrated chiral photoluminescence without any additional chiral building blocks. This suggests utilizing such structures as functional chiroptical sensors, or in optoelectronic devices, by creating a tunable optical bandgap.

2. Results and Discussion

A typical representation of the Moiré effect is illustrated in **Figure 1**. The supra-periodic pattern is formed by superimposing two 1D gratings (gratings 1 and 2) with the same lattice constant at various relative in-plane rotation angles. Its appearance is then solely defined by geometric parameters of the lattices and relative rotation and can be analytically predicted with high precision (see Figure S1 in the Supporting Information). In its turn, the visibility of the produced supra-periodic pattern depends on the amplitude of the lateral contrast, i.e., the difference between the maximum and minimum luminance of a selected profile. For a complete lateral characterization, one can measure the contrast amplitude along two principal directions: the *M*-axis follows one of the gratings, crossing the Moiré
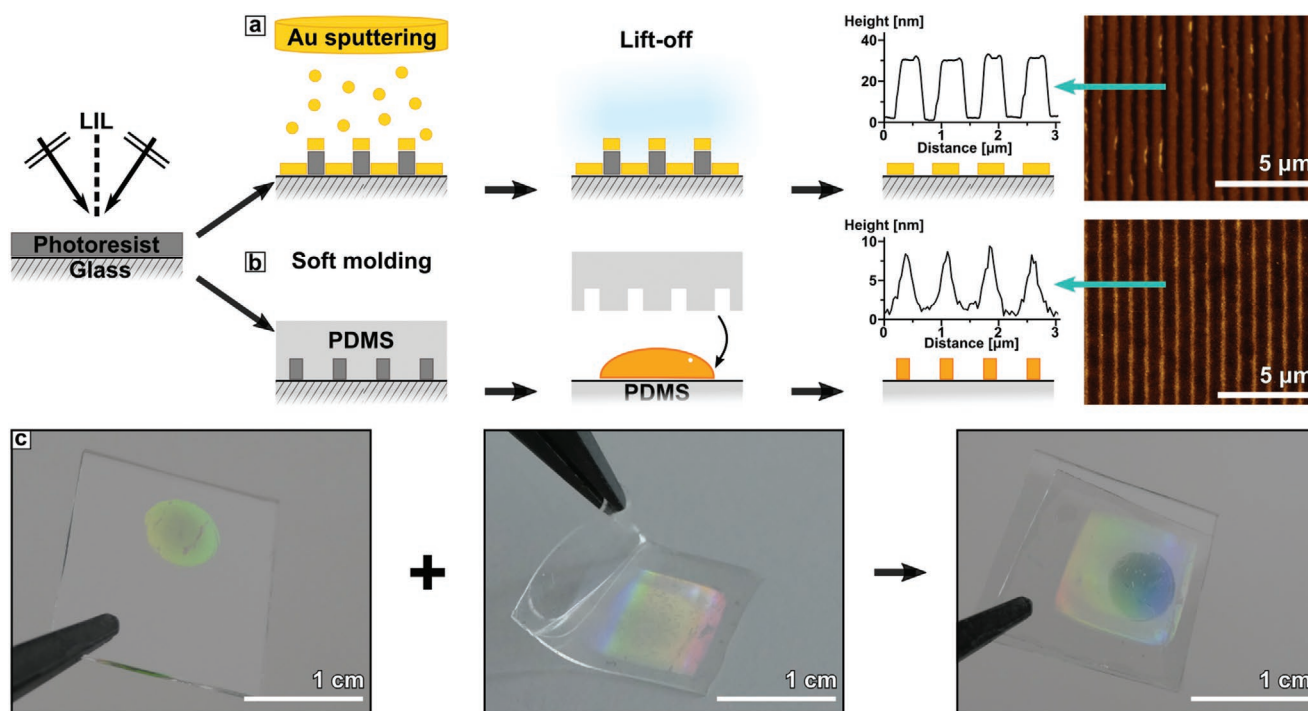
**ADVANCED
SCIENCE NEWS**

www.advancedsciencenews.com

**ADVANCED
OPTICAL
MATERIALS**

www.advopticalmat.de

Figure 2. a) Metal grating, fabricated by laser interference lithography (LIL), sputtering of Au, and lift-off process. b) Emitter grating, produced by confinement self-assembly from core–shell quantum emitters with a soft polymer PDMS template. Geometric parameters, determined by AFM: a) periodicity of 790 nm and height of 30 nm, b) periodicity of 820 nm and height of 10 nm. c) Photographs of the metal grating on the glass substrate, superimposed with emitter grating on flexible PDMS substrate.

pattern that appears as a set of interference lines, and the R-axis serves as a reference and goes parallel to the lines of a Moiré pattern. Thus, contrast along the M-axis (C_M) reflects a profile, governed by the Moiré pattern, while C_R shows the contrast profile, dictated by one of the gratings. The Moiré pattern itself is defined through the relative rotation of the two stacked lattices, thus, C_M can be laterally tuned across the large range of distances, since the positions of maximum and minimum intensities are shifted through the changing angle. At the same time, the contrast along the R-direction, being independent of the Moiré pattern, is fixed by the lattice constant.

In further experiments, gratings 1 and 2, having the same lattice constant of ≈800 nm, are systematically replaced by one of these materials: gold (Au) or emitting self-assembled semiconductor nanocrystals. To ensure the practical applicability of such gratings, one has to make sure that manufacturing includes low-cost and reproducible techniques. Therefore, laser interference lithography (LIL) and wet-chemical processing were employed. Au periodic structures were obtained after subsequent sputtering and in-solution lift-off process, as described in **Figure 2**a. Fabrication of the emitter gratings involved polydimethylsiloxane (PDMS) soft molding process, as represented in Figure 2b. A defined volume of nanocrystals was then drop-casted on the flexible substrate, followed by applying the PDMS master template and drying under pressure (flexibility of at least one of the substrates is required to bring the gratings in close contact with each other and ensure the near-field energy transfer). The periodic structure was exposed after peeling-off the PDMS master. Both gratings were characterized by atomic force microscopy (AFM), revealing

periodic structures with uniform geometric parameters over a large scale (see Figure 2c).

Moiré interference effects were first compared between various combinations of periodic structures at the same angle (see **Figure 3**): emitter and emitter (E&E), metal and metal (M&M), and metal and emitter (M&E). A single, emitter-only grating was used as a reference. The photoluminescent signal was captured by confocal fluorescent microscopy (CFM) imaging under the excitation of 405 nm laser that selectively excited the quantum emitters. In such a configuration, metal grating appeared as dark background, since the reflected excitation light was filtered out and the fluorescence of bulk Au was not detected. To observe the interference of M&M structure, 640 nm laser was used, and the reflected light was collected by the CFM setup. According to the abovementioned formalism of principal axes, to characterize the lateral contrast in various grating combinations, the axes were assigned in the following way: the M-axis always followed the line of assembled QDs in E&E, M&E, and emitter-only gratings, or one of the Au lines in the M&M combination, while the R-axis was parallel to the lines of the Moiré pattern. It is important to note that R and M are not perpendicular to each other and their orientation depends on the relative rotation of the gratings.

To characterize the lateral contrast along R- and M-directions, the following notions were used: single emitter grating was considered as a contrast reference with a maximum intensity value C_0 measured along the M-axis and corrected to the background signal. The contrast C was calculated as the difference between the maximum and minimum value, normalized to C_0 for both directions. The contrast ratio C_M for the emitter grating only
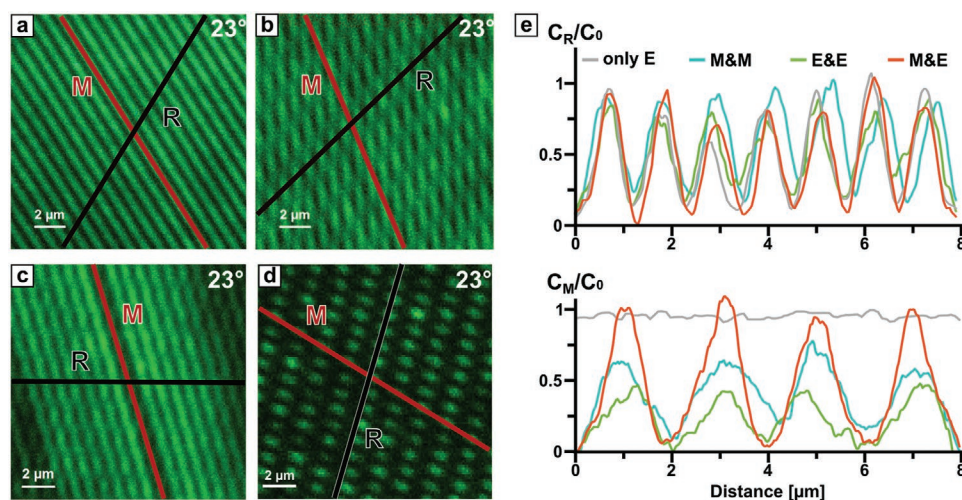
ADVANCED
SCIENCE NEWS
www.advancedsciencenews.com

ADVANCED
OPTICAL
MATERIALS
www.advopticalmat.de

Figure 3. Various combinations of metal and emitter gratings with a fixed lattice constant (≈800 nm) and relative rotation angle (≈23°). a) CFM image of an emitter grating only. The drawn R- and M-axes (shown in black and red lines) indicate principal directions to characterize the contrast amplitude. b–d) CFM images of superimposed metal (b), emitter (c) gratings as well as (d) a combination of both. e) The intensity profiles along *R*- and *M*-directions for the various cases. The intensity was shifted to 0 for clarity and normalized to the reference value C_0-intensity signal, recorded from the emitter grating only.

was then considered as an error rate of 11% for all the following measurements. Along the *R*-axis, parallel to the Moiré lines, the contrast was comparable within all four samples, resembling the contrast produced by one of the gratings. Following the intensity profile, produced by the Moiré interference, the contrast of ≈70% can be achieved for combined identical gratings. However, when stacking absorbing and emitting counterparts, the contrast can be improved by 30% and is comparable to the contrast of only a single emitter grid (exact C_M and C_R values are given in Section T3 in the Supporting Information). This combination allows for high-contrast patterns, where the positions of high/low intensity are not strictly fixed and can be tuned through the in-plane twisting of the superimposed substrates, as demonstrated in **Figure 4**.

Such a simple approach enables obtaining varied intensity profiles of different periodicities within one structure

(as shown in Figure 4b). Those patterns are defined by the Moiré supra-periodicity and can be as twice as small, or far higher than the initial lattice constant (see Equation (S1) in the Supporting Information), with the lateral resolution limit reaching $\frac{\lambda}{\pi \text{NA}} \approx 143$ nm, where $\lambda = 405$ nm represents the central wavelength of the laser and NA = 0.9.

Besides lateral contrast, one can consider it in a vertical direction by changing the spacing between metal and emitter gratings. For sensor applications these distance investigations are important, because the analyte layer can be placed at the most sensitive point between the grids. Thus, for a proof of concept, a transparent polymer film of polymethyl-methacrylate (PMMA) spacer was introduced in between the two gratings (**Figure 5**).

The contrast was maintained in the range of several hundreds of nanometers that is within at least half of the vertical
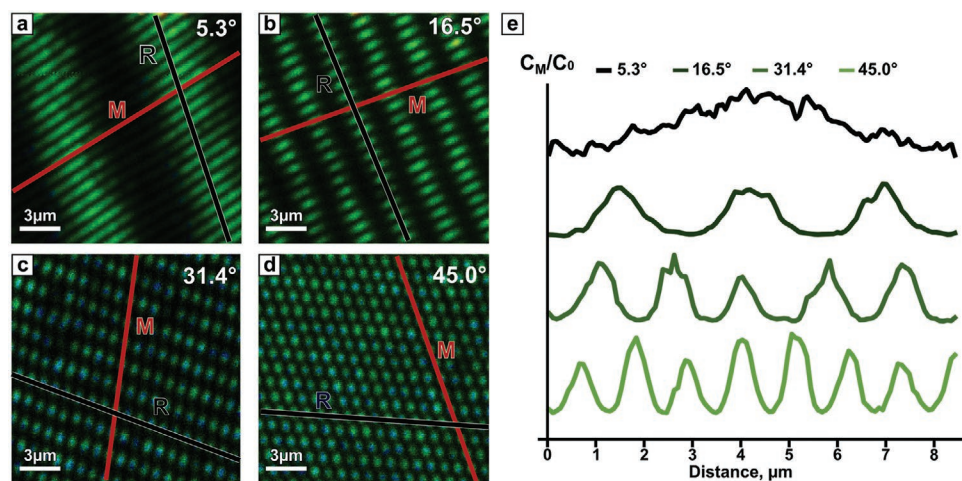

Figure 4. Interference pattern of a superimposed metal and emitter lattices at different angles of orientation. a–d) CFM images at 5.3°, 16.5°, 31.4°, and 45.0° relative rotation angles, respectively, as well as e) the corresponding intensity profiles of the Moiré interference pattern.
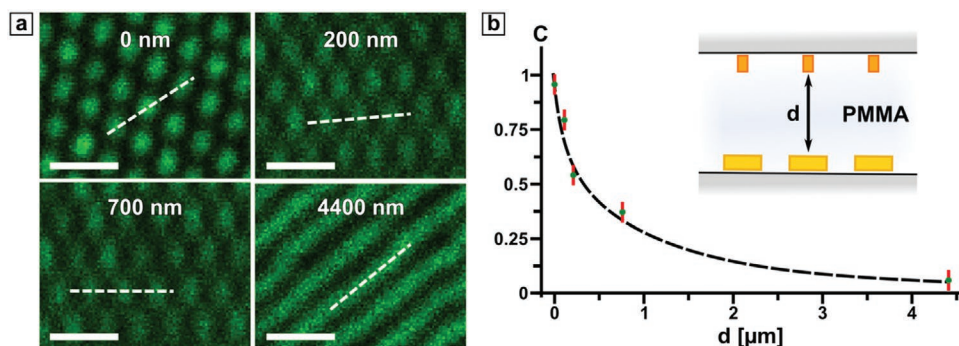
Figure 5. Implementation of a PMMA spacer material to study the interaction depth between the metal and emitter lattice. a) The CFM images show the Moiré inference at spacer distances between 100 nm and 4.4 µm. The contrast C was measured along the white dotted line that follows one of the emitter lines and crosses the lines of the Moiré pattern, if visible. The scale bar is 2 µm. b) The contrast with respect to the spacer thickness. The error is indicated by the red vertical line.

resolution of the objective, estimated as $\frac{2n\lambda}{\mathrm{NA}^2} \approx 1490$ nm, with the refractive index n of PMMA being 1.49. It was sufficient to observe the Moiré pattern, even with more than a two-fold decrease in contrast. The change of contrast amplitude with the interlattice distance (as shown in Figure 5b) features power-law decay and supports the near-field nature of the observed interaction. Moreover, the contrast quality was maintained even on the flexible substrate that was constantly prone to mechanical deformations over five months of sample utilization.

The considered configuration of two 1D gratings with a possibility of an arbitrary in-plane rotation also suggests its benefit for creating an emitter-based circular polarizer, since superposition of similar, but only metal-based structures demonstrated strong CD effect.[11] In our case, however, it implies the transformation of linearly polarized excitation light to the circularly polarized emission. This chiroptical effect was measured and quantitatively evaluated as a degree of polarization at the maximum emission wavelength $g_{\mathrm{PL}} = \frac{2(I_{\mathrm{RCP}} - I_{\mathrm{LCP}})}{(I_{\mathrm{RCP}} + I_{\mathrm{LCP}})}$, where $I_{\mathrm{RCP/LCP}}$ are the intensities of the detected right (RCP) or left circularly polarized (LCP) emission light, respectively. Spectral analysis of the output light, presented in Section T2 in the Supporting Information, revealed the absence of a spectral shift in the emission of stacked M&E and E&E which allowed to consider the intensity values at the same wavelength of 608 nm. The experimental setup is shown in **Figure 6**a. The sample was excited at a normal incidence with a continuous p-polarized laser at 405 nm and the photoluminescence signal was collected in the forward direction after passing through a zero-order quarter-wave plate and a linear polarizer to dissect right and left polarization. The RCP and LCP emission intensities of two types of hybrid structures, M&E and E&E, were measured for several in-plane rotation angles, as summarized in Figure 6b.

When the emitter lines were combined with the metal grating, the maximum g_{PL} value of 0.19 was observed for 45° angle of relative rotation between the crossed lines, together with the comparable negative value −0.16 for −45°. Interestingly, the intrinsic chirality of the structure, where two emitter gratings are superimposed, is not only able to give rise of circularly polarized emission but also demonstrates remarkably high g_{PL}-factors: 0.64 and −0.72 for the left and right rotation of the

stacked gratings, respectively. The absence of perfect symmetry for the opposite rotations was possibly caused by slightly mismatched angles and geometrical variations within the gratings. The obtained values are comparable with the ones reported so far in the literature, where achiral QDs were combined with the chiral metal template: 0.34 for the ion-beam patterned gold film[16] and 0.95 when less lossy silver nanoarcs were employed.[17] The suggested structure is, on the other hand, completely loss-free and features low-effort self-assembly of colloidal QDs that can be used as a compact circular polarizer for on-chip photonic circuits and benefit as a component for an optical isolator.
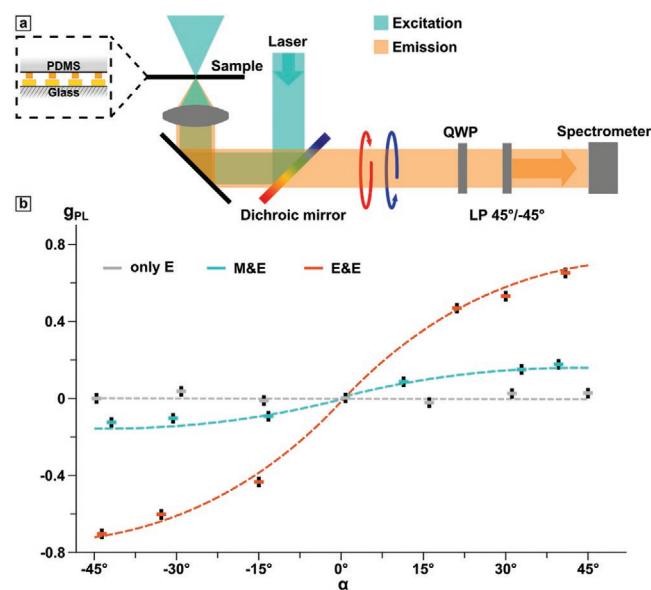

Figure 6. Measurement of polarized photoluminescence. a) Experimental setup shows the laser excitation (polarization of the beam is shown with a blue arrow and the direction of propagation with pink) and analysis of the reflected light using a $\lambda/4$ wave plate (QWP) and linear polarizer (LP) that is oriented at 45° or −45° to the fast axis of the QWP. b) The g_{PL}-factor at 608 nm with respect to various orientation angles for superimposed gratings. The error rate of 0.008, marked as a vertical black line, was measured as the degree of polarization of only the emitter grating.
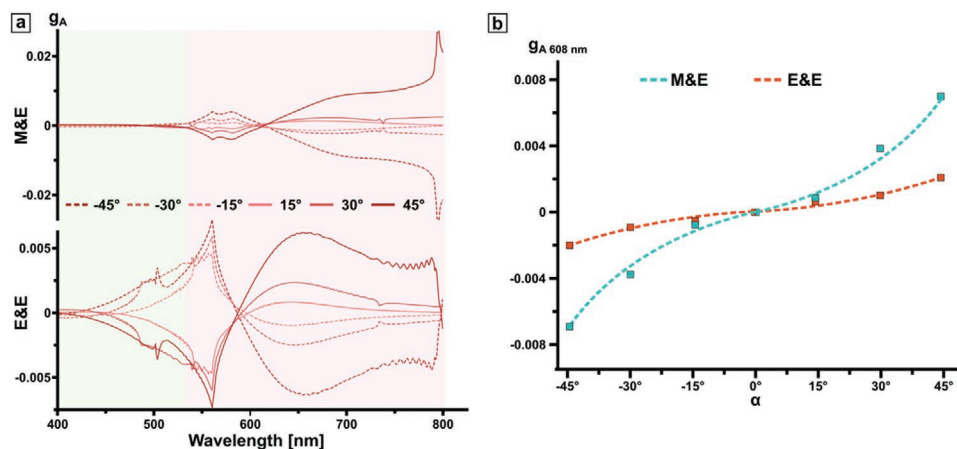
ADVANCED
SCIENCE NEWS
www.advancedsciencenews.com

ADVANCED
OPTICAL
MATERIALS
www.advopticalmat.de

Figure 7. Electromagnetic simulations of polarized photoluminescence. a) The chiral response of stacked M&E and E&E at several complementary angles α between $-45°$ and $45°$. Absorption and emission bands of the QDs are shown in light green and red respectively. b) The g_A-factor, measured at the maximum emission wavelength, with respect to various orientation angles for superimposed gratings.

To get further insight into the origin of the chiral response for those stacked structures, finite-difference time-domain (FDTD) simulations were performed (described in detail in Section T5 in the Supporting Information). In contrast to the experimental setup, where the structures were illuminated by the linearly polarized light and the chiral emission was detected, here both configurations were studied under the circularly polarized light, differentiating between the absorption ($A_{RCP/LCP}$) of RCP or LCP light. The degree of polarization was then estimated as $g_A = \dfrac{2(A_{RCP} - A_{LCP})}{(A_{RCP} + A_{LCP})}$.

The latter allows for uncovering the relation between the intrinsic circular dichroism of the crossed-bar-structures and the spectral properties of the emitter. As shown in **Figure 7**a, both stacked M&E and E&E structures demonstrate a mirror symmetry of the CD response for the opposite angles. Both combinations show a resonance near the maximum emission wavelength of the QDs that is characterized by crossing the zero g_A-value. The strongest CD signal corresponds the first and second diffraction orders at normal incidence (800 nm in air, and 560 nm in PDMS) that suggests the possible origin of chiral properties from the diffractive channels. Simulating CD effect in absorption gives further insight into the nature of the chiral emission: the strongest response matches the spectral region of photoluminescence that is in accordance with the results from one of the earlier reports.[17] Moreover, the broad emission spectrum of QDs allows for a broad wavelength range of the dichroic effect.

3. Conclusion

In conclusion, we propose a robust method for large-area manufacturing of light-emitting periodic 1D structures. When combined with a similar, but composed of light-absorbing gold, grating, the rising Moiré interference effect enables to achieve contrast values, significantly higher than when using material-wise identical gratings. The observed effect can be easily tuned over the micrometer-range distance and maintained for large

interlattice separation that opens up a possibility to replace the spacer with various functional materials, such as photosensitive polymers,[33] activated at the QDs emission wavelength, or electrically conductive resins,[34] to extend the discussed concept to stimuli-responsive metasurfaces. Moreover, such spatially controllable, yet strong contrast can be further employed for security labeling,[32] taking the advantage of the simplicity of mass production and optical durability. On the other hand, Moiré's combination of two emitter gratings allows for a strong photoluminescent chiroptical effect. It demonstrates, for the first time, a reconfigurable chiral arrangement of semiconductor QDs without the need for supplementary chiral building blocks. To further increase the degree of polarization, one can benefit from the colloidal self-assembly approach and change the lattice geometry simply by designing a different stamp to introduce more hybridization states or implement additional emitter-based or plasmonic 1D gratings into the structure to obtain a more complex lattice overlay.[35,36] Moreover, one can confine the proposed chiral Moiré system within a nanocavity, taking the advantage of fluorescent enhancement.[37]

4. Experimental Section

Laser Interference Lithography (LIL): To produce a structured film on the glass substrate, laser interference lithography was employed. Right before use, microscopy glass slides were divided into individual pieces (2 × 2 cm) and cleaned with isopropyl alcohol and ultrapure water in a 1:1 ratio by sonication for 20 min at 37 kHz. Positive photoresist (mr-P 1202LIL, Microresist Technology GmbH, Germany) was spin-coated onto the cleaned and dried under a stream of nitrogen substrate. Optimized spin parameters of 3000 rpm, acceleration of 1000 rpm s^{-1}, and total spin time of 33 s produced a thin film of 185 nm thickness, as confirmed by spectroscopic ellipsometry (RC2-DI, J.A. Woollam Co., Inc.). The coated substrates were baked at 95 °C for 60 s and further exposed to the 325 nm laser with a dose of 12 mJ cm^{-2}. The backside of the substrate was covered with black adhesive tape to avoid unnecessary reflections. To develop the exposed photoresist, the sample was submerged into the developer (mr-D 374/S, Microresist Technology GmbH, Germany) for 2 min, rinsed with ultrapure water, and dried under a stream of nitrogen.

**ADVANCED
SCIENCE NEWS**

www.advancedsciencenews.com

**ADVANCED
OPTICAL
MATERIALS**

www.advopticalmat.de

Fabrication of Gold Gratings: To fabricate a metal grating, a structured photoresist film was sputtered with gold at 20 rpm rotation speed with 0.1 nm s^{-1} until the thickness of 35–40 nm was achieved. The sacrificial photoresist was then dissolved with acetone and sonication at 45 °C, 37 kHz for 15 s.

Synthesis of Quantum Dots: AgInS/ZnS core/shell QDs were prepared in aqueous alkaline solutions as described in detail in earlier works.[19,30] In short, AgInS core was formed via breaking the Ag(I) and In(III) complexes with thioglycolic acid (TGA). A ZnS shell was then overgrown over the AgInS core by the addition of a Zn(II)–TGA complex. The formed QDs were then purified by centrifugation and redispersed in pure DI water. The final molar concentration of nanocrystals is determined through Ag(I) concentration, being 0.1 M. The atomic ratio of metals in the final AgInS/ZnS particles was kept at Ag/In/Zn = 1:4:8. The average size of the synthesized particles was reported to be 2–3.5 nm.[19] Further insight into the optical properties of QDs is given in Section T2 in the Supporting Information.

Soft Lithographic Fabrication of QD Grating: Produced by LIL, the structured film of a photoresist was replicated using an elastomeric silicone kit (Sylgard 184, Dow Chemicals, USA) with a ratio of prepolymer and catalyst of 10:1 to create the mold. The resulting mold was trimmed and fused by plasma treatment to an elastomeric silicone film in a petri dish. Right before use, the replica was immersed in 2 M hydrochloric acid for 30 min, rinsed with water, and dried under a stream of nitrogen to create a sufficiently hydrophilic surface. In the next step, 4 µL of a water-based dispersion of the colloidal solution (TGA-capped AgInS/ZnS QDs) was placed on a flat target substrate. The hydrophilized mold was placed on the quantum dot dispersion and 750 g of weights were placed on the Petri dish to ensure close contact between the mold and the flat surface. The assembly was dried for eight hours at room temperature and relative humidity of 32%. The stamp was then removed by peeling off. The quantum yield (QD) of the assembled structures was estimated up to 25% (see Section T2 in the Supporting Information).[38]

Confocal Fluorescence Microscopy: Confocal fluorescence microscopy (CFM) measurements were acquired with an inverted confocal scanning microscope (MicroTime 200, PicoQuant, Germany) with a 100× air objective (UPLFLN, NA 0.9, Olympus, Japan). For excitation, a picosecond pulsed p-polarized laser diode source (LDH-D-C-405, PicoQuant, Germany) with a center wavelength of 405 nm and a pulse width of 110 ps (full width at half-maximum, FWHM), driven at a repetition rate of 0.5 MHz. For fluorescence collection, a dichroic mirror (ZT405-442/510rpc-UF3, Chroma, USA), a long pass filter with a cut-off below 425 nm (FF01-519/LP, Shamrock, USA) and a single photon counting module (SPCM-AQRH, Excelitas, USA) were used. For evaluation, SymphoTime 64 2.3 was used. For spectroscopy measurements, the sample was excited under a constant illumination at 405 nm and the signal was recorded by the spectrometer Newton 920 (Oxford Instruments, UK). For time-correlated single-photon counting (TCSPC), a single-photon counting module (SPCM-AQRH, Excelitas, USA) was used. The lifetime was then calculated by SymphoTime 64 2.3. Fluorescence life time images were recorded at 1 µW excitation power (before objective) and a dwell time of 2 ms per pixel.

Finite-Difference Time-Domain (FDTD) Simulations: A commercial-grade simulator based on the finite-difference time-domain (FDTD) method is used to perform the calculations (FDTD: 3D electromagnetic simulator).[39] To simulate the optical response, two total-field scattered-field sources (λ = 400–800 nm) were used, illuminating the structure at a normal incidence with a relative phase shift of 90° or −90° for right- and left-circularly polarized light. Perfectly matching layer boundary conditions were used in the Y-direction, and periodic boundary conditions were used along X- and Z-axes. The grating lines were represented by parallelepipeds with the dimensions, matching the ones, experimentally measured with atomic force microscopy. To obtain the optical responses of the system, frequency-domain field monitors were used. The frequency points were matching the wavelength span of the source. For the dielectric properties of gold, data from Johnson and Christy were fitted using six coefficients, with a root-mean-square (RMS) error of 0.25. For QDs, a Lorentz oscillator model was employed, with a

resonance wavelength at the emission maximum of the QDs (608 nm) and a linewidth of 110 nm, matching the actual spectral width of the emission band. For the best simulation stability, the mesh area was set around the existing structure in all three principal directions with a mesh step size of 1 nm and the auto-shutoff level was set to 10^{-7}.

Moiré Interference Measurements: To obtain Moiré interference pattern, the substrates need to be stacked with the structure side facing each other. The soft elastomeric substrate has to be pressed onto the glass substrate to ensure the close contact between the gratings. For the distance-dependent measurements, polymethyl methacrylate (PMMA A2 950 kDa, Microchemicals GmbH, Germany) was spin-coated at 1000 rpm for 60 s, followed by soft-baking at 180 °C for 60 s that resulted in a transparent polymeric film with the thickness of approximately 100 nm, determined by spectroscopic ellipsometry (RC2-DI, J.A. Woollam Co., Inc.). For larger film thicknesses, the latter was repeated up to maximum total thickness of approximately 4.4 µm. For the comparative contrast measurements, when two identical metal gratings are combined, index matching oil was applied between two glass substrates. In this case, the stacked structures were illuminated with a 640 nm laser and the reflected light was not filtered out.

Surface Characterization: Produced line structures were imaged by atomic force microscopy (AFM). The scanning was performed in the tapping mode with silicon nitride probes (typical resonant frequency in air: 296 kHz). Amplitude set point was adjusted within the range of 100–200 mV at the scanning frequency 0.5–1 Hz.

Supporting Information

Supporting Information is available from the Wiley Online Library or from the author.

Acknowledgements

Conflict of Interest

The authors declare no conflict of interest.

Keywords

[1] I. Amidror, *The Theory of the Moiré Phenomenon*, Springer, London **2009**.

[2] S. Kishimoto, M. Egashira, N. Shinya, *Opt. Eng.* **1993**, *32*, 522.

[3] J. K. Drinkwater, B. W. Holmes, K. A. Jones, *Proc. SPIE* **2000**, *3973*, 66.

[4] Z. Wu, G. Kelp, M. N. Yogeesh, W. Li, K. M. McNicholas, A. Briggs, B. B. Rajeeva, D. Akinwande, S. R. Bank, G. Shvets, Y. Zheng, *Nanoscale* **2016**, *8*, 18461.

[5] S. Balci, A. Kocabas, C. Kocabas, A. Aydinli, *Appl. Phys. Lett.* **2011**, *98*, 031101.

[6] S. M. Lubin, W. Zhou, A. J. Hryn, M. D. Huntington, T. W. Odom, *Nano Lett.* **2012**, *12*, 4948.

[7] C. Jin, B. C. Olsen, E. J. Luber, J. M. Buriak, *ACS Nano* **2017**, *11*, 3237.

[8] K. Chen, B. B. Rajeeva, Z. Wu, M. Rukavina, T. D. Dao, S. Ishii, M. Aono, T. Nagao, Y. Zheng, *ACS Nano* **2015**, *9*, 6031.

[9] L. A. Ibbotson, A. Demetriadou, S. Croxall, O. Hess, J. J. Baumberg, *Sci. Rep.* **2015**, *5*, 8313.

[10] W. Gao, H. M. Leung, Y. Li, H. Chen, W. Y. Tam, *J. Opt.* **2011**, *13*, 115101.

[11] J.-G. Yun, S.-J. Kim, H. Yun, K. Lee, J. Sung, J. Kim, Y. Lee, B. Lee, *Opt. Express* **2017**, *25*, 14260.

[12] V. Gupta, P. T. Probst, F. R. Goßler, A. M. Steiner, J. Schubert, Y. Brasse, T. A. F. König, A. Fery, *ACS Appl. Mater. Interfaces* **2019**, *11*, 28189.

[13] V. Lesnyak, N. Gaponik, A. Eychmüller, *Chem. Soc. Rev.* **2013**, *42*, 2905.

[14] Y. Shirasaki, G. J. Supran, M. G. Bawendi, V. Bulović, *Nat. Photonics* **2013**, *7*, 13.

[15] X. Gao, B. Han, X. Yang, Z. Tang, *J. Am. Chem. Soc.* **2019**, *141*, 13700.

[16] Z. Wang, Y. Wang, G. Adamo, J. Teng, H. Sun, *Laser Photonics Rev.* **2019**, *13*, 1800276.

[17] S. P. Rodrigues, Y. Cui, S. Lan, L. Kang, W. Cai, *Adv. Mater.* **2015**, *27*, 1124.

[18] M. Noh, T. Kim, H. Lee, C.-K. Kim, S.-W. Joo, K. Lee, *Colloids Surf., A* **2010**, *359*, 39.

[19] A. Raevskaya, V. Lesnyak, D. Haubold, V. Dzhagan, O. Stroyuk, N. Gaponik, D. R. T. Zahn, A. Eychmüller, *J. Phys. Chem. C* **2017**, *121*, 9032.

[20] F. Prins, D. K. Kim, J. Cui, E. De Leo, L. L. Spiegel, K. M. McPeak, D. J. Norris, *Nano Lett.* **2017**, *17*, 1319.

[21] V. Reboud, P. Lovera, N. Kehagias, M. Zelsmann, C. Schuster, F. Reuther, G. Gruetzner, G. Redmond, C. M. Sotomayor Torres, *Appl. Phys. Lett.* **2007**, *91*, 151101.

[22] T. S. Mentzel, D. D. Wanger, N. Ray, B. J. Walker, D. Strasfeld, M. G. Bawendi, M. A. Kastner, *Nano Lett.* **2012**, *12*, 4404.

[23] M. Tagliazucchi, V. A. Amin, S. T. Schneebeli, J. F. Stoddart, E. A. Weiss, *Adv. Mater.* **2012**, *24*, 3617.

[24] S. T. Malak, G. Liang, R. Thevamaran, Y. J. Yoon, M. J. Smith, J. Jung, C. H. Lin, Z. Lin, E. L. Thomas, V. V. Tsukruk, *J. Phys. Chem. C* **2017**, *121*, 13370.

[25] J. Yang, M. K. Choi, D.-H. Kim, T. Hyeon, *Adv. Mater.* **2016**, *28*, 1176.

[26] Z. Zhang, Z. Wang, Z. Xu, Q. Gao, P. Liu, J. Ren, M. Li, C. Zhou, Q. Liao, H. Fu, *Adv. Opt. Mater.* **2018**, *6*, 1800219.

[27] Z. Dai, Q. Ou, C. Wang, G. Si, B. Shabbir, C. Zheng, Z. Wang, Y. Zhang, Y. Huang, Y. Dong, J. J. Jasieniak, B. Su, Q. Bao, *J. Mater. Chem. C* **2019**, *7*, 5954.

[28] B. Jeong, H. Han, H. H. Kim, W. K. Choi, Y. J. Park, C. Park, *ACS Nano* **2020**, *14*, 1645.

[29] L. Kim, P. O. Anikeeva, S. A. Coe-Sullivan, J. S. Steckel, M. G. Bawendi, V. Bulović, *Nano Lett.* **2008**, *8*, 4513.

[30] O. Stroyuk, A. Raevskaya, F. Spranger, O. Selyshchev, V. Dzhagan, S. Schulze, D. R. T. Zahn, A. Eychmüller, *J. Phys. Chem. C* **2018**, *122*, 13648.

[31] H. H. Kim, J. W. Shim, Y.-J. You, Y. J. Lee, C. Park, D. K. Hwang, W. K. Choi, *J. Mater. Chem. C* **2017**, *5*, 1596.

[32] Y. Liu, F. Han, F. Li, Y. Zhao, M. Chen, Z. Xu, X. Zheng, H. Hu, J. Yao, T. Guo, W. Lin, Y. Zheng, B. You, P. Liu, Y. Li, L. Qian, *Nat. Commun.* **2019**, *10*, 1.

[33] J. Jelken, S. Santer, *RSC Adv.* **2019**, *9*, 20295.

[34] G. Scordo, V. Bertana, L. Scaltrito, S. Ferrero, M. Cocuzza, S. L. Marasso, S. Romano, R. Sesana, F. Catania, C. F. Pirri, *Mater. Today Commun.* **2019**, *19*, 12.

[35] M. Mayer, M. J. Schnepf, T. A. F. König, A. Fery, *Adv. Opt. Mater.* **2019**, *7*, 1800564.

[36] P. Probst, M. Mayer, V. Gupta, A. M. Steiner, Z. Ziwei, G. Auernhammer, T. A. F. König, A. Fery, unpublished, **2020**.

[37] F. R. Goßler, A. M. Steiner, O. Stroyuk, A. Raevskaya, T. A. F. König, *J. Phys. Chem. C* **2019**, *123*, 6745.

[38] M. J. Schnepf, Y. Brasse, F. R. Goßler, A. M. Steiner, J. Obermeier, M. Lippitz, A. Fery, T. A. F. König, *Z. Phys. Chem.* **2018**, *232*, 1593.

[39] FDTD Solutions, Lumerical Inc., https://www.lumerical.com/products/fdtd-solutions/ (accessed: November 2020).

7   Conclusion and perspective

This habilitation thesis studies colloidal nanostructures that meet the large-area, flexible, and ultrathin requirements for future developments in nanophotonics. By using predefined building blocks with concepts from colloidal self-assembly, a functional optical surface with emergent spectroscopic properties can be created. Moreover, the colloidal approach can be successfully combined with other functional polymers, such as temperature-responsive,[42, 73] photo-responsive[25, 74] and conducting polymers.[58] This leads to the development of tunable plasmon modes,[42b] which can be used for energy conversion[66] and energy transport.[75]

The concept of functional colloidal nanostructure can be further extended by considering each colloid or assembly as a resonator. This makes large-scale, flexible and high-quality resonators readily available. When an emitter comes in close contact with a colloidal nanostructure, the excitation is used for superior performance (such as faster decay rates, lower thresholds and lower power consumption) in comparison to traditional photonic devices.[76] Efficient coupling of light to the plasmon mode is important for distributing and directing energy. There has been significant interest in colloid-to-film coupling to understand weak and strong coupling scenarios, where the latter is also known as Rabi-splitting.[77] For colloidal polymers, a colloidal emitter at one end can excite dark plasmon modes. These dark modes couple poorly into the far field and are suitable for energy transport below the diffraction limit[78] with mode sizes smaller than the photon wavelength.[71, 75] Alternatively, fluorescent emitters can coherently couple to the hybrid plasmonic modes in a lattice assembly of plasmonic nanoparticles to generate lasing.[79]

The colloidal concept is inspired by the concept of metasurfaces. In this new class of materials, artificially produced building blocks also form the starting point. The precise size, shape, orientation, and arrangement of the unit structures give the metasurface its smart properties, i.e. its capability to manipulate electromagnetic radiation. These materials have optical properties beyond those of conventional materials and can exhibit a negative index of refraction for a particular wavelength.[80] They can be used for imaging below the diffraction limit (superlenses),[81] or for redirecting the flow of light to cloak objects;[82] these are just a few of numerous potential applications. The unique approach of colloidal self-assembly for tailored pre-synthesized building blocks opens up a new class of optical metasurfaces for large scale assembly: colloidal metasurfaces.[31]

Finally, the arranged colloids can be transferred to glass or graphene substrates by means of a pressure transfer.[29, 69, 71] This method allows the colloidal metasurface concept[31] to be extended to the third dimension as a colloidal crystal. Early on, Weller *et al.* examined such colloidal photonic crystals by the self-organization of submicrometer sized polystyrene latex spheres covered with luminescent semiconductor nanocrystals.[83] However, the hexagonal assemblies suffer from differently oriented domains, which limits the use on a large area. This limitation can be solved by developing a hierarchical printing technique with existing self-assembly methods.

8   Appendix

8.1   Further publications during the habilitation period

An exemplary selection of publications was made for this habilitation thesis. The thesis was written between September 2015 and May 2020. Moreover, during this period, other releases have been published. These publications are listed in this chapter.

1. Aftenieva, Olha, Max Schnepf, Börge Mehlhorn, and Tobias AF König. "Tunable Circular Dichroism by Photoluminescent Moiré Gratings." Advanced Optical Materials (2020): 2001280.
2. Brasse, Yannic, Vaibhav Gupta, HC Tomohiro Schollbach, Matthias Karg, Tobias AF König, and Andreas Fery. "Mechanotunable Plasmonic Properties of Colloidal Assemblies." Advanced Materials Interfaces 7, no. 5 (2020): 1901678.
3. Brasse, Yannic, Mareen B Müller, Matthias Karg, Christian Kuttner, Tobias AF König, and Andreas Fery. "Magnetic and Electric Resonances in Particle-to-Film-Coupled Functional Nanostructures." ACS applied materials & interfaces 10, no. 3 (2018): 3133-41.
4. Castelli, Andrea, Alberto Striolo, Anna Roig, Catherine Murphy, Javier Reguera, Luis Liz-Marzán, Axel Mueller, et al. "Anisotropic Nanoparticles: General Discussion." Faraday Discussions 191 (2016): 229-54.
5. Goßler, Fabian R, Anja Maria Steiner, Oleksandr Stroyuk, Alexandra Raevskaya, and Tobias AF König. "Active Plasmonic Colloid-to-Film-Coupled Cavities for Tailored Light–Matter Interactions." The Journal of Physical Chemistry C 123, no. 11 (2019): 6745-52.
6. Gupta, Vaibhav, Patrick T Probst, Fabian R Goßler, Anja Maria Steiner, Jonas Schubert, Yannic Brasse, Tobias AF König, and Andreas Fery. "Mechanotunable Surface Lattice Resonances in the Visible Optical Range by Soft Lithography Templates and Directed Self-Assembly." ACS applied materials & interfaces 11, no. 31 (2019): 28189-96.
7. Gür, Fatih N, Cillian PT McPolin, Søren Raza, Martin Mayer, Diane J Roth, Anja Maria Steiner, Markus Löffler, et al. "DNA-Assembled Plasmonic Waveguides for Nanoscale Light Propagation to a Fluorescent Nanodiamond." Nano letters 18, no. 11 (2018): 7323-29.
8. Karg, Matthias, Tobias AF König, Markus Retsch, Christian Stelling, Paul M Reichstein, Tobias Honold, Mukundan Thelakkat, and Andreas Fery. "Colloidal Self-Assembly Concepts for Light Management in Photovoltaics." Materials Today 18, no. 4 (2015): 185-205.
9. Köhn Serrano, Melissa S, Tobias AF König, Johannes S Haataja, Tina I Löbling, Holger Schmalz, Seema Agarwal, Andreas Fery, and Andreas Greiner. "Self-Organization of Gold Nanoparticle Assemblies with 3d Spatial Order and Their External Stimuli Responsiveness." Macromolecular rapid communications 37, no. 3 (2016): 215-20.
10. Magnozzi, Michele, Yannic Brasse, Tobias AF König, Francesco Bisio, Eva Bittrich, Andreas Fery, and Maurizio Canepa. "Plasmonics of Au/Polymer Core/Shell Nanocomposites for Thermoresponsive Hybrid Metasurfaces." ACS Applied Nano Materials 3, no. 2 (2020): 1674-82.
11. Mayer, Martin, Pavel L Potapov, Darius Pohl, Anja Maria Steiner, Johannes Schultz, Bernd Rellinghaus, Axel Lubk, Tobias AF König, and Andreas Fery. "Direct Observation of Plasmon Band Formation and Delocalization in Quasi-Infinite Nanoparticle Chains." Nano letters 19, no. 6 (2019): 3854-62.

12. Mayer, Martin, Max J Schnepf, Tobias AF König, and Andreas Fery. "Colloidal Self-Assembly Concepts for Plasmonic Metasurfaces." Advanced Optical Materials 7, no. 1 (2019): 1800564.

13. Mayer, Martin, Anja Maria Steiner, Falk Röder, Petr Formanek, Tobias AF König, and Andreas Fery. "Aqueous Gold Overgrowth of Silver Nanoparticles: Merging the Plasmonic Properties of Silver with the Functionality of Gold." Angewandte Chemie International Edition 56, no. 50 (2017): 15866-70.

14. Mayer, Martin, Moritz Tebbe, Christian Kuttner, Max J Schnepf, Tobias AF König, and Andreas Fery. "Template-Assisted Colloidal Self-Assembly of Macroscopic Magnetic Metasurfaces." Faraday Discussions 191 (2016): 159-76.

15. Potapov, Pavel, Martin Mayer, Axel Lubk, Darius Pohl, Johannes Schultz, Tobias AF Konig, and Andreas Fery. "Surface Plasmon Modes in Long Chains of Au Nanoparticles." Microscopy and Microanalysis 24, no. S1 (2018): 1748-49.

16. Probst, Patrick T, Sribharani Sekar, Tobias AF König, Petr Formanek, Gero Decher, Andreas Fery, and Matthias Pauly. "Highly Oriented Nanowire Thin Films with Anisotropic Optical Properties Driven by the Simultaneous Influence of Surface Templating and Shear Forces." ACS applied materials & interfaces 10, no. 3 (2018): 3046-57.

17. Sarkar, Swagato, Vaibhav Gupta, Mohit Kumar, Jonas Schubert, Patrick T Probst, Joby Joseph, and Tobias AF König. "Hybridized Guided-Mode Resonances Via Colloidal Plasmonic Self-Assembled Grating." ACS applied materials & interfaces 11, no. 14 (2019): 13752-60.

18. Schnepf, Max J, Yannic Brasse, Fabian R Goßler, Anja Maria Steiner, Julian Obermeier, Markus Lippitz, Andreas Fery, and Tobias AF König. "Single Particle Spectroscopy of Radiative Processes in Colloid-to-Film-Coupled Nanoantennas." Zeitschrift für Physikalische Chemie 232, no. 9-11 (2018): 1593-606.

19. Schnepf, Max J, Martin Mayer, Christian Kuttner, Moritz Tebbe, Daniel Wolf, Martin Dulle, Thomas Altantzis, et al. "Nanorattles with Tailored Electric Field Enhancement." Nanoscale 9, no. 27 (2017): 9376-85.

20. Schwarz, Dana, Amitava Acharja, Arun Ichangi, Pengbo Lyu, Maksym V Opanasenko, Fabian R Goßler, Tobias AF König, et al. "Fluorescent Sulphur-and Nitrogen-Containing Porous Polymers with Tuneable Donor–Acceptor Domains for Light-Driven Hydrogen Evolution." Chemistry–A European Journal 24, no. 46 (2018): 11916-21.

21. Singh, Prem, Tobias AF König, and Amit Jaiswal. "Nir-Active Plasmonic Gold Nanocapsules Synthesized Using Thermally Induced Seed Twinning for Surface-Enhanced Raman Scattering Applications." ACS applied materials & interfaces 10, no. 45 (2018): 39380-90.

22. Steiner, Anja Maria, Martin Mayer, Daniel Schletz, Daniel Wolf, Petr Formanek, René Hübner, Martin Dulle, et al. "Silver Particles with Rhombicuboctahedral Shape and Effective Isotropic Interactions with Light." Chemistry of Materials 31, no. 8 (2019): 2822-27.

23. Steiner, Anja Maria, Martin Mayer, Maximilian Seuss, Svetoslav Nikolov, Kenneth D Harris, Alexander Alexeev, Christian Kuttner, Tobias AF König, and Andreas Fery. "Macroscopic Strain-Induced Transition from Quasi-Infinite Gold Nanoparticle Chains to Defined Plasmonic Oligomers." ACS nano 11, no. 9 (2017): 8871-80.

24. Stelling, Christian, Chetan R Singh, Matthias Karg, Tobias AF König, Mukundan Thelakkat, and Markus Retsch. "Plasmonic Nanomeshes: Their Ambivalent Role as Transparent Electrodes in Organic Solar Cells." Scientific reports 7, no. 1 (2017): 1-13.

25. Striolo, Alberto, Jongwook Kim, Catherine Murphy, Luis Liz-Marzán, Joerg Lahann, Javier Reguera, Yu Zhou, et al. "Particles at Interfaces: General Discussion." Faraday Discussions 191 (2016): 407-34.

26. Sun, Xiaojun, Junki Kim, Kyle D Gilroy, Jingyue Liu, Tobias AF König, and Dong Qin. "Gold-Based Cubic Nanoboxes with Well-Defined Openings at the Corners and Ultrathin Walls Less Than Two Nanometers Thick." ACS nano 10, no. 8 (2016): 8019-25.

27. Tebbe, Moritz, Christian Kuttner, Martin Mayer, Max Maennel, Nicolas Pazos-Perez, Tobias AF König, and Andreas Fery. "Silver-Overgrowth-Induced Changes in Intrinsic Optical Properties of Gold Nanorods: From Noninvasive Monitoring of Growth Kinetics to Tailoring Internal Mirror Charges." The Journal of Physical Chemistry C 119, no. 17 (2015): 9513-23.

28. Tebbe, Moritz, Martin Mayer, Bernhard A Glatz, Christoph Hanske, Patrick T Probst, Mareen B Müller, Matthias Karg, et al. "Optically Anisotropic Substrates Via Wrinkle-Assisted Convective Assembly of Gold Nanorods on Macroscopic Areas." Faraday discussions 181 (2015): 243-60.

29. v. Klitzing, Regine, Walter Richtering, and Thomas Zemb. "Preface to the Growth of Colloid and Interface Science Special Issue." American Chemical Society, 2019.

30. Volk, Kirsten, Joseph PS Fitzgerald, Pia Ruckdeschel, Markus Retsch, Tobias AF König, and Matthias Karg. "Reversible Tuning of Visible Wavelength Surface Lattice Resonances in Self-Assembled Hybrid Monolayers." Advanced Optical Materials 5, no. 9 (2017): 1600971.

31. Wang, Juanjuan, Yang Zheng, Lele Li, Enping Liu, Chuanyong Zong, Jingxin Zhao, Jixun Xie, et al. "All-Optical Reversible Azo-Based Wrinkling Patterns with High Aspect Ratio and Polarization-Independent Orientation for Light-Responsive Soft Photonics." ACS applied materials & interfaces 11, no. 28 (2019): 25595-604.

32. Ye, Jingjing, Richard Weichelt, Ulrich Kemper, Vaibhav Gupta, Tobias AF König, Alexander Eychmüller, and Ralf Seidel. "Casting of Gold Nanoparticles with High Aspect Ratios inside DNA Molds." Small 16, no. 39 (2020): 2003662.

33. Yu, Ye, Charlene Ng, Tobias AF König, and Andreas Fery. "Tackling the Scalability Challenge in Plasmonics by Wrinkle-Assisted Colloidal Self-Assembly." Langmuir 35, no. 26 (2019): 8629-45.

34. Zessin, Johanna, Max Schnepf, Ulrich Oertel, Tetyana Beryozkina, Tobias AF König, Andreas Fery, Michael Mertig, and Anton Kiriy. "Remarkable Mechanochromism in Blends of a Π-Conjugated Polymer P3teot: The Role of Conformational Transitions and Aggregation." Advanced Optical Materials 8, no. 2 (2020): 1901410.

35. Zhou, Ziwei, Ye Yu, Ningwei Sun, Helmuth Möhwald, Panpan Gu, Liyan Wang, Wei Zhang, et al. "Broad-Range Electrically Tunable Plasmonic Resonances of a Multilayer Coaxial Nanohole Array with an Electroactive Polymer Wrapper." ACS applied materials & interfaces 9, no. 40 (2017): 35244-52.

8.2   Curriculum vitae of the author

Dr. rer. nat. Dipl.-Phys. Tobias A.F. König

Status   Freigeist-Fellow, TU Dresden Young Investigator and IPF Junior Group Leader

Web   kingslab.de

Citations   60 publications with total citations: >1600, Hirsch-index: 23, Article as corresponding author: 22, Article as first author: 14, 60 contributions at conferences, 14 invited lectures

Professional Education

- Apprenticeship to electronic engineer in communication at Deutsche Telekom AG (9/1995-6/1998), civilian service (9/1989-8/1999) and qualifying for university admission via continuation education (8/1999-7/2001)

Scientific Degrees

- Physics, University of Hamburg and University of Karlsruhe, Diplom, A. Hemmerich (The Institute of Laser Physics)/D. Heitmann (Solid state physics) (10/2001 – 01/2008)
- PhD in Physical Chemistry, Prof. Dr. Svetlana Santer and Prof. Dr. Jürgen Rühe, University of Freiburg (12/2011)

Professional Experience

- Deputy Head of Department Functional Colloidal Materials at the Leibniz-Institut für Polymerforschung Dresden e.V. (since 01/2020)
- Junior Group Leader at Leibniz Institute of Polymer Research (IPF) Dresden and Dresden University of Technology (TUD), Dresden (since 09/2015)
- Postdoctoral Assistant at the Institute of Physical Chemistry, Prof. Dr. Andreas Fery, University of Bayreuth (2014-2015)
- Postdoctoral Assistant at the School of Materials Science and Engineering, Prof. Dr. Vladimir V. Tsukruk, Georgia Institute of Technology, Atlanta, GA, USA (2012-2014)

Miscellaneous

- Richard Zsigmondy Scholarship of the German Colloid Society (2021)
- Freigeist-Fellow VolkswagenStiftung
- TU Dresden Young Investigator (accepted by the faculty as an assessor and examiner in doctoral procedures)
- Best Poster Award, Zsigmondy Colloquium, Saarbrücken (2017)
- Best Poster Award, Chemical and Polymer Physics Division (CPP), DPG, Regensburg (2016)
- Nomination for best Poster Award, MRS, San Francisco, CA. (2012)

9 Acknowledgments

10 Declaration

Erklärung gemäß §6 Abs. 2 Habilitationsordnung der Technische Universität Dresden, Bereich Mathematik und Naturwissenschaften (Stand vom 12.12.2010)

gemäß Ziffer 2: Hiermit erkläre ich, Tobias A.F. König, dass die vorliegende Habilitationsschrift vom Bewerber selbst und ohne andere als die darin angegebenen Hilfsmittel angefertigt sowie die wörtlich oder inhaltlich übernommenen Stellen als solche gekennzeichnet wurden.

Bei den gemeinschaftlichen Arbeiten wurde angegeben worauf sich die Mitarbeit des Bewerbers erstreckt (siehe Autorenbeitragserklärung / engl.: author contribution statement).

gemäß Ziffer 6: Hiermit erkläre ich, Tobias A.F. König, keine frühere Habilitationsgesuche an anderen Hochschulen gestellt habe.

Dresden, den 13. Mai 2020